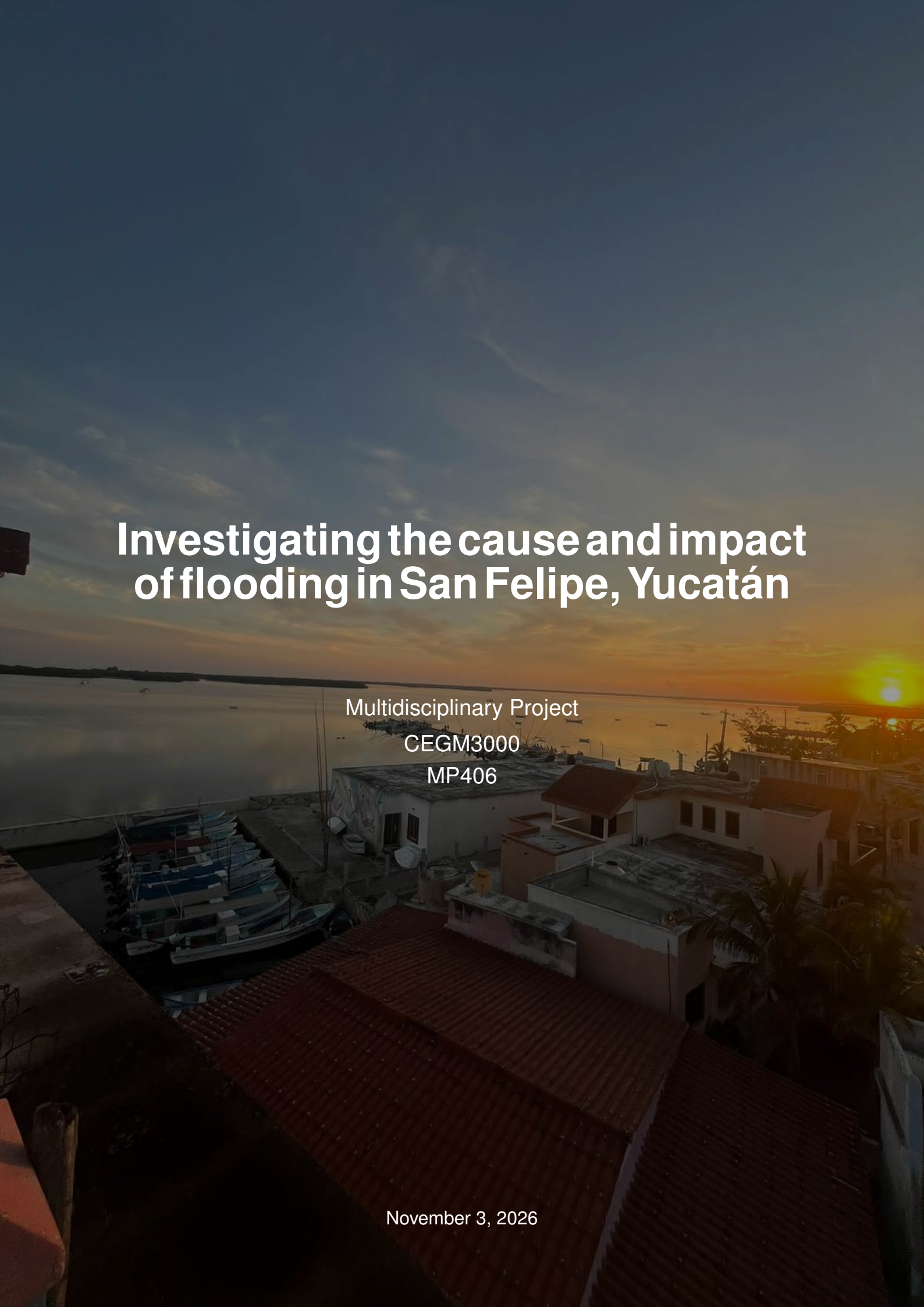


Investigating the cause and impact of flooding in San Felipe, Yucatán

Multidisciplinary Project

CEGM3000

MP406

November 3, 2026

What is the cause and impact of flooding in San Felipe, Yucatán?

MULTIDISCIPLINARY PROJECT

CEGM3000

Authors:

Daan Beeren	5545137	MSc CIE - Hydraulic & Offshore Structures
Thirza van Esch	5561752	MSc CIE - Hydraulic Engineering
Davida van Krimpen	5508649	MSc CIE - Geotechnical Engineering
Mynke Sijsling	5596491	MSc CIE - Hydraulic Engineering
Bjarne Vink	5617065	MSc CIE - Structural Engineering

Supervisors:

Dr. Alec Torres Freyermuth	UNAM LIPC
Dr. Roger Pacheco Castro	UNAM LIPC
Dr.ing. José Álvarez Antolínez	TU Delft CEG
Dr. Jaime Arriaga Garcia	TU Delft CEG
Dr.ir. Paul Korswagen Eguren	TU Delft CEG
Dr. Miguel Cabrera	TU Delft CEG

November 3, 2026



Abstract

San Felipe is a low lying coastal town on the northern coast of the Yucatán Peninsula, bordered by a lagoon and surrounded by wetlands. The town is repeatedly flooded by hurricanes, tropical storms and cold fronts (Nortes). This report investigates the cause and impact of flooding in San Felipe and identifies the critical drivers behind it. A system analysis of the coastal, geohydrological and urban system is combined with an analysis of historical data and fieldwork, consisting of interviews with the local community and GPS measurements. Waves are modelled with SWAN, groundwater flow with MODFLOW and overland flooding with SFINCS. The contribution of precipitation, storm surge and initial infiltration is quantified with a 2^3 factorial design of eight SFINCS simulations, using 50-year return period values for precipitation (306 mm in three days) and storm surge (0.87 m). Finally, the SFINCS simulation of the 2024 Norte event is used to assess the impact of the flood event on the building structures of San Felipe.

Storm surge is the primary driver for the total flooded area (51.8%) and for the average maximum inundation depth (87.4%), whereas precipitation is the primary control on the inundation duration (81.5%). The drivers amplify each other non-linearly, while the infiltration capacity dampens the maximum inundation depths and the duration of the floods. Waves have a significant influence on flooding in San Felipe, but are not yet included in the compound flooding analysis.The MODFLOW model shows that the areas along the quay walls in the north, the main street and the south east of the town are most prone to flooding. This corresponds largely with the experiences of the local residents, but not all critical locations are captured, which indicates that groundwater is not the only driver. The structural vulnerability analysis indicates that timber buildings with a low floor level and no additional protection are the most susceptible to flood damage, whereas more elevated concrete and masonry structures with a protective finish are the least susceptible. Combined with the flood hazard characteristics of the simulated February 2024 event the results suggest that buildings located in the areas bordering the mangroves, the quay wall and the low-lying main street are expected to experience the greatest damage during flood events.

Preface

This research is the final project of the multidisciplinary project (MDP) course (CEGM3000) for the master programmes of the faculty Civil Engineering and Geosciences from Delft University of Technology (TU Delft). As a group of MSc Civil Engineering students in different master tracks, investigating the cause and impact of flooding in San Felipe offers us a multidisciplinary subject for this project.

Readers interested in the modelling aspects used in the analysis on compound flooding, can find more information in Chapter 5. Readers more interested in the method used to define the mutual contribution of the drivers can refer to Chapter 6. The technical reader does not need prior knowledge for reading the research. The report can be used to obtain a better understanding of the system components contributing to floods in San Felipe or to broaden knowledge on modelling of groundwater flow.

Dr.ing. José Álvarez Antolínez connected us with "El Laboratorio de Ingeniería y Procesos Costeros (LIPC) del Instituto de Ingeniería de la Universidad Nacional Autónoma de México (UNAM)" located in Sisal, Yucatán. In collaboration with Dr. Alec Torres Freyermuth a suitable research was found that aligned with all our interests. We show a depth of gratitude to the responsible supervisors José and Alec for the well-considered guidance regarding the set-up of the project in San Felipe. In addition, we highly appreciate the contributions of Dr. Jaime Arriaga Garcia, Dr.ir. Paul Korswagen Eguren and Dr. Miguel Cabrera to the project by steering our project in the right direction to contribute to the problems identified. Alec provided us a warm welcome in México. Besides, in collaboration with M.Eng. Juan Alberto Gómez Liera all necessary resources to conduct the fieldwork in San Felipe were made available. We also want to thank Luisa Méndez for organizing the workshop. During the fieldwork, the local residents made an important contribution by their openness about their experiences during floods. Without their voluntary responses, the critical flooding locations would not have been indicated in this much detail. Special thanks is given to Dr. Roger Pacheco Castro and José Alejandro Medina-Rosado for the help given and time invested in guiding the understanding and modelling of the groundwater. Lastly, we want to express great gratitude to Dr. Cecilia Elizabeth Enríquez Ortiz for providing us with necessary measurements in the area of San Felipe. We would like to thank the Lamminga fund and Fastfund for their financial support.

Sisal, 30 October 2026

Daan Beeren
Thirza van Esch
Davida van Krimpen
Mynke Sijsling
Bjarne Vink



Contents

1 Introduction **1**

2 System Analysis **3**
2.1 Water Balance . . . 3
2.2 System analysis of San Felipe . . . 4
2.2.1 Coastal analysis . . . 5
2.2.2 Geohydrological analysis . . . 6
2.2.3 Urban analysis . . . 9

3 Methodological Framework **11**

4 Data Collection and Processing **13**
4.1 Methodology . . . 13
4.2 Available Data . . . 13
4.3 Historical data . . . 14
4.3.1 Methodology . . . 14
4.3.2 Results . . . 15
4.4 Fieldwork . . . 17
4.4.1 Methodology . . . 17
4.4.2 Results . . . 18
4.5 Results . . . 22

5 Modelling **24**
5.1 SWAN . . . 24
5.1.1 Methodology . . . 24
5.1.2 Model setup . . . 24
5.1.3 Results . . . 25
5.2 MODFLOW . . . 26
5.2.1 Methodology . . . 27
5.2.2 Model setup . . . 27
5.2.3 Validation . . . 30
5.2.4 Sensitivity Analysis . . . 31
5.2.5 Results . . . 32
5.3 SFINCS . . . 34
5.3.1 Methodology . . . 34
5.3.2 Model setup . . . 34
5.3.3 Validation . . . 37
5.3.4 Sensitivity Analysis . . . 38
5.3.5 Results . . . 40
5.4 Damage model . . . 40
5.4.1 Methodology . . . 40
5.4.2 Preparation . . . 40
5.4.3 Model setup . . . 42
5.4.4 Results . . . 46

6 Compound Flooding Analysis **50**
6.1 Methodology . . . 50
6.2 Analysis . . . 51
6.3 Results . . . 53

7 Discussion **55**
7.1 SWAN . . . 55
7.2 Digital elevation model . . . 55
7.3 MODFLOW . . . 56
7.4 SFINCS . . . 56
7.5 Structural damage . . . 57
7.6 Compound flooding analysis . . . 57

8 Conclusion **58**

9 Recommendations **60**
9.1 Sharing data . . . 60
9.2 Future research suggestions . . . 60

References **61**

A Summary of Assumptions in this Report **67**

B Changes Barrier Island over time **70**

C Data visualisation **84**

D Atmospheric Model Reliability **87**

E Data Time Series Visualisation **88**
E.1 ERA5 data . . . 88
E.2 Copernicus and Aviso data . . . 90

F Fieldwork set-up **92**
F.1 Interview set-up . . . 92
F.2 Measurement Set-Up . . . 93

G Fieldwork interview results **94**

H Interviews San Felipe **99**
H.1 Attendance list interviews . . . 99
H.2 Spanish transcription interview 1 . . . 99
H.3 English translation interview 1 . . . 101
H.4 Spanish transcription interview 2 . . . 102
H.5 English translation interview 2 . . . 103

I Reference system **105**
I.1 Reference system LiDAR and GPS data . . . 105
I.2 Offset LiDAR and GPS . . . 107
I.3 Validation Offset GPS Pole . . . 108
I.4 Interpolation San Felipe . . . 110
I.5 Tidal gauge measurements . . . 110
I.6 GTSM Model comparison . . . 111
I.7 Mangrove elevation correction . . . 112

J MODFLOW **113**
J.1 Interpolated map . . . 113
J.2 Boundary and input data . . . 114
J.3 10 dry and wet days input and output MODFLOW . . . 115
J.4 Sensitivity Analysis . . . 116
J.5 February 2024 storm . . . 122
J.5.1 February 2024 10 days . . . 122
J.5.2 February 2024 20 days . . . 123
J.6 October 2020 storm . . . 125
J.6.1 October 2020 storm 10 days . . . 125
J.6.2 October 2020 storm 20 days . . . 127
J.7 Simulation time MODFLOW . . . 128

K Building typologies **129**

L Structural Impact **130**
L.1 Extracting flood hazard from SFINCS 130
L.2 K-Means Clustering 130

M 50-Year Return Period Calculation **133**
M.1 Precipitation 133
M.2 Storm Surge 133

N Synthetic forcings **134**

O Soil AI box with soil samples San Felipe **136**

Chapter 1

Introduction

San Felipe is a low-lying coastal town situated on the northern coast of the Yucatán Peninsula along the Gulf of Mexico (Gobierno del Estado de Yucatán, 2012). Due to its geographical setting, the community is particularly vulnerable to flooding. The town is bordered by a coastal lagoon that connects to the Gulf of Mexico to the north and is surrounded by inland wetlands. Because the sea, lagoon and wetlands are interconnected, elevated water levels can inundate the area from multiple directions simultaneously.
Flooding in San Felipe can be triggered by a variety of hydrometeorological processes. Tropical storms and hurricanes present a major threat due to storm surges, which raise coastal water levels and force seawater into the village and the surrounding lagoon and wetland system. However, extreme flooding events are not exclusively driven by tropical cyclones. Nortes, strong cold-front systems, can also generate onshore winds and elevated water levels that result in coastal inundation (Brinkkemper, Torres-Freyermuth, Mendoza, & Ruessink, 2013). Additionally, intense rainfall contributes to flooding through runoff accumulation, particularly when local drainage capacity is insufficient (Metcalfe, Schmook, & Boyd, 2020), (Gómez-Pompa, Allen, Fedick, & Jiménez-Osornio, 2003).
Table 1.1 provides an overview of historical events that have led to flooding in San Felipe. The analysed events span several decades and were documented through literature reviews and fieldwork interviews. This inventory is not complete, Nortes occur annually in winter months and regularly cause flooding. A comprehensive understanding of the cause and impact of flooding in San Felipe is therefore critical for system understanding and risk assessment.

Table 1.1: List of historical flooding (hurricanes and Nortes) events based on internet sources San Felipe ranging from 1995-2026.

2026	10 October	Hurricane Isaías	(Por Esto!, 2026)
2026	28 January	Norte event	(Yucatán Independiente, 2026)
2024	7-9 October	Hurricane Milton	(Sánchez, 2024)
2024	July	Hurricane Beryl	(National Weather Service, 2024)
2024	5 February	Norte event	(Grillo de Yucatán, 2024)
2022	23 November	Norte event	(Consigna Yucatán, 2022)
2020	October (end)	Hurricane Zeta	(El Heraldo de México, 2020)
2020	October (begin)	Hurricane Delta	(PorEsto!, 2020)
2020	October (begin)	Hurricane Gamma	(Byrne & Travis, 2020)
2005	October	Hurricane Wilma	(NU.nl, 2005)
2002	September	Hurricane Isidore	(Universidad Nacional Autónoma de México, 2014)
1995	September	Hurricane Gilbert(o)	(Yucatán Magazine, 2018)

The flood response of the area is further complicated by the interaction between surface water and subsurface processes (Bauer-Gottwein, Gondwe, & Charvet, 2011). Rainfall infiltration, groundwater dynamics and the exchange of water between the wetlands, lagoons and the sea can influence both the extent and duration of inundation. As a result, floods in San Felipe might be governed by a combination of coastal, meteorological and geohydrological processes rather than a single flooding mechanism. The main goal of this research is therefore to thoroughly understand the cause and impact of flooding in San Felipe. The main research question is formulated as follows:

"What is the cause and impact of flooding in San Felipe?"

To answer this, the research addresses three subquestions:

- What are the main drivers for compound flooding?
- What are the most critical areas prone to flooding and damage in San Felipe based on groundwater flow and interview results?
- What is the impact of flooding on building structures in San Felipe?

Applying the SFINCS model (Super Fast INundation of Coastal Systems) represents a new application for this region. By modelling the interactions between coastal, meteorological and hydrological processes, this study helps fill a gap in understanding local flood dynamics. Additionally, the outcomes contribute to ongoing, long-term research on the mangrove system and wetland restoration within the Ría Lagartos area, where San Felipe is located.

At first, a full system analysis is performed in Chapter 2. Then, a methodological framework is presented in Chapter 3. This could be used as a guide for the rest of the report. Subsequently, Chapter 4 starts with identifying available data and collection of more data through fieldwork. Some data is already processed to later be used in the Chapter 5, Modelling. In this chapter analyses in SWAN, MODFLOW, SFINCS and a structural damage model are prepared. Furthermore, Chapter 6 focusses on the compound flooding analysis. Finally, the report ends with the discussion of the results in Chapter 7 and conclusion in Chapter 8 followed by additional research recommendations suggested in Chapter 9.

Chapter 2

System Analysis

In San Felipe multiple roots might be causing the past flooding events. Floods are a result of a disbalance in the watersystem. To thoroughly understand the interactions of water within the various subsystems, the fundamental water balance is first explained in Section 2.1. Subsequently, Section 2.2 explores the characteristics of San Felipe's main subsystems: the coastal system, the geohydrological system, and the urban system.

2.1 Water Balance

> *"As ripples of heat rise into the air, the raindrop will slowly evaporate. But it won't disappear. Sooner or later, that tiny, translucent bead of water will ascend back to the blue skies. Once there, it will bide its time, waiting to return to this troubled earth again... and again."*
>
> *— Elif Shafak, There Are Rivers in the Sky (Shafak, 2023)*

As cited above, water will not suddenly disappear. It is in a constant cycle, the so called water cycle, which is driven by the radiation of the sun. Water undergoes different processes, as shown in Figure 2.1. Most of the water is located in the seas and oceans. Due to the solar radiation water evaporates and becomes part of the atmosphere as a gas. During the cooling down of the water, condensation, clouds are formed. After this, water turns into precipitation whereafter it returns to the sea.

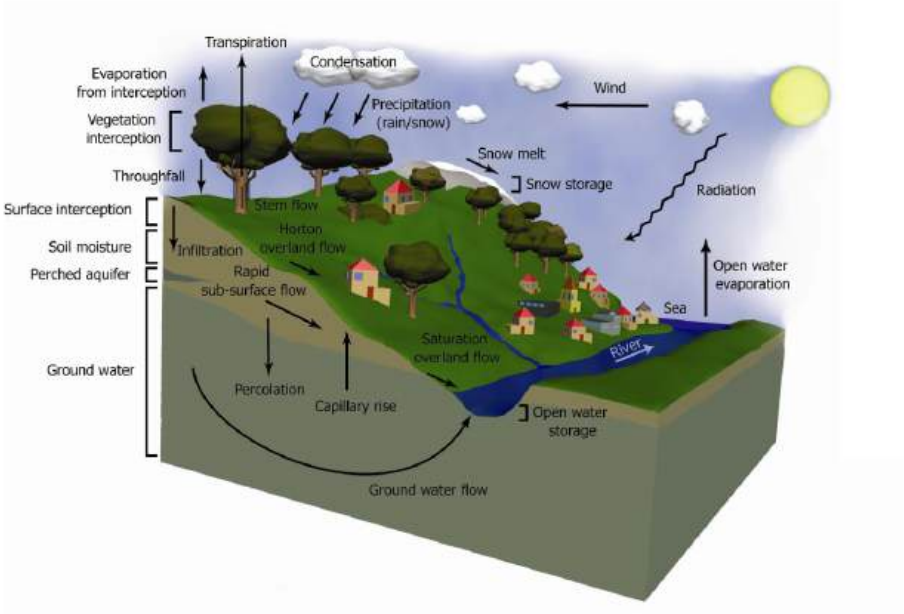


Figure 2.1: Schematisation water cycle within landscape TU Delft (2022).

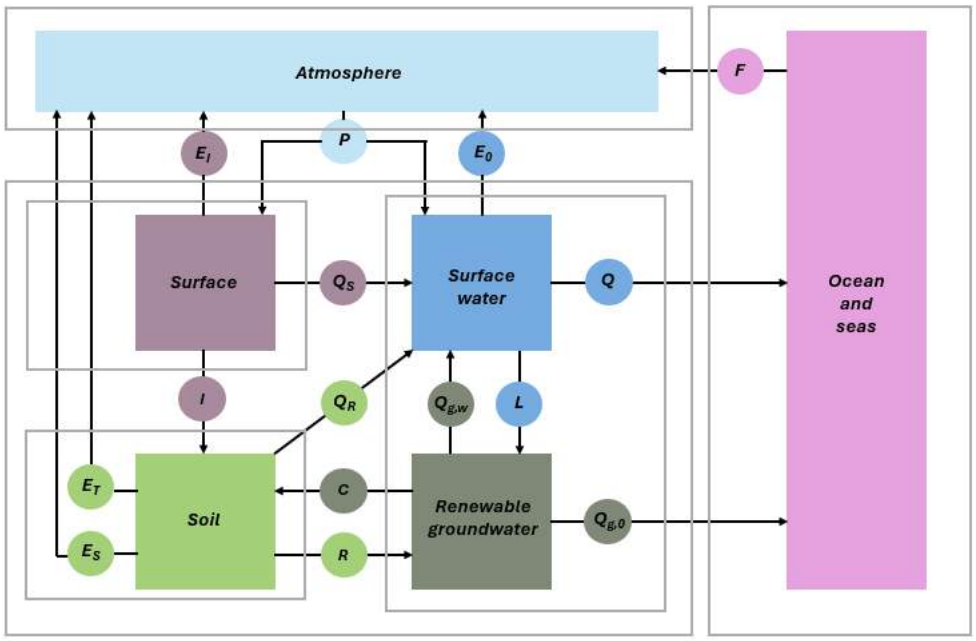


Figure 2.2: Block scheme water cycle, based on TU Delft (2022). Schematic representation of the water cycle visualised in Figure 2.1.

Equations can be formed for the different components of the water cycle in Figure 2.2. When the equations of the surface, the soil, the renewable water and the surface water are added, the total water balance for the land surface looks as follows:

$$\frac{d(S_s + S_u + S_g + S_w)}{dt} = (P - E_I - E_T - E_s)A_s + (P - E_o)A_w - Q - Q_{g,o} \quad [\mathrm{L^3T^{-1}}] \tag{2.1}$$

On the left hand side the derivatives of different water storage terms with respect to time are shown. The total water storage consists of four terms:

S_s : Storage on the surface [L^3]
S_u : Storage in the unsaturated soil [L^3]
S_g : Storage of groundwater in the saturated zone [L^3]
S_w : Open water storage [L^3]

On the right hand side, the flux and area terms are defined as follows:

P : Precipitation [LT^{-1}]
E_I : Interception evaporation [LT^{-1}]
E_T : Transpiration [LT^{-1}]
E_s : Soil evaporation [LT^{-1}]
E_o : Open water evaporation [LT^{-1}]
A_s : Surface area [L^2]
A_w : Open water area [L^2]
Q : Discharge / River flow [$\mathrm{L^3T^{-1}}$]
$Q_{g,o}$: Groundwater outflow [$\mathrm{L^3T^{-1}}$]

A water balance equation can also be made for both oceans and seas, and the atmosphere. This scheme is presented in Figure 2.2 and shows that floods do not have one driver. Often, a flood can occur due to more factors such as infiltration, precipitation and wind speed. The different systems influencing the floods in San Felipe are described in the next sections.

2.2 System analysis of San Felipe

2.2.1 Coastal analysis

San Felipe is located on the coast of the Gulf of Mexico, see Figure 2.3. Since the Gulf is sheltered from the Atlantic Ocean and the Caribbean Sea, swell waves have a limited influence on the coast of San Felipe. The coastal sea north of the Yucatán Peninsula has a wide and shallow continental shelf. This means that the local wave climate is dominated by locally generated wind sea waves. Currents over the Yucatán Shelf are influenced not only by wind, but also by the momentum received from the Yucatán Current (YC) from the Yucatán Channel. If the YC is blocked by eddies in the north of Cuba, it travels west to the Yucatán shelf. If the YC travels north undisturbed, it does not reach the Yucatán Shelf and local winds are dominant (González-Herrera, Solís-Pimentel, Zetina-Moguel, & Mariño-Tapia, 2015).

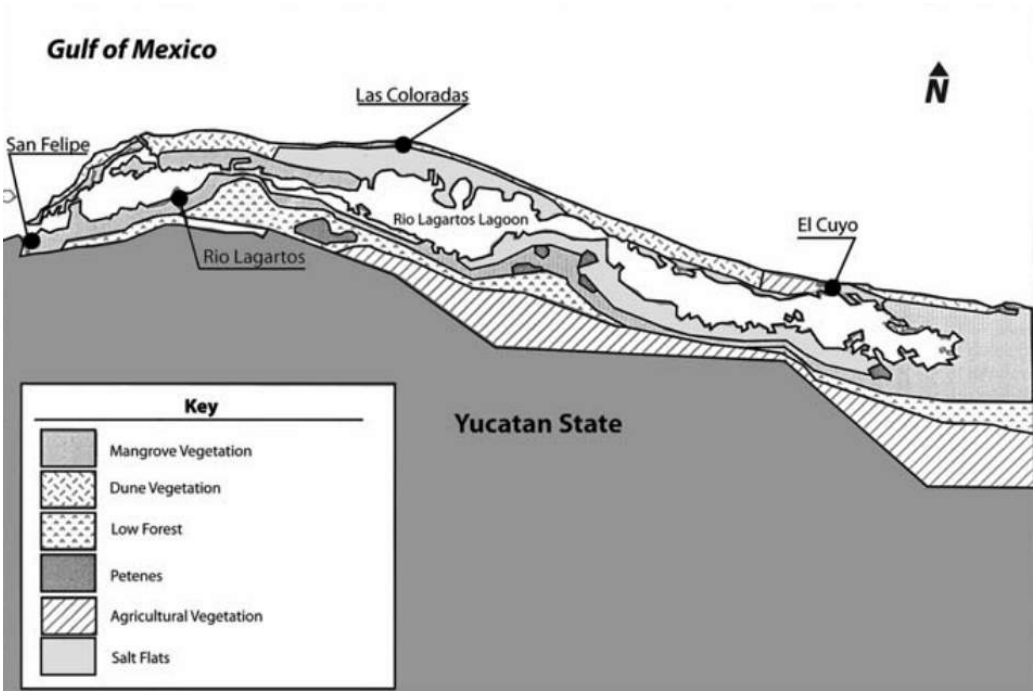


Figure 2.3: Location of San Felipe, Rio Lagartos, Las Coloradas and El Cuyo within the Rio Lagartos Wildlife Reserve. Different labels are given for land cover classifications. (Moan, 1993a)

The average wave climate in Yucatán is relatively mild, with a mean wave height of approximately 0.8 m at a water depth of 10 m. During summer, the coast is affected by tropical cyclones, which can generate waves with significant wave heights of up to 3.6 m. In winter, cold fronts reach Yucatán from the north, generating waves that approach the coast at near-normal incidence (Brinkkemper et al., 2013).

The tidal regime at the north coast of Yucatán is a diurnal mixed tide with a tidal range of 0.1 m for neap tides and 0.8 m for spring tides. (Appendini, Salles, Mendoza, López, & Torres-Freyermuth, 2012) A diurnal mixed tide consists of two high tides and two low tides of which the water levels are unequal (Nidzieko, 2010).

A vegetated barrier island (Ría Lagartos Peninsula) is located in front of San Felipe, see Figure 2.4. This island protects San Felipe from direct physical forces and storms of the Gulf. As the barrier island protects the lagoon from waves and tidal action, mangrove vegetation established itself on the shore of the lagoon. The vegetation stabilises the coastal landforms and makes succession of vegetation possible. This vegetation stabilises the soils and thus provides protection from wind and salt spray. Taller vegetation is present more inland from the shore, along with freshwater petenes. Petenes are freshwater pools forced from the limestone by the subsurface hydraulic gradient. (Smardon, 2009)

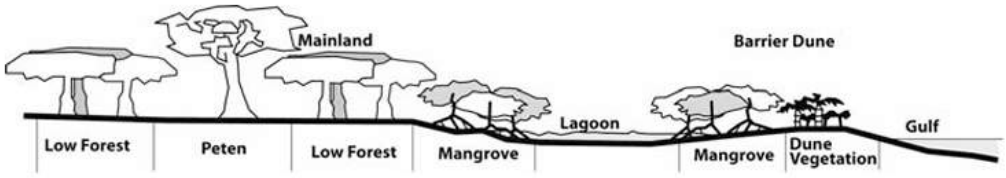


Figure 2.4: Shoreline north coast Yucatán Peninsula including the different stages of vegetation (Moan, 1993b).

Sand is deposited in the westward direction as that is the dominant direction of the current on the north side of the Yucatán Peninsula. An extensive analysis has been conducted on the changes of the barrier island between 1985 and 2026 (see Appendix B). The barrier island was mainly developing between 1985 and 2003. Figure 2.5 shows the barrier island system. The system was growing in westward direction. During the period between 2003 and 2013 the island and breaches on the west side of the island became more stable. Since 2013 the barrier island is (relatively) stable in size. The Ría Lagartos Peninsula reached equilibrium. (Smardon, 2009)



Figure 2.5: Barrier island in front of San Felipe from bird view perspective (Google, 2026c).

The lagoon between the barrier island and the coast has two inlets: the Boca San Felipe and the Ría Lagartos inlet. The Boca San Felipe inlet is the natural mouth of the lagoon and is located on the west side of the barrier close to San Felipe. The lagoon is a closed system and the main driver for water circulation is wind action. Water comes into the lagoon through a barrier breach, trade winds into the lagoon and fresh water through the limestone subsurface. Changes in the surrounding area have a direct influence on the aquatic populations. During the hurricane season (June to November), breaches can occur on the Riá Lagartos barrier peninsula, allowing more wave action closer to San Felipe. Changes in upland erosion levels disrupt nutrients from entering in the lagoon and consequently the water quality. (Smardon, 2009)

2.2.2 Geohydrological analysis

The Yucatán Peninsula can be divided into three physiographic regions. In the northern part, where San Felipe is located, a broad coastal plain is present with a low relief and gradient (Gobierno del Estado de Yucatán, 2012). The surface runoff is little due to this shallow slope. The top soil variates. In San Felipe sand is the main component (Terich, 1970). In marshlands, more organic soils are present. In Figure 2.7 the swamp represents the more organic soils and the Barrier Island Aquifer (BA) represents the sand. The water table in this unconfined aquifer is sensitive to rainfall. The thickness of the soil cover over bedrock is only a few centimetres at most in northern Yucatán (Gómez-Pompa et al., 2003). The bedrock consists of limestones, dolomites and evaporites reaching a depth up till 1500 meter (Weidie, 1985). This is the regional karst aquifer shown in Figure 2.7. This limestone lies on top of igneous and metamorphic rocks. Within this limestone bedrock, karstic areas can be found. These karstic areas are formed due to a large meteorite stuck ~ 66 Ma ago in

a place called Chicxulub (Urrutia-Fucugauchi et al., 2025). The crash of the meteorite fractured and faulted the limestone, resulting in the ring of cenotes, also called sinkholes (Moreno-Gómez, Martínez-Salvador, Liedl, Stefan, & Pacheco, 2021). This ring of cenotes is shown in Figure 2.6.



Figure 2.6: Ring of Cenotes located in the Yucatán Peninsula (Monroy-Ríos, 2020)

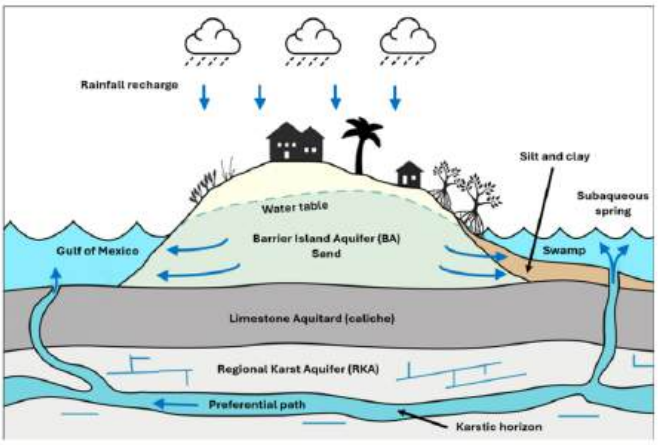


Figure 2.7: Conceptualisation of the hydrogeological system of the northwestern coast of Yucatán (Medina-Rosado et al., 2026)

San Felipe belongs to the hydrological Coastal Area (Moreno-Gómez et al., 2021). The high density of cenotes and the thin soil cover in the coastal plains may be attributed to a more dynamic interaction with intruding seawater and precipitation, thus, faster rates of limestone dissolution, due to the fact that permeable layers zones are developed along the faulted area (Bauer-Gottwein et al., 2011). Karstic areas act as aquifers and drainage systems, see Figure 2.8. This way of drainage is a major reason for the absence of surface drainage on the peninsula (Gómez-Pompa et al., 2003).

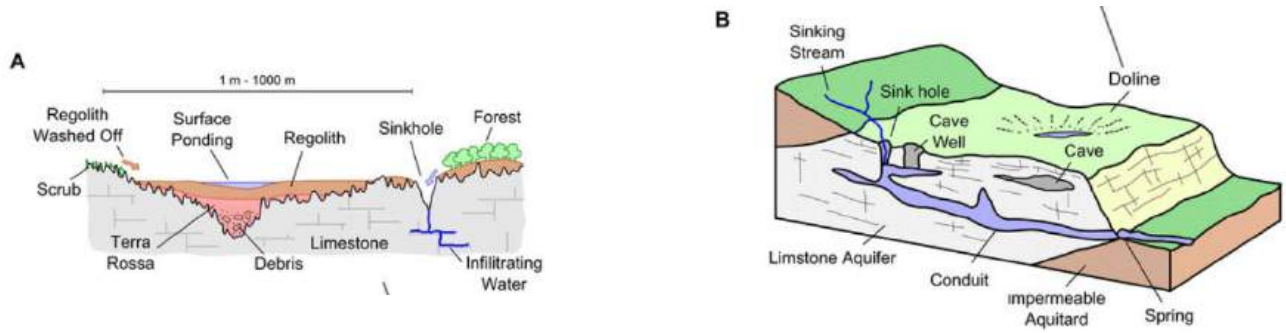


Figure 2.8: Key hydrological characteristics on a karst landscape including (A) the deposition of fine-grained material into a doline depression providing a focus for local drainage and (B) the interception of streams in limestones leading to the development of cave systems and ground water aquifers (Ford & Williams, 2007)

The thin top soil covers an impermeable layer of calcrete in the north. This, with the rising sea level, resulted in a confining layer, also called aquitard, in the north. The thin layer of organic layer from the swamps seal the possible cracks in the limestone which keeps the confining layer in the north intact. This aquitard extends into the Gulf of Mexico, meaning that groundwater needs to flow under or over this aquitard to reach the ocean. This is the reason that the groundwater is under positive head in the north, see Figure 2.9 (Gómez-Pompa et al., 2003).

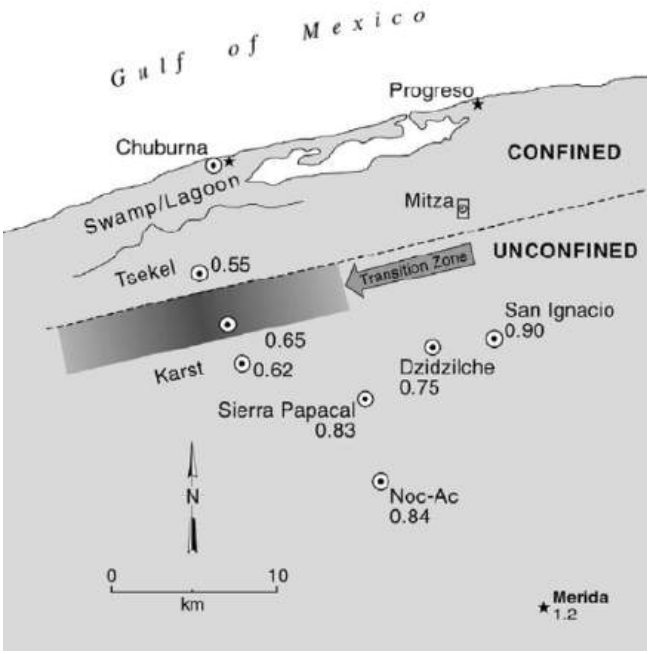
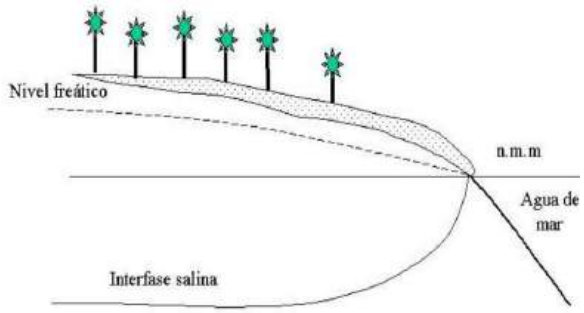
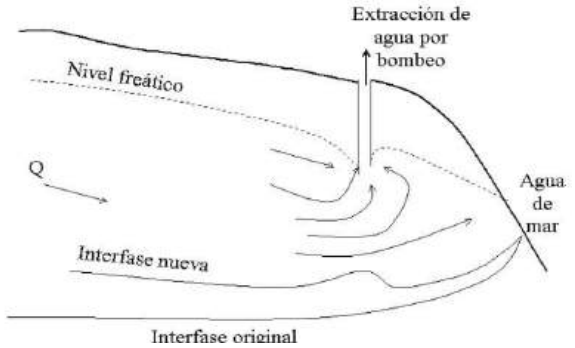


Figure 2.9: Detail of the coast showing water table elevations and coastal zones (confined, transition and unconfined). Groundwater table comes to surface seasonally in the "transition zone". Numbers are depth to the groundwater table in metres (Gómez-Pompa et al., 2003)

Groundwater storage and flow occur in a regional karst aquifer with major cave systems, where groundwater flow is dominated by turbulent conduit flow. This is in the unconfined area in Figure 2.9. Seawater intrusion into the karst aquifers is extensive, extending tens of kilometres inland. As a result, groundwater extraction is confined to a relatively thin freshwater lens, typically less than 10 to 100 m thick. Accurate estimates of groundwater abstraction from the Yucatán Peninsula karst aquifer remain unavailable due to limited monitoring infrastructure (Bauer-Gottwein et al., 2011). (Lesser, 1976) provides the first estimate of regional-scale groundwater recharge, based on simple water balance calculations. He gives the recharge as 150 mm/year, or roughly 14% of mean annual precipitation. However, there are concerns. Due to increased economic activity the extraction of groundwater is expected to rise (Beltrán, 2025). This causes the sweet and salt water interface to shift up, see Figure 2.10a and 2.10b.



(a) Interphase sweet and salt water (Eduardo et al., 2004).



(b) Flow of water when groundwater is extracted (Eduardo et al., 2004)

Figure 2.10: Salt and sweet water interface and the response of groundwater extraction.

The meteorological properties for the Yucatán Peninsula are diverse. In coastal areas, annual rainfall is approximately one-third of that recorded in inland regions. According to Figure 2.11 the annual rainfall in San Felipe is approximately 500 mm/year (CICESE, 2017). The annual rainfall is not reducing over time, however due to climate change the timing of rainfall has changed. There will be more mid-summer drought while weather events generally become more extreme (Metcalfe et al., 2020).

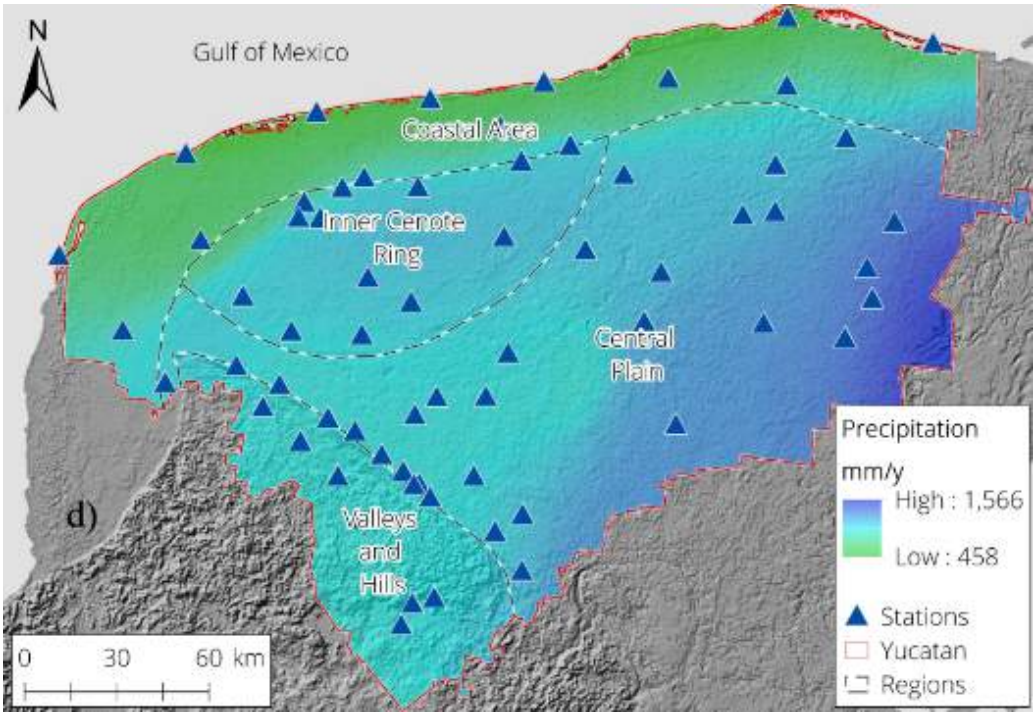


Figure 2.11: Annual rainfall map (high precipitation in dark blue and low in green) for different stations in Yucatán divided in coastal area, inner cenote ring, central plain and valleys and hills. (CICESE, 2017)

In conclusion, San Felipe is sensitive to flooding. Both from sea and from the land. When water arrives from sea, water cannot easily infiltrate due to the impermeable limestone and organic top soil of the swamp in the confined area. The same holds for rainwater.

2.2.3 Urban analysis

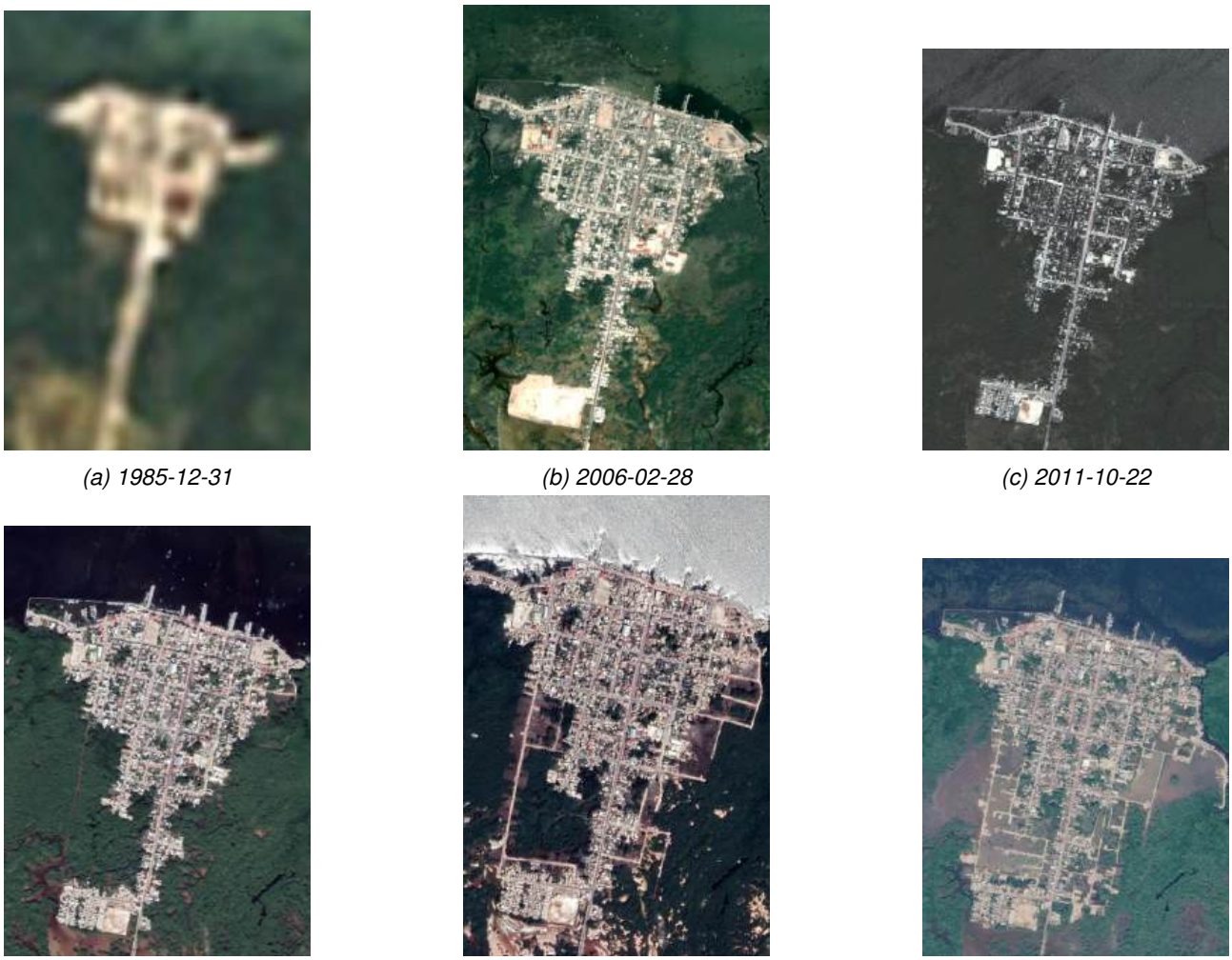
San Felipe has a population of approximately two thousand residents. The town originally developed on an existing natural coastal area even before it was colonised by the Spanish (H. Ayuntamiento de San Felipe, n.d.). Fishery is the main economic activity for San Felipe. Many of the fishers are united in the local fishing cooperative (Chuenpagdee, Fraga, & Euán, 2002). The community mainly fishes on grouper, lobster, squid, shark and seasonally for sea cucumber. The highly profitable sea cucumber industry has encouraged both temporary and permanent immigration from other parts of México. This has lead to conflicts between locals and incomers (Metcalfe et al., 2020).

The quay structure edges the town's shoreline along the Gulf of Mexico, providing a protective seawall barrier and acting as the main mooring area for the local fisherman's collective fleet. The paved road running directly alongside the quay is lined with the characteristic colourful wooden houses that have become a defining feature of San Felipe. The town is famous for its colourful wooden houses but also serves as entrance to the Marine Reserve Ría Lagartos (En Yucatán, n.d.). Tourism has increased in recent years and is therefore another important economic activity for the town (Metcalfe et al., 2020). Despite the fact that approximately 70% of the population in the San Felipe region lives below the poverty line, access to drinking water remains high, with approximately 98% of residents having access to water (Metcalfe et al., 2020).

San Felipe consists predominantly of low-rise detached residential buildings, with a higher building density near the town centre and harbour area (Google Street View, 2026). The built environment behind the quay wall consists of a mix of traditional wooden houses and other types such as reinforced concrete buildings and masonry buildings. These materials allow the buildings to escape heat quickly (Maldonado, Veleva, & Díaz-Ballote, 2011). The building materials used influence the vulnerability of the urban environment to compound flooding. While reinforced concrete structures generally possess adequate resistance against short-duration inundation, prolonged exposure to saline floodwaters and elevated groundwater levels can accelerate material degradation and reinforcement corrosion.

The urban expansion over the years is depicted in Figure 2.12. The expansion took place in the natural protected area that was created to protect the ecosystem of the mangrove wetlands (Procuraduría Federal de

Protección al Ambiente (PROFEPA), 2024). In recent years the expansion mainly took place in the south west and the east part of the town.



(a) 1985-12-31 *(b) 2006-02-28* *(c) 2011-10-22*

(d) 2018-12-12 *(e) 2022-04-16* *(f) 2026-01-09*

Figure 2.12: Urban expansion of San Felipe captured with satellite images from 1985 to 2026 (Google, 2026a).

Chapter 3

Methodological Framework

In this chapter the methodological framework applied in this research is explained. It is summarised in Figure 3.1.

The input data is categorised into four parts: spatial data [4.2], sample data [4.2], climate data [4.3] and data provided by the "San Felipe Research Group" [4.2]. The spatial data includes bathymetric and topographic datasets, LiDAR observations, transects, channel geometries and building footprints, which collectively serve as input for the DEM, SWAN, MODFLOW, SFINCS and the damage model. The sample data includes offshore soil samples collected near San Felipe, used to derive soil parameters for MODFLOW. Climate data consists of time series retrieved from ERA5 (Hersbach et al., 2023), Copernicus (European Space Agency, 2026) and AVISO (AVISO+, 2026), providing boundary conditions and atmospheric forcing for SWAN, MODFLOW and SFINCS. Finally, the data from the San Felipe Research Group includes measured water level time series for SFINCS validation and pressure head sensor data, from which mangrove ground elevations are extracted to build the DEM.

Fieldwork is divided into measurements [4.4] and interviews [4.4]. The measurement data consists of GPS observations used to construct the Digital Elevation Model (DEM) in combination with the spatial data and mangrove elevation information. The interview data consists of a map indicating areas prone to flooding in San Felipe, which is used to validate the spatial flooding extents simulated by MODFLOW and SFINCS, and the structural impact determined by the damage model. Additionally, photo's and videos collected during interviews are used to validate the inundation depths modelled by SFINCS. The integrated DEM [4.4] is implemented in both MODFLOW and SFINCS.

The models each fulfill a specific role within the framework. SWAN [5.1] simulates offshore to nearshore wave propagation for different water level scenarios. MODFLOW [5.2] evaluates groundwater head fluctuations beneath San Felipe during dry and wet conditions. SFINCS [5.3] reconstructs a representative flooding event, generating inundation depths and durations that are directly used by the damage model [5.4] to assess structural impacts. Furthermore, the validated SFINCS model is used to perform a compound flooding analysis [6] that evaluates driver contributions to flooding. The outputs from all models and the compound flooding analysis are interpreted in the discussion [7] and conclusion [8].

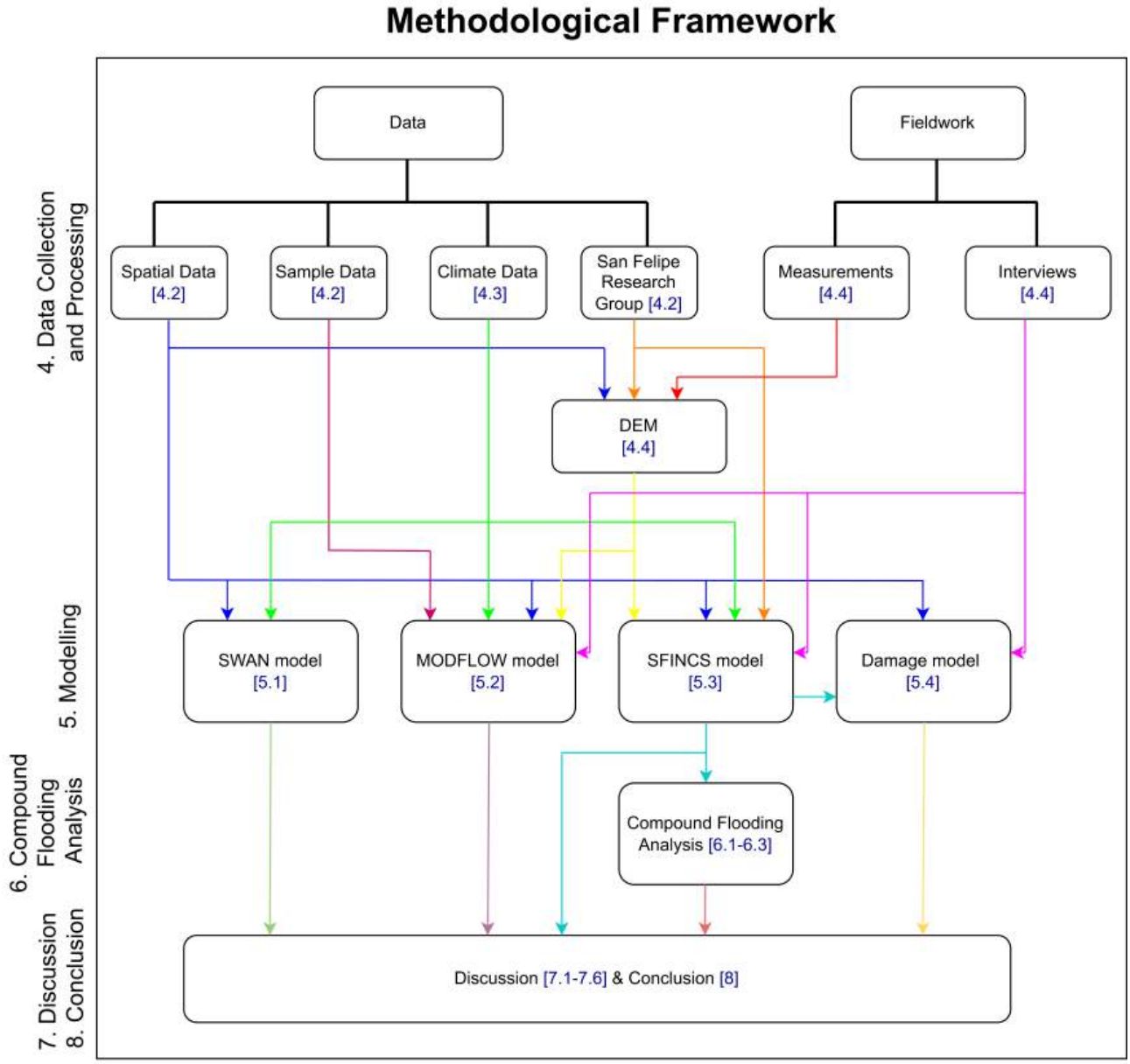


Figure 3.1: Methodological Framework

Chapter 4

Data Collection and Processing

In this chapter the available data is evaluated. Section 4.2 shows in data the kind of data that is available. The available data is supplemented with historical and fieldwork data, described in Section 4.4.

4.1 Methodology

At the onset of the project, available data was limited, see Table 4.1. To satisfy the input requirements for SWAN, SFINCS and MODFLOW model simulations, additional data was gathered through historical records and field investigation. Historical datasets are used as model inputs, whereas fieldwork is conducted to construct a complete elevation profile of San Felipe and to provide observational data for model validation.

4.2 Available Data

Table 4.1 shows an overview of all the available data. Visualisations of some datasets can be found in Appendix C.

Table 4.1: Overview of already available datasets

Dataset	**Description / Source**	**Period / Availability**
Pressure Sensor Data	San Felipe Research Group	03/2025 - 07/2026
Water Level Data Ria Lagartos	San Felipe Research Group	31/05/2025 - 15/06/2026
Water Level Data San Felipé	San Felipe Research Group	19/02/2025 - 14/01/2026
Water Level Data 10 km offshore Sisal	LIPC-UNAM	15/08/2024 - 21/11/2024
Water Level Data El Cuyo	LIPC-UNAM	20/10/2025 - 23/01/2026
LiDAR Data Northern San Felipe	LIPC-UNAM	10/09/2026
Offshore Transect Continental Shelf	LIPC-UNAM	22/10/2025
Channel Data Barrier Island	LIPC-UNAM	-
Bathymetry Data	(GEBCO Compilation Group, 2026)	2026
Topography Data	(INEGI, 2026)	2026
Soil samples Offshore San Felipe	LIPC-UNAM	October 2025
Building footprints	OpenBuildingMap	26/09/2024

Pressure Sensor Data: Pressure sensors measure the hydrostatic pressure exerted by the water column. The dataset also provides both ellipsoidal and orthometric heights for each station location, measured at three reference levels: the ground surface, the casing cap and the pressure sensor position.

Water level Data: Water level timeseries are available from stations in Ría Lagartos, San Felipe, 10 km offshore Sisal and in El Cuyo.

LiDAR Data: The northern part of San Felipe is covered by the Light Detection And Ranging technique (LiDAR) (National Ecological Observatory Network (NEON), 2026), see Figure C.1. LiDAR is a method used to measure the distance between a sensor and the surface. Energy is generated by the laser sensor and reflected from the earth surface. The two-way travel time of the laser is used to estimate the distance.

Offshore Transect: A transect of the bottom profile from the barrier island in front of San Felipé to 10 km offshore made using a boat is available. It shows the slope of the continental shelf. The transect is visible in Figure C.2.

Channel Data: Using a boat, a bottom profile of the channel in the barrier island in front of San Felipé is made. It is visible in Figure C.3.

Bathymetry Data: Bathymetry data is downloaded from (GEBCO Compilation Group, 2026).

Topography Data: Topography data is downloaded from (INEGI, 2026).

Soil Samples: Offshore of San Felipe, different samples are taken, see Figure C.4. Grain size distributions for the different samples are available.

Building footprints: Building footprints and associated building attributes are obtained from OpenBuildingMap, a global building dataset combining OpenStreetMap, Google Open Buildings and Microsoft ML Building Footprints (Oostwegel, Schorlemmer, & Guéguen, 2025). From this dataset the buildings in San Felipe are extracted and displayed in a map with the use of QGIS software, see Figure C.5.

4.3 Historical data

4.3.1 Methodology

To establish a solid foundation for the numerical models, data from multiple sources are analysed. The process consists of three main steps:

1. **Collecting data from multiple sources:** Historical time series of marine, weather and hydrological parameters are gathered from the databases ERA5 (Hersbach et al., 2023), Copernicus (European Space Agency, 2026), and Aviso (AVISO+, 2026).
2. **Analysing time series and extremes:** The collected data is analysed to identify peak values and patterns across historical flooding events and to verify whether the documented flooding events coincide with true physical extremes.
3. **Selecting the storm for modelling:** Based on this data analysis, a specific historical storm event is chosen to be simulated. This selected baseline event is then used to validate the models against field observations.

To understand the causes of flooding in San Felipe, detailed information on weather and sea conditions is required. However, along the northern coast of the Yucatán, there are no reliable, long-term measuring stations or local monitoring networks available. Because of this lack of local data, the research relies on global satellite and modelled re-analysis datasets.

Two distinct types of global products are utilised: re-analysis datasets and satellite-based observations. ERA5 functions as a meteorological re-analysis, meaning it combines physical weather models with historical observations through data-assimilating grids to provide continuous parameters (Hersbach et al., 2020). Conversely, Copernicus and Aviso marine products rely primarily on satellite remote sensing combined with interpolation models to capture sea surface heights and wave dynamics.

Additionally, along-track satellite altimetry data from Aviso is incorporated alongside gridded products. While gridded datasets (L4) offer continuous spatial coverage through interpolation, they can introduce smoothing errors in very shallow coastal zones and near narrow barrier islands like the Ría Lagartos peninsula (Ducet, Le Traon, & Reverdin, 2000). By utilising along-track (L3) data which captures raw sea surface height measurements directly along the satellite's orbital paths passing near San Felipe, more observations are obtained to verify extreme events.

Using satellite and re-analysis data has specific implications for this analysis. While these products provide consistent, multi-decade coverage, they also introduce uncertainties. For instance, satellite measurements of

sea level and waves can be less accurate in very shallow coastal waters, such as the Yucatán shelf, due to interference from nearby land (Vignudelli, Kostianoy, Cipollini, & Benveniste, 2011). Similarly, atmospheric models like ERA5 have a relatively coarse spatial resolution, which means they can sometimes underestimate small, intense local rainstorms. Furthermore, satellite instruments only revisit a given location periodically (temporal resolution), meaning their overpass intervals can sometimes be longer than the duration of extreme events, which can potentially lead to data gaps during peak conditions. Therefore, multiple independent datasets for critical parameters (such as significant wave height and sea level anomaly) are obtained to compare and complement each other in case of these data gaps. The reliability of the atmospheric models are investigated by comparing modelled total water levels driven by ERA5 with ADCP measurements 10 km offshore from Sisal, see Appendix D. Based on these results, the atmospheric data is considered reliable and is used throughout this research.

The methodology involves plotting all timeseries of atmospheric and marine parameters and marking the identified historical flood events as vertical reference lines. The main purpose of this approach is to identify clear patterns and correlations. It helps to determine whether specific drivers are dominating historical flooding events. Data is gathered from three primary global sources: 1- ERA5 Re-analysis, 2- Copernicus Marine Service and 3- Aviso. Different parameters are obtained from different sources as can be seen in Appendix E. Below, the chosen parameters are listed with a short explanation why this parameter could effect the compound flooding:

- **Significant Wave Height (SWH):** Represents the height of the waves, which directly influences flooding through wave setup and overtopping.
- **Windspeed:** Exerts surface shear stress on ocean surface, forcing coastal water accumulation.
- **Sea Level Anomaly (SLA):** Directly influences flooding through a temporary higher baseline water level.
- **Wind setup:** Accumulates large volumes of water towards the coast.
- **Precipitation:** More precipitation over time increases the groundwater table and decreases the soil infiltration capacity.
- **Storm Surge:** The combination of storm's powerful winds with low atmospheric pressure pushes water onto the coast.
- **Peak Wave Period:** Longer wave periods carry more energy and creates a higher run-up.
- **Wind Wave Direction:** The wind wave direction can control the location of the flooding and from which direction wind waves are coming.

Total water level is important for further modelling, but is not used as a driver for compound flooding. The total water level consists of the pure tide, storm surge and changes in annual mean sea level (Copernicus Climate Change Service, 2022).

4.3.2 Results

In Table 4.2, the maximum values for the different parameters are displayed per identified flooding event. These values are extracted from the time series in Appendix E. The highest values are coloured dark red, and the lowest values are coloured white. It can be observed that for the flooding in June 2020, all parameters had relatively low values, while for October 2005, more extremes are observed. This indicates that floods do not only occur with extremes, but can also be caused by multiple moderate drivers acting simultaneously. The data is extracted from following sources: ERA5 (Hersbach et al., 2023), Copernicus (European Space Agency, 2026) and AVISO (AVISO+, 2026).

Table 4.2: Different parameters affecting compound flooding. Sea Wave Height (from ERA5 and Copernicus), Wind speed (from ERA5), Sea Level Anomaly (from Copernicus and Aviso), Wind Setup (from Aviso), Precipitation for the different months (for the Nortes in February 2024 data from half January to half February is used) (from ERA5), Storm Surge (from ERA5), Peak Wave Period (from Copernicus) and Wind Wave Direction (Copernicus).

Event	SWH (ERA5) (m)	Windspeed (ERA5) (m/s)	SLA (Cop) (m)	SWH (Cop) (m)	SLA (Aviso) (m)	Windsetup (Aviso) (m)	Precipitation (ERA5) (mm, cum.)	Storm Surge (ERA5) (m)	Peak Wave Period (Copernicus) (s)	Wind Wave Direction (Cop) (Direction)
Sept 1988 (Gilbert)	6,9	–	–	–	–	–	–	0,52	12	NE to N
Sept 2002 (Isidore)	5,9	22	0,32	5,1	–	–	411	0,66	9,9	N
Oct 2005 (Wilma)	6,9	27	0,25	5,7	0,14	0,019	349	0,52	10	NE to N
Jun 2020 (Cristóbal)	2,5	13	0,25	2,5	0,029	-0,054	164	0,22	7,1	E to SE
Oct 2020 (Gamma(G)/Delta(D)/Zeta(Z))	4,0	19	0,41	3,8	0,35	-0,068	387	0,25	11	G: NE, D: N, Z: N to SE
Feb 2024 (Nortes)	3,9	16	0,16	4,2	0,091	-0,15	34	0,43	11	NW
Oct 2024 (Milton)	3,9	19	0,43	3,9	0,18	0,022	160	0,34	10	NW to NE

Flooding Typologies

By analysing the parameter distributions across these historical events, different distinct flooding typologies emerge for San Felipe, highlighting the compound flooding:

Hurricanes (Hurricane Wilma 2005, Hurricane Gilbert 1988, and Hurricane Milton 2024)

These major tropical cyclones represent the most severe compound threat to San Felipe, because they simultaneously trigger extremes across multiple parameters. For instance, Hurricane Wilma (October 2005) exhibits the highest recorded significant wave heights (> 6.8 m in ERA5 and > 5.7 m in Copernicus), maximum wind speeds exceeding 27 m/s, and an exceptional cumulative rainfall total of 349 mm (NU.nl, 2005). Similarly, Hurricane Milton (October 2024) and Hurricane Delta/Zeta/Gamma (October 2020) combine high Sea Level Anomalies (> 0.41 m) with heavy precipitation (> 159 mm) (El Heraldo de México, 2020; PorEsto!, 2020; Sánchez, 2024). This demonstrates that severe hurricanes inflict flooding through a compounding mechanism: extreme coastal storm surges with intense local rainfall that cannot drain due to the high coastal water tables.

Tropical storms (Tropical storm Cristóbal June 2020)

In contrast, events such as tropical storm Cristóbal (June 2020) show less extreme marine conditions while being driven primarily by heavy precipitation. During June 2020, significant wave heights remained relatively low (2.5 m) and winds were moderate (13 m/s), yet the system produced a substantial cumulative rainfall of 164 mm (Novedades Yucatán, 2020; Santana, 2020). This highlights an alternative flooding mechanism: minimal coastal overtopping, where inundation is driven purely by pluvial accumulation and a rapidly rising water table exceeding drainage capacity of the urban area.

Cold fronts (Nortes)

In addition to extreme tropical cyclones during the summer and early autumn, the monthly aggregated Sea Level Anomaly, see Figure 4.1, reveals a distinct seasonal pattern driven by winter weather systems (Nortes). From September through December, both the mean SLA and the standard deviation (representing storm variability) increase significantly compared to the calmer summer months. This indicates that seasonal cold fronts push water volumes onto the shallow Yucatán shelf, creating a structurally higher baseline water level and increasing vulnerability to compound flooding events during the autumn and winter seasons.

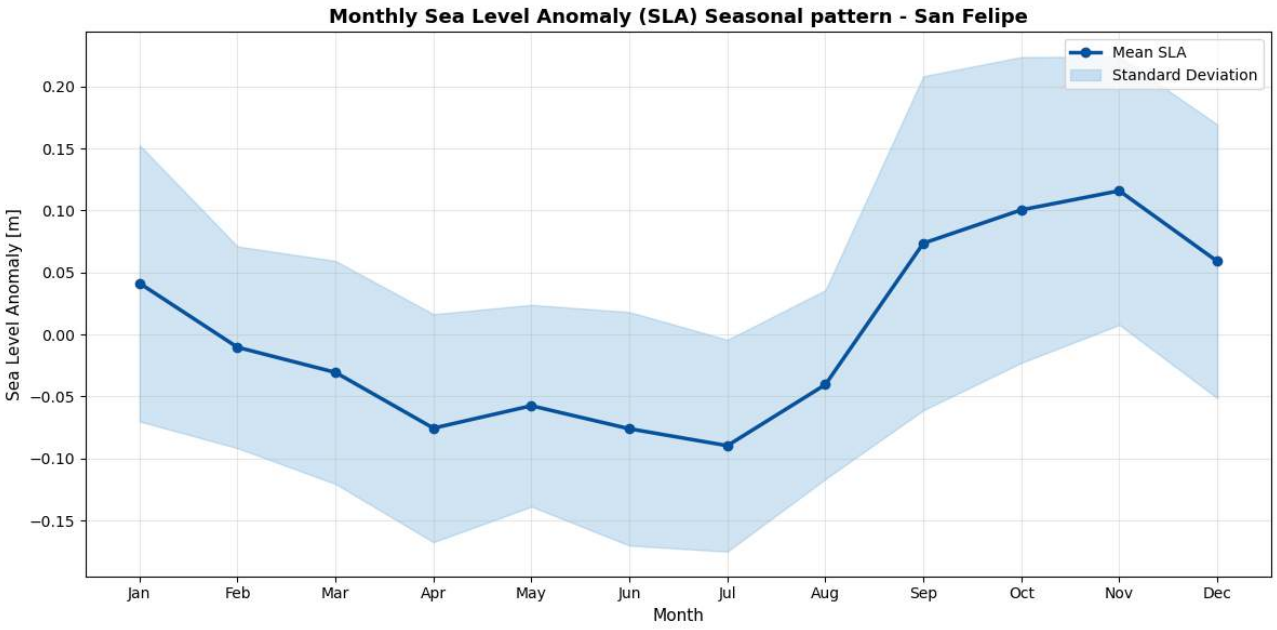


Figure 4.1: Monthly Sea Level Anomaly (SLA) seasonal pattern and standard deviation for San Felipe (1995–2026), illustrating the elevated water levels and storm variability during the autumn and winter Nortes season

Overall, the data analysis confirms that San Felipe's flood risk is driven either by simultaneous multi-hazard hurricane impacts (marine surge combined with heavy rain) or by prolonged atmospheric depressions trapping large volumes of freshwater on land. Numerical modelling using SFINCS and MODFLOW is therefore essential to simulate these interacting drivers accurately.

4.4 Fieldwork

4.4.1 Methodology

Interview

Interviews are carried out among local San Felipe residents to capture their personal observations of past flooding events. These sessions are used to reconstruct a timeline of historical floods and generate spatial mapping of residential locations, safe areas and unsafe areas. The interviews also investigate the specific mechanisms and causes behind the flood events.

GPS

Measurement devices

To accurately use the GPS Rover, a base station is installed on top of "Hotel San Felipe de Jesús". The GPS measurements of the GPS Rover are relative to an unknown reference system. There are three types of GPS measurements taken: GPS Rover on pole, GPS Rover in a backpack and GPS Rover attached to a car. The height of the GPS Rover pole is 1.8 m.

Next to the GPS Rover, a large ruler is used to measure the water depth at several locations. Appendix F.2 visualises the measurement devices used.

GPS Measurements

Measurements by car, foot and pole are performed at the locations indicated in Figure 4.2. The GPS pole measurements are most accurate as the pole is hold into place for approximately a minute.

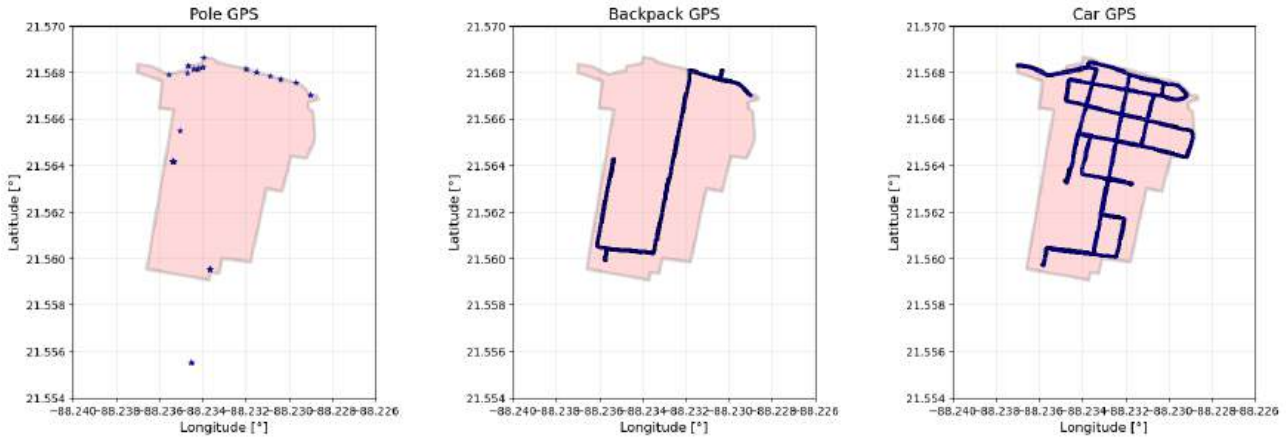
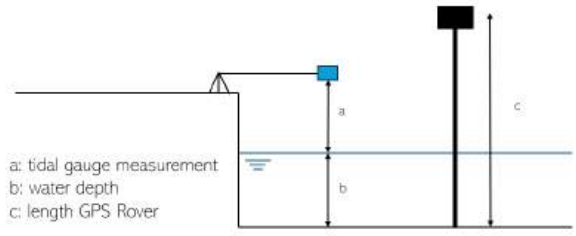


Figure 4.2: The GPS Rover measurements by pole (left), backpack (middle) and car (right) given in the same spatial reference as San Felipe. The polygon of San Felipe is given in red. The blue stars visualise the exact location of the measurements.

Tidal measurement

To establish a consistent vertical reference datum for the SFINCS and MODFLOW model, a temporary tide gauge is deployed in San Felipe during the fieldwork. A tide gauge, an ultrasonic sensor, was placed at 21°34'05.9"N 88°14'04.8"W, see Figure 4.3b. A schematisation of the setup can be found in Figure 4.3a. The length of the GPS Rover (c) is known. This is 1.8 m. The GPS location has been measured directly below the tide gauge. In order to find the water level, the water depth (b) is added to the GPS location. This is the reference from which the tidal fluctuations are plotted. Appendix F.2 shows the setup of these measurements. The sensor recorded water distance data over a 5 hour period.



(a) Schematisation of tide gauge setup during fieldwork



(b) Location of tide gauge at 21°34'05.9"N 88°14'04.8"W (Google, 2026a)

Figure 4.3: Tide gauge setup and location in San Felipe.

4.4.2 Results

Interview

Map
A mapping exercise with the local community is conducted to capture local flood vulnerabilities of historical flooding events in San Felipe (See Appendix F.1).

The interviewees identified safe and less safe regions on a map of San Felipe. The different maps can be found in Appendix G. Combining these maps resulted in the map displayed in Figure 4.4. The following can be concluded from this map:

- **High-risk zones (red markers):** Red stickers, denoting areas prone to flooding, are mostly clustered along the edges of San Felipe and the main street, including areas like the waterfront, harbour and edges of the mangrove wetlands. Residents distinguished between zones flooded primarily by storm surges and high tides (concentrated near the waterfront and boundaries) and areas prone to severe water stagnation during precipitation events (the main street)

- **Safe elevations (green markers):** Green stickers, denoting safer areas, are sparsely distributed on the higher laying areas of the town.

Marine and storm-driven flooding is concentrated along the coastal waterfront, harbour and the edges bordering the mangrove wetlands, where severe storms, tropical cyclones and seasonal Nortes cause wind setup that pushes water into the Ría Lagartos lagoon, overtopping the northern seawall or flooding the town from the backside via low-lying mangrove borders. Conversely, pluvial and hydrological flooding is observed along the main street and inland depressions, where the flat topography, low permeability of the subsurface and restricted urban drainage capacity prevent efficient infiltration or runoff during intense rainfall, resulting in water stagnation.

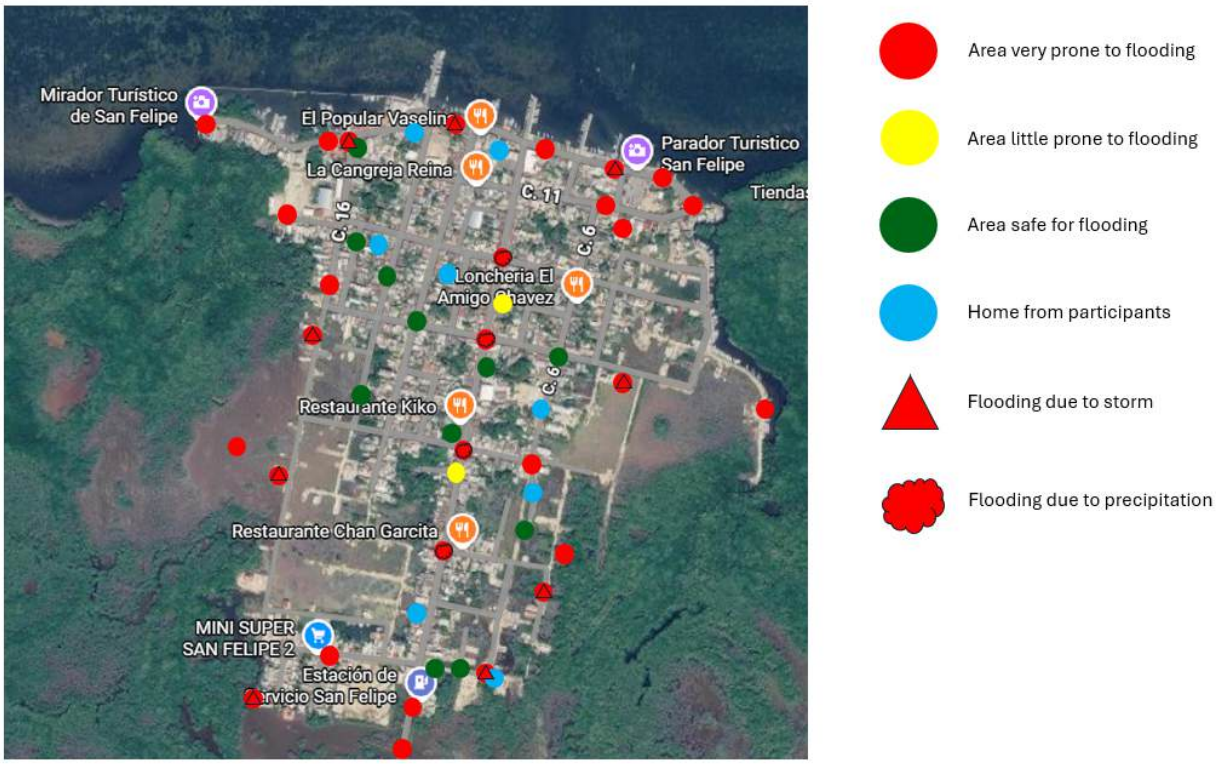


Figure 4.4: Participatory mapping results of San Felipe: identification of high-risk flood zones (red), safe elevations (green), participant home locations (blue), and specific historical flooding drivers based on community interviews, see Appendix G.

Timeline

A total timeline is made for all participants and can be seen in Figure 4.5 below. This timeline guides the selection of the target flood event for modelling.

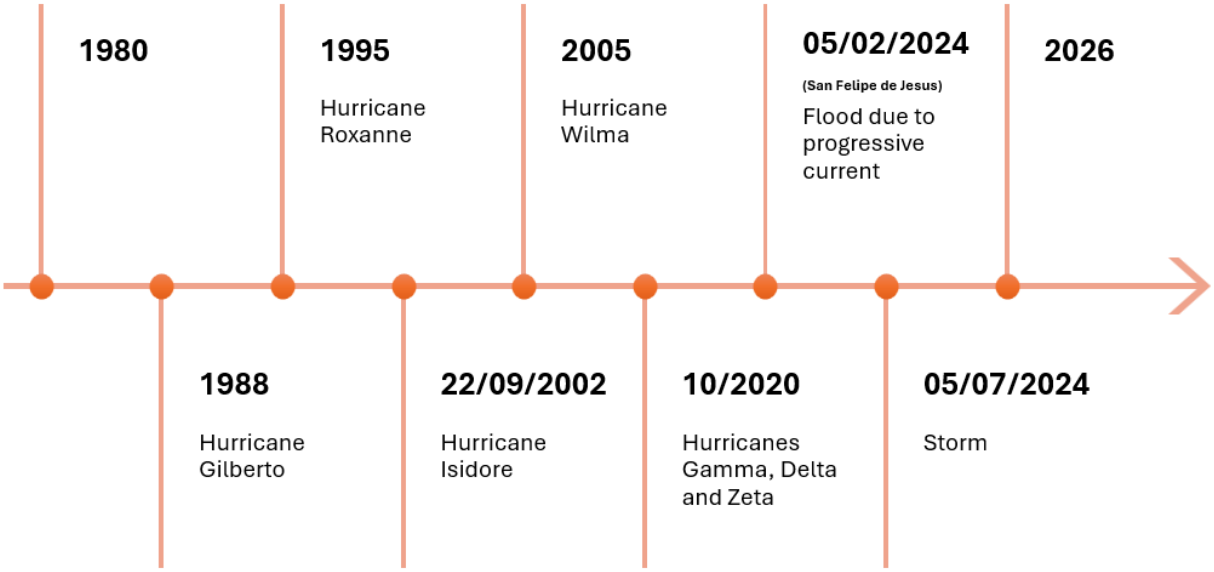


Figure 4.5: Historical floods placed on timeline ranging from 1980 up to 2026 by participants of the interviews in San Felipe.

Conversation
When the maps were finalised by the interviewees an additional conversation regarding the findings took place in Spanish, see Appendix H for the Spanish transcription and the English translation. Also, additional questions about flood characteristics and structural damage were asked. This section discusses the findings that can later be used to validate the numerical model outcomes. It is also used for the analysis of structural damage in San Felipe. The most important findings are listed below.

Flood characteristics:

- During frequent events of combined spring tide and rainfall, the water level reaches a height of approximately 15 cm in the lower parts of the town. The water is only present for a couple of hours during the more frequent spring tides.
- Especially in the 2024 February storm the water rose very quickly. Most people had not seen that much of water in the town before.
- Hurricane Isidore (2002) caused severe structural damage. The water almost reached the height of the ceiling.
- During heavy rainfall two flows of waters from the mangroves merges at the sound part of the town close to the gas station. Usually the water level there rises 20 cm leading to closure of entrance and exit of the town.
- Due to Isidore (2002) the water level almost reached 2.5 m.
- During normal storm the water level generally reaches 20 to 30 centimetres.
- The north wind season starts in autumn. The water level gradually rises until it flows over and floods the lower parts of the town. The residents want quick drainage of the flooded area because stagnant water easily causes road damage.

Damage characteristics:

- During frequent events of spring tide there is not a lot of garbage taken in the town by the water
- Delta (2020) was an event with extreme rainfall. The road to Panabá was severely damaged due to being inundated for days.
- Hurricane Isidore (2002) caused severe structural damage. The water almost reached the height of the ceiling.
- The residents want quick drainage of the flooded area because stagnant water easily causes road damage.

- The saltpeter in the water chemically attacks the houses in town when there are floods.

Building characteristics:

- Houses are protected from salt attack by building a layer of masonry, concrete or protective tiles of 0.5 to 1.5 m.
- Utilities are protected by putting them as high as possible during floods.

GPS

Based on the GPS measurements a continuous interpolated map is made based on Inverse Distance Weighted (IDW) interpolation, see Appendix I, Section I.4. The interpolation covers the whole urban area of San Felipe, see Figure 4.6.



Figure 4.6: Continuous grid resulted after IDW interpolation (p=2) based on GPS measurements during fieldwork in San Felipe. Elevations are ranging from 0.6 m (dark-green) to 0.01 m (white).

The already available LiDAR map underestimates the GPS measurements, see Figure I.3. To compensate for this underestimation, the LiDAR is adjusted with $+0.48$ m. The method for the shift of the LiDAR data can be found in Appendix I.

Tidal measurement

In Figure 4.7, the blue curve represents the five-hour tidal measurements collected during fieldwork. A more detailed plot of these measurements is provided in Appendix I, Section I.5, Figure I.8. The red curve represents the future water level time series obtained from the Global Tide and Surge Model (GTSM), which is based on meteorological datasets from Copernicus/ERA5 ((Hersbach et al., 2023) and European Space Agency (2026)). The data is extracted from the nearest available model station to San Felipe (latitude 21.5770° N, longitude 88.3450° W).

The GTSM data are aligned with the field measurements using a least-squares minimisation approach, resulting an optimal vertical offset of -0.656 m. This offset is applied to correct the topographic (INEGI, 2026)), bathymetric (GEBCO Compilation Group, 2026) and other datasets to ensure consistency across all model components. This adjustment is intended to align the model elevations with the local GPS reference system.

However, considerable uncertainty comes with the estimated offset, as it is derived by comparing field measurements with future water level data. Consequently, the calculated offset may not accurately represent the

actual local water level reference. This uncertainty should be taken into account when interpreting the simulation results, as the applied correction may introduce systematic errors into the model elevations.

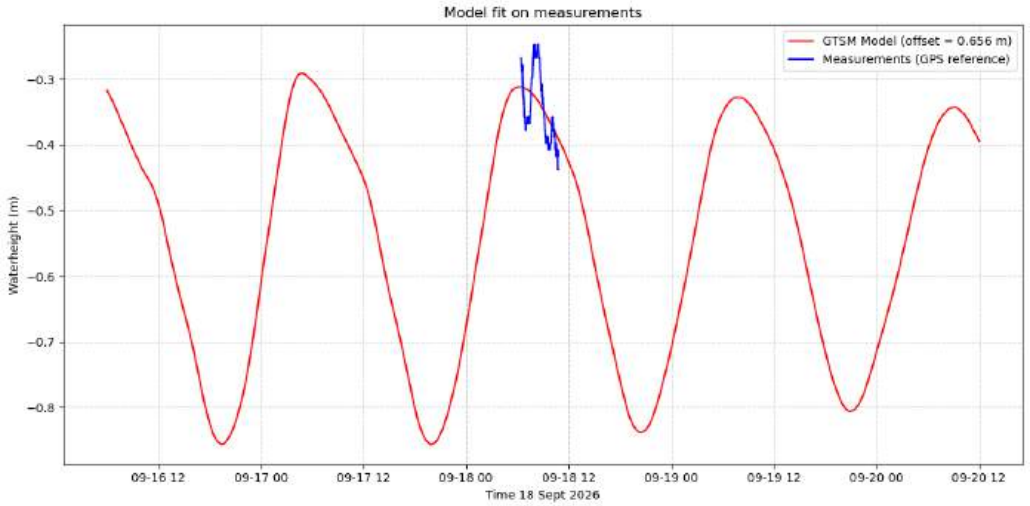


Figure 4.7: Comparison between the corrected GTSM model tide and field measurements (GPS reference) on September 18, 2026. The GTSM model is shifted with an offset of -0.656m.

4.5 Results

After the historical data gathering and the fieldwork, the table with available data (see Table 4.1) is expanded, see Table 4.3.

Table 4.3: Overview of available data and historical and fieldwork data used for modelling purposes

Dataset	**Description / Source**	**Period / Availability**
Pressure Sensor Data	San Felipe Research Group	03/2025 – 07/2026
Water Level Data Ría Lagartos	San Felipe Research Group	31/05/2025 – 15/06/2026
Water Level Data San Felipe	San Felipe Research Group	19/02/2025 – 14/01/2026
Water Level Data 10 km offshore Sisal	LIPC-UNAM	15/08/2024 – 21/11/2024
Water Level Data El Cuyo	LIPC-UNAM	20/10/2025 – 23/01/2026
LiDAR Data Northern San Felipe	LIPC-UNAM	10/09/2026
Offshore Transect Continental Shelf	LIPC-UNAM	22/10/2025
Channel Data Barrier Island	LIPC-UNAM	–
Bathymetry Data	(GEBCO Compilation Group, 2026)	2026
Topography Data	(INEGI, 2026)	2026
Soil samples	Offshore San Felipe	October 2025
Building footprints	OpenBuildingMap	26/09/2024
Significant Wave Height (SWH)	(European Space Agency, 2026), (Hersbach et al., 2023)	1980–2026, 1995–2026
Windspeed	(Hersbach et al., 2023)	1997–2026
Sea Level Anomaly (SLA)	(European Space Agency, 2026)	1993–2026
Wind setup	(AVISO+, 2026)	1995–2026
Precipitation	(Hersbach et al., 2023)	1995–2026
Storm Surge	(Hersbach et al., 2023)	1980–2024
Peak Wave Period	(Hersbach et al., 2023)	1988–2026
Wind Wave Direction	(Hersbach et al., 2023)	1988–2026
Total Water Level	(Copernicus Climate Change Service, 2022)	1950–2024
Map San Felipe (safe/unsafe)	Fieldwork	–
Timeline of historical floodings	Fieldwork	1988–2024
Interpolated elevation map	Fieldwork	–
Vertical offset (tidal measurements)	Fieldwork	5 hours (18/09/2026)
Photos and videos of 2024 flooding	Fieldwork	05/02/2024

Next to this new data, it is concluded that the cold front (Norte) event of February 2024 is selected for further analysis using SWAN, MODFLOW, SFINCS and the damage model. While hurricanes represent more extremes, their low frequency and localised intensity often lead to data gaps. In contrast, Nortes occur with high frequency on the Yucatán Peninsula, making their risk and impact highly relevant for the local residents

of San Felipe. Furthermore, the availability and completeness of hydrodynamic and meteorological data for the February 2024 storm results in higher reliability. Choosing this recent Norte event enables model validation since photographs, videos and field measurements are available to validate the models and verify the inundation height and extent calculated by SFINCS.

Chapter 5

Modelling

In this chapter different models are explained. The SWAN model propagates waves from offshore to nearshore, see Section 5.1. The MODFLOW model is used to simulate groundwater flow in San Felipe, see Section 5.2. The SFINS model is used to simulate compound flooding, see Section 5.3.

5.1 SWAN

First in Section 5.1.1 the methodology of propagating waves from offshore to nearshore is described, followed by the model setup in Section 5.1.2 and its results in Section 5.1.3.

5.1.1 Methodology

The third-generation wave model SWAN (Simulating WAves Nearshore) can be used to propagate waves from far offshore to nearshore. Within the scope of this research, this wave characteristic translation is between an offshore location on the Gulf of Mexico and a nearshore location at San Felipe. SWAN is a numerical model developed for coastal water areas. It is based on the action balance equation in which the action density spectrum and energy density spectrum are included. The initial wave conditions are generated according to a JONSWAP spectrum, as the model will simulate wind generated waves. The domain of interest is determined by a rectangular grid with a constant resolution in longitudinal and lateral direction. (Holthuijsen, 2007)

SWAN includes processes such as refraction, shoaling and wind growth. Diffraction is only roughly included (Holthuijsen, 2007). In the model, wave growth is determined by wind, triad wave-wave interactions and quadruplet wave-wave interactions (SWAN Team, 2023). On the other hand, wave energy decays through dissipation. Dissipation of wave energy is included based on three components: white-capping, bottom dissipation and surf-breaking (Holthuijsen, 2007) (Booij, Ris, & Holthuijsen, 1999).

The bathymetry is retrieved from GEBCO (GEBCO Compilation Group, 2026) and combined with boat measurements. The used datasets need to be vertically calibrated. On the boundaries of the domain, a representative significant wave height is assigned. This significant wave height is based on ERA5 data. The main output variables are the significant wave height, the spectral energy period and the peak wave direction.

5.1.2 Model setup

Domain and computational grid
The computational domain spans 104 km in the east-west direction (1° in longitude) and 55 km in the north-south direction (0.5° in latitude). An orientation angle of $\alpha = 0^\circ$ is selected to align with the north-oriented coastline.

Spatial discretisation
The bathymetry captures the continental shelf north of San Felipe. The depth data used in the bathymetry is relative to Mean Sea Level (MSL). Next to the existing bathymetry, cross-shore elevation measurement data is available. This transect is extrapolated along the coastline to refine the bathymetry with actual measured heights. The extrapolation is carried out with QGIS. The navigation channel is captured by boat measurements. This data is used to refine the bathymetry data. The complete combined bathymetry is implemented in SWAN,

with a resolution of 30 m by 30 m. SWAN is run in two dimensional mode.(SWAN Team, 2023)

The grid has a resolution of 300 x 300 m, this is within the range of recommended discretisation for application in coastal areas (SWAN Team, 2023).

Time discretisation
SWAN is run in stationary mode.

Model parameters
The initial wave conditions are generated according to a JONSWAP spectrum, as the model simulates wind generated waves. The spectral directional resolution is set to $10°$, since wind sea waves are expected to be dominant. The frequency range is set from 0.03 Hz to 1 Hz (SWAN Team, 2023).

Input parameters
In Table 5.1 the boundary conditions can be found that are set on the Northern, Eastern and Western boundaries:

Table 5.1: Norther, Eastern and Western Boundary Conditions SWAN

Parameter	Value	Based on
Significant wave height	4.03 m	Table 4.2 (Average ERA5 and Copernicus)
Peak wave period	10.89 s	Table 4.2
Peak wave direction	$330°$	Figure E.11 Appendix E
Directional spreading	$24.9°$	Wind sea waves (SWAN Team, 2023)
Wind direction	$330°$	Figure E.5 Appendix E
Wind speed	16.02 m/s	Table 4.2

The values of these boundary conditions are based on the storm that is chosen to simulate: February 2024 (Nortes). The data for the different parameters is obtained from different sources, but since most of the data is obtained from ERA5 for the coordinate $[22, -88]$, this coordinate is used as the 'datapoint' coordinate. By running SWAN with these boundary conditions across various water levels, the wave parameters along the coast of San Felipe can be estimated for different water level scenarios.

Figure 4.1 shows that during Nortes, the waterlevel can reach up to 0.2 m above MSL. Under scenarios of high greenhouse gas emissions, the sea level is expected to rise 0.8 m in the Gulf of Mexico (Sánchez-García et al., 2023). The combination of expected sea level rise and the Nortes results in the modelled water level predictions ranging from 0.0 m above MSL to 1.0 m above MSL.

5.1.3 Results

The output of SWAN for the different water level scenarios can be found in Table 5.2.

Table 5.2: SWAN output parameters for different water levels calculated at $[21.569992, -88.234242]$ (San Felipe)

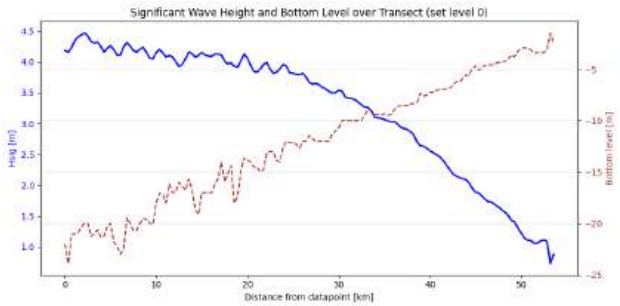
		Water Level above MSL (m)						
Parameter	**Description**	**0.0**	**0.1**	**0.2**	**0.4**	**0.6**	**0.8**	**1.0**
`HSIG` (H_{m0})	Significant wave height (m)	0.8752	0.9075	0.9404	1.006	1.073	1.14	1.207
`TMM10` ($T_{m-1,0}$)	Spectral energy period (s)	4.366	4.525	4.679	4.976	5.257	5.516	5.758
`PDIR` (θ)	Peak wave direction (°)	305	305	305	305	305	305	305

As presented in Table 5.2, the hydrodynamic parameters show a clear increase as the water level rises. Across the range from 0.0 m to 1.0 m, both the significant wave height (H_{m0}) and the spectral energy period ($T_{m-1,0}$) increase continuously. H_{m0} grows from 0.8752 m at MSL to 1.207 m at a 1.0 m water level, while $T_{m-1,0}$ increases from 4.366 s to 5.758 s. This increase is mainly caused by the greater water depth, which reduces bottom friction and depth-induced wave breaking, allowing higher wave energy to reach the shore. In contrast, the peak wave direction (θ) remains unchanged at $305°$ for all scenarios at this location.

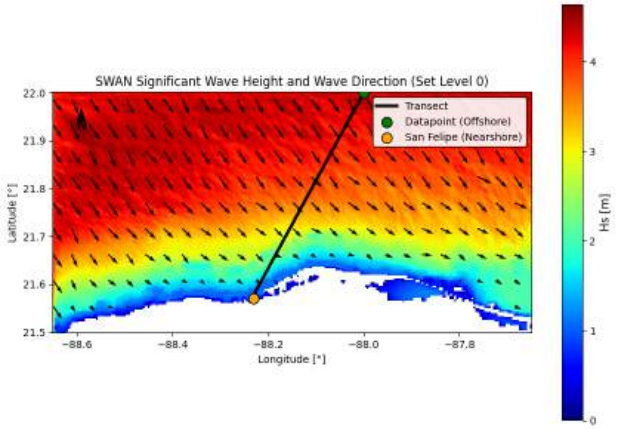
Figures 5.1b and 5.1d show the wave field calculated by SWAN for water levels of 0.0 m and 1.0 m above MSL, including the significant wave height and wave direction. The wave direction is visualised by black arrows. As shown, for all water level scenarios, the direction of the wave changes in onshore direction. Closer to the coast the waves are redirected due to wave refraction. Under higher water levels, this refraction process shifts closer to the shore, because the water stays deeper for longer.

Figures 5.1a and 5.1c visualise how the significant wave height and the bottom level change along the transect between the data point and the nearshore point at San Felipe. For all the water level scenarios, the significant wave height gradually decreases in onshore direction as the bottom level decreases. With decreasing water depth, the significant wave height becomes progressively smaller due to energy dissipation and depth-limited wave breaking. Higher water levels allow larger waves to propagate much further along the transect before breaking occurs.

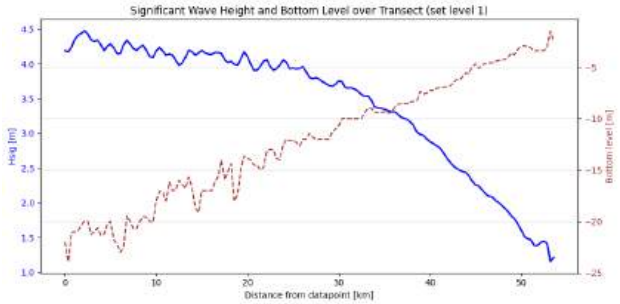
The combined increase in total water level, wave height and wave period has significant implications for coastal flooding in San Felipe. Higher water levels directly elevate the reach of incoming waves, while the higher H_{m0} and longer wave period ($T_{m-1,0}$) intensify wave run-up and wave setup along the shoreline. Because larger wave energy penetrates much closer to the coast during high water levels, the low-lying areas of San Felipe become considerably more vulnerable to overtopping and flooding.



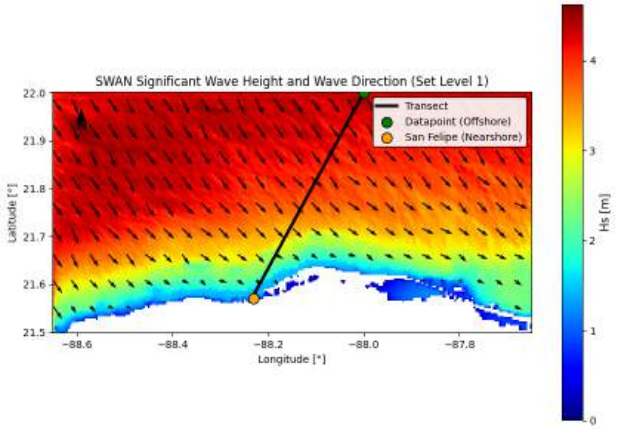
(a) Significant Wave height and Bottom Level along transect (water level 0 m)



(b) Significant Waveheight and Wave Direction (water level 0 m)



(c) Significant Wave height and Bottom Level along transect (water level 1 m)



(d) Significant Wave height and Wave Direction (water level 1 m)

Figure 5.1: Overview of wave parameters under 0 m (top row) and 1 m (bottom row) water level scenarios at San Felipe constructed with SWAN.

5.2 MODFLOW

First in Section 5.2.1 the methodology of simulating groundwater flow with MODFLOW is explained, followed by the model setup in Section 5.2.2. Section 5.2.3 contains the validation of MODFLOW, Section 5.2.4 the

sensitivity analysis and Section 5.2.5 its results.

5.2.1 Methodology

Geohydrological conditions play a role in the dynamics of compound flooding by controlling surface water infiltration as mentioned in Section 2.2.2.

High groundwater levels cause the subsurface to become saturated. This prevents rainwater from infiltrating and leads to groundwater inundation (GWI) (Becker, Reichel, Bachmann, & Schinke, 2022). Using the Groundwater Flow (GWF) model of MODFLOW 6, regions prone to GWI can be identified. To identify the regions prone to flooding, the Groundwater Flow (GWF) model is used to simulate three-dimensional, transient, groundwater flow based on a generalized control-volume finite-difference (CVFD) approach in which a cell can be hydraulically connected to any number of surrounding cells (Langevin et al., 2026). An analysis is performed for the unconfined aquifer as shown in Figure 2.7. The outcome of the MODFLOW simulation is a classification of critical areas which are prone to groundwater flooding.

5.2.2 Model setup

Domain and computational grid
The top of the aquifer follows the elevation model from the GPS measurements during the fieldwork. The bottom of the aquifer is assumed to be at -6 m. From the backpack and car GPS measurements, one out of seven GPS points are included for interpolation. Inverse Distance Weighting (IDW) interpolation is used. To predict a value for any unmeasured location, IDW uses the measured values surrounding the prediction location. The measured values closest to the prediction location have more influence on the predicted value than those farther away based on the given p-value (Esri, 2025). The default p-value is equal to 2, which is also used for further simulation. Explanation why this p-value is used can be read in Appendix J.1.

Groundwater flow is simulated within the boundaries of San Felipe, with only the surface area of the town included in the active model domain, see white area in Figure 5.2. The red and blue boundaries illustrates the location of the domain boundaries corresponding to the edges of San Felipe. Spatial discretisation is applied across this area using a uniform 5m $\times$ 5 m grid.

Time discretisation
Precipitation and water level data are hourly retrieved for 10 days. The simulation is performed in minutes. The simulation is run for transient flow for 14400 time steps (10 days transient) + 1 time step for the steady state (1 minute steady state). Therefore, the total length of the simulation is equal to 14401 time steps.

Model parameters
Hydraulic conductivity
An easy definition for hydraulic conductivity is as follows: "A property of soil or rock, which describes the ease with which water can move through pore spaces or fractures. It depends on the intrinsic permeability of the material and on the degree of saturation. Saturated hydraulic conductivity describes water movement through saturated media."(Bureau of Meteorology, 2026).

Following Budhu, the hydraulic conductivity depends on the following parameters: 1 - soil type, 2 - particle size, 3 - pore fluid properties, 4 - void ratio, 5 - pore size, 6 - homogeneity, layering and fissuring, 7 - entrapped gases and 8 - validity of Darcy's law (Budhu, 2011). Since the hydraulic conductivity is dependent on many parameters, it is complicated to assign a value to this parameter.

Different samples were retrieved in front of San Felipe, see Appendix C Figure C.4. Sample SF05 and SF06 are not included in the figure since they are more NW offshore. Sample SF01, SF02, SF03 and SF04 are relatively close to each other. The samples are classified according to their soil type following the unified soil classification system (California Department of Transportation, 2020). The result per sample is shown in Table 5.3.

Table 5.3: Soil Classification of Samples following the Unified Soil Classification System based on (California Department of Transportation, 2020)

Sample	Soil Classification	Sand Classification	d_{10} [mm]	C_u [-]	Hydraulic conductivity [m/s]
SF01	Coarse-grained soil – Sand	Clean sand	0.219	2.88	5.54×10^{-4}
SF02	Coarse-grained soil – Sand	Clean sand	0.228	2.96	6.00×10^{-4}
SF03	Coarse-grained soil – Sand	Clean sand	0.160	4.09	2.95×10^{-4}
SF04	Coarse-grained soil – Sand	Sand with fines	0.00820	22.0	–
SF05	Coarse-grained soil – Sand	Sand with fines	0.0521	4.44	–
SF06	Coarse-grained soil – Sand	Sand with fines	0.0350	9.77	–
SF07	Coarse-grained soil – Sand	Sand with fines	0.0880	18.4	–
SF08	Coarse-grained soil – Sand	Sand with fines	0.00770	30.4	–
SF09	Fine-grained soil	–	0.00360	7.44	–
SF10	Coarse-grained soil – Sand	Sand with fines	0.0240	14.8	–

Sands are classified as clean (well-graded or poorly graded) or fine-containing (silty or clayey). Fine-grained soils consist of silts and clays, which explains the low d_{10} values observed in both fine-grained soils and sands with fines. Empirical formulas for hydraulic conductivity typically require d_{10} and coefficient of uniformity (C_u) values within specific ranges; because the d_{10} for sands with fines is too small, these formulas cannot be applied. For instance, Hazen's empirical formula requires 0.1 mm $\leq d_{10} \leq 3$ mm and $C_u \leq 5$, conditions met only by the clean sand samples (SF01, SF02, and SF03).

Previous research in Sisal indicates that the regional aquifer is composed of clean sand (Medina-Rosado et al., 2026). Assuming the San Felipe aquifer has a similar soil composition, only samples SF01, SF02, and SF03 were considered for hydraulic conductivity calculations. Consequently, the hydraulic conductivity in the x- and y-directions is set to 5.54×10^{-4} m/s. To account for soil anisotropy, the vertical hydraulic conductivity (z-direction) is assumed to be one-tenth of the horizontal conductivity (Xiao et al., 2018). These values are applied in the Node Property Flow (NPF) package to model subsurface flow velocities through the aquifer.

Storage coefficients
Storage changes within a groundwater system are governed by two fundamental parameters: specific yield (S_y) and specific storage (S_s). Specific storage represents compressible storage, which quantifies the volume of water released or taken into storage per unit change in head due to the elastic compression of the fluid and matrix skeleton (Uliana, 2025). In contrast, specific yield represents unconfined storage, accounting for the volumetric yield of water driven by gravity drainage as the water table declines. In unconfined aquifers, the volume of water released through gravity drainage (S_y) exceeds the specific storage response (S_s) by several orders of magnitude. Consequently, the specific storage contributions are negligible in unconfined aquifers, making specific yield the primary governing parameter for storage in the numerical model (Langevin et al., 2017).
This unconfined aquifer specific yield (S_y) is set to an average of 26% based on the paper of (Johnson, 1967).

Forcings
Total water level boundaries
The blue line in Figure 5.2 denotes the seaward boundary, whereas the red line highlights the boundary bordering the mangrove area. A Time-Varying Specified Head (CHD) package is assigned to the sea boundary to impose a Dirichlet boundary condition, allowing time-dependent hydraulic heads to be specified for individual cells (Winston, 2019b). Input data for this boundary consist of a total water level time series derived from ERA5 reanalysis data (Copernicus Climate Change Service, 2022), which accounts for astronomical tide, storm surge and changes in annual mean sea level (MSL). The CHD dataset is extracted from an offshore coordinate representative of sea level conditions, see Appendix J.2, and lowered by a constant offset of -0.5 m since this is more representative following the validation of the SFINCS model, see Section 5.3.3.

The remaining landward boundary surrounding San Felipe, shown in red in Figure 5.2 is represented using a General-Head Boundary (GHB) package. The boundary heads for the GHB package are derived using the same approach as the sea boundary, but extracted at a location within the lagoon, as indicated by the red marker in Appendix J.2, Figure J.2. The conductance (C) at the GHB boundary is calculated based on the hydraulic conductivity (m/d), the depth of the aquifer (m), cell size (m) and the distance to the varying water level (m), see Figure J.2 in Appendix J.2. The larger the distance of the varying water level to the boundary, the lower the conductance (Medina Rosado, 2024). For the boundary cells, the incoming water flux is calculated by

multiplying the hydraulic head gradient with the conductance (Winston, 2019a). Details regarding conductance calculations are provided in Appendix J.2, Figure J.3.

An initial water level is added for the steady-state run. The value for the steady-state run is equal to the mean total water level of the 10 days at the GHB and CHD boundary .

Precipitation
The aquifer is recharged by the precipitation in San Felipe. Hourly precipitation data is retrieved from (Hersbach et al., 2023) with one hour extra for the steady-state run. The recharge is obtained by multiplying the precipitation by a recharge coefficient (C_r) of 0.4 (Medina-Rosado et al., 2026). The recharge is applied to the highest active cells and equally distributed over the domain (Langevin et al., 2017).

Observation points
The Observation package (OBS) is used to record simulated heads over time at specific locations for model post-processing. The coordinates of these observation points are listed in Table 5.4 and mapped in Figure 5.2. Points are selected at varying distances from the boundaries, both near and far, to evaluate the spatial propagation and influence of the boundary conditions across the model domain.

Table 5.4: x- and y-coordinates in UTM 16N coordinate system of the observation points P1 (North), P2 (Middle), P3 (South), P4 (East) and P5 (West) with corresponding elevations.

Observation point	x-coordinate	y-coordinate	Elevation [m]
P1	372403	2385400	0.35
P2	372330	2385123	0.35
P3	372241	2384697	0.37
P4	372105	2385149	0.32
P5	372584	2385048	0.33

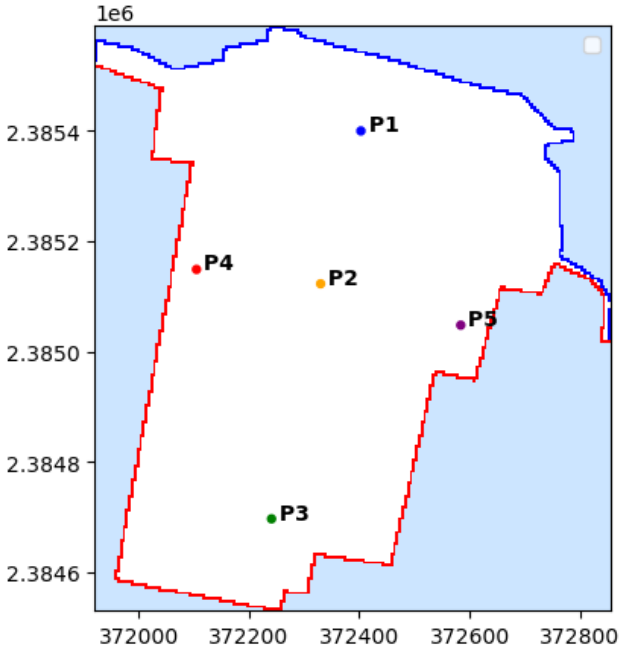


Figure 5.2: Locations of the observation points specified in Table 5.4. The mangrove water level boundary (GHB) is given in red, the sea water level boundary (CHD) is given in blue.

Initial conditions water head
The initial condition defines the head at the beginning of the groundwater flow (GWF) simulation, and it generally does not affect the simulation (Langevin et al., 2018). In this simulation the height of the elevation is used as the initial condition.

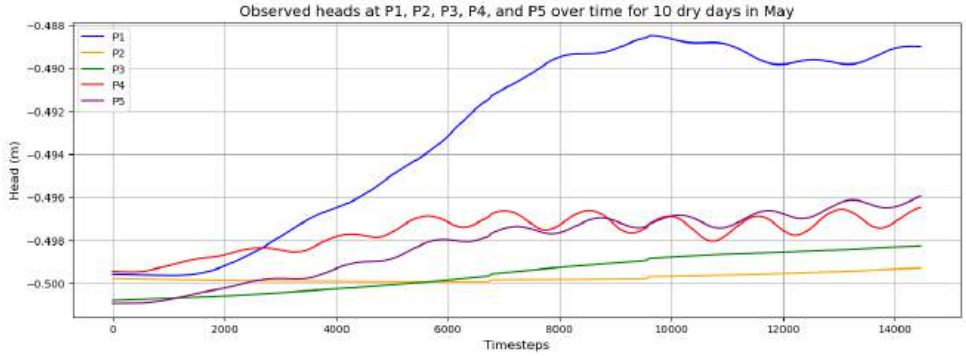
5.2.3 Validation

A dryer period is compared with a wetter period. The simulated dry period is from 01-05-2023 to 10-05-2023. May is chosen since the SLA is low in this month, see Figure 4.1, and precipitation is relatively low, see Appendix E Figure E.4. Based on these same figures a wet period is simulated from 01-11-2023 to 10-11-2023 since the SLA and precipitation are relatively high in this month.

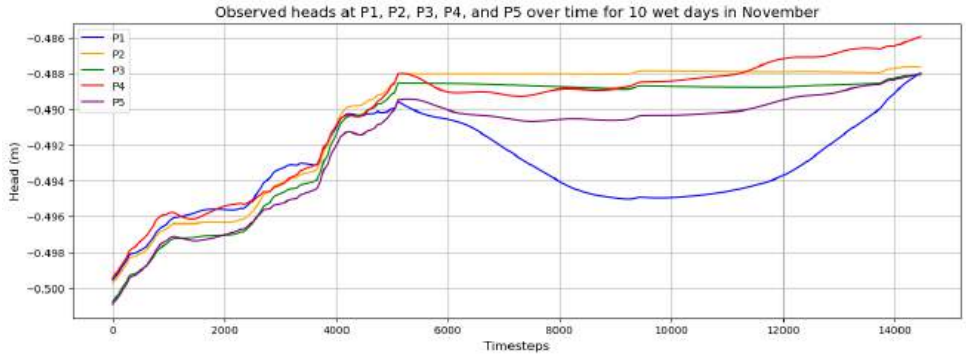
Both simulation periods are run with a steady-state value of -0.5 m. As shown in Figure 5.3, the final hydraulic heads at locations P1 through P5 after 10 days (14,400 time steps) are lower in May than in November. This is expected, as precipitation is higher in November than in May, demonstrating that the precipitation data correctly forces the model in the expected direction.

The aquifer's response is directly visible in Figure 5.3. During the dry period in May, two small precipitation peaks occur, as seen in Figure J.4a in Appendix J.3. These peaks cause an immediate jump in the hydraulic heads. Following the rain events, locations P4 and P5, which are close to the general head boundary (GHB), exhibit the tidal response of this boundary. Similarly, P1 shows the tidal response at the constant head boundary (CHD) after the rainfall, whereas P2 and P3 located further from both boundaries do not show this tidal behaviour.

During the wet period in November, precipitation continues up to the 5000th time step, as shown in Figure J.5a in Appendix J.3. The hydraulic head increases during the precipitation events and subsequently drops when the precipitation event is over as the system adjusts to a new equilibrium. Once again, locations P1, P4 and P5 reflect the tidal influence of the boundaries, while P2 and P3 display minimal tidal fluctuation due to their greater distance from the boundaries.



(a) Hydraulic head between the 1st of May (time step 1) and the 10th of May (time step 14400).



(b) Hydraulic head between the 1st of November (time step 1) and the 10th of November (time step 14400).

Figure 5.3: Observation points in the dry (May 2023) and wet (November 2023) period. Hydraulic head of P1 (blue), P2 (orange), P3 (green), P4 (red) and P5 (purple). The hydraulic head (m) is given on the y-axis, the time steps on the x-axis.

5.2.4 Sensitivity Analysis

A sensitivity analysis is performed to estimate the relative influence of the following model parameters: the hydraulic conductivity, specific yield, infiltration coefficient, the offset of the water levels at the boundaries and the steady state start values for the CHD and GHB boundaries. The analysis is performed using the first 10 days in November as the simulation period (01-11-2023 to 10-11-1023). For the sensitivity analysis, the model input parameters are increased or decreased within a certain range to see how sensitive the model is to changes of specific model parameters.

The hydraulic conductivity of samples SF01, SF02 and SF03 (see Section 5.3) are defined as medium to coarse sands by Domenico and Schwartz (Domenico & Schwartz, 1990). The model will be tested for medium to coarse sands therefore, the hydraulic conductivity will range between 9×10^{-7} m/s and 3×10^{-2} m/s.

The unconfined aquifer releases water from storage per unit decline of water table. This volume of water release is called the specific yield (Duffield, 2019). As stated above, the aquifer consists of medium to coarse sands and the specific yield ranges respectively from 15% to 35% (Johnson, 1967).

The recharge or infiltration (Cr) is determined to be 40% of the total rainfall. The range that is tested in the sensitivity analysis is 18% to 60% (Medina Rosado, 2024).

The water levels at the sea and mangrove boundary are shifted to the reference system of the elevation map, see Section I.6. The chosen offset value adjusts the water levels down to the used reference system. This shift of the water levels at the boundary influences the response within the San Felipe ground water system. The original value for the offset is used, which is equal to -0.5 m. A sensitivity analysis is done for an offset of -0.344 m and -0.656 m.

The first time step in the model represents the steady-state situation. The effect of the steady-state value taken for the first time step is evaluated by taking a lower and higher value at the boundaries. The initial value for the first time step at the CHD and GHB boundary is the mean value of the total water level of the 10 days.

Table 5.5: Summary of parameter ranges used in sensitivity analysis of MODFLOW (hydraulic conductivity, specific yield, infiltration coefficients, steady state value and the offset of the water levels). The first column describes the scenarios that are analysed and the baseline situation. The values show the specific values used for the parameter for each run of MODFLOW.

Scenario	**Hydraulic conductivity** k $[m/s]$	**Specific yield** S_y $[\%]$	**Infiltration** C_r $[\%]$	**Offset** $[m]$	**Steady State** **CHD** $[m]$	**GHB** $[m]$
Baseline	5.54×10^{-4}	26	40	-0.5	-0.488	-0.483
k **Low**	9×10^{-7}	26	40	-0.5	-0.488	-0.483
k **High**	3×10^{-2}	26	40	-0.5	-0.488	-0.483
S_y **Low**	5.54×10^{-4}	15	40	-0.5	-0.488	-0.483
S_y **High**	5.54×10^{-4}	35	40	-0.5	-0.488	-0.483
C_r **Low**	5.54×10^{-4}	26	18	-0.5	-0.488	-0.483
C_r **High**	5.54×10^{-4}	26	60	-0.5	-0.488	-0.483
Offset Low	5.54×10^{-4}	26	40	-0.344	-0.332	-0.327
Offset High	5.54×10^{-4}	26	40	-0.656	-0.644	-0.639
Steady State Low	5.54×10^{-4}	26	40	-0.5	-0.588	-0.583
Steady State High	5.54×10^{-4}	26	40	-0.5	-0.388	-0.383

The sensitivity analysis is based on the five identified observation points (P1 to P5), see Figure 5.2. As described in Table 5.5 an upper and lower bound is taken for each model parameter, while the other parameters are set to the "baseline" value. Visualisations of the effects of the model parameters on the head level over time are given in the appendix J.4. The effect of each model parameter is evaluated below.

Hydraulic conductivity, k

The head elevation over time shows for all observation points (P1 to P5) a tidal response for the relative high hydraulic conductivity, see Figure J.6. A high hydraulic conductivity (3×10^{-2} m/s) implies that water can easily infiltrate and thus move in and out of the aquifer. A lower hydraulic conductivity (9×10^{-7} m/s) means that it

is relatively harder for water to flow in and out of the aquifer, and thus the tidal effects are not observed. The original hydraulic conductivity (5.54×10^{-4} m/s) does not show tidal effect over time.
Over time, a large hydraulic conductivity shows relatively large differences in hydraulic head levels, compared to the lower hydraulic conductivity values. The original and low hydraulic conductivity shows the same pattern and magnitude at each observation point over time.

Specific yield, S_y
For all observation points a low specific yield (15%) causes a higher head over time than a higher specific yield (35%), see Figure J.7. The head difference between the original and the low specific yield is larger over time than the head difference between the original and the low specific yield for observation points P2, P3, P4 and P5. However, observation P1 shows a different behaviour. Between time step 6000 and 8000, the simulation with a low specific yield shows a larger reduction of the head level over time than the high specific yield simulation, due to an unstable simulation and a short run time.

Recharge coefficient, C_r
For all observation locations (P1 to P5), an increase of the recharge coefficient leads to a larger value of hydraulic head over time, see Figure J.8). A larger recharge coefficient implies a larger volume of precipitation that is added to the system.

Offset
By comparing the low (-0.344 m), original (-0.5 m) and high offset (-0.656 m), it becomes clear that the head level shows the same pattern over time for all observation points, see Figure J.9. The head level value at all observation points is influenced by the offset chosen to adjust the water level data at the boundaries, see Appendix I.6, as all observation points show an absolute increase of head level over time with decreasing offset. In conclusion, the chosen offset has a direct influence on the absolute head level in the aquifer. It is extremely important for the magnitude of the head over time.

Steady-state
A low head level (GHB and CHD Boundary) value for the steady state (CHD:-0.583 m; GHB -0.588 m), results in an increase of head level over time at all observation points, see Figure J.10. A high initial head level (CHD:-0.383 m; GHB -0.388 m) results in a decrease of head level over time, mainly for observation point P1. The original baseline steady state head values are set to the average of the water levels at the CHD and GHB boundaries, respectively -0.488 m and 0.483 m. This 'baseline' simulation shows a relatively small head level change over time for P2, P3, P4 and P5. For this reason, taking the average of the water levels at the CHD and GHB boundary is a sufficient method to determine the steady-state start value for this model.

In conclusion, the change of head over time at all observation points is relatively small for the simulation with the steady-state head value set to the average of the water levels at the boundary. Based on this effect, the choice to take the average water levels at the CHD and GHB boundaries is justified.

5.2.5 Results

On the 5th of February 2024 local residents experienced flooding in the town of San Felipe. To obtain a better understanding of the ground water response during that period, the head levels are simulated for a time period of 10 days. The heads in the aquifer are plotted in Figure 5.4 for 01-02-2024 to 10-02-2024. The dashed line represents the flooding on the 5th of February (time step: $5 * 24 * 60 * 60 = 7200$). At this time, a peak in precipitation is observed together with a high total water head at the boundaries, see Figure J.11a and Figure J.11b in Appendix J.5.

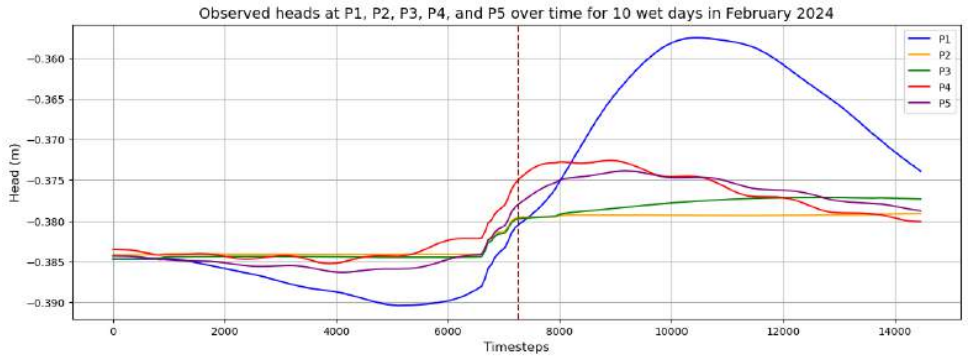


Figure 5.4: Hydraulic head between the 1st of February 2024 (time step 1) and the 10th of February 2024 (time step 14400). A vertical line is shown on 05 Feb 2024, the time when interviewees experienced flooding.

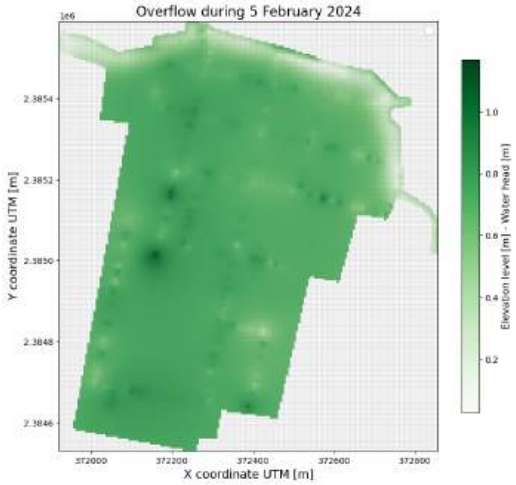
For this time step (5th of February), an overflow map is shown in Figure 5.5a. The overflow is equal to the elevation minus the groundwater head. When the groundwater head is greater than the elevation, flooding occurs. This means that there is flood when:

$$\text{If overflow} \leq 0 \text{ then flooded}$$

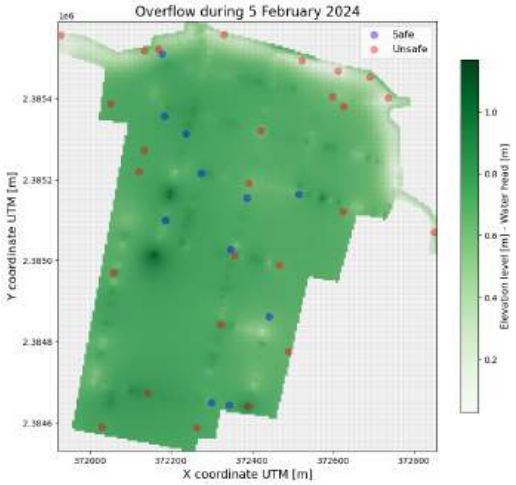
This means that the lower the value and thus the more white the colour, see Figure 5.5a, the more critical this area is to flooding (more prone to flooding). The markers in Figure 5.5b represent the map of the interviewees in Chapter 4, Figure 4.4. Flooding is not caused only because of upcoming groundwater during this event. However, it can be seen that most red markers are located in critical/white areas and blue markers in less critical/darker green areas. This is a validation that the model works as expected. It can be observed that the street at the west of San Felipe (Francisco Lopez Mena Calle 14 street) shows darker green areas compared to the main street (Carr. A. San Felipe). More red markers are also shown for the main street.

In addition, the heads over time are significantly larger during these days in February, see Figure 5.4, compared to wet days in November as shown in Figure 5.3b for all observation points, making the town of San Felipe more susceptible to flooding during the February storm.

The heads over time are also plotted for 01-10-2020 to 10-10-2020, see Figure J.17 Appendix J.6. An overflow map is also made in Figure J.18 where a flood is shown in south east of the town of San Felipe. This point on the map shows the most critical location, as this is the point where flooding occurs in case of extreme precipitation. This is also a critical/white area in Figure 5.5.



(a) Overflow map 05-02-2024 with the lighter green/white indicates safer areas and darker green indicates less safe areas which are more prone to flooding.



(b) Overflow map 05-02-2024 including markers based on fieldwork. The blue markers are safe zones and the red markers are unsafe zones.

Figure 5.5: Overflow map for 05-02-2024. The left overflow map shows critical areas (white) and less critical areas (darker green). The right shows an overflow map with markers from fieldwork added with safe and unsafe areas.

5.3 SFINCS

First in Section 5.3.1 the methodology of simulating compound flooding with SFINCS is explained, followed by the model setup in Section 5.3.2. Section 5.3.3 contains the validation of SFINCS, Section 5.3.4 the sensitivity analysis and in Section 5.3.5 its results.

5.3.1 Methodology

To simulate compound flooding and overland flooding in San Felipe efficiently and accurately, the numerical model SFINCS (Super-Fast INundation of CoastS) is utilised. Developed by Deltares, SFINCS is a reduced-physics numerical solver specifically designed to compute compound flooding in coastal systems driven by a combination of fluvial, pluvial, tidal, wind-driven surge and wave-driven processes (Leijnse, van Ormondt, Nederhoff, & van Dongeren, 2021). In the upcoming paragraphs the governing equations and forcing mechanisms are elaborated on.

Governing equations and formulation
The computational framework of SFINCS is based on a rectangular grid where height levels, boundary conditions and forcing mechanisms are defined in specific cells.

SFINCS can operate under two main formulations, depending on advection being taken into account or not.

1. **SFINCS-LIE (Local Inertial Equations):** This model is based on simplified shallow water equations. The momentum equation accounts for local acceleration, bed-level and water-level gradients and bottom friction (calculated using Manning's roughness coefficient n). This mode is computationally extremely fast and well-suited for regional flood plains and riverine routing where advection plays a minor role (Leijnse et al., 2021).
2. **SFINCS-SSWE (Simplified Shallow Water Equations):** Incorporates an explicit advection term into the momentum equations. As demonstrated by Leijnse et al. (2021), including advection is critical for resolving rapidly varied flows, shock waves (such as dam breaks) and wave-driven processes like short wave and infragravity wave run-up on the coast.

Forcing mechanisms
To capture compound flooding drivers comprehensively, SFINCS allows for multiple parameter forcing:

- **Wind shear stress:** Computed via a quadratic drag relation based on wind speed and air density to simulate local wind setup over shallow water bodies.
- **Meteorological & Hydrological inputs:** Spatially uniform or gridded time series for precipitation rates and infiltration losses (governing pluvial contributions and soil absorption).
- **Point sources:** User-defined point discharges to represent localised inflows or drainage structures.
- **Wave-driven forcing:** Implemented at the edge of the swash zone. This boundary implementation allows the model to be forced simultaneously by slowly-varying water levels (tides and large-scale storm surges) and rapidly-varying surface elevations (such as wind waves or infragravity waves), while actively absorbing outgoing wave energy to prevent artificial reflections within the domain (Leijnse et al., 2021). In combination with the SSWE formulation, the model accurately resolves wave run-up and wave setup overland without needing to resolve the outer surf zone.

To prioritise the calibration of the other parameters, explicit wave forcing is excluded from the main validation model, though its potential impact is explored via a static wave setup, see Section 5.3.2.

5.3.2 Model setup

Domain and computational grid
The model is built using the HydroMT framework (Deltares, 2024). Because explicit wave dynamics are omitted and the focus lies on overland flooding and compound water levels, the model utilises the computationally efficient SFINCS-LIE (Local Inertial Equations) formulation. To optimally model the complex coastline and lagoon, the grid is rotated ensuring that the orientation of the grid cells is roughly parallel to the coastline. The overall model domain spans an area of approximately 4.4 by 5 km. Within this spatial framework, the coarse grid cells have a resolution of 40 m, while the locally refined fine grid cells have a resolution of 2.5 m. This configuration results in a total of 185730 active computational grid cells.

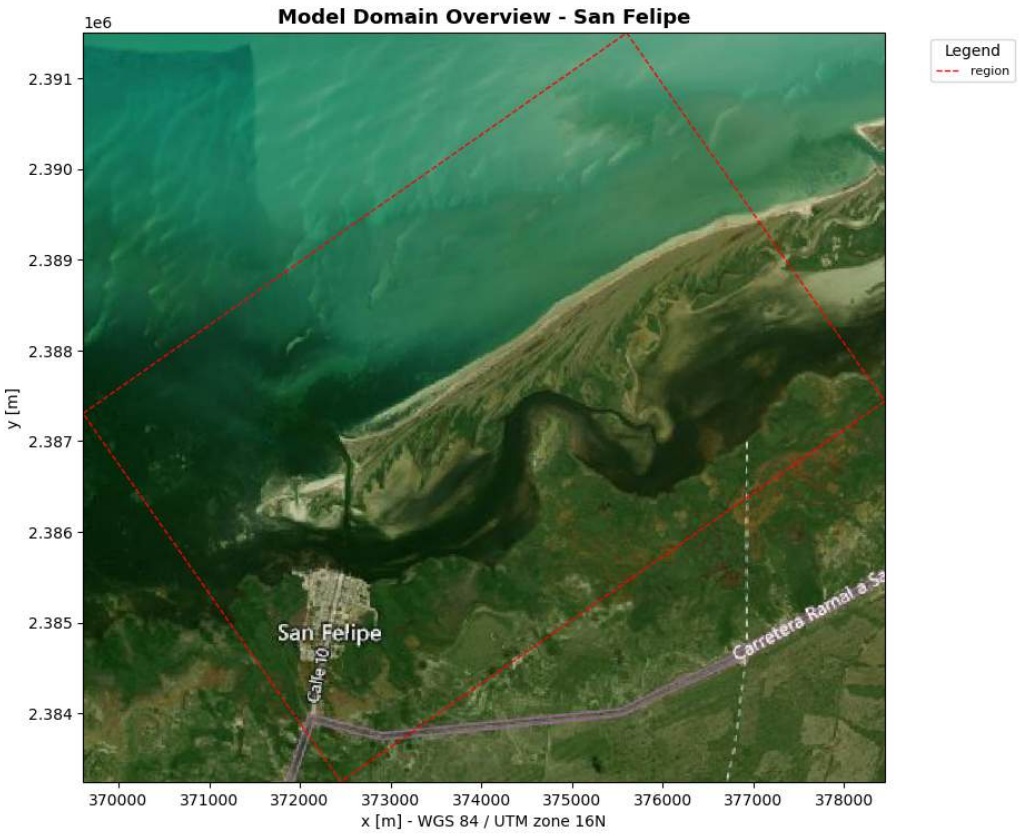


Figure 5.6: SFINCS domain of the San Felipe area indicated by red dashed line.

Quadtree configuration is chosen for the construction of the computational grid, which allows the resolution to vary within the model. Therefore the model contains fine cell sizes in the city area to capture all relevant details and rough cell sizes in the rest of the domain.
The elevation model constructed in Chapter 4 is interpolated onto the computational grid to supply SFINCS with the required bed levels. This grid incorporates both nearshore bathymetry (GEBCO Compilation Group, 2026), topography (INEGI, 2026) and high-resolution LiDAR and GPS data of San Felipe, as listed in Table 4.1. The mangrove elevation is corrected as described in Appendix I.7.
To define the active computational domain and specify the hydrodynamic boundary conditions, the grid mask was configured using two cell classifications:

- **Mask value = 2 (Offshore Boundary):** Assigned to cells along the offshore boundary of the domain to define open boundary locations where water level conditions are prescribed.
- **Mask value = 1 (Active Domain):** Assigned to all remaining interior cells within the model domain to designate active grid points where hydrodynamic equations are solved.

Time discretisation
SFINCS utilises a dynamic time step governed by the Courant-Friedrichs-Lewy (CFL) condition. The 2D continuity equation couples both spatial directions using a first-order explicit backward-in-time scheme with central differences for spatial derivatives (Leijnse et al., 2021). The model is run in transient mode covering the full duration of each simulated storm event (e.g., 3 days for the February 2024 event).

Model parameters
Structures
To obtain a realistic representation of the city area, the structures are included in the model. Polygons are imported to precisely elevate the model at the locations of the structures in the bottom area of the city (Oostwegel, Schorlemmer, Lingner, & Evaz Zadeh, 2025). By doing this, the structure cells remain active. For the upper part of the city, the structures are captured by the LIDAR data.

Manning roughness
Spatial variation in hydraulic roughness is implemented in SFINCS to account for bottom friction and land-cover resistance during overland flow. Land-use classes are derived from the ESA WorldCover dataset (Zanaga et al., 2022). Each land-use class is mapped to a representative Manning roughness value (n) and interpolated onto the computational grid.
The assigned Manning roughness values per land-cover class are summarised in Table 5.6.

Table 5.6: ESA WorldCover land-use classes (Zanaga et al., 2022) and assigned Manning roughness coefficients (n) (Koper, 2024)

Class Value	ESA WorldCover Class	Manning n (s/m$^{1/3}$)
10	Tree cover	0.120
20	Shrubland	0.050
30	Grassland	0.034
40	Cropland	0.037
50	Built-up	0.100
60	Bare / sparse vegetation	0.023
80	Permanent water bodies	0.020
90	Herbaceous wetland	0.035
95	Mangroves	0.070
100	Moss and lichen	0.025

Infiltration
The hydraulic conductivity of the underlying unconfined aquifer in San Felipe is 5.54×10^{-4} m/s, see Section 5.2.2), which corresponds to 1994.4 mm/h. This is used as estimation for the infiltration rate. For areas with a denser vegetation cover such as tree cover, shrubland, grassland and cropland, lower infiltration rates are assumed for infiltration to the aquifer. The specific infiltration rates assigned to each land-use class are summarised in Table 5.7.
This is not the same as the infiltration rate in the urban area, since the presence of urban infrastructure reduces the effective infiltration capacity across the area. However, because San Felipe is not fully paved, an infiltration rate of 5 mm/h is assumed for the urban area to account for the unpaved areas where this highly conductive fine sand is exposed. Permanent water bodies do not let water infiltrate, which means that the infiltration rate is 0.0 mm/h. For the mangrove and wetland areas, unweathered marine clay is assumed which is increased with a factor 10 to account for the root system and biological activity in the systems. This results in a hydraulic conductivity of $2e-08$ m/s and thus an infiltration rate of 0.072 mm/h is used (Clarkson, 2021). Biocrusts, such as moss and lichen, limit infiltration (Chamizo, Cantón, Lázaro, Solé-Benet, & Domingo, 2012). Therefore an infiltration rate of 0.0 mm/h is assumed for moss and lichen. The ESA worldcover classes with corresponding infiltration rates are summarised in Table 5.7.

Table 5.7: ESA WorldCover land-use classes (Zanaga et al., 2022) and infiltration rates

Class Value	ESA WorldCover Class	Infiltration rate (mm/hr)
10	Tree cover	50.0
20	Shrubland	100.0
30	Grassland	50.0
40	Cropland	20.0
50	Built-up	5.0
60	Bare / sparse vegetation	1994.4
80	Permanent water bodies	0.0
90	Herbaceous wetland	0.072
95	Mangroves	0.072
100	Moss and lichen	0.0

Forcings
The open offshore boundaries of the model are forced by total water level time series. Two events are modelled with SFINCS: 8-11 November 2025 and 5 February 2024 (Norte).
For modelling the Norte of 5 February 2024, the total water level time series, which accounts for both astronomical tides and meteorological storm surge, is derived from Copernicus (Copernicus Climate Change Service,

2022) which provides output at discrete coastal stations. The two stations closest to San Felipe are used: one west of the town at 21.577°N, 88.345°W (11.5 km away) and one east of the town at 21.606°N, 88.110°W (13.5 km away), see Figure J.2. The water level along the offshore boundary is interpolated between these two stations.
For 8-11 November 2025, no reanalysis data is available. Instead the total water level time series is derived from a measured ADCP time series in El Cuyo. In Figure 5.7 this time series is compared to the measurement data in the lagoon of San Felipe. It can be seen that the two datasets match quite well in phase and amplitude. It is therefore assumed that using the ADCP data from El Cuyo is a reliable assumption for the total water level offshore San Felipe. These water levels are imposed along the offshore boundary to simulate the tidal dynamics and surge entering the model domain.

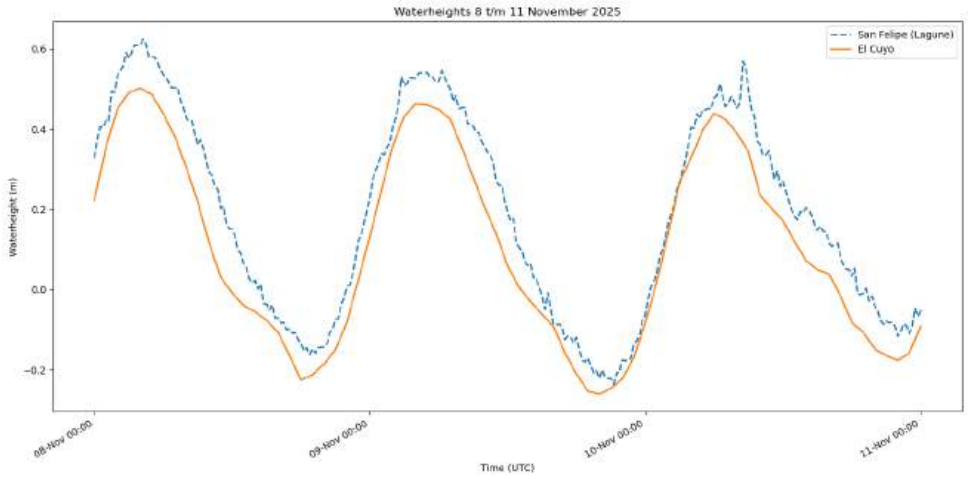


Figure 5.7: Total water level [m] El Cuyo vs San Felipe Lagoon from 08 November 00:00 to 11 November 00:00

Atmospheric forcing conditions are derived from ERA5 atmospheric reanalysis data (Hersbach et al., 2023), which is a gridded product, so no measuring stations are involved. The horizontal resolution is $0.25°$ (≈ 26–28 km). The ERA5 grid point nearest to San Felipe lies at 21.50°N, 88.25°W, 8.0 km from the town. The four grid points surrounding the town, between which SFINCS interpolates spatially, are located 8.0 to 31.4 km away. Since the model domain is only a few kilometres across, the wind and precipitation fields are practically uniform over the domain. Small-scale rainfall variability is therefore not resolved, in line with the limitations of ERA5 described in Section 4.3.

While wave dynamics are excluded from the main compound flooding analysis, their potential impact is roughly investigated. To approximate this effect without explicitly modelling waves, a static wave setup ($\langle\eta\rangle$) is calculated using the Yucatán specific empirical formulation by Medellín et al. (2016) and added to the total water level at the offshore boundary. Dynamic wave run-up is excluded from the boundary forcing, as applying high-frequency run-up peaks to an offshore boundary in SFINCS would act as an unrealistic constant inflow of water, leading to an overestimation of the flood volume inside the lagoon.
The wave setup for high water level conditions is calculated using the empirical formula by Medellín et al. (2016):

$$\langle\eta\rangle = 0.35 \tanh(0.53 H_0) \tag{5.1}$$

The deep-water wave parameters are derived from the offshore boundary conditions for the February 5, 2024 Norte event, featuring a deep-water significant wave height of $H_0 = 4.41$ m, see Appendix E.
Applying this parameter results in a static wave setup of approximately 0.34 m (34 cm). This calculated wave setup is later added to the total water level offshore boundary condition during the sensitivity analysis, allowing for a quantitative comparison of the flood extent with and without wave influence.

5.3.3 Validation

The flooding event of 5 February 2024 is modelled using the model setup explained in Section 5.3.2 and can be validated using information and photo's obtained during the fieldwork. After the first run, no flooding is visible in the town, while there should be flooding according to the obtained information during fieldwork. It is concluded that the mangrove area in the DEM is too simplified for the area around the city. The mangrove elevation is improved based on pictures, to capture the mangrove more realistically. Next to the mangrove elevation, the Manning roughness coefficient is modified to identify the roughness value that results in modelled flooding

closest to the actual event. However, this is still insufficient. Therefore, the assumed offset of -0.656 m is re-evaluated. Because this offset is originally derived from future total water level projections rather than historical observations for this specific event, it likely differs from reality. Adjusting this offset is therefore a suitable correction. By decreasing this offset to 0.5 m, which means increasing the total water level and the elevation of the topography and bathymetry, the model simulated flooding extent and inundation levels are similar to the actual event.

Figure 5.8 displays the resulting water depths in San Felipe at peak water level (19:00 local time) during the 5 February 2024 storm event. This aligns closely with gathered information during community interviews, which confirms that the main street was flooded that evening.

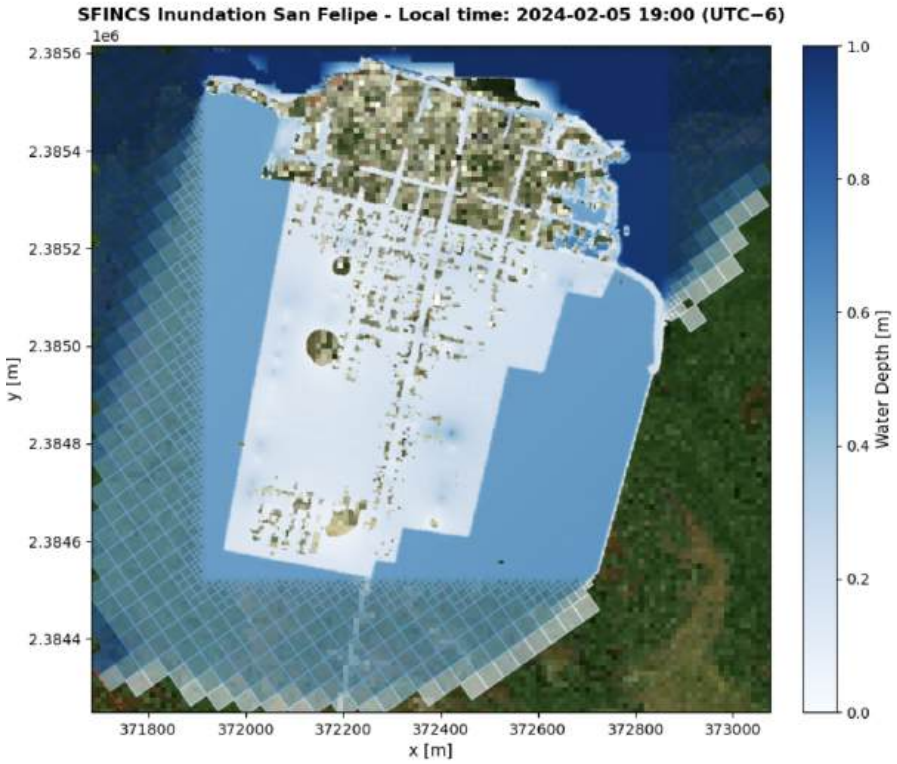


Figure 5.8: Simulated inundation depth and extent for San Felipe at peak water level (19:00 local time, 5 February 2024).

The event of 8 to 11 November 2025 is modelled in SFINCS and can be validated using the water level time series in the lagoon in front of San Felipe of the "San Felipe Research Group". This is visualised in Figure 5.9. It can be observed that the modelled water levels by SFINCS are slightly lower than the measured values. However, the model captures the overall tidal dynamics and phase very well. Based on this alignment, the model is considered reliable for this setup.

Together, these two validation steps confirm that the model captures both the regional hydrodynamics and the local inundation dynamics. The similarity between the measured and modelled water levels proves that the total water level forcing and tidal propagation are correctly represented, while the refined mangrove topography and revised offset resolves the local flooding patterns observed during fieldwork. With this validated SFINCS setup, the model provides a reliable basis to perform the statistical analysis and answer the main research question: 'What is the cause and impact of flooding in San Felipe?'

5.3.4 Sensitivity Analysis

Preliminary SFINCS runs indicates that inundation levels are highly sensitive to the Manning roughness coefficient (n), mangrove bed elevation around San Felipe and the offset. To evaluate the sensitivity of the model, these three parameters are varied within realistic physical boundaries. The manning roughness values for mangroves are altered for $n = 0.045$ s/m$^{1/3}$ and $n = 0.15$ s/m$^{1/3}$, which is the range of manning roughness values for mangroves found in literature (Medeiros, 2023).

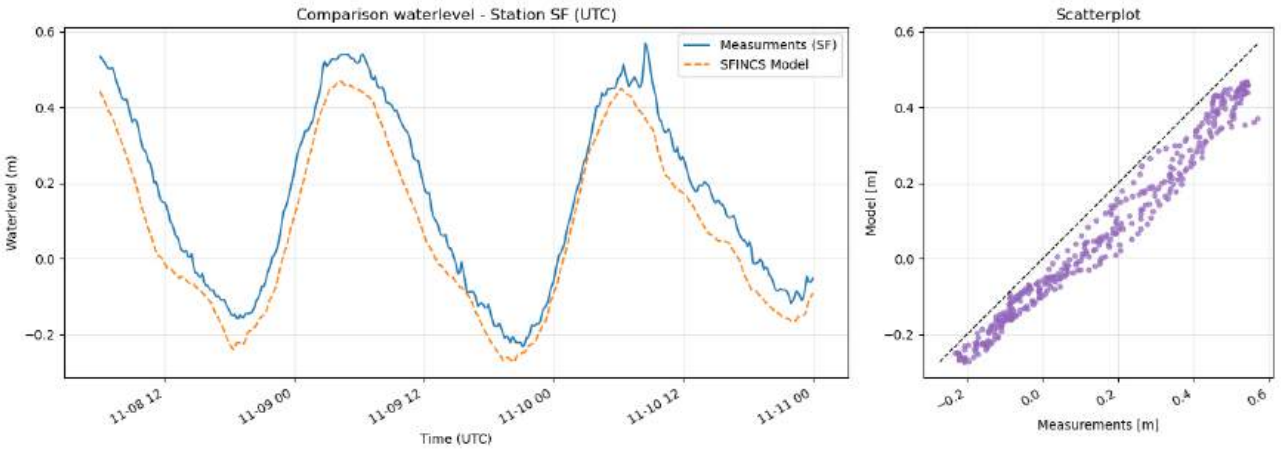


Figure 5.9: Comparison between modelled and measured water levels in the lagoon. Left: Time series of modeled and measured water levels. Right: Scatter plot comparing each timestep, illustrating a slight model underestimation relative to measurements.

The mangrove bed elevation around San Felipe is altered to -0.475 m, which is the elevation of the mangrove bed level further away from San Felipe, and to 0.38 m, which is the bed level at the boundary of San Felipe. The offset is altered to -0.656 m and -0.344 m. The baseline offset is set to -0.50 m, while -0.656 m represents the initial setting. The tested variation of 0.156 m corresponds to the difference between this initial offset and the baseline value.
Table 5.8 summarises the values of the three parameters on which the sensitivity analysis is based.

Table 5.8: Overview of the modelled sensitivity scenarios and the resulting water levels in SFINCS.

Scenario	**Manning n [s/m$^{1/3}$]**	**Mangrove Elev. [m]**	**Offset [m]**	**Waterlevel [m]**
Baseline	0.070	-0.044	-0.50	**0.140**
Manning Low	0.045	-0.044	-0.50	**0.148**
Manning High	0.150	-0.044	-0.50	**0.039**
Elevation Low	0.070	-0.475	-0.50	**0.140**
Elevation High	0.070	0.380	-0.50	**0.000**
Offset Low	0.070	-0.044	-0.344	**0.332**
Offset High	0.070	-0.044	-0.656	**0.000**

The sensitivity of the different parameters is compared using the maximum water level in the main street, at the coordinate [-88.232373, 21.565493]. The results show that the model is most sensitive to variations in the offset. Decreasing the offset from -0.50 m to -0.344 m leads to an increase in water level in the main street to 0.332 m, which is 0.192 m higher than the baseline. Increasing the offset to -0.656 m reduces the water level to 0.000 m, indicating that the threshold for inundation is no longer exceeded at this location. Although the parameter range is symmetric relative to the baseline, the resulting water level response is asymmetric. Decreasing the offset results in a large relative increase in water level of $+137.1\%$, while increasing the offset leads to a total water level reduction of -100%.

The Manning roughness shows a non-linear effect on the calculated water levels. Increasing the friction parameter to $n = 0.150$ causes significant attenuation, reducing the peak water level from 0.140 m to 0.039 m. Decreasing the roughness to $n = 0.045$ results in a small increase to 0.148 m. It should be noted that the tested parameter range is asymmetric relative to the baseline. While increasing n by $+114\%$ causes a water level reduction of 72%, decreasing n by -36% results in an increase of only $+5.7\%$. This indicates a decreasing impact of hydraulic resistance below $n = 0.070$, while higher Manning roughness values significantly decrease water levels in the main street.

Variations in the mangrove elevation show a highly asymmetric and threshold-dominated response. Lowering the mangrove elevation from -0.044 m to -0.475 m does not change the maximum water level compared to the baseline. Raising the elevation to 0.380 m leads to a reduction of the water level to 0.000 m. This indicates

that further lowering the mangroves around San Felipe does not increase water levels in the main street, while increasing the mangrove elevation around San Felipe creates a barrier that prevents inundation.

In addition to the parameters tested in the matrix, the potential impact of wave forcing is evaluated by testing a wave setup scenario. Following section 5.3.2 a static wave setup of $\langle \eta \rangle \approx 0.34$ m is calculated. Incorporating this wave setup results in a significantly increased peak water level in the main street of **0.510 m** (compared to the baseline of 0.140 m). This increase demonstrates that wave setup has a large impact, particularly given that wave overtopping is still neglected here. To safeguard the foundational reliability of the starting model, the scope is intentionally constrained. However, it is acknowledged that waves should be included in further research, to have a broader understanding of all drivers.

Overall, these results demonstrate that the model output is highly sensitive to the chosen parameter values. Given that the Manning roughness, mangrove bed elevation, and offset are all highly uncertain due to limited field data, these parameters were adjusted during the model validation to reproduce realistic inundation levels. Consequently, the choices for these parameter values play a critical role in assessing the extent and severity of the modelled floods in San Felipe.

5.3.5 Results

Following model validation, the SFINCS setup is applied to simulate the response of San Felipe during the February 2024 Norte storm. The resulting water levels, maximum water depths and inundation times directly provide the necessary hazard parameters to evaluate building damage in Section 5.4.
In addition to this specific event analysis, the validated SFINCS model serves as the tool for the compound flooding analysis, see Chapter 6. By simulating a range of synthetic storm events combining different water levels and meteorological forcings, the model results enable the evaluation of various flooding scenarios to answer the main research question.

5.4 Damage model

The impact of flooding on building structures in San Felipe is analysed using a comparative damage model. To this end, a general methodology for mapping the impact of floods on structures is first defined in Section 5.4.1. Then, Section 5.4.2 lists flood and damage characteristics as well as building characteristics specifically for San Felipe. Section 5.4.3 presents a building inventory analysis and a damage analysis, which together form the basis of the comparative damage model for cold front flooding. Finally, the resulting structural vulnerability and flood hazard are combined into a comparative damage overview of the town in Section 5.4.4

5.4.1 Methodology

To map the impact of floods on structures in towns along the northern coast of Yucatán, the methodology illustrated in Figure 5.10 is proposed. The first stage focuses on analysing historical flood events in terms of both flood characteristics and the resulting structural damage. Simultaneously, the buildings within the study area are characterised based on key properties such as construction materials, building height, foundation type and structural geometry. This preparatory analysis involves looking at news articles, pictures and videos on social media, as well as articles on flood characteristics. Furthermore, insights from the local community on recent flood events are valuable.

The second stage involves processing the output data obtained from a numerical flood model. Interesting parameters from the model include inundation zones, levels and duration, flow direction and velocity. Finally, impact is assessed by combining flood characteristics from the numerical model with building properties from each building class. This is achieved using damage functions based on flood hazard and structural vulnerability. For example, inundation duration contributes to flood hazard while a building's construction material defines its structural vulnerability.

5.4.2 Preparation

The preparatory analysis focuses on understanding the historical flood characteristics and the resulting structural damage as well as the building characteristics. Also the approach for using SFINCS data for a simulated event is discussed.

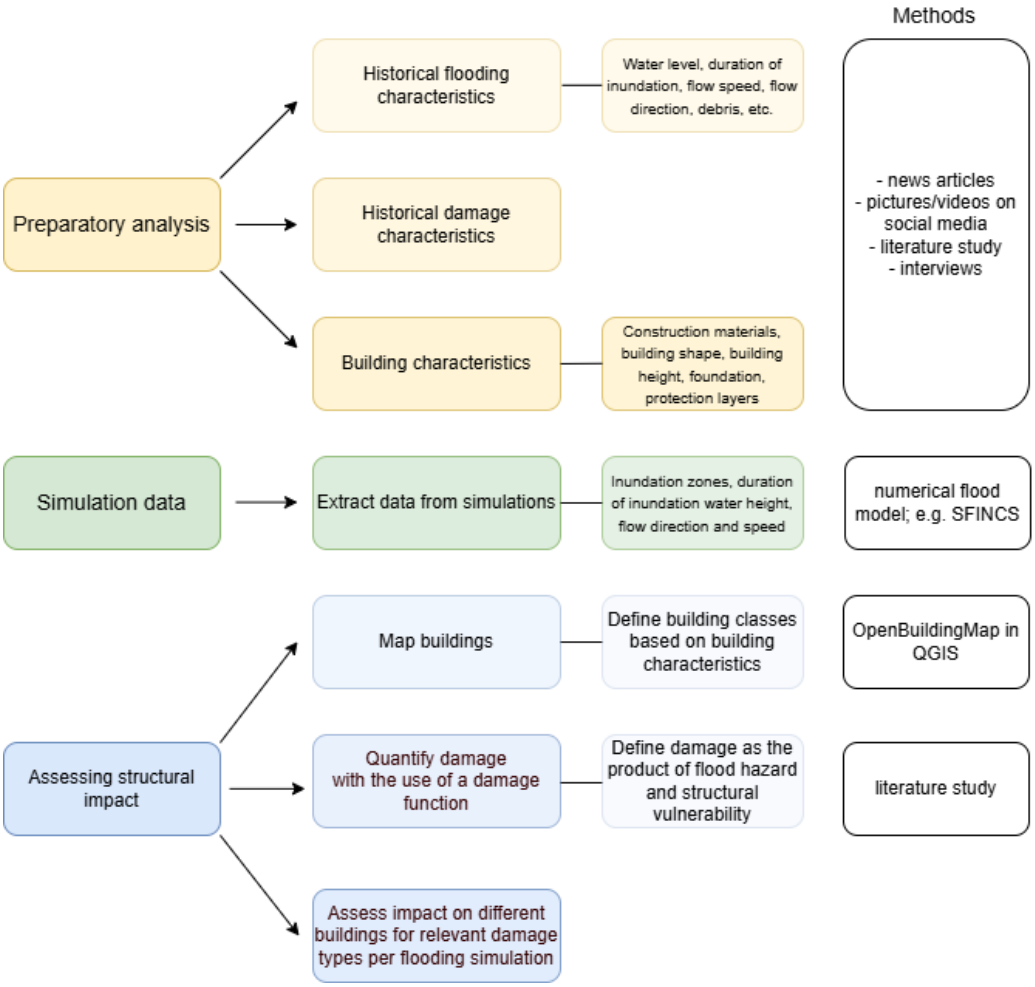


Figure 5.10: Overview of methodology for assessing structural impact due to flooding

Flood and damage characteristics
During the visit to San Felipe conversations with the local community helped to understand the historical flood characteristics, see Section 4.4.2. Two types of floods can be distinguished: hurricane flooding and cold front flooding. Hurricane flooding is characterised by high water levels, dynamic loads and debris-laden flows. This type of hurricane has not hit San Felipe, Yucatán since Isidore in 2002. More often the town floods due to cold fronts, also known as Nortes.

During flood events caused by Nortes, water levels typically rise by 15 to 30 cm, resulting in inundation of the ground floors of buildings throughout the town. The saline water comes into direct contact with walls, floors, and foundations, accelerating the deterioration of construction materials.

Repeated exposure to seawater can lead to the accumulation of chlorides within concrete, which may initiate corrosion of reinforcement steel and over the long term reduce the strength and durability of concrete structures (Melchers, 2020). Whereas repeated seawater exposure may lead to chloride-induced deterioration in reinforced concrete, timber structures are primarily affected by increased moisture levels and biological degradation, which can reduce their long-term strength and durability in coastal environments (Treu, Zimmer, Brischke, et al., 2019). Repeated exposure of masonry buildings to seawater flooding can result in salt accumulation within bricks and mortar. During subsequent drying, salt crystallisation may cause cracking, surface scaling and gradual material loss (Lubelli, van Hees, et al., 2018).

Building characteristics
Most buildings in San Felipe are low-rise residential structures, typically consisting of one or two storeys. Based on field observations, the following building characteristics were identified:

- The majority of buildings are one- or two-storey residential structures.
- A variety of construction materials are used, including reinforced concrete, masonry, and timber.

- Some houses incorporate a protective masonry or stone cladding along the lower portion of the exterior walls, typically up to a height of approximately 50 cm, to reduce direct water damage to the underlying concrete or timber elements.
- Most houses are founded on shallow concrete foundations. In some cases, the foundation or plinth is elevated above the surrounding ground level to reduce the likelihood of floodwater entering the ground floor.
- Building resistance to flooding varies considerably depending on construction material, maintenance condition and the presence of flood protection measures.

This online map shows the pictures that are taken from a variety of buildings during the visit and its location, see Figure C.6.

Extract results from SFINCS
The project focuses on simulating the coldfront storm that caused flooding of San Felipe in February 2024 in a numerical flood model. The main damage that can be expected from frequent flooding with low inundation levels is deterioration due to salt water attack. Therefore, relevant parameters are inundation zones, levels and duration.

From the SFINCS model for a set of points the closest cell in the numerical model is calculated and the cell's parameters of interest are extracted. These parameters of interest are time series of

- topography with respect to mean sea level; which does not vary over time
- water level; which is with respect to mean sea level
- inundation level; which is the result of subtracting water level from the topography

The time series span the whole event of the flooded simulation and data is extracted every 10 minutes. With the use of this set of parameters a flood hazard map of the chosen simulation is constructed. The markers chosen are located on the streets of San Felipe at every intersection and in between the intersections the points are spaced approximately 50 m to 100 m. Points in between the streets are not selected, because the closest numerical cell might have properties of buildings, without information about the topography, water level and inundation level.

5.4.3 Model setup

Building analysis
Building typologies are defined for incorporation into the comparative damage model. A variety of factors are considered when defining the building typologies in San Felipe. The primary construction material is a key characteristic, as discussed in Section 5.4.2, since the dominant damage mechanisms differ between materials. In addition, the floor level of a building is taken into account, as elevated floors may prevent floodwaters from entering the building and thereby reduce or even eliminate damage to interior walls. Existing protective measures are also considered. For example, some masonry buildings are finished with ceramic tiles that limit direct exposure of the walls to saline water. In timber buildings, a common protective measure is the construction of a concrete base wall of approximately 50 cm in height, which reduces the exposure of the timber elements to floodwater and salt contamination. See Table 5.9 and Table 5.10 for an overview of different building characteristics. For low, medium and high floor levels mean heights of 0.05 m, 0.15 m and 0.25 m are used for the typologies. Appendix K shows example buildings from San Felipe for each building typology.

Damage analysis
Damage characteristics due to frequent exposure to salt water is explored using relevant literature for concrete, masonry and timber.

Concrete
Physical salt attack (PSA) is one of concretes main damage mechanisms. This type of damage must also be considered for the case of San Felipe, because the water contains salt water from the sea during the Nortes. Two types of mechanics can be identified: chloride-induced corrosion of reinforcing steel and salt crystallisation damage in the pore network of concrete (Chen, Ren, Ren, & Li, 2022). The latter one is most relevant for this project, because this one is severely influenced by frequent drying and wetting cycles. The risk of chloride-induced corrosion of reinforcing steel is more relevant for concrete structures that are permanently exposed to salt water.

Table 5.9: Typologies based on material and floor height

abbreviation	Material	Floor level
CL	Concrete	Low level floor
CM	Concrete	Medium level floor
CH	Concrete	High level floor
ML	Masonry	Low level floor
MM	Masonry	Medium level floor
MH	Masonry	High level floor
TL	Timber	Low level floor
TM	Timber	Medium level floor
TH	Timber	High level floor

Table 5.10: Typologies based on material and protective measures

abbreviation	Material	Protective measures
MP	Masonry	Protective tiles
TM	Timber	Protective masonry layer
TC	Timber	Protective concrete layer
CF	Concrete/	Plastered finish
MF	Masonry	

Salt crystallisation damage works as follows:

- Salt water intrudes in the pores of concrete.
- During drying the salt water evaporates while leaving the salt crystals behind, see Figure 5.11.
- These crystals start to grow and create internal stresses in the concrete pores.
- This causes microcracking of the concrete.
- During frequent exposure to wet conditions these microcracks might develop into larger cracks.

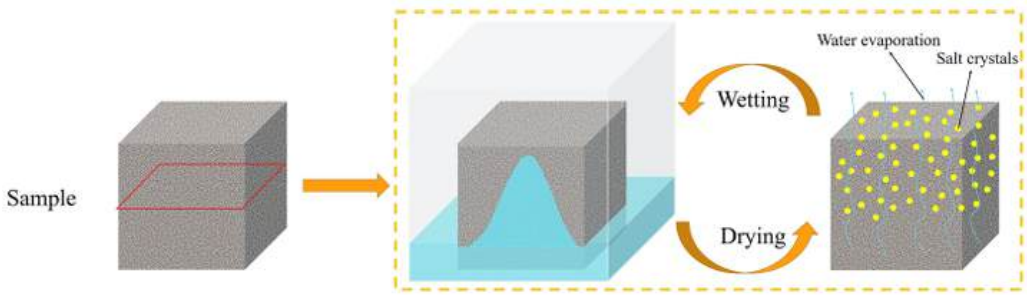


Figure 5.11: The penetration of salt crystals in concrete due to exposure to wet conditions (Huang et al., 2025).

Salt crystallisation damage is considered in this study not because of the impact of a single inundation event, but because of the cumulative effect of repeated saline flooding throughout the lifetime of a building. Recurrent exposure to salt water during Nortes and other coastal flooding events can lead to progressive material deterioration through successive wetting and drying cycles (Sælensminde & Samarakoon, 2016).

Masonry
For masonry structures salt crystallisation is again a relevant damage mechanism (Balksten & Strandberg-de Bruijn, 2021). The mechanism is similar to that from concrete. Saline water might penetrate into both the mortar and the brick components of the structure. Subsequent drying leaves dissolved salt behind. This salt crystallises and causes internal stresses (Niu, Gao, Guan, Li, & Qian, 2025). This results in the following damage:

- deterioration and gradual loss of mortar joints;
- surface damage of masonry units, including flaking, scaling and spalling, see Figure 5.12;
- development of microcracks within bricks and mortar;
- reduction in compressive strength and masonry bond strength.

Although the impact of an individual flooding event is expected to be limited, repeated exposure to saline inundation throughout the lifetime of a building may result in cumulative material degradation due to successive wetting and drying cycles.



Figure 5.12: Damage of masonry structure caused by salt crystallisation (Mydin et al., 2017).



Figure 5.13: Damage of timber structure caused by exposure to water (The Preservation Company, n.d.).

Timber
Wood deterioration is primarily associated with moisture-induced damage and biological decay. Although the salt content increases capture of moist in wood, the damage in timber components is mainly caused by moisture unlike for concrete and masonry damage. During flooding events, timber elements absorb water, which causes

- swelling of the wood;
- drying results in shrinkage, which lead to warping, cracking and progressive material deterioration especially for repeated wetting and drying cycles;
- fungal activity which leads to wood decay;
- reduction of the mechanical properties of timber structures.

Although the impact of a single flooding event is expected to be limited, repeated exposure to inundation throughout the lifetime of a building may result in cumulative degradation of timber components (Brischke & Alfredsen, 2020; Goodell, Winandy, & Morrell, 2020).

Comparative damage model
In order to perform a comparative vulnerability assessment Equation 5.2 is used. The weighted sum in between the brackets accounts for the flooding characteristics, while the material factor and the protection factor are mainly based on building characteristics.
A weighting factor of 0.7 is assigned to inundation depth and 0.3 to inundation duration. Inundation depth is considered the most important parameter, as it determines how much of a building is exposed to floodwater. Inundation duration is given a lower weight, since flooding in San Felipe usually lasts only a limited amount of time. However, longer exposure can still contribute to additional moisture-related damage and is therefore included in the damage function.
The weighted sum of inundation depth and inundation duration represents the flood intensity, while the material and protection factors account for the susceptibility of a building to flood damage. These factors are multiplied to reflect the interaction between flood intensity and building characteristics. As a result, the damage score increases both for more severe flooding conditions and for more vulnerable building types. The resulting damage score ranges from 0 to 1, where 0 represents no expected damage and 1 represents the highest level of damage within the comparative assessment. This approach is consistent with commonly used vulnerability and depth-damage functions in flood risk assessment, which express damage as a fraction of the maximum damage (Huizinga, De Moel, & Szewczyk, 2017). Therefore, the scores should be interpreted as a relative indicator of vulnerability rather than an absolute prediction of damage.
In case the area is inundated ($h_{water} > 0$) but does not reach the floor level of a building ($h_{eff} < 0$) only foundation damage is taking into account. Based on the field visit and the use of Google Streetview (Google Street View, 2026), it is assumed all buildings use concrete slab foundations with similar characteristics. A damage score is calculated by multiplying time factor T by 0.10. Higher coefficients were tested, but these occasionally resulted in damage scores for elevated buildings without interior flooding exceeding those of low-floor buildings experiencing direct inundation. Since direct intrusion of floodwater into the building is expected to

cause substantially greater damage than foundation exposure alone, a lower coefficient is adopted to preserve a physically realistic ranking of damage severity. In the event of no inundation in a certain zone the damage score is simply set to zero.

$$D = \begin{cases} M \times (0.7 \cdot H + 0.3 \cdot T) \times P & h_{eff} > 0 \\ 0.10 \cdot T & h_{eff} = 0, h_{water} > 0 \\ 0 & h_{eff} = 0, h_{water} = 0 \end{cases} \tag{5.2}$$

in which:
D = damage score
M = material factor
H = height factor
T = time factor
P = protection factor

This damage function can also be split in its two components: vulnerability and hazard, because $damage = vulnerability \times hazard$. Vulnerability is dependent on the material factor and hazard is dependent on the specific flood characteristics. It is insightful to map the vulnerability scores and the hazard scores separately as well.
The vulnerability score is calculated as the product of a material factor, floor level factor and protection factor, see Equation 5.4.3. This multiplicative formulation is selected because all three properties act as vulnerability modifiers: a low score in any one factor reduces the overall susceptibility of the building.

$$vulnerability = M \times (1 - h_{floor}/h_{max}) \times P$$

in which:
M = material factor
h_{floor} = floor height of building
P = protection factor

The flood hazard function is defined in Equation 5.3. For each zone it calculates the score taking into account the normalised inundation level and the time factor T.

$$hazard = 0.7 \times h_{water}/h_{max} + 0.3 \times T \tag{5.3}$$

in which:
h_{water} = inundation level from flood model
h_{max} = maximum inundation level from flood model
T = time factor

Material factor
For the three most common building material types in San Felipe, material factors are determined to represent their relative vulnerability to moisture-related damage. Timber exhibits by far the highest vulnerability due to the multiple damage mechanisms involved. Repeated wetting and drying cycles cause shrinkage, warping and cracking, while retained moisture promotes biological deterioration in the form of wood rot. The warm climate of San Felipe further increases the likelihood of such damage because of the consistently high humidity throughout the year (Servicio Meteorológico Nacional (SMN), 2026). Consequently, timber is assigned a material factor of 1.0.
Concrete and masonry are also vulnerable to the intrusion of saltwater. Residual salts left behind after inundation can crystallize within the pore structure, causing internal stresses that lead to cracking and a reduction in material strength. In masonry structures, an additional damage mechanism is the deterioration of the mortar joints, which further compromises structural integrity. Besides, bricks and mortar possess a more interconnected pore network than concrete, which results in higher risk for salt intrusion in the pore structure of masonry compared to concrete (Niu et al., 2025). Therefore, a material factor of 0.60 is assigned to concrete, while masonry is assigned a material factor of 0.75, see Table 5.11.

Height factor
The height factor accounts for the influence of flood depth on the expected level of building damage. Interviews with local residents indicate that floodwater levels during the February 2024 storm reached approximately 0.30 m at their maximum. However, as this estimate is based on a limited number of interviews, higher water levels

Table 5.11: Material factors for concrete, masonry and timber.

	Concrete	Masonry	Timber
Factor M	0.60	0.75	1.00

Table 5.12: Height factors based on effective water depths and maximum inundation levels.

	$h_{eff} \leq 0$	$0 < h_{eff} < h_{max}$	$h_{eff} \geq h_{max}$
Factor H	0	h_{eff}/h_{max}	1.0

Table 5.13: Time factors based on a quadratic relationship for inundation time

	$0 < t < t_{max}$	$t > t_{max}$
factor T	$(\frac{t}{t_{max}})^2$	1.0

Table 5.14: Protective factors for protective tiles, concrete and masonry layers and plastered finish

	protective tiles	concrete layer	masonry layer	plastered finish	no
factor P	0.5	0.6	0.75	0.85	1.0

cannot be excluded. Therefore, a maximum effective flood depth is adopted for the normalisation of the height factor. The linear relation results in the height factors as shown in Table 5.12.

$$h_{eff} = max(h_{water} - h_{floor}, 0) \tag{5.4}$$

in which
h_{eff} = effective waterdepth in zone
h_{water} = inundation level from flood model
h_{floor} = floor height of building

Time factor
Flood depth directly determines which building elements are exposed to floodwater and is therefore considered the dominant damage driver. Inundation duration primarily affects the progression of moisture-related deterioration processes, such as water absorption, salt penetration and biological degradation. Since these processes generally require prolonged exposure before significant damage develops, a non-linear duration factor is considered more physically realistic than a linear relationship (Adeloye, Rustum, & Kariyama, 2020). This results in a time factor as shown in Table 5.13.

Protection factor
Protective measures can significantly reduce the vulnerability of buildings to flood damage. In San Felipe, several timber structures are observed to incorporate a concrete or masonry plinth extending up to approximately 0.5 m above ground level. Some masonry buildings use protective ceramic tiles of a similar height to prevent the lower part of the masonry wall from coming into direct contact with floodwater.
For buildings protected by a concrete plinth, a protection factor of 0.60 is assumed. Given that the expected maximum flood depth is approximately 0.5 m, the concrete layer effectively shields the most vulnerable lower parts of the structure, resulting in a damage response comparable to that of a standard concrete building.
For buildings protected by ceramic tiles, a protection factor of 0.50 is adopted, corresponding to a 50% reduction in damage compared to similar unprotected structures. The tile layer reduces the direct exposure of the building materials to saline floodwater and limits moisture uptake at the base of the walls. However, the protection is not assumed to be complete, as floodwater may still enter the building through door frames, window frames, interior surfaces or other openings. Consequently, some degree of damage is still expected during flood events.
The last protective measure considered in the damage assessment is the presence of a plastered finish on masonry or concrete walls. Although the plaster layer itself remains susceptible to moisture-related deterioration, it provides an additional barrier that delays the ingress of saline floodwater into the underlying structural material. To account for this protection effect, a protection factor of 0.85 is assigned to plastered surfaces, as shown in Table 5.14.

5.4.4 Results

Structural Vulnerability
The vulnerability scores for the main building typologies are depicted in Figure 5.14. The calculations are based on Equation 5.4.3. The assumed floor heights for low, medium and high floor buildings are 0.05 m, 0.15 m and 0.25 m respectively. Besides, the maximum inundation level is assumed to be 0.5 m. As expected, timber structures are the most vulnerable to flooding. However, the implementation of protective measures

reduce the vulnerability scores. In addition, elevated ground floor levels decrease the susceptibility to flood damage. In general, concrete and masonry structures are less prone to damage. The application of protective measures, such as a plastered finish or protective tiles, further reduces the vulnerability scores.

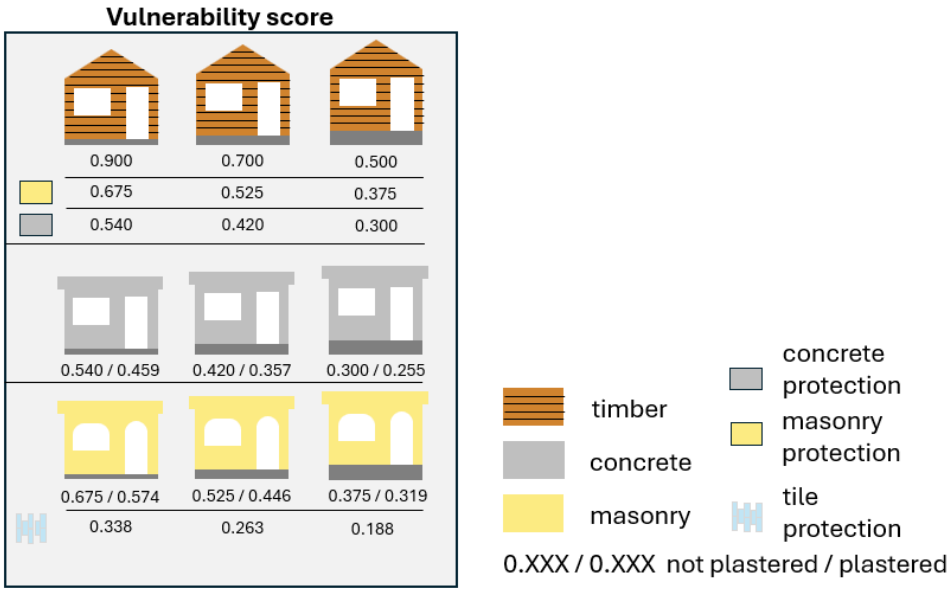


Figure 5.14: Vulnerability scores for main building typologies in San Felipe calculated with 5.4.3 on a comparative scale from 0 *to* 1*.*

Flood Hazard

For the set of markers, as described in Section 5.4.2 and shown in Appendix L the hazard score is calculated using Equation 5.3. Therefore, the maximum inundation of 0.50 m, as shown in Figure L.1, is used to normalise all other values to find the height factor. The maximum total inundation of 28 h, as shown in Figure L.2, is used for the normalisation of the time factor. The resulting hazard scores are shown in Figure 5.15. Hazardous areas are mainly located close to the mangrove areas on the west and east side of San Felipe, as well close to the lagoon along the quay wall in the north. Furthermore, some lower and higher elevated streets can be identified across the town.

Damage Score

In order to combine the flood hazard and the structural vulnerability in one visual result K-Means clustering was performed to identify zones with similar inundation levels and similar inundation duration. The K-Means clustering process is described in Appendix L. Setting $k = 10$ results in the clusters described in Table 5.15 with acceptable standard deviations. The average maximum inundation depth and inundation duration within a cluster is plot with black crosses in Figure 5.16 for each cluster found through the process. This plot also shows coloured dots representing marker points belonging to similar clusters.

After K-Means clustering it can be seen that there are certain hazardous parts of the town (clusters 7, 8, 9 and 10) which are expected to experience more damage due to flooding. Heavily damaged buildings are located in hazardous areas on the western and eastern sides bordering the mangrove area, as well as other hazardous areas located along the quay wall in the north and along the relatively low-lying main street. In contrast, some higher elevated areas do not experience flooding and are therefore not expected to sustain flood damage.

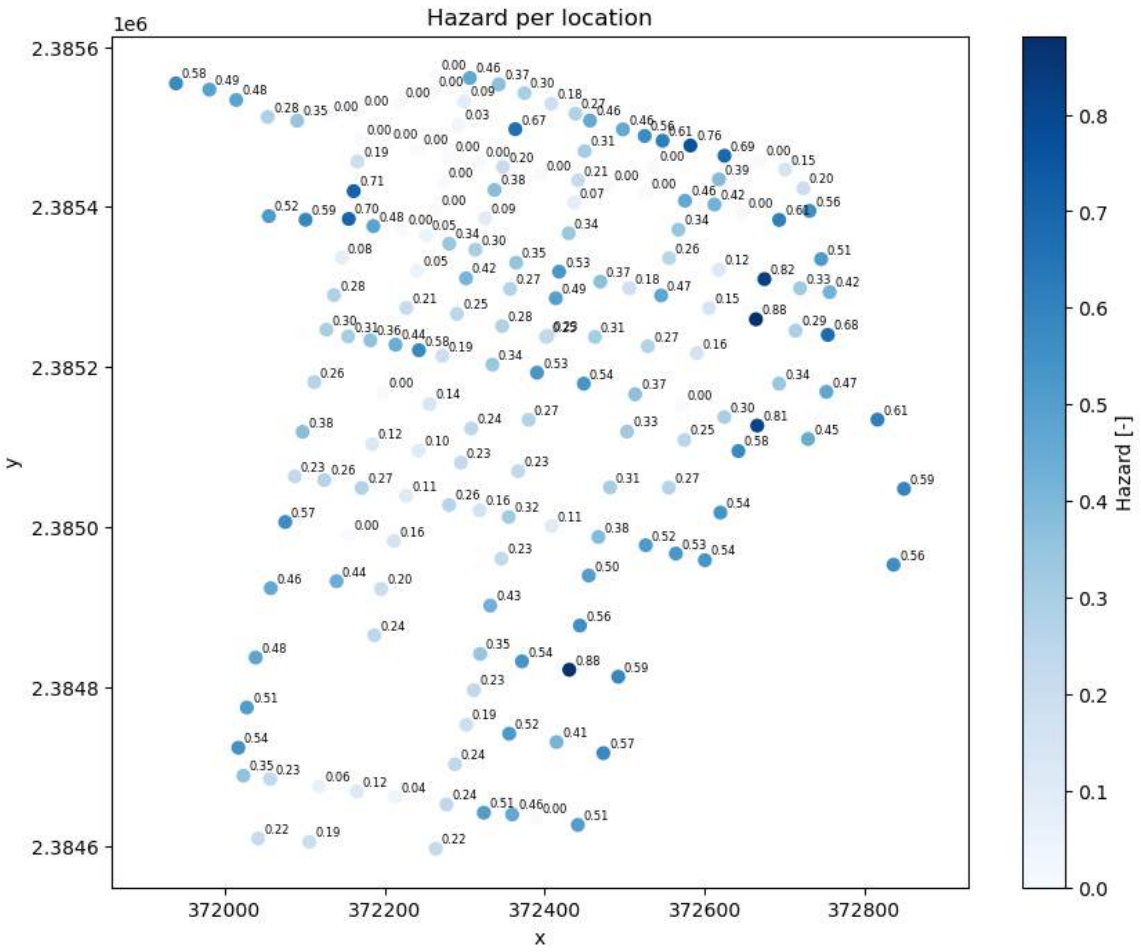


Figure 5.15: Hazard score for the set of markers in San Felipe according to the SFINCS simulation for the February 2024 flooding

Table 5.15: Results of K-Means clustering with $k = 10$. For each cluster, the mean inundation level, the mean cumulative inundation time, and the corresponding standard deviations are given.

	h_{max}		t_{max}		
	mean	std	mean	std	size
1	0.055	0.017	4.84	1.09	184
2	0.127	0.023	7.61	1.04	358
3	0.145	0.010	12.1	1.05	236
4	0.251	0.036	9.71	1.60	62
5	0.171	0.028	16.2	1.21	214
6	0.157	0.021	20.7	1.20	73
7	0.204	0.025	24.2	1.12	118
8	0.388	0.056	12.4	0.69	26
9	0.296	0.033	18.7	1.21	46
10	0.352	0.062	26.4	0.39	51

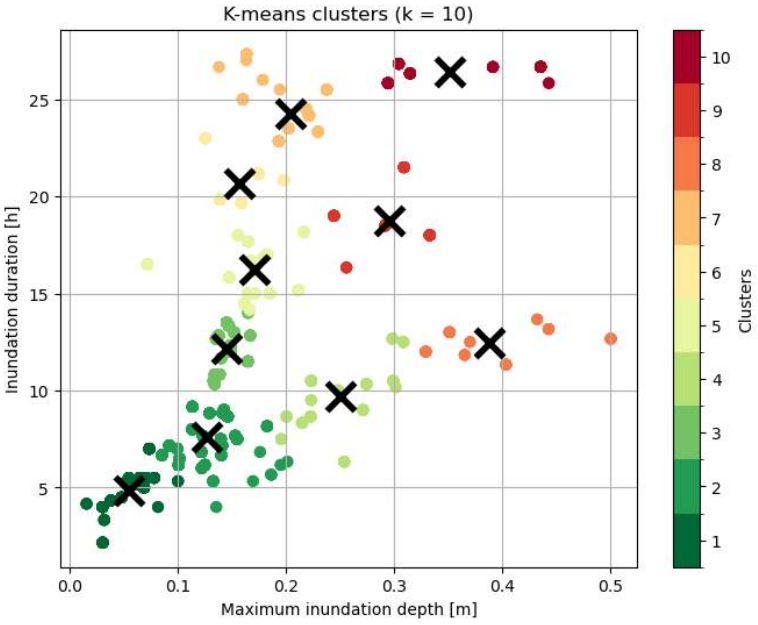


Figure 5.16: Graphical result of the K-Means clustering process with $k = 10$. The black markers indicate the location of each cluster's centre.



Figure 5.17: Final result shows the impact of the February 2024 flooding event on the building structures in San Felipe. Each building is assigned to a cluster. Within each cluster, relative damage scores ranging from 0 to 1 are given for different building typologies.

Chapter 6

Compound Flooding Analysis

First, the methodology of the compound flooding analysis is explained in Section 6.1. The analysis itself is conducted in Section 6.2. The results are discussed in Section 6.3.

6.1 Methodology

To quantify the influence of the different drivers of compound flooding in San Felipe, the statistical analysis method known as factorial design is applied (Montgomery, 2013). This method enables the contribution of individual factors and their interactions to the overall variability of a system response to be quantified. In this study, the factors correspond to the three principal drivers of flooding: precipitation, total water level and initial infiltration. The objective is to determine the extent to which each driver, as well as their interactions, contributes to the simulated flood extent. This analysis provides a quantitative basis for identifying the dominant mechanisms governing flood extent in San Felipe.

The factorial design framework also determines the number of simulations required. For a system with k factors, a full two-level factorial design requires 2^k simulations, where each factor is assigned a low level and a high level. Historical observations are used to define realistic lower and upper bounds for each factor. Since three factors are considered in this study, a total of $2^3 = 8$ simulations are performed. The corresponding simulation matrix is presented in Table 6.1.

For each factor and interaction effect, a contrast is calculated. The contrast represents the difference between the average response at the high level and the average response at the low level of a factor. The contrasts are determined according to the standard sign structure of a 2^3 factorial design. Examples for factor A, the interaction between factor A and B and factor A, B and C are given below:

$$\begin{aligned}
\text{contrast}_A &= -(1) + a - b - c + ab + ac - bc + abc \\
&\vdots \\
\text{contrast}_{AB} &= +(1) - a - b + c + ab - ac - bc + abc \\
&\vdots \\
\text{contrast}_{ABC} &= -(1) + a + b + c - ab - ac - bc + abc
\end{aligned}$$

The contribution of each factor to the total variability is subsequently quantified through its sum of squares:

$$SS_A = \frac{\text{contrast}_A^2}{2^k n}$$

where n is the number of replicates. Since each simulation is evaluated only once in this study, $n = 1$.
The total sum of squares is obtained by summing the contributions of all main effects and interaction effects. The relative contribution of a factor to the simulated flood extent can then be expressed as:

$$P_A = \frac{SS_A}{SS_T} \times 100\%$$

where SS_T denotes the total sum of squares. The percentage contribution provides a direct measure of the relative importance of each flooding driver and interaction effect. Based on these results, the dominant processes controlling flood extent in San Felipe can be identified and compared.

It is important to note that the percentage contributions presented for individual factors and their interactions represent independent orthogonal components of the total variance, summing up to 100%. Consequently, simply summing the contributions of two individual factors does not equal their combined effect, as the system may exhibit non-linear behaviour. Interaction terms capture how factors amplify or reduce each other's impact, meaning the influence of one factor depends on the state of another.

In classical factorial design analysis, the significance of the estimated effects is often assessed using an analysis of variance (ANOVA). This requires the calculation of an error term (SS_E), which is obtained from repeated observations at identical factor settings (Montgomery, 2013). The error term is used to determine the mean square error and the associated F-statistics for each factor and interaction effect. However, only a single simulation is performed for each factor combination, resulting in an unreplicated 2^3 factorial design. Since an estimate of SS_E is unavailable, F-tests and formal significance testing cannot be performed. This does not limit the applicability of the factorial design approach for the objectives of this study. The primary goal is not to determine statistical significance, but to quantify and compare the relative influence of the different flooding drivers on the simulated flood extent. The contribution of each factor is therefore evaluated through its share of the total sum of squares. The resulting percentages provide an indication of the importance of each driver and interaction effect within the investigated range of conditions.

	(1)	a	b	c	ab	ac	bc	abc
A	-	+	-	-	+	+	-	+
B	-	-	+	-	+	-	+	+
C	-	-	-	+	-	+	+	+
score Y	x	x	x	x	x	x	x	x

Table 6.1: According to Factorial Designs theory 8 simulations (from (1) to abc) have to be run.

6.2 Analysis

The statistical method Factorial Design is used to determine the relative contribution of different drivers. The drivers considered are:

- Precipitation
- Storm surge
- Initial infiltration in urban area

Local wind is not included as a driver in the factorial design, because the numerical domain is too small for local wind setup to develop, which means its effect on the system's response negligible. Non-local, large-scale wind effects are captured through the storm surge. Because three drivers are included in the analysis, a 2^3 factorial design is performed one time, which requires the run of eight simulations. Each factor needs a high and a low value.

The lower and upper precipitation values were derived from the time series in Figure E.4 in Appendix E. The lower value was set to 0.0 mm/h to represent dry conditions. The upper value was based on the maximum 3-day cumulative precipitation, since the simulation duration is 3 days. Again, the Peak Over Threshold method was used to calculate the 50-year return period for this cumulative precipitation, resulting in 306 mm precipitation during 3 days, see Figure M.1 in Appendix M.
For storm surge, the lower value was set to 0.0 m instead of a negative value. This ensures that the baseline water level is high enough to induce flooding, as large negative surge values would completely prevent inundation. The upper value was again determined by calculating the 50-year return period for storm surge using the Peak Over Threshold method, resulting in a high value of 0.87 m for storm surge, see Figure M.2 in Appendix M. For the lower value, this means that only a synthetical tide is applied, while for the higher value the Gaussian storm surge curve is added to this synthetical tide.
To ensure numerical stability and avoid introducing sudden shocks into the model, precipitation and storm surge are implemented using a Gaussian curve. For precipitation, achieving the total volume of 306 mm under

this Gaussian profile requires a peak precipitation of 13.4 mm/h and a duration of the entire simulation.
For the initial infiltration rate in the urban area, a lower value of 0.0 mm/h is assumed. This corresponds to a fully paved urban area, where no infiltration is possible. The upper value is assumed to be 50 mm/h. This value is the same as the infiltration rate of land use 'Grassland', see Table 5.7, and corresponds to an urban area with more green areas where water is able to infiltrate.

The lower and upper values for the drivers are summarized in Table 6.2. The time series of the drivers that are used as forcings in SFINCS, which is visualised in Appendix N.

Table 6.2: Lower and upper values for drivers to include in the factorial design

	driver	lower bound	upper bound	unit
P	precipitation	0.0	306	mm
S	storm surge	0.0	0.87	m
I	initial infiltration	0.0	50	mm/h

For each run the flood extent Y has to be quantified. In SFINCS there is no direct output that can be used for this flood extent. Therefore, multiple indirect effects can be used to estimate the flood extent. These effects are Y_1*: total flooded area*, Y_2*: average maximum inundation depth*, Y_3*: average inundation duration* and Y_4*: peak inundation depth*. It is challenging to combine these factors in one score for the flood extent. Therefore, the factors can only be treated separately and conclusions can be drawn upon different flood impacts.

Table 6.3: For all 8 simulations (from (1) to psi) the scores Y_1 (total flooded area), Y_2 (average maximum inundation depth), Y_3 (average inundation duration), and Y_4 (peak inundation depth) are extracted.

	(1)	p	s	i	ps	pi	si	psi
P	-	+	-	-	+	+	-	+
S	-	-	+	-	+	-	+	+
I	-	-	-	+	-	+	+	+
score Y_1	x	x	x	x	x	x	x	x
score Y_2	x	x	x	x	x	x	x	x
score Y_3	x	x	x	x	x	x	x	x
score Y_4	x	x	x	x	x	x	x	x

The scores for Y_1 (total flooded area), Y_2 (average maximum inundation depth), Y_3 (average inundation duration), and Y_4 (peak inundation depth) are determined as follows:

- **Total flooded area (Y_1):** Defined as the maximum percentage of observation points being flooded recorded at a single timestep during the simulation. This indicator captures the spatial extent of the flood, showing how much of the urban or surrounding area is impacted. Defined in a percentage of the total amount of observation points.
- **Average maximum inundation depth (Y_2):** Defined as the average of the maximum inundation depths recorded at all flooded observation points during the simulation. This metric reflects the general severity of water accumulation across the affected zone. The average maximum inundation depth is calculated in m.
- **Average inundation duration (Y_3):** Defined by calculating the total inundation time for each individual observation point, and then taking the average across all flooded observation points. This captures the temporal persistence of the flooding. The average inundation duration is defined in total hours.
- **Peak inundation depth (Y_4):** Defined by the 95^{th} percentile of the maximum inundation depths across all flooded observation points. Instead of relying on an absolute maximum, which can be sensitive to model errors, the 95^{th} percentile provides a metric for extreme peak flooding. The peak inundation depth is calculated in m.

Using these simulation scores, the relative contribution (%) of each individual driver is calculated as well as their combined interactions to determine their influence on flood extent indicators Y_1, Y_2, Y_3 and Y_4.

6.3 Results

Scores for total flooded area (Y_1), average maximum inundation depth (Y_2), average inundation duration (Y_3) and peak inundation depth (Y_4) are quantified across all 8 runs of the factorial design. The three evaluated drivers are: precipitation (P), storm surge (S), and infiltration (I). The resulting scores for each simulation are summarised in Table 6.4. Note that the resulting scores reflect the system's sensitivity within the specific upper and lower bounds defined for each factor in Table 6.2.

Table 6.4: For all 8 simulations (from (1) to psi) the scores Y_1 (total flooded area), Y_2 (average maximum inundation depth), Y_3 (average inundation duration), and Y_4 (peak inundation depth) are calculated.

	(1)	p	s	i	ps	pi	si	psi
P	-	+	-	-	+	+	-	+
S	-	-	+	-	+	-	+	+
I	-	-	-	+	-	+	+	+
score Y_1	0.00	90.29	78.29	0.00	98.86	17.71	77.71	77.71
score Y_2	0.00	0.18	0.33	0.00	0.38	0.03	0.33	0.34
score Y_3	0.00	37.22	19.17	0.00	35.50	22.49	6.88	10.87
score Y_4	0.00	0.86	0.53	0.00	0.84	0.12	0.53	0.53

The scores for total flooded area (Y_1) remain at 0.00% for baseline (1) and only high infiltration (i) runs. Simulations with high precipitation (p) show high scores for total flooded area, reaching 90.29% in run p, and an overall peak score of 98.86% observed in run ps. Only high storm surge (s) results in a score of 78.29%, while combinations with high infiltration (i) generally reduce the flooded area, such as 17.71% in run pi and 77.71% in run psi.

Average maximum inundation depths (Y_2) are 0.00 m for baseline (1) and only high infiltration (i) runs. Only high storm surge (s) results in an average maximum depth of 0.33 m, while only high precipitation (p) reaches 0.18 m. The largest average maximum inundation depth of 0.38 m is achieved in run ps. While the infiltration-precipitation combination (pi) shows a lower inundation depth of 0.03 m, adding infiltration to only high storm surge and the combination of precipitation, storm surge and infiltration (psi) results in a substantially higher average maximum inundation depth of 0.34 m.

Average inundation duration (Y_3) equals 0.00 h for baseline (1) and only high infiltration (i) runs. Simulations with only high storm surge (s) result in a flooding duration of 19.17 h. High precipitation (p) contributes most significantly to inundation duration, reaching a peak duration of 37.22 h in run p, and 35.50 h in run ps. Adding high infiltration (i) reduces the flooding duration to 6.88 h for run si and 10.87 h for run psi.

Peak inundation depths (Y_4) are 0.00 m for baseline (1) and i runs. Only high storm surge (s) reaches a peak depth of 0.53 m, while only high precipitation (p) results in the highest overall peak inundation depth of 0.86 m, closely followed by 0.84 m in run ps. Runs combining infiltration (i) result in lower peak depths, ranging between 0.12 m (pi) and 0.53 m (psi).

The relative contributions (%) of the individual drivers precipitation (P), storm surge (S), infiltration (I) and their interactions on total flooded area (Y_1), average maximum inundation depth (Y_2), average inundation duration (Y_3) and peak inundation depth (Y_4) are evaluated and summarised in Table 6.5. Note that the relative contributions reflect the system's sensitivity within the specific upper and lower bounds defined for each factor in Table 6.2.
As a reminder, the contributions of the combined drivers (e.g., PS, PI) represent non-linear interaction effects, capturing the extent to which one driver amplifies or mitigates the impact of another.

For total flooded area (Y_1), the relative contribution is primarily governed by storm surge (S, 51.75%), followed by precipitation (P, 16.96%) and infiltration (I, 9.12%). Important combined effects include the interactions between precipitation and infiltration (PI, 8.90%) and precipitation and storm surge (PS, 7.84%).

Average maximum inundation depth (Y_2) is highly dominated by storm surge (S), which accounts for 87.39% of the relative contribution. Other individual drivers and interactions, such as precipitation (P, 4.77%), infiltration (I, 2.53%), and the interaction terms PI (2.46%) and PS (1.53%), have small relative contributions.

Table 6.5: Relative contribution (%) of drivers and interactions on Y_1 (total flooded area), Y_2 (average maximum inundation depth), Y_3 (average inundation duration), and Y_4 (peak inundation depth).

Effect	**Contribution Y_1 (%)**	**Contribution Y_2 (%)**	**Contribution Y_3 (%)**	**Contribution Y_4 (%)**
P	16.96	4.77	81.46	24.19
S	51.75	87.39	0.24	31.43
I	9.12	2.53	10.65	16.11
PS	7.84	1.53	1.38	6.54
PI	8.90	2.46	5.83	16.10
SI	2.65	0.64	0.38	2.81
PSI	2.77	0.68	0.06	2.82
Total	**100.00%**	**100.00%**	**100.00%**	**100.00%**

Average inundation duration (Y_3) is largely dominated by precipitation (P), with a relative contribution of 81.46%. Infiltration (I) also provides a significant contribution of 10.65%, while driver interactions such as PI (5.83%) and PS (1.38%) play smaller roles in the average inundation duration.

Peak inundation depth (Y_4) is influenced more evenly among multiple drivers, dominantly by storm surge (S, 31.43%) and precipitation (P, 24.19%), but also by infiltration (I, 16.11%). Additionally, combined effects such as the interaction between precipitation and infiltration (PI, 16.10%) and storm surge with precipitation (PS, 6.54%) significantly influence the peak inundation depth.

Chapter 7

Discussion

This chapter discusses the main limitations of the used data and the applied modelling strategy. Options to improve these limitations are recommended as well. For clarity, a bullet wise summary of all assumptions made in this research is provided in Appendix A.

7.1 SWAN

SWAN is executed in stationary mode, assuming constant boundary conditions. This ignores the dynamic wave growth, decay and shelf travel time during storm events like Nortes. Nevertheless, it provides a safe upper-bound estimate of maximum wave conditions for each water level scenario. To resolve time-dependent wave dynamics, non-stationary simulations should be performed for peak storm periods.
Because SWAN uses a simplified diffraction formulation, it may not fully capture wave bending and spreading through the navigation channel and around the barrier island. Testing a phase-resolving model near the channel is recommended.
Although bathymetry is prepared at a fine 30 m resolution, the computational grid is set to 300 m $\times$ 300 m. This coarse resolution may smooth out narrow channels and sharp elevation changes near San Felipe. Implementing a finer grid around the shoreline and channel would improve spatial accuracy.
Mangroves on the barrier island are represented purely as land elevation rather than vegetation, neglecting wave dissipation during high water levels. Incorporating drag parameters to account for wave attenuation is recommended.
The 10° directional resolution is standard for wind-dominated seas, but it may be coarse for capturing fine-scale refraction around bathymetry near the channel and shore. Increasing the directional resolution for nearshore domains is advised to better capture directional spreading.

7.2 Digital elevation model

The available LiDAR data of the northern part of San Felipe is shifted to the reference system of the GPS measurements. GPS measurements are only performed at the street areas. The southern part of San Felipe is only covered by an interpolated map based on GPS measurements. The more GPS measurement points between the streets, the more precise and representative the elevation map would be for the entire area. In addition, the chosen interpolation method highly affects the elevation between the measured streets. Consequently, using a LiDAR map that covers the whole area of San Felipe would make the elevation map in the southern part of San Felipe more reliable. In that case no interpolated map based on GPS measurement locations would be necessary.
In addition, the GPS measurements are performed by foot, car and pole. The GPS Rover attached to the car was not completely fixed, allowing the GPS Rover to move a few centimetres while driving. This inaccuracy affects the outcome of the final elevation model, as the GPS measurements function as the base of the elevation model. In addition, the GPS Pole measurements were carried out mainly at locations less reliable for comparison with other datasets, such as the quay wall and pavements.
Based on the tide gauge measurements the offset of the bathymetry, topography and water levels at sea is estimated. The evolution of heads over time are also strongly affected by the offset applied to the boundary inputs. Collecting a longer time series (> 5 hours) of tidal data would give a more precise estimation of this offset, allowing for more accurate alignment between the input data and the GPS reference datum. Based on the simulations of SFINCS the offset is calibrated, however the offset is highly sensitive to the model parameters used during modelling.

Moreover, the horizontal and vertical alignment of the tide gauge affects the accuracy of the measurements. Based on one GPS pole measurement and one depth measurement, the height of the tide gauge is determined. Besides, the tide gauge is placed next to the quay wall in the semi-closed harbour. Measurements can be disturbed by the reflection of water to the quay wall. In addition, the semi-closed harbour is not representative for sea conditions and thus the measurements can not be related accurately to the water levels at sea. The practical uncertainties of the tide gauge set-up affect the overall reliability of the elevation model and model outcomes.
The elevation of the mangrove areas are set to one uniform value based on two measurement locations close to each other in the mangrove near San Felipe. From these measurement stations the average elevation of the mangrove is taken. Due to the lack of data describing the elevation of the mangrove areas, one uniform value is set to all areas. More ground elevation measurement locations in the mangrove area surrounding San Felipe would make the mangrove areas in the elevation map more reliable.

7.3 MODFLOW

There are several sources of uncertainty in the MODFLOW simulation, beginning with the assumed model parameters. The unconfined aquifer is assumed to consist of the same sand types as the offshore samples shown in Figure C.4. However, the sand beneath San Felipe may differ from the natural sands near the barrier island. Because the head over time is sensitive to the value of the hydraulic conductivity (k) prior experimental testing (for example a constant-head permeameter test or empirical formulas based on grain-size distributions (for example based on grain-size distribution of soil from San Felipe, Appendix O)) should be conducted on local soil samples from the town of San Felipe to obtain a more reliable estimate.
Regarding spatial discretisation, the bottom of the aquifer is assumed to be at -6 m. This elevation could be determined more accurately using boreholes or seismic refraction testing. Then, the thickness of the unconfined aquifer can be determined accurately, knowing how much this aquifer will contribute to the total water system. Additionally, the model uses a 5×5 m grid size. A Digital Elevation Model (DEM) with a higher resolution would allow for a finer grid, leading to more precise results. The current DEM significantly influences the outcome of the groundwater model as the heads are equal for the southern area on the 5th of February, see Figure J.13. Therefore, the groundwater model is very simplified.
For temporal discretisation, only one steady-state stress period is used, which caused an unstable hydraulic head response during the initial time steps. Extending the steady-state period would likely cause more stable and less uncertain results. Furthermore, while most simulations were run for 10 days, some extended to 20 days, see Appendix J.7. Because differences in the magnitude of the total hydraulic head were observed between these runs, longer simulation times appear to produce a more stable aquifer response and reduce uncertainty.
Given that heads over time are dependent on so many variables, the sensitivity analysis is limited to a qualitative assessment. Moreover, the analysis evaluated the aquifer's response to changing only one model parameter at a time, without accounting for interaction between model parameters.
Total water levels from offshore and lagoon locations are applied as boundary conditions, see Figure J.2 in Appendix J.2. Nevertheless, site-specific monitoring data from the nearby mangrove wetlands and the coastal waters in front of San Felipe would contribute to less-uncertainty. Also, it would be highly beneficial when wells would be installed as observation points for validation. The offset is influencing the boundary conditions directly, described in Section 7.2. Moreover, the boundaries are placed on the edge of San Felipe's town, resulting in a disturbed result at the edges of the domain.
Finally, the GWF simulation only considers the unconfined aquifer, see Figure 2.7. In reality, there is an interaction between this upper unconfined aquifer and the underlying confined aquifer, which is not considered in these simulations.

7.4 SFINCS

The SFINCS domain spans a small area of 4.4 km $\times$ 5 km. While uniform wind is applied, the short fetch limits local wind setup development, meaning the model fully relies on prescribed boundary water levels to capture regional surge. Expanding the domain offshore is recommended to fully capture local wind-setup.
Wave forcing, dynamic run-up and overtopping are excluded, leading to an underestimation of total inundation during wave-dominated events. Sensitivity tests showed static wave setup increased main street water depth from 0.140 m to 0.510 m. Furthermore, the continuous two-way feedback between waves and water levels is neglected. Dynamic two-way coupling with SWAN should be implemented to accurately represent wave-current interactions and wave-driven inundation.

Model results are highly sensitive to vertical offset and mangrove topography. Adjusting the offset to 0.50 m aligned simulations with field observations, but small shifts alter flood extent from dry conditions to severe flooding. Additionally, uniform mangrove elevation zones ignore local creeks and bed variations. Conducting high-resolution topography surveys and implementing spatially variable bed levels in mangrove zones is advised.
Infiltration is modelled using static land-use classes, ignoring temporal variations in soil capacity caused by fluctuating groundwater levels during storm events. Infiltration values are based on hydraulic conductivity. However, it should be taken into account that the hydraulic conductivity is a soil property and the infiltration is a flux based on different parameters (under which the hydraulic conductivity) (Acharya, 2019). Coupling SFINCS with MODFLOW is recommended to account for elevated water tables and reduced infiltration capacity during compound flooding events.

7.5 Structural damage

A number of limitations should be considered when interpreting the results of the structural impact assessment. First, the structural damage assessment is limited to the building typologies defined within the scope of this report, see Appendix K. Other building types that may be present in San Felipe were not included and could respond different in flood events and lead to different damage estimates.
Furthermore, several components of the proposed methodology rely on engineering judgement due to the limited availability of detailed vulnerability data. Parameters such as material and protective factors were selected based on professional judgement and available literature. As a result, alternative assumptions made by other researchers could lead to different comparative damage scores, introducing subjectivity into the assessment.
Buildings assigned to the same typology were assumed to have similar vulnerability characteristics. However, in reality significant differences may exist due to variations in age, construction quality, maintenance condition and material properties. Additionally, the effects of saltwater exposure were represented using simplified vulnerability assumptions. The actual deterioration of structural materials also depends on factors such as exposure duration, salinity concentration, previous environmental degradation and maintenance history. Consequently, the adopted vulnerability scores may not fully capture the variability in flood resistance between individual buildings within the same typology.
The methodology produces relative damage scores that enable comparison between locations and scenarios. However, these scores cannot be directly interpreted as actual economic losses, limiting their applicability for detailed cost-benefit analyses and financial risk assessments.
Finally, the methodology developed in Section 5.4.1 is applied specifically for nortes-driven flooding events in San Felipe, where water depth and inundation duration were considered the dominant parameters for the expected damage type. The potential effects of flow velocity were not incorporated into the damage calculations. It is unlikely that this will significantly affect the assessment of the relatively low-velocity flooding conditions associated with Nortes. However, flow velocity may become an important parameter influencing structural damage under other flood mechanisms. Therefore, if the methodology is applied to different types of flooding, such as storm surges, river floods or rapidly flowing coastal inundation, the influence of flow velocity should be investigated as well. The damage assessment framework should be extended to incorporate flow velocity.

7.6 Compound flooding analysis

While the 2^3 factorial design provided valuable insights, several methodological limitations remain. Applying overlapping Gaussian curves for precipitation and storm surge ignores realistic temporal phase lags; future studies should incorporate timing differences between peaks as an additional factor. Second, treating infiltration as a static factor neglects progressive soil saturation. Dynamically coupling surface and groundwater models, see Section 7.3, would provide a more realistic representation of this process. Third, evaluating only extreme upper and lower bounds assumes a linear system response, missing intermediate topographical tipping points. This simplification can lead to an inaccurate representation of the threshold-driven flooding behaviour. Finally, the purely deterministic model means there is no random error variance (SS_E), which precludes formal ANOVA significance testing. Consequently, it is not possible to establish a statistical threshold to objectively verify whether minor percentage contributions, such as small interaction effects, represent physical processes or are simply negligible model artifacts. Introducing stochastic variations in boundary conditions would enable such formal statistical testing in future assessments.

Chapter 8

Conclusion

Understanding the cause and impact of flood dynamics in San Felipe requires a holistic view of its complex water system, where coastal, hydrogeological, and urban processes all play an important role.

The three investigated drivers (precipitation, storm surge and infiltration) exhibit different impact across the flooding metrics. Storm surge is the primary driver governing the scale and severity of the flooding, since it has the highest relative contribution to both the total flooded area and the average maximum inundation depth. Precipitation is the primary control on the flooding duration. Furthermore, the drivers do not act in isolation, when occurring simultaneously, they exert a non-linear amplifying effect on each other that intensifies the overall flooding. While storm surge and precipitation mutually enhance each other for inundation severity and extent, initial infiltration acts as a crucial mitigating mechanism, actively dampening both the duration and depth of the flood. Finally, the waves have a significant impact on flooding events in San Felipe. However, they haven't been fully investigated in the compound flooding analysis. Ultimately, compound flooding in San Felipe is driven by precipitation and storm surge, of which the impact is mitigated by the infiltration of the soil.

The MODFLOW groundwater flow model is driven by precipitation and total water levels around San Felipe. The precipitation influences directly the water levels in the sea and mangrove which become higher due to rainfall. With high precipitation, the groundwater head rises due to infiltration of water into the unconfined aquifer. The rate of infiltration and rise in groundwater head are highly dependent on the model parameters (hydraulic conductivity, specific yield and recharge coefficient). Based on precipitation and total water levels, the areas most prone to flooding are in the north of San Felipe's town (near the sea) and in the south east. The same can be concluded based on the elevation map.
Interviewees from San Felipe experienced most flooding at the main street, the gas station (in the south) and near the quay walls. The groundwater model shows that the area behind the quay walls is indeed more prone to flooding. Also, the main street shows more critical locations (higher head values compared to elevation) compared to the western street. However, the groundwater model does not assign the gas station (middle south point) as a critical location. The groundwater flow model shows similarity with the fieldwork outcomes, however: not all critical areas from interviewees are covered, meaning that solely groundwater is not the only driver for compound flooding.

Due to frequent cold front storms, the building inventory of San Felipe is prone to repeated saltwater exposure. Cold front storms cause relatively low inundation levels for short durations of time; however, all common building materials suffer from saline water exposure and repetitive drying and wetting cycles. Timber structures may deform through swelling and shrinkage, while fungal activity may cause wood decay. For masonry and concrete structures, salt crystallisation is the main deterioration mechanism.
According to the defined damage model, buildings with low floor levels, made of timber and without additional protection, are the most vulnerable to flooding. High-floor-level concrete structures with a plastered finish or high-floor-level masonry structures with protective tiles are the least vulnerable.
Combining structural vulnerability and flood hazard leads to a comparative damage model. Flood hazard for Norte events is determined by inundation duration and inundation level. Using the SFINCS simulation of the February 2024 cold front flood as input for the comparative damage model shows considerable spatial variability in flood hazard. However after K-Means clustering it can be concluded that there are certain hazardous parts of the town (clusters 7, 8, 9 and 10) in which buildings are expected to experience more damage due to flooding. Some of these areas on the western and eastern sides border the mangrove area, while other hazardous areas are located along the quay wall in the north and along the relatively low-lying main street. In contrast, some higher-elevated areas do not experience flooding and are therefore not expected to sustain flood damage.

Based on these findings, flooding events are driven by extreme atmospheric and marine forces, whose impacts are amplified by non-linear compound interactions between the drivers. Aquifer storage and groundwater levels are critical factors in determining whether an area is sensitive to flooding and therefore also an important factor for compound flooding. Structural vulnerability of specific building typologies combined with flood hazard from simulated events show the impact of flooding on the building structures of San Felipe.

Chapter 9

Recommendations

The way of data sharing is presented in Section 9.1. Recommendations for future research are given in Section 9.2.

9.1 Sharing data

A structured GitHub repository is made with separate folders for the MODFLOW -, SFINCS - and damage model. This setup ensures that the outcomes of this study are easily accessible and simple to build upon in future research.

Github link: https://github.com/bjarnevink/MP406_SanFelipe.git

9.2 Future research suggestions

This research started with a system analysis aiming to quantify how these different environments interact. Throughout this research, coastal, geohydrological and urban systems were modelled. However, no direct coupling was performed. For future research, it would be valuable to dynamically couple the regional MODFLOW model with SFINCS using a Basic Model Interface (BMI) (Hughes et al., 2024). Further investigation is also needed to determine whether SWAN can be dynamically coupled with SFINCS.

Each primary system consists of multiple sub-systems. Within the groundwater model, there is a key interaction between the upper unconfined aquifer and the deeper confined aquifer that warrants further study. In addition, obtaining multiple soil profiles within San Felipe and the surrounding mangrove areas would be useful to determine the depth of the topsoil above the bedrock. Mangrove ecosystems are particularly complex: they can function both as storage basins and as active pathways for surface flow. Consequently, more research is required to understand how mangroves interact with both coastal and geohydrological systems. Furthermore, mapping San Felipe's drainage network is essential for evaluating its surface drainage efficiency and storage capacity.

Moreover, it is important to examine how the different systems respond to extreme events. While the barrier island was assumed to be stable in this study, its response to extreme weather remains uncertain. Future work should investigate how hurricanes impact various components of the environment, including the barrier island, mangrove/swamp area and urban area. Studying extreme events will also provide critical data for validating the existing models and testing their limits.

Finally, while this research focused primarily on identifying the key drivers of compound flooding, recommending flood prevention measures is of high importance for the residents of San Felipe. Future studies should evaluate both local and offshore protection strategies. These mitigation measures could directly be added into the models to understand how San Felipe will react. This to identify which protection measure would be most efficient.

References

Acharya, B. S. (2019). *Infiltration rate vs hydraulic conductivity.* ResearchGate Discussion. Retrieved from https://www.researchgate.net/post/Infiltration_rate_Vs_hydraulic_conductivity (Accessed: 2026-10-30)

Adeloye, A. J., Rustum, K., & Kariyama, N. (2020). A review of flood damage analysis for a building structure and contents. *Natural Hazards*, *102*(3), 967–995. Retrieved from https://link.springer.com/article/10.1007/s11069-020-03941-w doi: 10.1007/s11069-020-03941-w

Appendini, C., Salles, P., Mendoza, E., López, J., & Torres-Freyermuth, A. (2012, 05). Longshore sediment transport on the northern coast of the yucatan peninsula. *Journal of Coastal Research*, *28*, 1404-1417. doi: 10.2112/JCOASTRES-D-11-00162.1

AVISO+. (2026). *Satellite altimetry data and products.* CNES/AVISO+. Retrieved from https://www.aviso.altimetry.fr/en/data.html (Accessed: 14 October 2026)

Balksten, K., & Strandberg-de Bruijn, P. (2021). Understanding deterioration due to salt and ice crystallization in scandinavian massive brick masonry. *Heritage*, *4*(1), 349–370. doi: 10.3390/heritage4010022

Bauer-Gottwein, P., Gondwe, B., & Charvet, G. e. a. (2011, 05). Review: The yucatán peninsula karst aquifer, mexico. *Regional Environmental Change*, 507-524. doi: 10.1007/s1040-010-0699-5

Becker, B., Reichel, F., Bachmann, D., & Schinke, R. (2022). High groundwater levels: Processes, consequences, and management. *WIREs Water*. Retrieved from https://doi.org/10.1002/wat2.1605 doi: 10.1002/wat2.1605

Beltrán, M. (2025, April 2). *Mexico: Aquifer salinization threatens fresh water in coastal communities in yucatán.* Causa Natura Media. Retrieved 2026-09-03, from https://causanaturamedia.com/en/notas/mexico-aquifer-salinization-threatens-fresh-water-in-coastal-communities-in-yucatan

Booij, N., Ris, R. C., & Holthuijsen, L. H. (1999). A third-generation wave model for coastal regions: 1. model description and validation. *Journal of Geophysical Research: Oceans*, *104*(C4), 7649-7666. Retrieved from https://agupubs.onlinelibrary.wiley.com/doi/abs/10.1029/98JC02622 doi: https://doi.org/10.1029/98JC02622

Brinkkemper, J., Torres-Freyermuth, A., Mendoza, E., & Ruessink, B. (2013). Parameterization of wave run-up on beaches in yucatan, mexico: a numerical study. *Preceedings Coastal Dynamics 2013*.

Brischke, C., & Alfredsen, G. (2020). Wood-water relationships and their role for wood susceptibility to fungal decay. *Applied Microbiology and Biotechnology*, *104*, 3781–3795. doi: 10.1007/s00253-020-10479-1

Budhu, M. (2011). *Soil mechanics and foundations* (3rd ed.). Hoboken, NJ: John Wiley & Sons.

Bureau of Meteorology. (2026). *Hydraulic conductivity.* https://www.bom.gov.au/water/awid/id-886.shtml. Commonwealth of Australia. (Accessed: 2026-09-29)

Byrne, K., & Travis, C. (2020, October). *Gamma turns deadly as it inundates Mexico's Yucatan Peninsula.* AccuWeather. Retrieved from https://www.accuweather.com/en/hurricane/tropical-storm-gamma-turns-deadly-as-it-inundates-mexicos-yucatan-peninsula/825143 (Accessed: 2026-09-23)

California Department of Transportation. (2020). *Unified soil classification system and symbol chart* (Technical Reference Sheet). California Department of Transportation (Caltrans). Retrieved from https://dot.ca.gov/-/media/dot-media/programs/maintenance/documents/office-of-concrete-pavement/pavement-foundations/uscs-a11y.pdf (Based on ASTM D2487 standard)

Chamizo, S., Cantón, Y., Lázaro, R., Solé-Benet, A., & Domingo, F. (2012). Role of biological soil crusts in infiltration and runoff generation in drylands. *Hydrological Processes*, *26*(10), 1480–1493. doi: 10.1002/hyp.8276

Chen, S., Ren, J., Ren, X., & Li, Y. (2022). Deterioration laws of concrete durability under the coupling action of salt erosion and drying–wetting cycles. *Frontiers in Materials*, *9*. doi: 10.3389/fmats.2022.1003945

Chuenpagdee, R., Fraga, J., & Euán, J. (2002, 04). Community perspectives toward a marine reserve: A case study of san felipe, yucatán, méxico. *Coastal Management*, *30*, 183-191. doi: 10.1080/08920750275350470 6

CICESE. (2017). *Datos climáticos diarios del clicom del servicio meteorológico nacional.* http://clicom-mex.cicese.mx. (Accessed: 2017-10-06)

Clarkson, L. (2021). *Comprehensive monitoring strategy for tailings dams* (Doctoral dissertation). doi: 10

.14264/d8a5619
Consigna Yucatán. (2022, November 23). *Se inundan calles y casas en el puerto de San Felipe, Yucatán este miércoles.* Facebook. Retrieved from https://www.facebook.com/ConsignaYuc/videos/se-inunda-calles-y-casas-en-el-puerto-de-san-felipe-yucat%C3%A1n-este-mi%C3%A9rcoles-las-c/1106771653363374/ (Video footage documenting coastal flooding in San Felipe due to a *norte*. Accessed: 2026-10-29)
Copernicus Climate Change Service. (2022). *Global sea level change time series from 1950 to 2050 derived from reanalysis and high resolution CMIP6 climate projections.* Copernicus Climate Data Store (CDS). Retrieved from https://cds.climate.copernicus.eu/datasets/sis-water-level-change-timeseries-cmip6?tab=overview (Accessed: 2026-10-14) doi: https://doi.org/10.24381/cds.a6d42d60
deepsoil. (2026). *grai — ai-powered soil analysis for construction.* Retrieved from https://www.deepsoil.at/ (BOKU Spin-off, Vienna, Austria. Accessed: 2026-10-28)
Deltares. (2024). *Hydromt: Water and climate model building and analysis tool.* Zenodo. Retrieved from https://github.com/Deltares/hydromt
Domenico, P. A., & Schwartz, F. W. (1990). *Physical and chemical hydrogeology*. New York: John Wiley Sons.
Ducet, N., Le Traon, P.-Y., & Reverdin, G. (2000). Global high-resolution mapping of ocean circulation from the combination of topex/poseidon and ers-1/2. *Journal of Geophysical Research: Oceans*, *105*(C8), 19477–19498.
Duffield, G. M. (2019). *Representative values of hydraulic properties: Specific yield.* Retrieved 2026-10-15, from http://www.aqtesolv.com/aquifer-tests/aquifer_properties.htm#Specific_Yield (Aquifer Testing 101)
Eduardo, G. C., Irany, V. M., & González Hita, L. (2004). Dinámica de la interfase salina y calidad del agua en la costa nororiental de yucatán. *Ingeniería*, *8*(3), 15-25.
El Heraldo de México. (2020). *Yucatán suspende clases por la tormenta tropical "ZETA".* Retrieved 2026-09-15, from https://elheraldodemexico.com.mx/nacional/2020/10/25/yucatan-suspende-clases-por-la-tormenta-tropical-zeta-218732.html
En Yucatán. (n.d.). *San felipe.* Retrieved 2026-09-02, from https://en-yucatan.com.mx/playas-yucatecas/san-felipe/
Esri. (2025). *How inverse distance weighted interpolation works—ArcGIS Pro 3.5.* Retrieved 2026-03-31, from https://pro.arcgis.com/en/pro-app/3.5/help/analysis/geostatistical-analyst/how-inverse-distance-weighted-interpolation-works.htm (ArcGIS Pro Documentation)
European Space Agency. (2026). *Copernicus Data Space Ecosystem: Sentinel-2 level-2a imagery.* https://browser.dataspace.copernicus.eu/. (Accessed: 14 October 2026)
Ford, D., & Williams, P. (2007). *Karst hydrogeology and geomorphology*. Chichester: John Wiley & Sons.
GEBCO Compilation Group. (2026). *GEBCO grid — general bathymetric chart of the oceans.* Retrieved from https://www.gebco.net/ (Geraadpleegd op 23 september 2026)
Gobierno del Estado de Yucatán. (2012). *Plan estatal de desarrollo 2012–2018* (Tech. Rep.). Gobierno del Estado de Yucatán. Retrieved 2026-09-02, from https://www.yucatan.gob.mx/docs/transparencia/ped/2012_2018/PED_2012_2018.pdf
Gómez-Pompa, A., Allen, M. F., Fedick, S. L., & Jiménez-Osornio, J. J. (Eds.). (2003). *The lowland maya area: Three millennia at the human-wildland interface*. New York: Food Products Press / Haworth Press.
González-Herrera, R., Solís-Pimentel, A., Zetina-Moguel, C., & Mariño-Tapia, I. (2015, 02). Modeling the northern coastline of yucatan, mexico, with genesis. *Environmental & Engineering Geoscience*, *21*(1), 47-61. Retrieved from https://doi.org/10.2113/gseegeosci.21.1.47 doi: 10.2113/gseegeosci.21.1.47
Goodell, B., Winandy, J. E., & Morrell, J. J. (2020). Fungal degradation of wood: Emerging data, new insights and changing perceptions. *Coatings*, *10*(12), 1210. doi: 10.3390/coatings10121210
Google. (2026a). *Google earth pro.* Google. Retrieved from https://earth.google.com/ (Satellite imagery accessed September 15, 2026)
Google. (2026b). *Google my maps.* Retrieved 2026-10-02, from https://www.google.com/maps/about/mymaps/
Google. (2026c). *Satellite image san felipe barrier island.* Google Earth Pro. Retrieved from https://earth.google.com/ (Geraadpleegd op 8 september 2026)
Google Street View. (2026). *Google street view: San felipe, yucatán, mexico.* Retrieved 2026-09-02, from https://www.google.com/maps (Street View imagery accessed on 2 September 2026)
Grillo de Yucatán. (2024). *Eco del "ciclón invernal" en el noreste: lanchas hundidas, sin luz e inundaciones.* Retrieved from https://grillodeyucatan.com/2024/02/07/eco-del-ciclon-invernal-en-el-noreste-lanchas-hundidas-sin-luz-e-inundaciones-video/ (Geraadpleegd in 2026)
H. Ayuntamiento de San Felipe. (n.d.). *Historia.* Retrieved 2026-09-02, from https://

ayuntamientosanfelipeyucatan.gob.mx/index.php/historia/
Henderson, A. R. (2005). The bootstrap: A technique for data-driven statistics. using computer-intensive analyses to explore experimental data. *Clinica Chimica Acta*, *359*(1), 1-26. Retrieved from https://www.sciencedirect.com/science/article/pii/S0009898105002433 doi: https://doi.org/10.1016/j.cccn.2005.04.002
Hersbach, H., Bell, B., Berrisford, P., Biavati, G., Horányi, A., Muñoz-Sabater, J., ... Thépaut, J.-N. (2023). *ERA5 hourly data on single levels from 1940 to present.* Copernicus Climate Change Service (C3S) Climate Data Store (CDS). (Accessed: 2026-10-14) doi: 10.24381/cds.adbb2d47
Hersbach, H., Bell, B., Berrisford, P., Hirahara, S., Horányi, A., Muñoz-Sabater, J., ... others (2020). The era5 global reanalysis. *Quarterly Journal of the Royal Meteorological Society*, *146*(730), 1999–2049.
Holthuijsen, L. H. (2007). *Waves in oceanic and coastal waters*. Cambridge: Cambridge University Press. doi: 10.1017/CBO9780511618536
Huang, D., Liu, F., Han, K., Ge, M., Zong, Y., Luo, Y., & Li, Y. (2025). Soluble salt crystallization effect on the weathering of sandstone at the shimao site. *npj Heritage Science*. Retrieved from https://doi.org/10.1038/s40494-025-02230-8 doi: 10.1038/s40494-025-02230-8
Hughes, J. D., Russcher, M., Herdman, L., Van Ormondt, M., Misut, P., & Jahn, K. L. (2024, December). Dynamic compound flooding simulation on long island, new york, usa. In *Agu24 annual meeting.* Washington, D.C.: American Geophysical Union (AGU). Retrieved from https://agu.confex.com/agu/agu24/meetingapp.cgi/Paper/1578709
Huizinga, J., De Moel, H., & Szewczyk, W. (2017). *Global flood depth-damage functions: Methodology and the database with guidelines* (Tech. Rep. No. JRC105688). Joint Research Centre, European Commission. doi: 10.2760/16510
Höhle, J., & Höhle, M. (2009). Accuracy assessment of digital elevation models by means of robust statistical methods. *ISPRS Journal of Photogrammetry and Remote Sensing*, *64*(4), 398-406. Retrieved from https://www.sciencedirect.com/science/article/pii/S0924271609000276 doi: https://doi.org/10.1016/j.isprsjprs.2009.02.003
INEGI. (2026). *National institute of statistics and geography (INEGI).* Retrieved from https://en.www.inegi.org.mx/ (Geraadpleegd op 9 oktober 2026)
Johnson, A. I. (1967). *Specific yield: compilation of specific yields for various materials* (Water Supply Paper No. 1662-D). Washington, D.C.: U.S. Geological Survey. Retrieved from https://doi.org/10.3133/wsp1662D doi: 10.3133/wsp1662D
Koper, H. P. (2024). *Investigating the implementation of nature-based solutions in the geul catchment using numerical modelling* (Master's thesis, Vrije Universiteit Amsterdam). Retrieved from https://www.jcar-atrace.eu/_default_upload_bucket/thesis_huub_koper_final_compressed.pdf
Langevin, C. D., Hughes, J. D., Banta, E. R., Niswonger, R. G., Panday, S., & Provost, A. M. (2017). *Documentation for the modflow 6 groundwater flow model* (Techniques and Methods Nos. book 6, chap. A55). Reston, VA: U.S. Geological Survey. Retrieved from https://doi.org/10.3133/tm6A55 doi: 10.3133/tm6A55
Langevin, C. D., Hughes, J. D., Banta, E. R., Niswonger, R. G., Panday, S., & Provost, A. M. (2018, August). *Modflow 6 – description of input and output* (Tech. Rep. No. Version mf6.0.3). U.S. Geological Survey. Retrieved from https://github.com/MODFLOW-USGS/modflow6 (Prepared in cooperation with the U.S. Geological Survey Water Availability and Use Science Program)
Langevin, C. D., Hughes, J. D., Provost, A. M., Russcher, M. J., Reno, M. J., Bonelli, W. P., ... Banta, E. R. (2026, September). *MODFLOW 6 Modular Hydrologic Model.* U.S. Geological Survey Software Release. Retrieved from https://doi.org/10.5066/P1PGE9XW (Version 6.8.0) doi: 10.5066/P1PGE9XW
Leijnse, T., van Ormondt, M., Nederhoff, K., & van Dongeren, A. (2021). Modeling compound flooding in coastal systems using a computationally efficient reduced-physics solver: Including fluvial, pluvial, tidal, wind- and wave-driven processes. *Coastal Engineering*, *163*, 103796. doi: 10.1016/j.coastaleng.2020.103796
Lesser, J. M. (1976). *Estudio hidrogeológico e hidrogeoquímico de la península de yucatán* (Tech. Rep. No. Proyecto CONACYT-NSF 704). Mexico City, Mexico: Secretaría de Recursos Hidráulicos, Dirección de Geohidrología y Zonas Áridas. (Hydrogeological and hydrochemical study of the Yucatan Peninsula)
Lubelli, B., van Hees, R., et al. (2018). *Salt weathering of building materials*. RILEM.
Maldonado, L., Veleva, L., & Díaz-Ballote, L. (2011). Characterization of limestones for building in the yucatan peninsula, mexico. *Applied Physics A*, *103*(4), 1105–1110. doi: 10.1007/s00339-010-6049-6
Medeiros, S. (2023, 10). Hydraulic bottom friction and aerodynamic roughness coefficients for mangroves in southwest florida, usa. *Journal of Marine Science and Engineering*, *11*, 2053. doi: 10.3390/jmse11112053
Medellín, G., Brinkkemper, J., Torres-Freyermuth, A., Appendini, C., Mendoza, E., & Salles, P. (2016). Run-up parameterization and beach vulnerability assessment on a barrier island: a downscaling approach. *Natural Hazards and Earth System Sciences*, *16*(1), 167–180.
Medina Rosado, J. A. (2024). *Caracterización hidrodinámica del acuífero de la isla de barrera de sisal,*

yucatán (Tesis de maestría, Ciudad de México). Retrieved 2026-10-16, from https://hdl.handle.net/20.500.14330/TES01000861934 (Asesores: Salles Afonso de Almeida, Paulo; Pacheco Castro, Roger Benito)

Medina-Rosado, J. A., González-Herrera, R., Pacheco-Castro, R., Canul-Macario, C., & Salles, P. (2026). Hydrogeological characterization of the sisal barrier island aquifer, yucatan, mexico. *Hydrology Research*, *57*, 100014. doi: 10.1016/j.hydrch.2026.100014

Melchers, R. E. (2020). Long-term durability of marine reinforced concrete structures. *Journal of Marine Science and Engineering*, *8*(4), 290. doi: 10.3390/jmse8040290

Metcalfe, S., Schmook, B., & Boyd, D. e. a. (2020, 02 17). Community perception, adaptation and resilience to extreme weather in the yucatan peninsula, mexico. *Regional Environmental Change*, 20-25. doi: 10.1007/s10113-020-01586-w

Moan, S. A. (1993a). *Ecotourism on the yucatan peninsula: Ecotourism potentials in the rio lagartos wildlife preserve.* (Tech. Rep.). State University of New York College of Environmental Science and Forestry. Retrieved from http://gateway.proquest.com/openurl?url_ver=Z39.88-2004&rft_val_fmt=info:ofi/fmt:kev:mtx:dissertation&res_dat=xri:pqm&rft_dat=xri:pqdiss:1351689

Moan, S. A. (1993b). *Ecotourism on the yucatan peninsula: Ecotourism potentials in the rio lagartos wildlife preserve.* (Tech. Rep.). State University of New York College of Environmental Science and Forestry. Retrieved from http://gateway.proquest.com/openurl?url_ver=Z39.88-2004&rft_val_fmt=info:ofi/fmt:kev:mtx:dissertation&res_dat=xri:pqm&rft_dat=xri:pqdiss:1351689

Monroy-Ríos, E. (2020). *Chicxulub crater and ring of cenotes.* Retrieved 2026-09-03, from https://sites.northwestern.edu/monroyrios/some-maps/chicxulub-and-ring-of-cenotes/ (Karst Geochemistry and Hydrogeology, Northwestern University)

Montgomery, D. C. (2013). *Design and analysis of experiments* (8th ed.). John Wiley & Sons.

Moreno-Gómez, M., Martínez-Salvador, C., Liedl, R., Stefan, C., & Pacheco, J. (2021). First application of the integrated karst aquifer vulnerability (IKAV) method. Potential and Actual vulnerability in Yucatan, Mexico. *Natural Hazards and Earth System Sciences Discussions*, *2021*, 1–31. Retrieved from https://doi.org/10.5194/nhess-2021-376 doi: 10.5194/nhess-2021-376

Morton, R., & Miller, T. (2005, 01). *National assessment of shoreline change: Part 2: Historical shoreline changes and associated coastal land loss along the u.s. southeast atlantic coast http://pubs.usgs.gov/of/2005/1401/.*

Mulcahy, N., & Blanchon, P. (2016, 03). Hurricane-induced shoreline change and post-storm recovery: northeastern yucatan peninsula, mexico. *Journal of Coastal Research*, *75*, 1192-1196. doi: 10.2112/SI75-239.1

Mydin, M., Mohd Nawi, M. N., & C. Munaaim, M. A. (2017, 01). Investigation of rising damp and salt attack problems of heritage buildings. *Malaysian Construction Research Journal*, *2*, 151-165.

National Ecological Observatory Network (NEON). (2026). *Lidar.* https://www.neonscience.org/data-collection/lidar. (NSF NEON, operated by Battelle. Accessed: 2026-10-05)

National Weather Service. (2024, July). *Hurricane Beryl 2024.* NOAA/National Weather Service Weather Forecast Office Lake Charles, LA. Retrieved from https://www.weather.gov/lch/2024Beryl (Accessed: 2026-09-23)

Nidzieko, N. J. (2010). Tidal asymmetry in estuaries with mixed semidiurnal/diurnal tides. *Journal of Geophysical Research: Oceans*, *115*(C8). Retrieved from https://agupubs.onlinelibrary.wiley.com/doi/abs/10.1029/2009JC005864 doi: https://doi.org/10.1029/2009JC005864

Niu, L., Gao, S., Guan, J., Li, L., & Qian, J. (2025). Impact of salt crystallization on the mechanical properties of masonry. *Journal of Materials in Civil Engineering*. doi: 10.1061/JMCEE7.MTENG-18668

Novedades Yucatán. (2020). *Termina Declaratoria de Emergencia tras inundaciones en Yucatán por tormenta 'Cristóbal'.* Retrieved 2026-09-15, from https://sipse.com/novedades-yucatan/termina-declaratoria-de-emergencia-tras-inundaciones-en-yucatan-tormenta-cristobal-371462.html

NU.nl. (2005). *Wilma laat spoor van verwoesting achter in Mexico.* Retrieved 2026-09-15, from https://www.nu.nl/algemeen/613523/wilma-laat-spoor-van-verwoesting-achter-in-mexico.html

Oostwegel, L. J. N., Schorlemmer, D., & Guéguen, P. (2025). From footprints to functions: A comprehensive global and semantic building footprint dataset. *Scientific Data*, *12*, 1699. doi: 10.1038/s41597-025-06132-z

Oostwegel, L. J. N., Schorlemmer, D., Lingner, L., & Evaz Zadeh, T. (2025). *Openbuildingmap.* GFZ Data Services. Retrieved from https://doi.org/10.5880/GFZ.LKUT.2025.002 doi: 10.5880/GFZ.LKUT.2025.002

Por Esto! (2026, October 10). *Marea alta invade calles y viviendas de Río Lagartos y San Felipe.* Retrieved from https://www.poresto.com/yucatan/2026/10/10/marea-alta-invade-calles-viviendas-rio-lagartos-san-felipe.html (Accessed: 2026-10-29)

PorEsto! (2020). *Así quedó San Felipe tras el paso del Huracán Delta.* Retrieved 2026-09-

15, from https://www.poresto.com/yucatan/2020/10/7/asi-quedo-san-felipe-tras-el-paso-del-huracan-delta.html

Procuraduría Federal de Protección al Ambiente (PROFEPA). (2024, August 23). *Clausuran construcciones irregulares en ría lagartos.* Retrieved 2026-09-15, from https://www.gob.mx/profepa/prensa/clausuran-construcciones-irregulares-en-ria-lagartos?state=published (Official press release of the Government of Mexico)

QGIS Project. (2025). *Spatial analysis (interpolation).* Retrieved 2026-10-09, from https://docs.qgis.org/3.44/en/docs/gentle_gis_introduction/spatial_analysis_interpolation.html

Sælensminde, J., & Samarakoon, S. S. M. (2016). Deterioration of concrete structures due to salt crystallization: Influence of salt types and relative humidity. In *Proceedings of the international rilem conference on materials, systems and structures in civil engineering* (pp. 120–127). RILEM Publications.

Santana, R. (2020). *Emiten Declaratoria de Desastre por daños causados por 'Cristóbal' en Yucatán.* Retrieved 2026-09-15, from https://www.proceso.com.mx/nacional/estados/2020/6/20/emiten-declaratoria-de-desastre-por-danos-causados-por-cristobal-en-yucatan-244822.html

SciPy community. (2026). *scipy.stats.bootstrap, scipy v1.18.0 manual.* Retrieved 2026-10-08, from https://docs.scipy.org/doc/scipy/reference/generated/scipy.stats.bootstrap.html

Servicio Meteorológico Nacional (SMN). (2026). *Normales climatológicas por estado: Estación río lagartos, yucatán.* Retrieved from https://smn.conagua.gob.mx/es/climatologia/informacion-climatologica/normales-climatologicas-por-estado?estado=yuc (Accessed: 6 October 2026)

Shafak, E. (2023). *There are rivers in the sky*. Viking.

Smardon, R. (2009). Estuaries on the edge, yucatan peninsula, mexico. In *Sustaining the world's wetlands: Setting policy and resolving conflicts* (pp. 211–266). New York, NY: Springer US. Retrieved from https://doi.org/10.1007/978-0-387-49429-6_8 doi: 10.1007/978-0-387-49429-6_8

SWAN Team. (2023). SWAN user manual, SWAN cycle III version 41.45 [Computer software manual]. Delft, The Netherlands. Retrieved from https://swanmodel.sourceforge.io/download/zip/swanuse.pdf (Available at: https://swanmodel.sourceforge.io/download/zip/swanuse.pdf)

Sánchez, A. (2024). *Huracán 'Milton' deja saldo blanco en Yucatán; Celestún y Progreso, los más afectados.* Retrieved 2026-09-15, from https://www.lajornadamaya.mx/yucatan/238127/huracan-milton-deja-saldo-blanco-en-yucatan-celestun-y-progreso-los-mas-afectados

Sánchez-García, E. A., Yañez-Arenas, C., Lindig-Cisneros, R., Lira-Noriega, A., Monroy Ibarra, R., & Moreno-Casasola, P. (2023). The expected impacts of sea level on the mexican atlantic coast. *Science of The Total Environment*, *903*, 166317. Retrieved from https://www.sciencedirect.com/science/article/pii/S0048969723049422 doi: https://doi.org/10.1016/j.scitotenv.2023.166317

Terich, T. A. (1970). *History of san felipe site utilization: Epilogue.* https://mexfish.com/sflp/sflp/terich/terichepi.htm. (Geraadpleegd via MexFish.com)

The Preservation Company. (n.d.). *Your guide to dry rot and wet rot.* Retrieved from https://www.thepreservationcompany.co.uk/blog/your-guide-to-dry-and-wet-rot/ (Accessed: 2026-10-01)

Treu, A., Zimmer, K., Brischke, C., et al. (2019). Durability and protection of timber structures in marine environments in europe: An overview. *BioResources*, *14*(4), 10195–10219. doi: 10.15376/biores.14.4.TREU

TU Delft. (2022). *Hydrologie* (Dictaat No. CTB2420-17). Technische Universiteit Delft. (Collegejaar 2022-2023)

UC Berkeley D-Lab. (2021). *A beginner's guide to bootstrap.* Retrieved from https://dlab.berkeley.edu/news/beginner%E2%80%99s-guide-bootstrap (Accessed: 2026-10-02)

Uliana, M. M. (2025). *Basic hydrogeology: An introduction to the fundamentals of groundwater science*. Guelph, Ontario, Canada: The Groundwater Project. Retrieved from https://books.gw-project.org/basic-hydrogeology-an-introduction-to-the-fundamentals-of-groundwater-science/ doi: 10.62592/CBIQ7579

Universidad Nacional Autónoma de México. (2014). *Fenómenos hidrometeorológicos* (Report). Universidad Nacional Autónoma de México (UNAM). Retrieved 2026-09-15, from https://ru.dgb.unam.mx/server/api/core/bitstreams/194084b8-1a3e-41f8-b958-23b642e2fdb6/content

Urrutia-Fucugauchi, J., Pérez-Cruz, L., Wittmann, A., Arz, J. A., Arenillas, I., Xiao, L., ... Salguero-Hernandez, E. (2025). Chicxulub central zone structure and stratigraphy—pemex exploration drilling program. *Frontiers in Earth Science*, *13*, 1550746. doi: 10.3389/feart.2025.1550746

Vignudelli, S., Kostianoy, A. G., Cipollini, P., & Benveniste, J. (2011). Coastal altimetry. *Springer Science & Business Media*, 1–578.

Vos, K., Splinter, K., Harley, M., Simmons, J., & Turner, I. (2019, 09). Coastsat: A google earth engine-enabled python toolkit to extract shorelines from publicly available satellite imagery. *Environmental Modelling Software*, *122*, 104528. doi: 10.1016/j.envsoft.2019.104528

Weidie, A. E. (1985). Geology of Yucatan platform. In W. C. Ward, A. E. Weidie, & W. Back (Eds.), *Geology and hydrogeology of the Yucatan and Quaternary geology of northeastern Yucatan peninsula* (pp. 1–19).

New Orleans, LA: New Orleans Geological Society.
Winston, R. B. (2019a). *GHB: General-head boundary package pane — ModelMuse documentation.* Retrieved from https://water.usgs.gov/nrp/gwsoftware/ModelMuse/Help/ghb_general_head_boundary_package.html (Accessed: 2026-10-14)
Winston, R. B. (2019b). *Specified head — ModelMuse documentation.* Retrieved from https://water.usgs.gov/nrp/gwsoftware/ModelMuse/Help/specified_head.html (Accessed: 2026-10-14)
Xiao, Y., Shao, J., Frape, S. K., Cui, Y., Dang, X., Wang, S., & Ji, X. (2018). Groundwater origin, flow regime and geochemical evolution in arid endorheic watersheds: a case study from the qaidam basin, northwestern china. *Hydrology and Earth System Sciences*, *22*(8), 4381–4400. Retrieved from https://doi.org/10.5194/hess-22-4381-2018 doi: 10.5194/hess-22-4381-2018
Yucatán Magazine. (2018, September). *30 years later, we remember Hurricane Gilberto.* Yucatán Magazine. Retrieved from https://yucatanmagazine.com/30-years-later-we-remember-hurricane-gilberto/ (Accessed: 2026-09-23)
Yucatán Independiente. (2026, January 28). *Por el norte, mar inundó calles de San Felipe.* Facebook. Retrieved from https://www.facebook.com/yucindependiente/videos/por-el-norte-mar-inund%C3%B3-calles-de-san-felipe/2120836492013074/ (Video footage documenting coastal flooding in San Felipe due to a *norte*. Accessed: 2026-10-29)
Zanaga, D., Van De Kerchove, R., Daems, D., De Keersmaecker, W., Brockmann, C., Kirches, G., ... Arino, O. (2022). *ESA WorldCover 10 m 2021 v200.* Zenodo. Retrieved from https://doi.org/10.5281/zenodo.7254221 doi: 10.5281/zenodo.7254221

Appendix A

Summary of Assumptions in this Report

Although the assumptions used in this report are mentioned in the text, they are summarised in this appendix for clarity. For convenience, the assumptions are categorised and written in bullet form.

Data analysis

- Based on comparisons with offshore ADCP measurements near Sisal, it is assumed that the ERA5-driven modelled water levels and atmospheric data are sufficiently reliable to be used throughout the study.
- It is assumed that selecting the February 2024 cold front (Norte) event is representative and optimal for model validation.

Elevation model

- It is assumed that Inverse Distance Weighted (IDW) interpolation with a p-value of 2 is appropriate for generating a continuous elevation grid from the discrete GPS fieldwork measurements, see Appendix I.
- It is assumed that the GPS measurements by foot, Pole and car are accurate measurements to obtain a representative elevation map of San Felipe.
- It is assumed that the tide gauge measurements are sufficiently accurate to determine to a certain extent, the offset of the water level (sea and mangrove), bathymetry and topography.
- The topography is downloaded from INEGI (INEGI, 2026). The mangrove areas indicated by ESA Worldcover (Zanaga et al., 2022) are lowered by 2.2183 m (Appendix I.7).
- It is assumed that the mangrove elevation immediately surrounding San Felipe is higher than the rest of the mangrove, set to -0.044 m based on fieldwork photographs.

SWAN

- The computational domain spans 104 km by 55 km with a uniform spatial resolution of 300 m by 300 m, assuming this resolution is sufficient to capture coastal wave dynamics.
- The model is run in stationary mode, assuming that steady-state wave conditions are reached and that temporal variations during the storm can be neglected.
- Boundary conditions are derived from ERA5 data 4.2 at a single representative coordinate $[22°\text{N}, -88°\text{W}]$, assuming spatially uniform wave and wind forces along the Northern, Eastern, and Western boundaries.
- Initial wave conditions are generated according to the JONSWAP spectrum with a directional spreading of $24.9°$ (SWAN Team, 2023), assuming wind-sea waves are dominant during Nortes events.
- Spectral directional resolution is set to $10°$ and the frequency range spans from 0.03 Hz to 1.0 Hz, assuming this discretisation sufficiently captures the dominant wave spectrum (SWAN Team, 2023).

MODFLOW

- An estimation of the hydraulic conductivity is based on samples from the barrier island (see Section 5.2.4). These samples are said to be medium to coarse sands according to (Domenico & Schwartz, 1990) as explained in Section 5.2.4.

- Based on the fact that the groundwater flow model is for an unconfined aquifer, a range for values for the specific yield is estimated (see Section J.4).
- The range for the recharge coefficients is used following the paper of (Medina Rosado, 2024).
- Precipitation data is used from coordinates 21°3000 N, 88°1500 W and it is assumed that this is distributed uniform over the domain.
- For the CHD boundary, the total water levels are retrieved from location 21.577000°N, -88.345000°W.
- For the GHB boundary, the total water levels are retrieved from location 21.606000°N, -88.110000°W
- The bottom of the aquifer is assumed to be at -6 m, since no ground profiles are available for the study area.
- To account for soil anisotropy, the vertical hydraulic conductivity (z-direction) is assumed to be one-tenth of the horizontal conductivity (Xiao et al., 2018).

SFINCS

- Manning roughness coefficients as defined in Table 5.6 are based on reference (Koper, 2024) and applied across different ESA WorldCover land-cover classes (Zanaga et al., 2022).
- Structures in the lower part of the city are included via imported polygons to keep structure cells active, whereas structures in the upper part of the city are captured by the LiDAR data.
- Infiltration rates as defined in Table 5.7 are based on engineering judgement, Section 5.2.2, and references (Clarkson, 2021) and (Chamizo et al., 2012).
- For modelling the Norte of 5 February 2024, the total water level along offshore boundaries is interpolated between the two stations closest to San Felipe: one west of the town at 21.577°N, 88.345°W (11.5 km away) and one east of the town at 21.606°N, 88.110°W (13.5 km away).
- For the modelling period of 8–11 November 2025, ADCP data from El Cuyo is assumed to be representative for the offshore water levels at San Felipe.
- It is assumed that wind and precipitation fields are uniform over the domain since the model domain spans only a few kilometres, meaning small-scale rainfall variability is not resolved (in line with ERA5 limitations described in Section 4.3).
- It is assumed that the downloaded topography from INEGI (INEGI, 2026) does not include the correct mangrove elevation; the mangrove area is lowered by 2.2182 m based on measurement stations "SF-04" and "KBN-01" from the San Felipe Research Group.
- It is assumed that the mangrove elevation immediately surrounding San Felipe is higher than the rest of the mangrove, set to -0.044 m based on fieldwork photographs.
- During model validation, the initial water level offset is adjusted from 0.656 m (derived from future projections) to 0.50 m to better match historical observations of the February 2024 event.
- Wave-driven forcing is excluded from the main validation model to prioritize parameter calibration, but its impact is separately investigated using a static empirical wave setup ($\langle\eta\rangle \approx 0.34$ m) based on Medellín et al. (2016).

Statistical analysis

- It is assumed that local wind can be neglected because the numerical domain is too small for local wind setup, while large-scale wind effects are captured through storm surge.
- For high values of precipitation and storm surge, it is assumed that the Peak Over Threshold method combined with a 50-year return period provides a realistic and representative upper value.
- It is assumed that an infiltration rate of 0.0 mm/h represents a fully paved urban area without infiltration, whereas 50 mm/h simulates an urban area with increased green spaces.

Structural impact

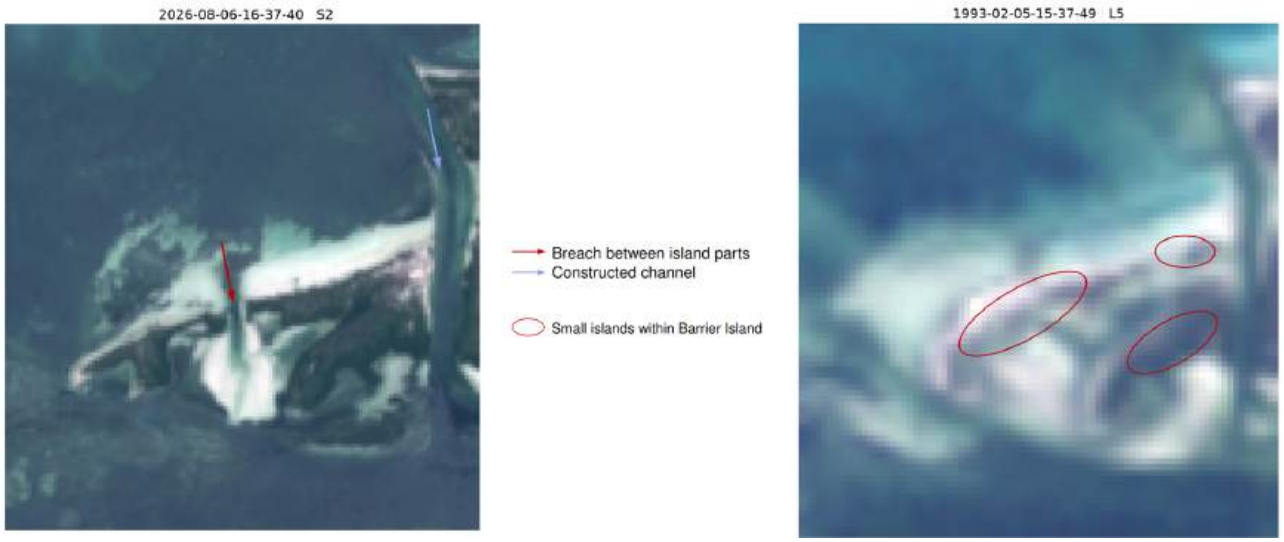
- Cold front events affect the town of San Felipe, resulting in low-level flooding. These inundation levels are expected to be below 0.50 m; during the field trip, the locals pointed out that they had witnessed inundation levels of $15\tilde{}30$ cm at their highest, see Appendix H.
- The damage that can be expected with this type of flooding is mainly deterioration due to salt water attack. Other structural damage mechanism are left out of the scope of this report.

- It is assumed that the concrete, masonry and timber used in San Felipe's buildings are not designed to resist the deterioration mechanisms associated with repeated saltwater exposure, unlike materials specifically engineered to meet the most severe environmental exposure class as for example defined in the Eurocode.
- Protective measures; the use of ceramic tiles, plastered finish, concrete and masonry base walls are assumed to protect the structure up to the maximum inundation level, initially assumed as 0.5 m.
- The damage score is a comparative score for buildings in San Felipe, in which a score of 0 refers to no damage and a score of 1 relates to the most heavily impacted structure type.
- If the inundation level is not exceeding the floor level of a building type, only foundation damage effects are considered in this assessment, see Equation 5.2. In which it is assumed all buildings use similar concrete slab foundations.
- Material factors as defined in Table 5.11 are based on engineering judgement and references (Niu et al., 2025), (Huang et al., 2025), (Sælensminde & Samarakoon, 2016), (Brischke & Alfredsen, 2020), (Goodell et al., 2020). Others might come up with different values for a comparative damage assessment.
- Height and time factors are based on normalisation, because the damage score is comparative. A linear relationship between damage and height and a quadratic relationship between damage and time is assumed based on (Adeloye et al., 2020), see Table 5.13 and 5.12.
- Protection factors as defined in Table 5.14 are based on engineering judgement. Others might come up with different values for a comparative damage assessment.

Appendix B

Changes Barrier Island over time

Barrier Islands emerge as a result of the following mechanisms: Dune Drowning, Spit elongation or Shoal emergence (Morton & Miller, 2005). The barrier Island in front of San Felipe protects the shore from wave and wind induced forces. The barrier island itself is also dependent on the several factors such as sediment supply, wind and wave conditions from the Gulf of Mexico, sea level and tectonics in the area. The effect of storms on the barrier island is variable. The amount of change due to a specific storm is dependent on a lot of factors (storm related and site specific) (Mulcahy & Blanchon, 2016).
The barrier island in front of San Felipe is analysed for the following time period: 1985 to 2026. CoastSat is used for the analysis between 1985 and 2003 and between 2013 and 2026. The satellite data of the time period 2003-2013 was not detailed enough/blurred to detect changes using CoastSat and for this reason Google Earth is used for that time period (Google, 2026c). The area of interest is the west side of the barrier island, starting from the west of the constructed channel. Figure B.1 shows the terms used to describe the barrier island changes.



(a) Breach and Constructed Channel *(b) Small Islands*

Figure B.1: Clarification of terms used: Breach, Constructed Channel and small Islands. Generated with CoastSat (Vos et al., 2019)

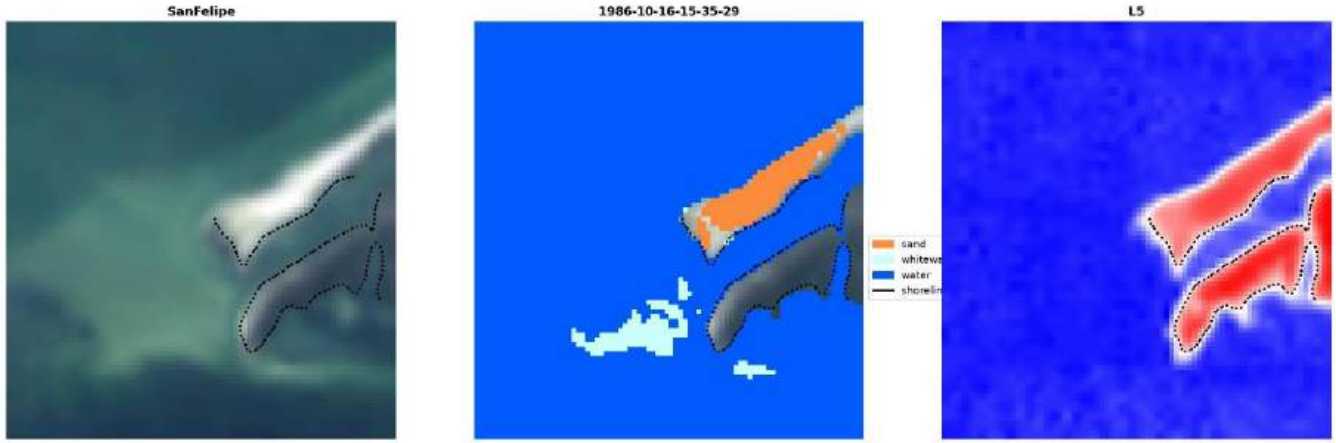
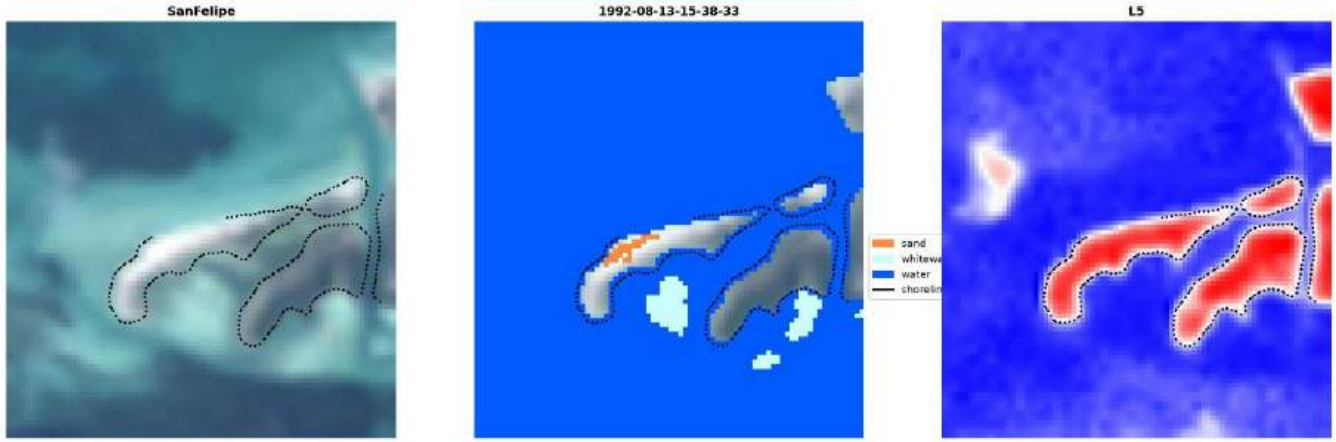
Results
The time period between 1985 and 2026 is analysed and findings are displayed in table B.1 below.

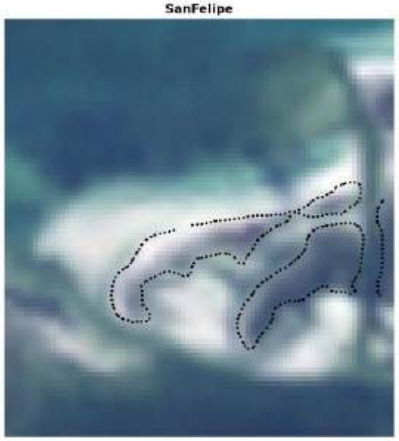
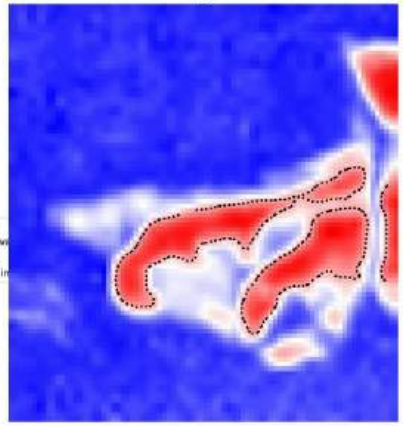
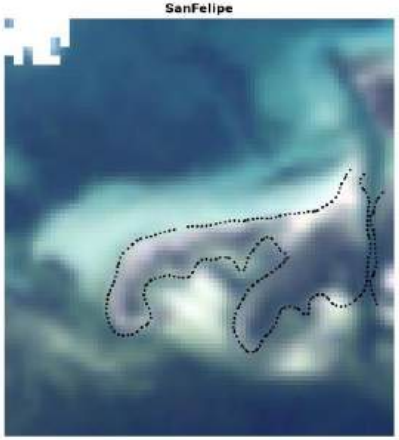
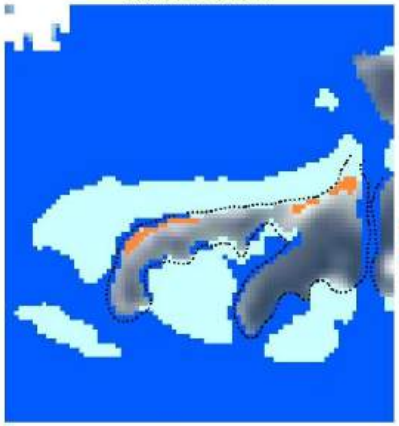
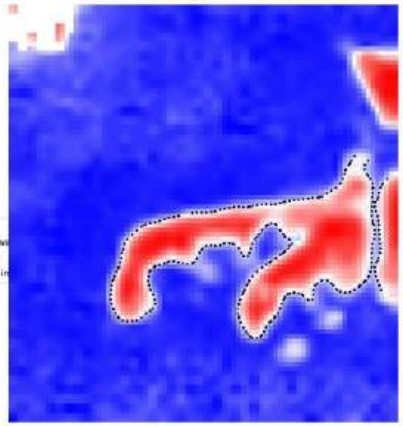
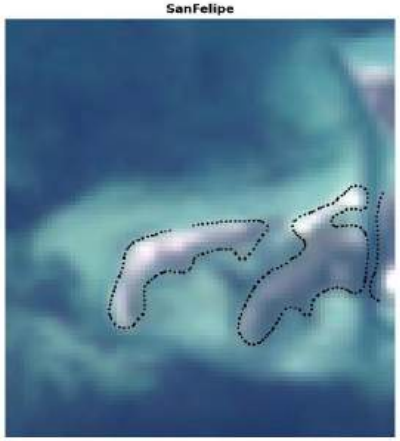
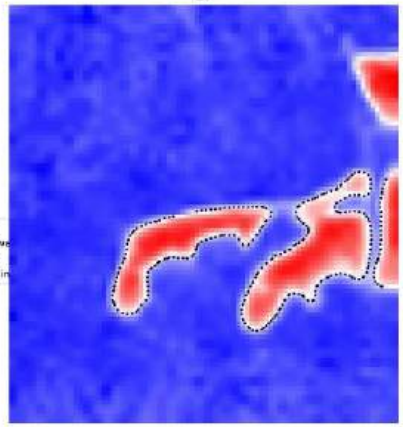
Table B.1: Observation changes barrier Island over time (1985-2026).

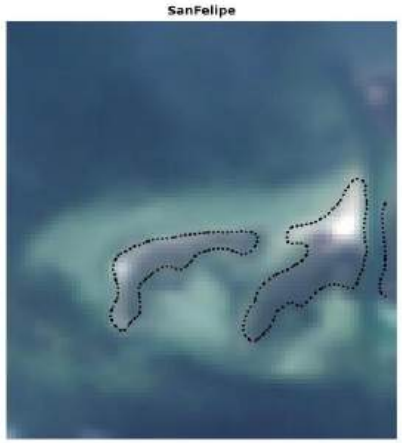
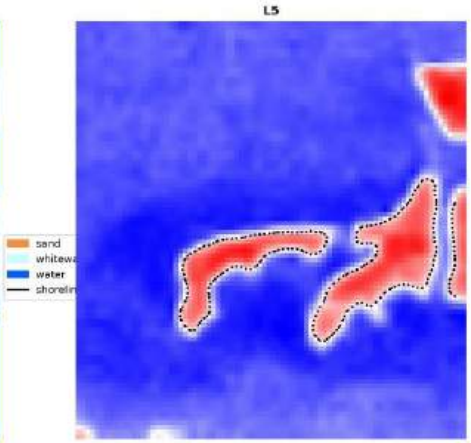
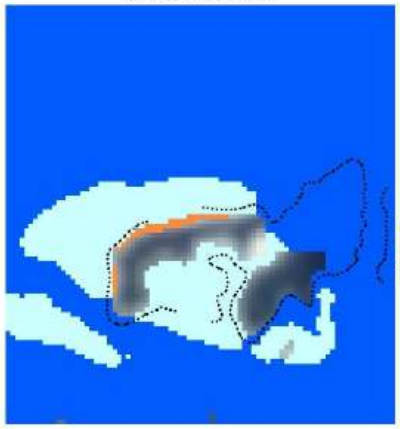
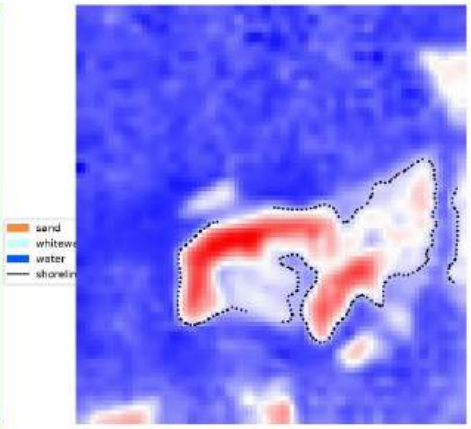
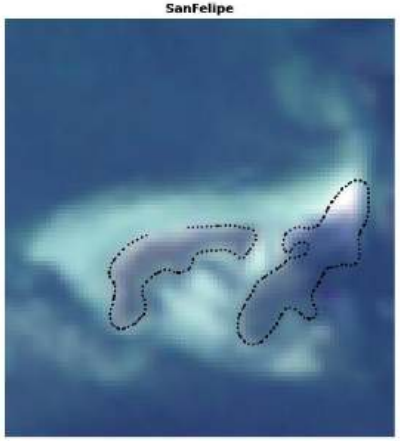
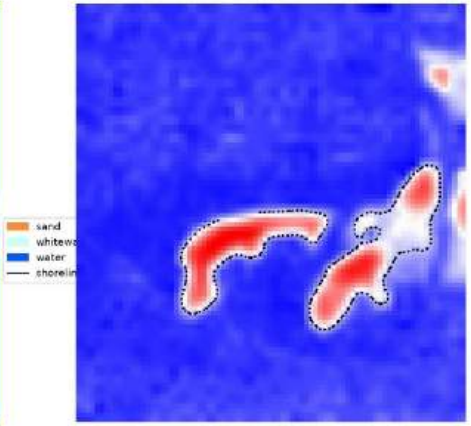
Time period	Observation	Based on	Conclusion
1985 - 2003	Relatively a lot of changes.	Video 1985 to 2003	Unstable, growing island system.
	Overall growth of island	1986/10/16 to 2000/12/09	
	Smaller islands detected, no fixed shape	1992/08/13	
	Breaches between island parts variable in width	1995/09/07 to 2000/10/22	
2003 - 2013	In 2006 a big breach between islands detected	2006	Transition period. The gap between islands is from 2011 onward stable.
	The gap at the picture of 2011 is small	2011	
2013 - 2026	Relatively stable system, no major changes in area.	Video 2013 to 2026	Barrier island stable, with minor changes in breaches between smaller islands.
	Breach between smaller islands stable until 2021/08/27. During 2022 relatively small breach. 2022 to 2026 varying width of breach	2021/08/27	

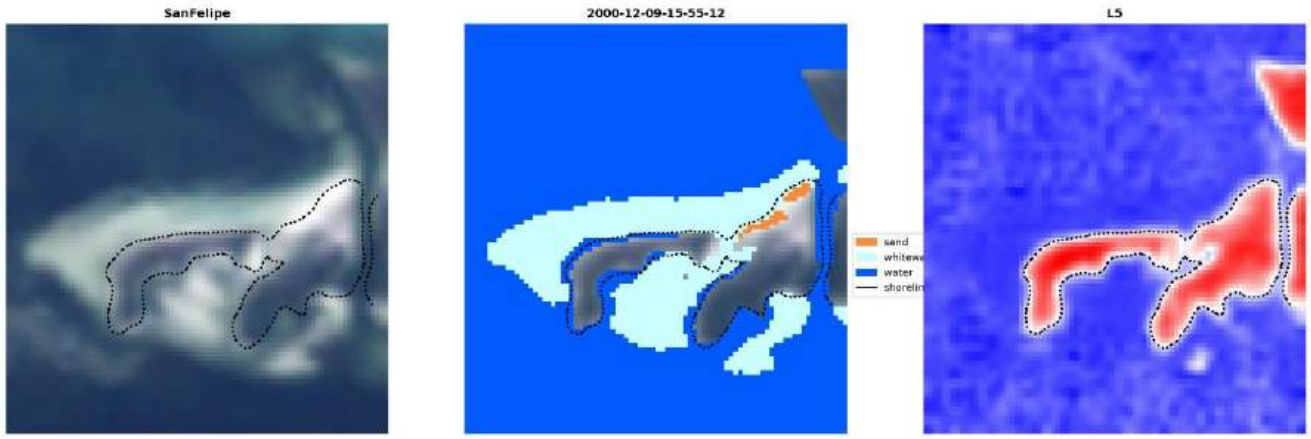
Overall conclusion
Between 1986 and 2003 the island was growing. The system was unstable during that time period. During the period between 2003 and 2011 the island became more stable with a more constant breach width. After 2011 the Island was stable with minor changes of the breach.

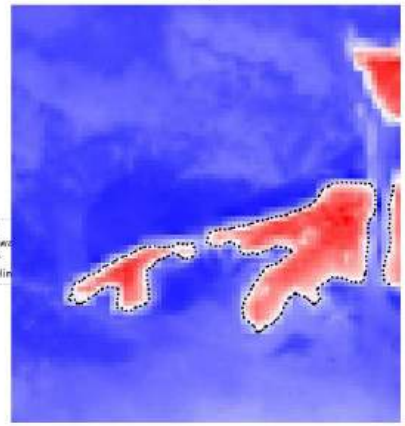
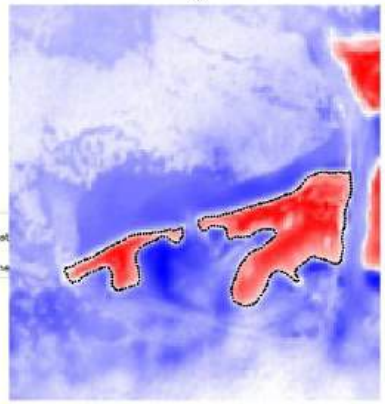
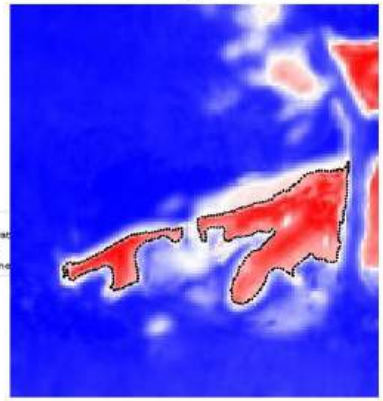
Satellite images 1985-2026
The following table shows the output images from CoastSat between 1985 and 2003 and between 2023 and 2026. Between 2003 and 2013 photos from Google Earth are used (Vos et al., 2019) (Google, 2026c).

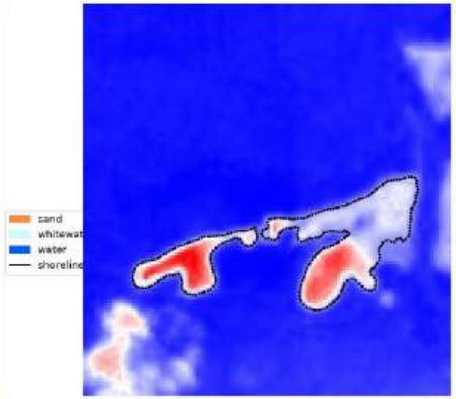
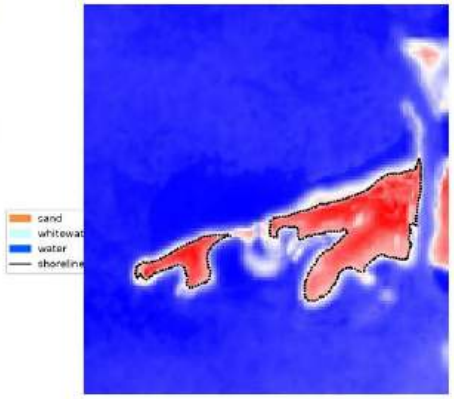
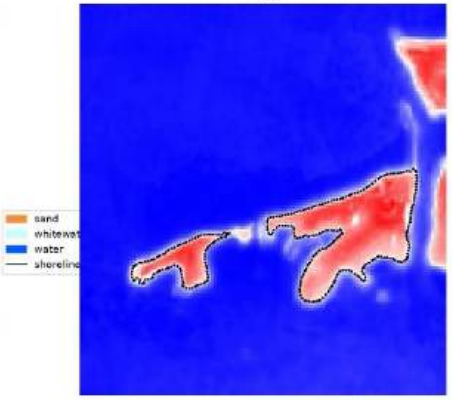
Time	Satellite image with shoreline detection	Satellite image (raw)
1986/ 10/16		
1992/ 08/13		

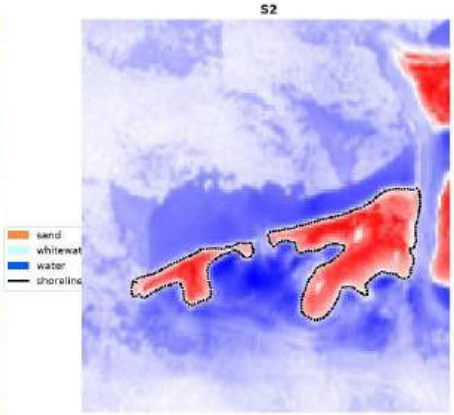
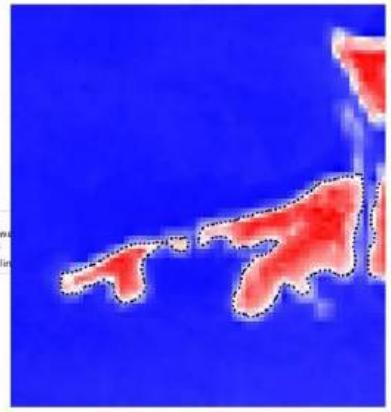
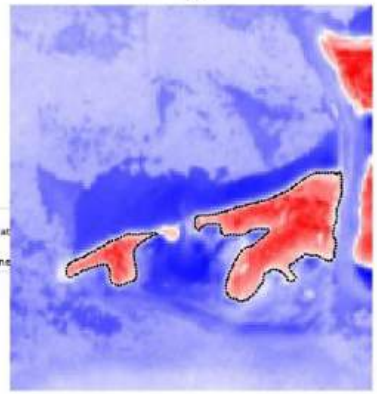
1993/ 01/20				
1995/ 01/10				
1995/ 09/07				

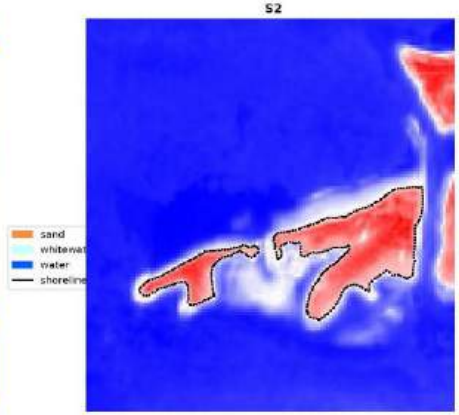
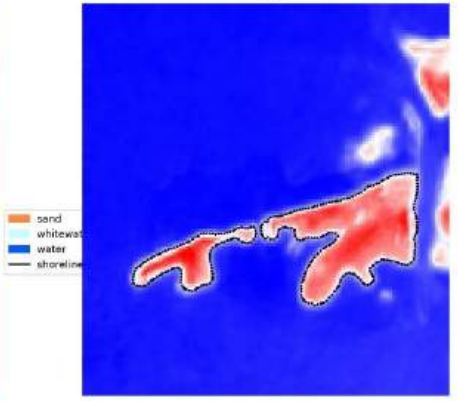
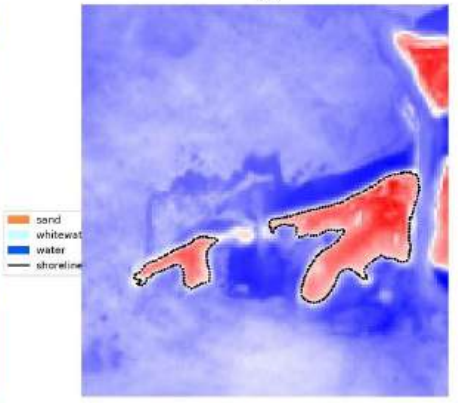
1997/ 06/24					
2000/ 01/08					
2000/ 10/22					

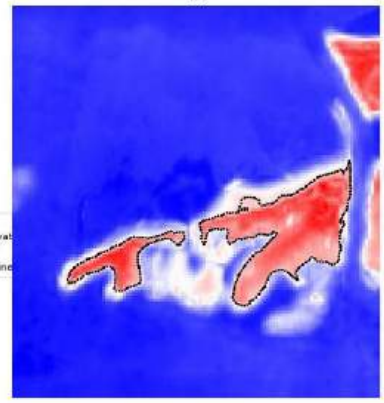
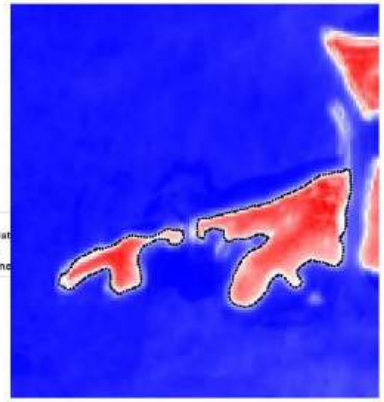
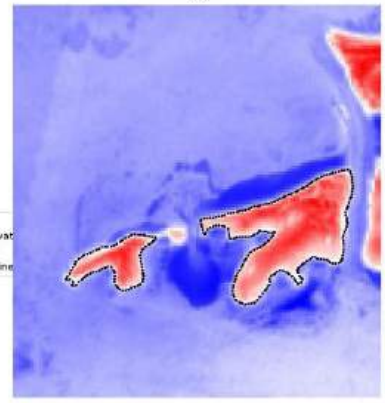
2000/ 12/09		
2006	No shoreline detection	
2011	No shoreline detection	

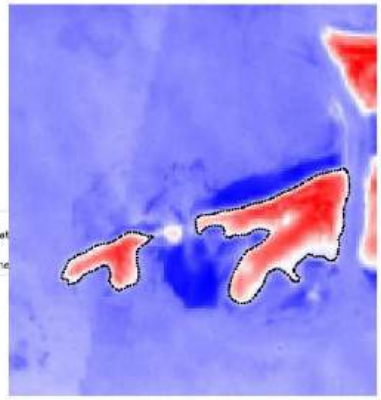
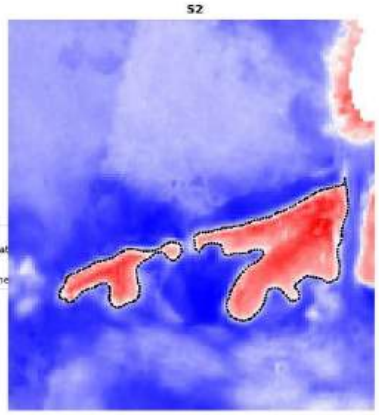
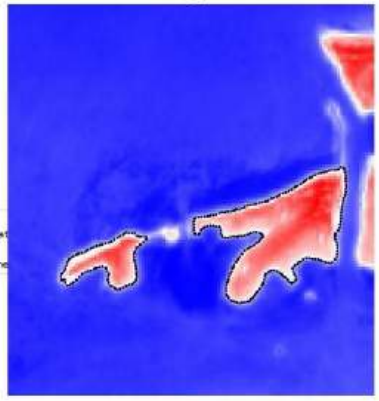
2014/ 07/09				
2016/ 06/29				
2016/ 12/16				

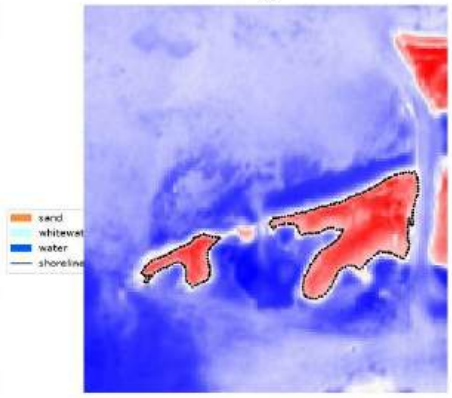
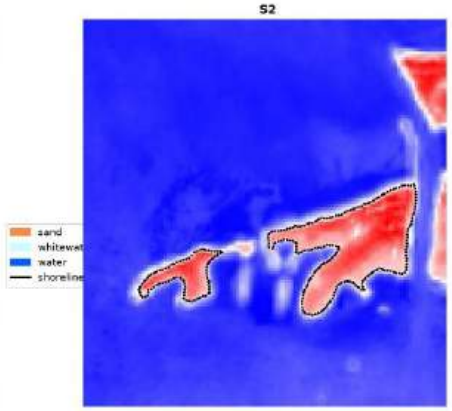
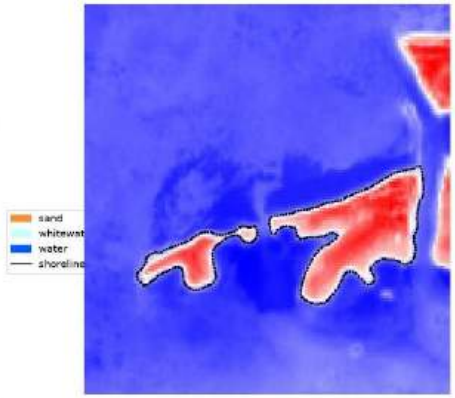
2017/ 11/26				
2017/ 12/01				
2018/ 01/05				

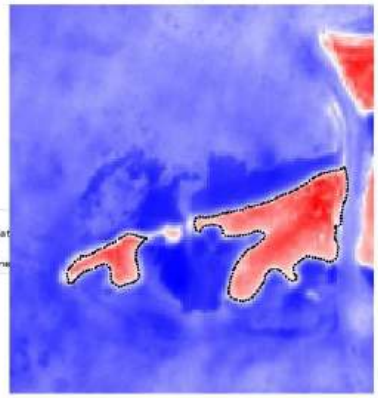
2018/ 05/15				
2018/ 10/24				
2019/ 06/29				

2020/ 01/25				
2020/ 12/20				
2021/ 08/27				

2022/ 02/28				
2022/ 10/31				
2023/ 08/12				

2024/ 05/18				
2024/ 09/05				
2025/ 02/17				

2025/08/16				
2026/01/18				
2026/03/24				

2026/08/31	SanFelipe	2026-08-31-16-37-37	sand water	S2	2026-08-31-16-37-37 S2

Appendix C

Data visualisation



Figure C.1: Available LiDAR data northern part of San Felipe. The LiDAR map is provided by LIPC-UNAM.

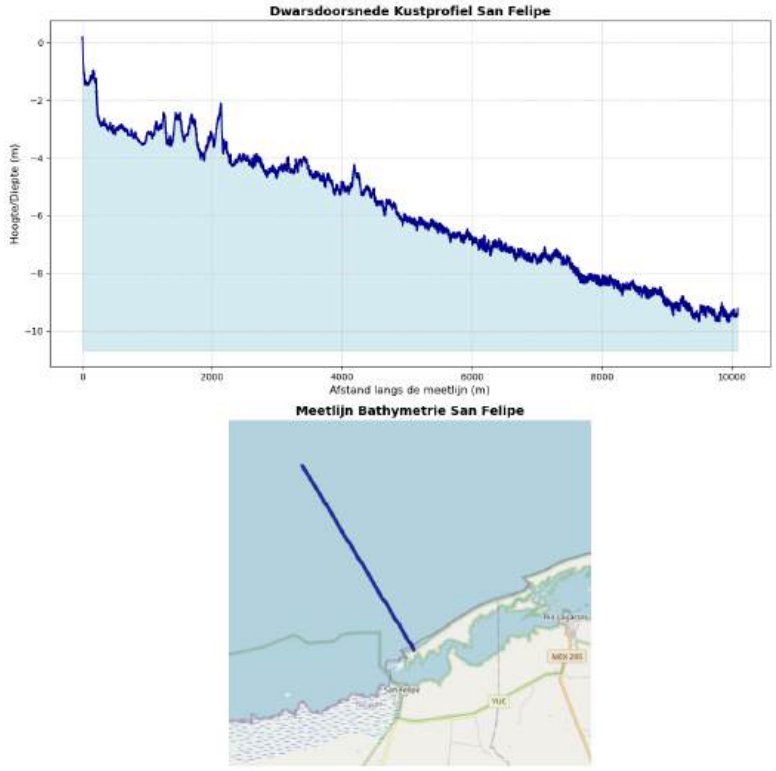


Figure C.2: Visualisation of measured transect of bottom profile from barrier island to 10 km offshore.

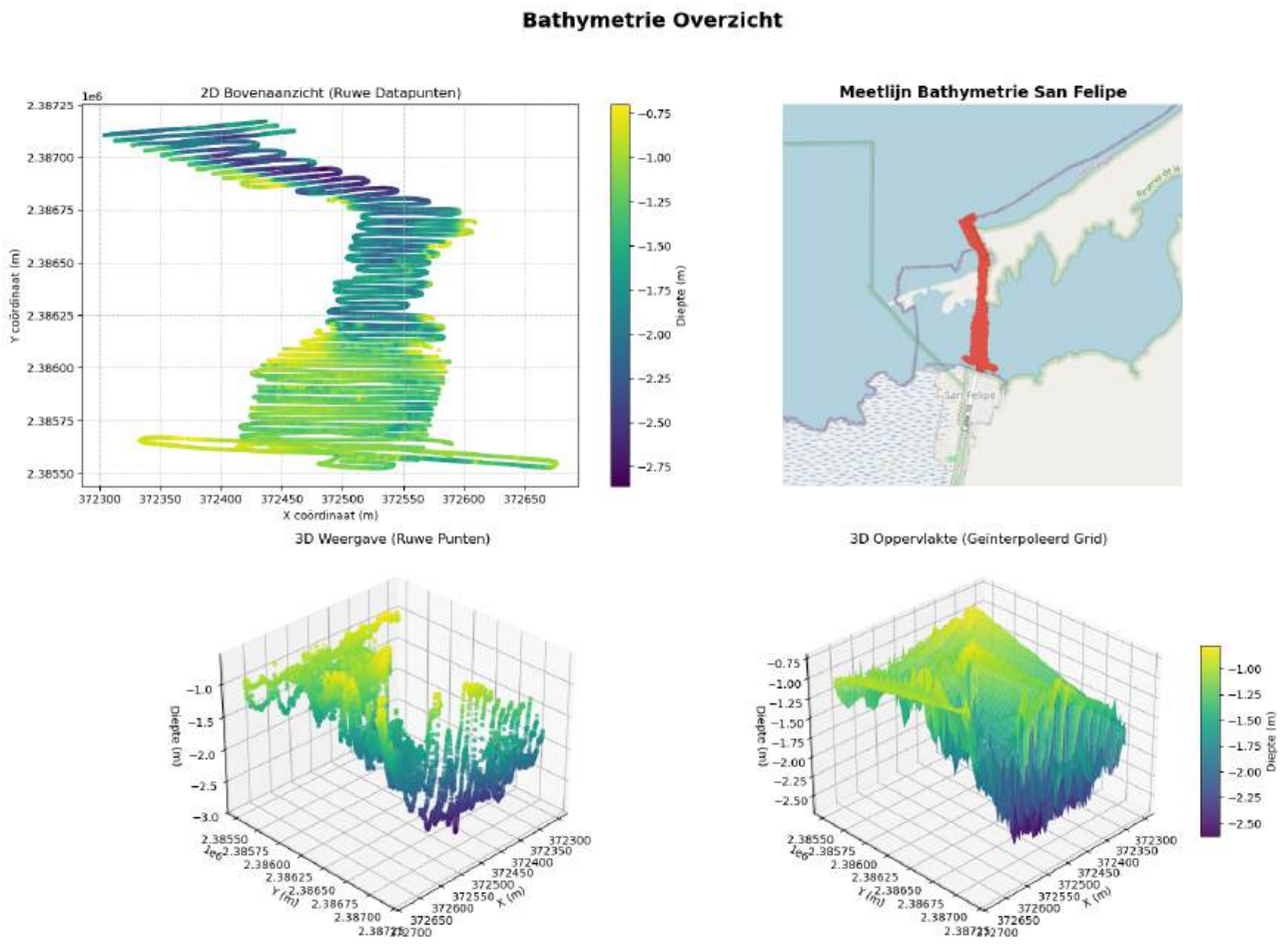


Figure C.3: Measured bottom profile of channel in barrier island in front of San Felipé



Figure C.4: Soil samples in front of San Felipe. Samples obtained at these locations are used to estimate the hydraulic conductivity of the soil.



Figure C.5: Buildings of San Felipe extracted from (Oostwegel, Schorlemmer, Lingner, & Evaz Zadeh, 2025).Visual inspection against high-resolution satellite imagery showed that individual building footprints contained inaccuracies. As the objective of this study is the classification of structural typologies rather than precise geometric characterisation of individual buildings, these inaccuracies were considered acceptable.



Figure C.6: Github map with pictures from visit (Own work)

Appendix D

Atmospheric Model Reliability

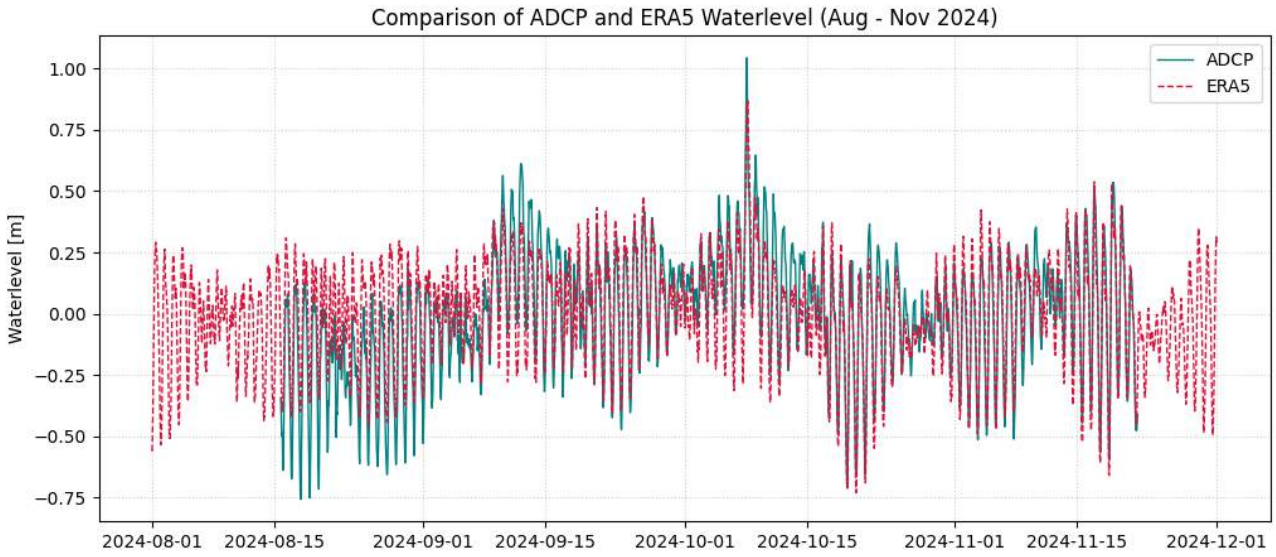


Figure D.1: Comparison of ERA5 Total water level data with measured ADCP data 10 km offshore from Sisal, Yucatán.

To assess the reliability of the atmospheric models such as ERA5 and the resulting total water level predictions, modelled water levels are compared to in-situ ADCP measurements collected 10 km offshore from the coast of Sisal, Yucatán. The observation period spans from August to November 2024. From both datasets the mean is subtracted to align their vertical reference levels and compare relative water level fluctuations. The resulting plot is visible in Figure D.1.

Table D.1: Metrics comparing modelled total water levels (ERA5) against offshore ADCP measurements.

Comparison Metric	**Observed Value**
Pearson Correlation Coefficient (r)	0.856
Root Mean Square Error (RMSE)	0.131 m
Amplitude Ratio ($\sigma_{\text{mod}}/\sigma_{\text{obs}}$)	0.864 (86.4%)
Phase Lag (Time Lag)	0 min

In Table D.1, the metrics and their values for comparing the two water level timeseries are stated. Modelled water levels align closely with ADCP observations in phase ($r = 0.86$, zero time lag), correctly capturing tide and surge timing along the coast of Yucatán. The model slightly underestimates peak amplitudes ($\sigma_{\text{mod}}/\sigma_{\text{obs}} = 86.4\%$, RMSE $= 13$ cm). Overall, the high temporal accuracy confirms the dataset as a reliable boundary condition for this research.

Appendix E

Data Time Series Visualisation

For all figures, October 2020 has been highlighted. Now, it is said that only Delta and Zeta are included in this month. However, also hurricane Gamma took place in October 2020.

E.1 ERA5 data

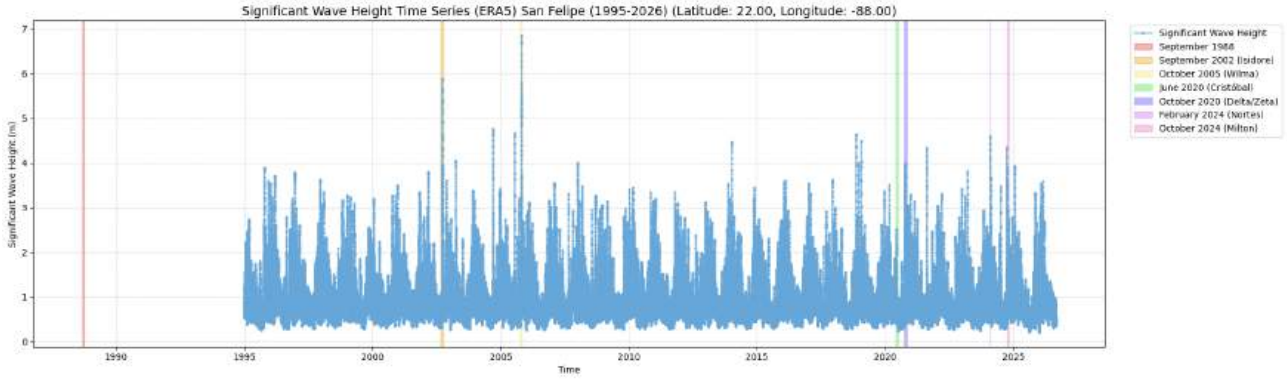


Figure E.1: Significant Wave Height Time Series (ERA5) San Felipe (1995 - 2026) (Lat=22, Lon=-88)

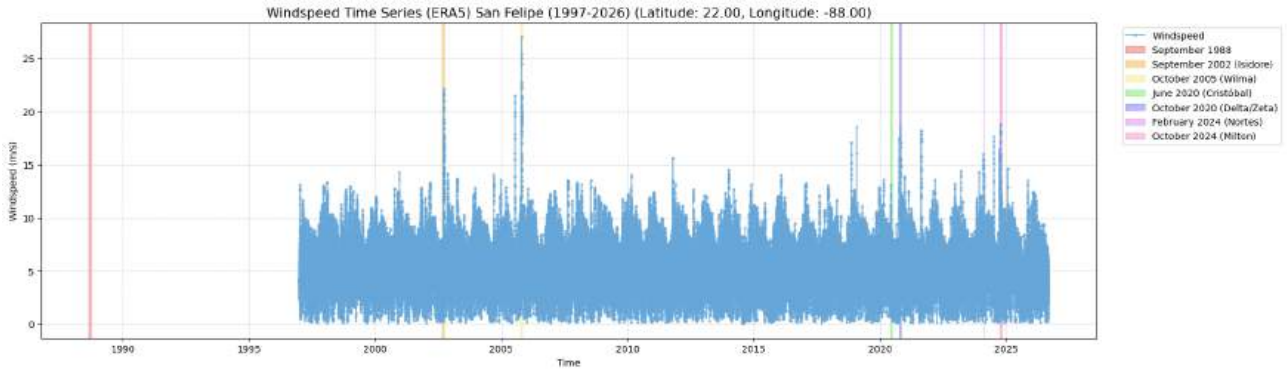


Figure E.2: Wind Speed Time Series (ERA5) San Felipe (1997 - 2026) (Lat=22, Lon=-88)

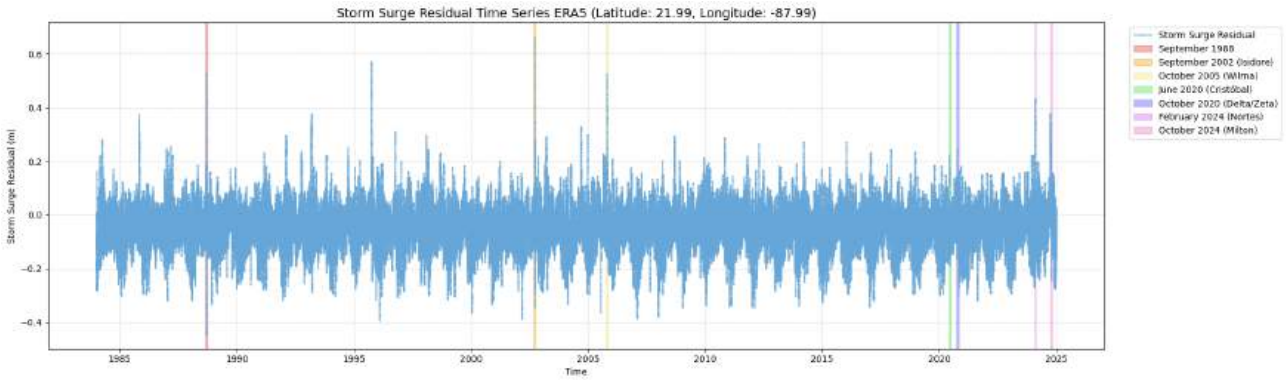


Figure E.3: Storm Surge Residual (ERA5) San Felipe (1980 - 2024) (Lat=21, Lon=-87.99)

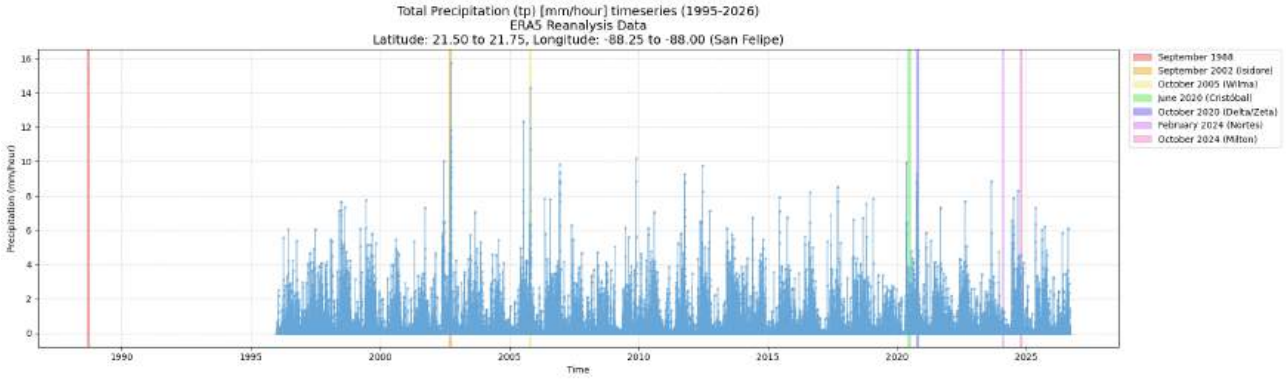


Figure E.4: Precipitation (ERA5) San Felipe (1988 - 2026)

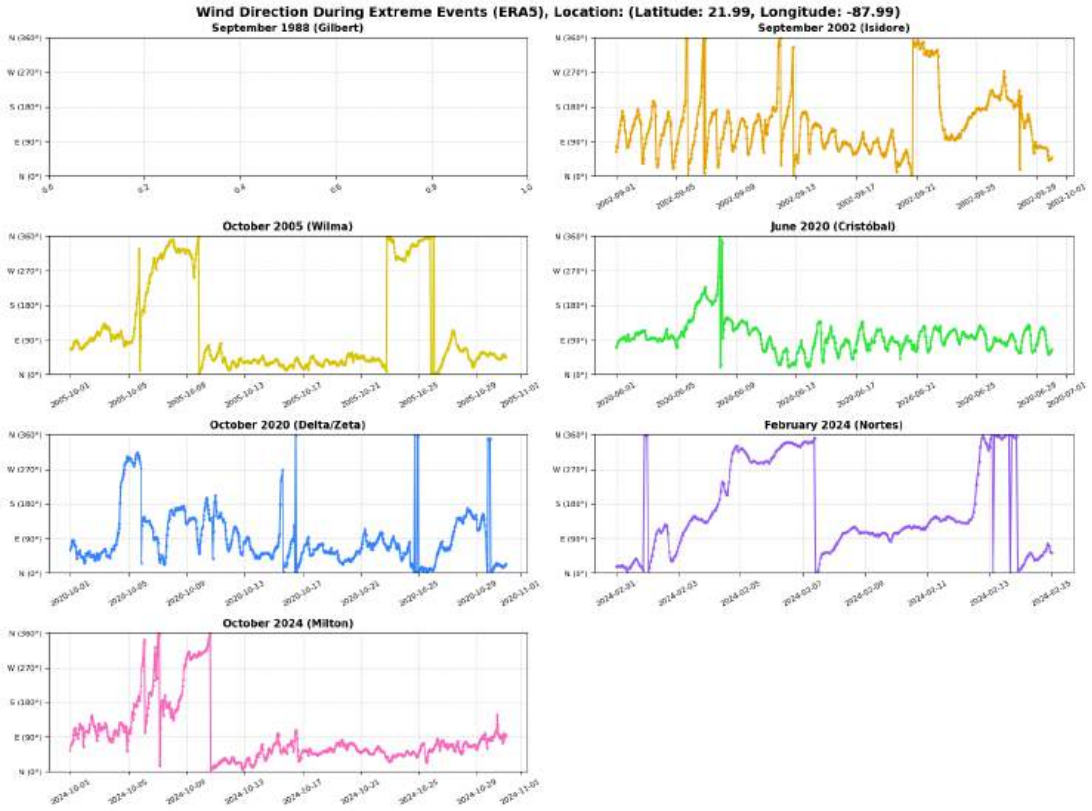


Figure E.5: Wind Direction [°] (ERA5) San Felipe for Extreme Events

E.2 Copernicus and Aviso data

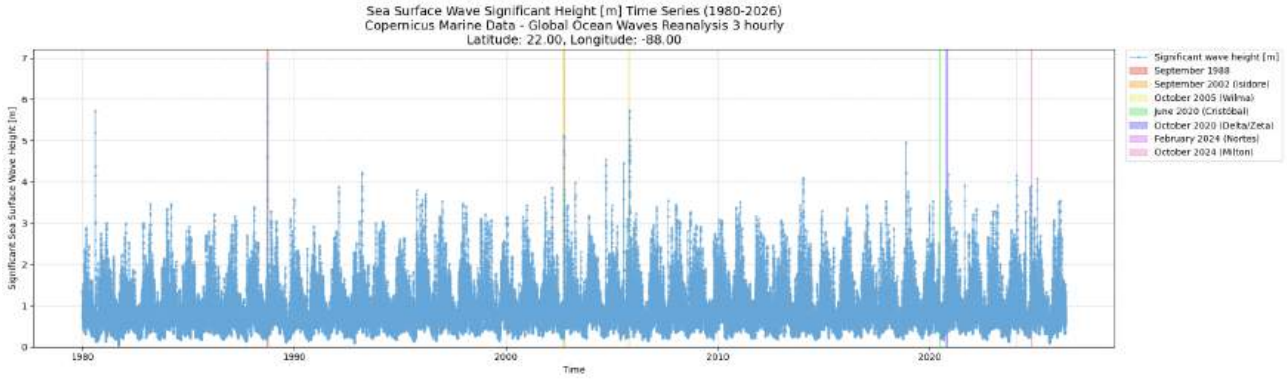


Figure E.6: Significant Wave Height Time Series (Copernicus) San Felipe (1997 - 2026)

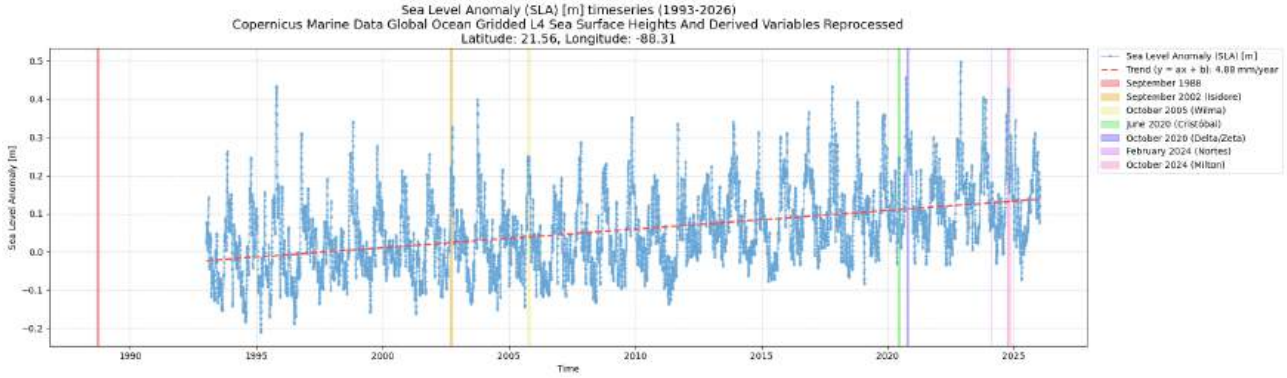


Figure E.7: Sea Level Anomalies (SLA) Time Series (Copernicus) San Felipe (1993-2026)

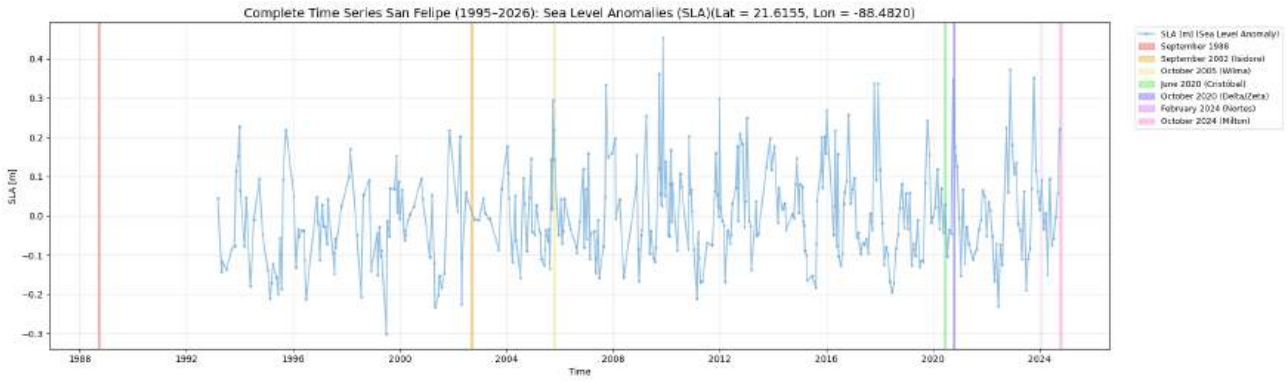


Figure E.8: Sea Level Anomalies (SLA) Time Series (Aviso L3) San Felipe (1995–2026)(Lat = 21.6155, Lon = -88.4820)

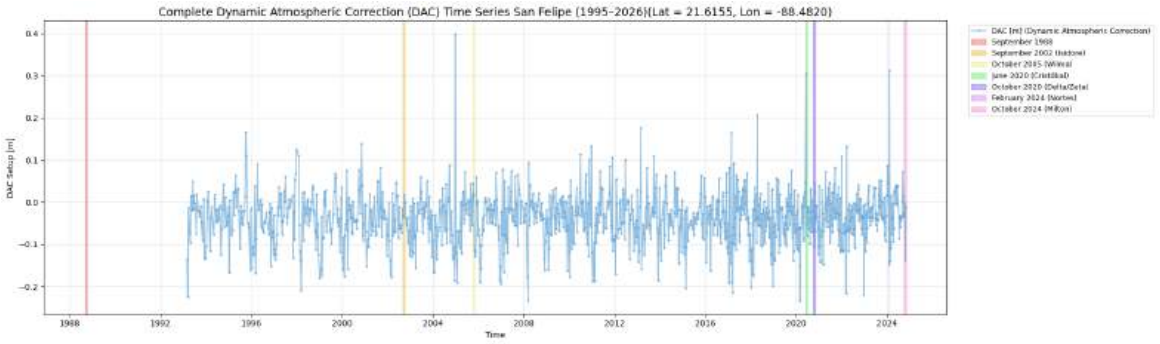


Figure E.9: Dynamic Atmospheric Correction (DAC) Time Series (Aviso L3) San Felipe (1995–2026) (Lat = 21.6155, Lon = -88.4820)

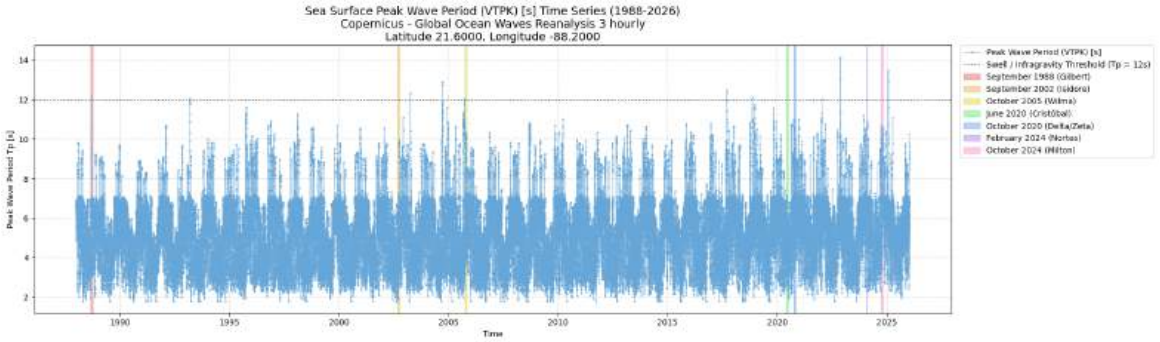


Figure E.10: Sea Surface Peak Wave Period [s] Time Series San Felipe (1988-2026)

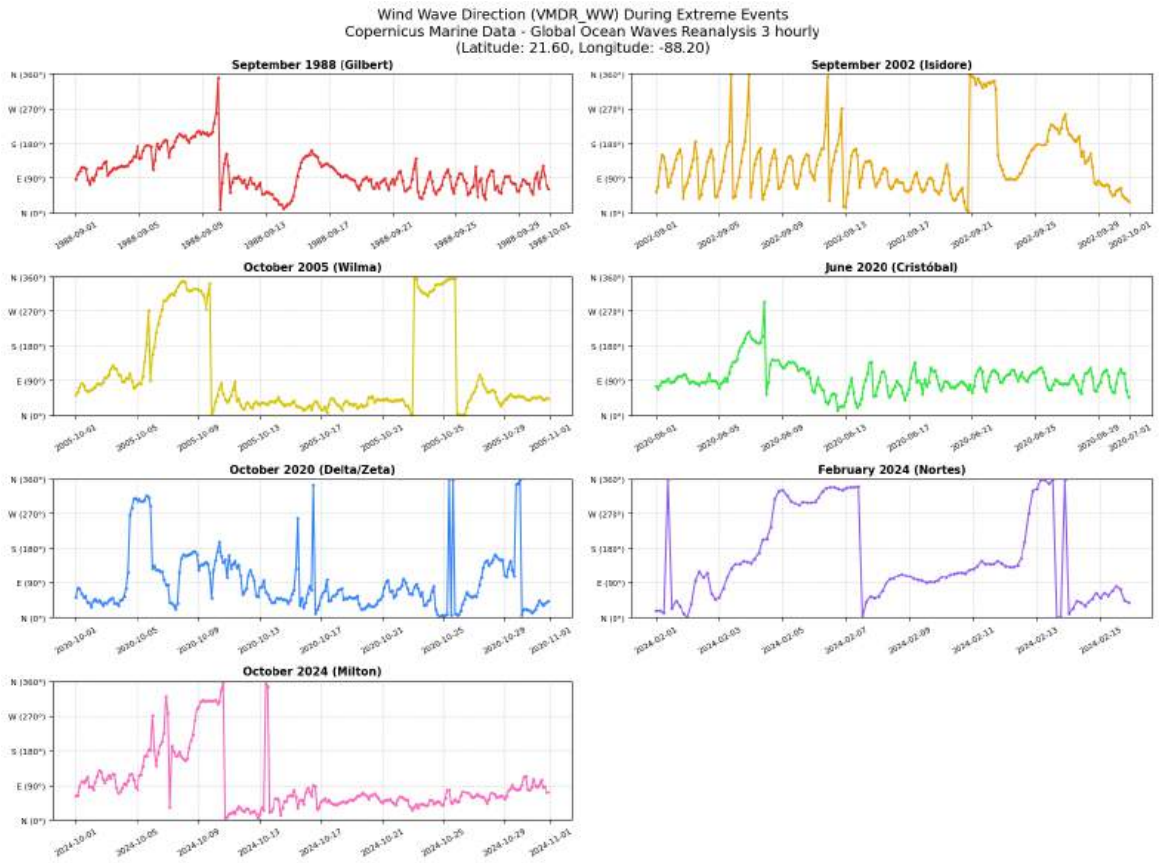


Figure E.11: Wind Wave Direction [°] (Copernicus) San Felipe for Extreme Events

Appendix F

Fieldwork set-up

F.1 Interview set-up

The interviewed participants are asked to put their house and points of interest (safe and prone to flooding) places on the map. Figure F.1 shows how the interviews were carried out.

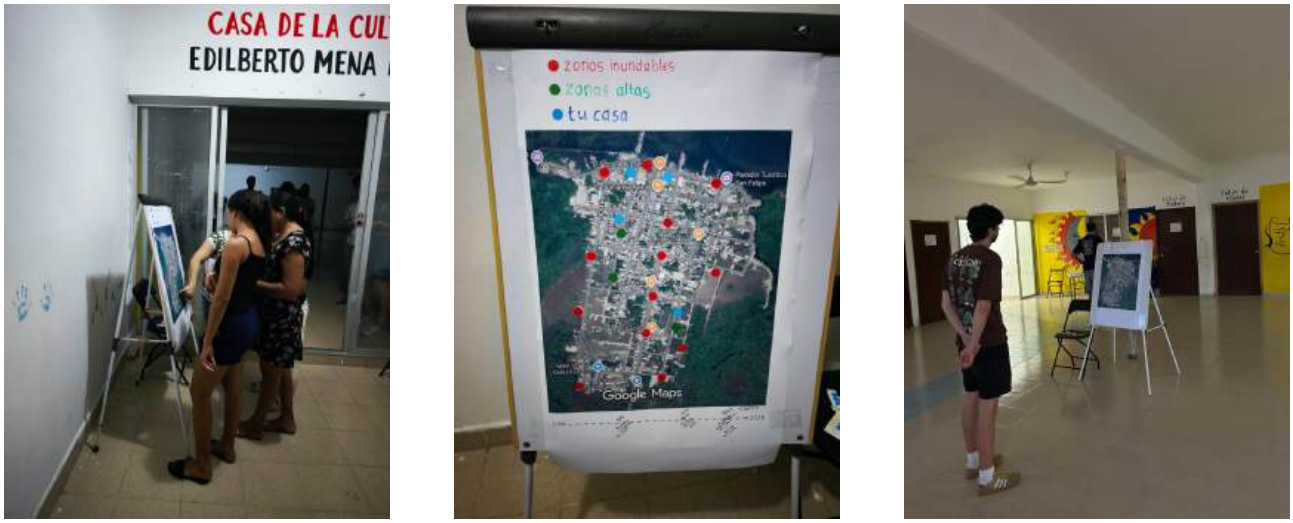
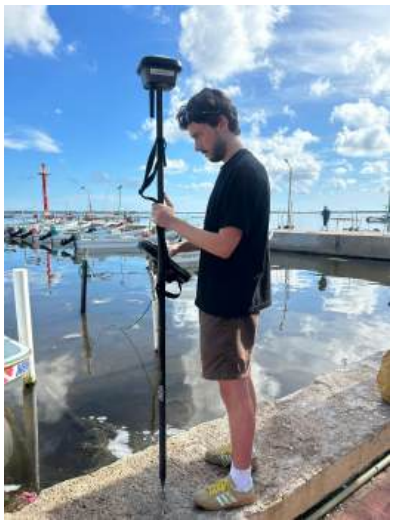


Figure F.1: Interview set-up

F.2 Measurement Set-Up

The elevation and water depth are measured using the devices listed in Figure F.2. The elevation map is created using the GPS Rover and the base station. The tide is investigated using a tide gauge.



(a) GPS Rover foot



(b) Water depth measurement



(c) Base station



(d) GPS Rover foot



(e) Base station



(f) Water level translation



(g) Tide gauge



(h) Tide gauge/GPS location



(i) GPS Rover Car

Figure F.2: Measurement set-up

Appendix G

Fieldwork interview results

During the fieldwork trip to San Felipe, 4 interviewee groups were interviewed. During the interview the participants were asked to put their house on the map and think about the higher (safe) and inundable places in San Felipe. The maps that were created are given in Figure G.1, G.2, G.3 and G.4.



Figure G.1: Interviewee group 1

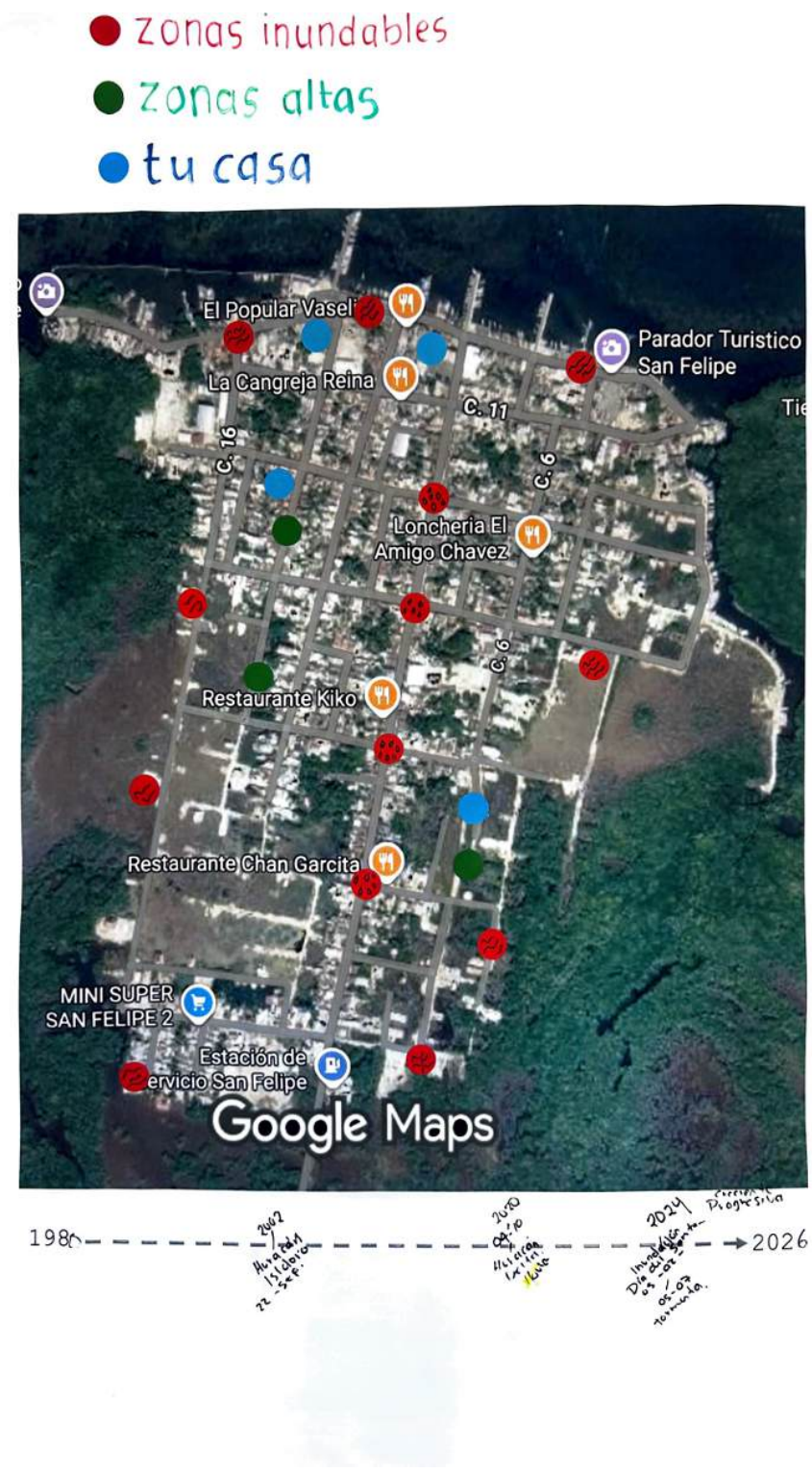


Figure G.2: Interviewee group 2

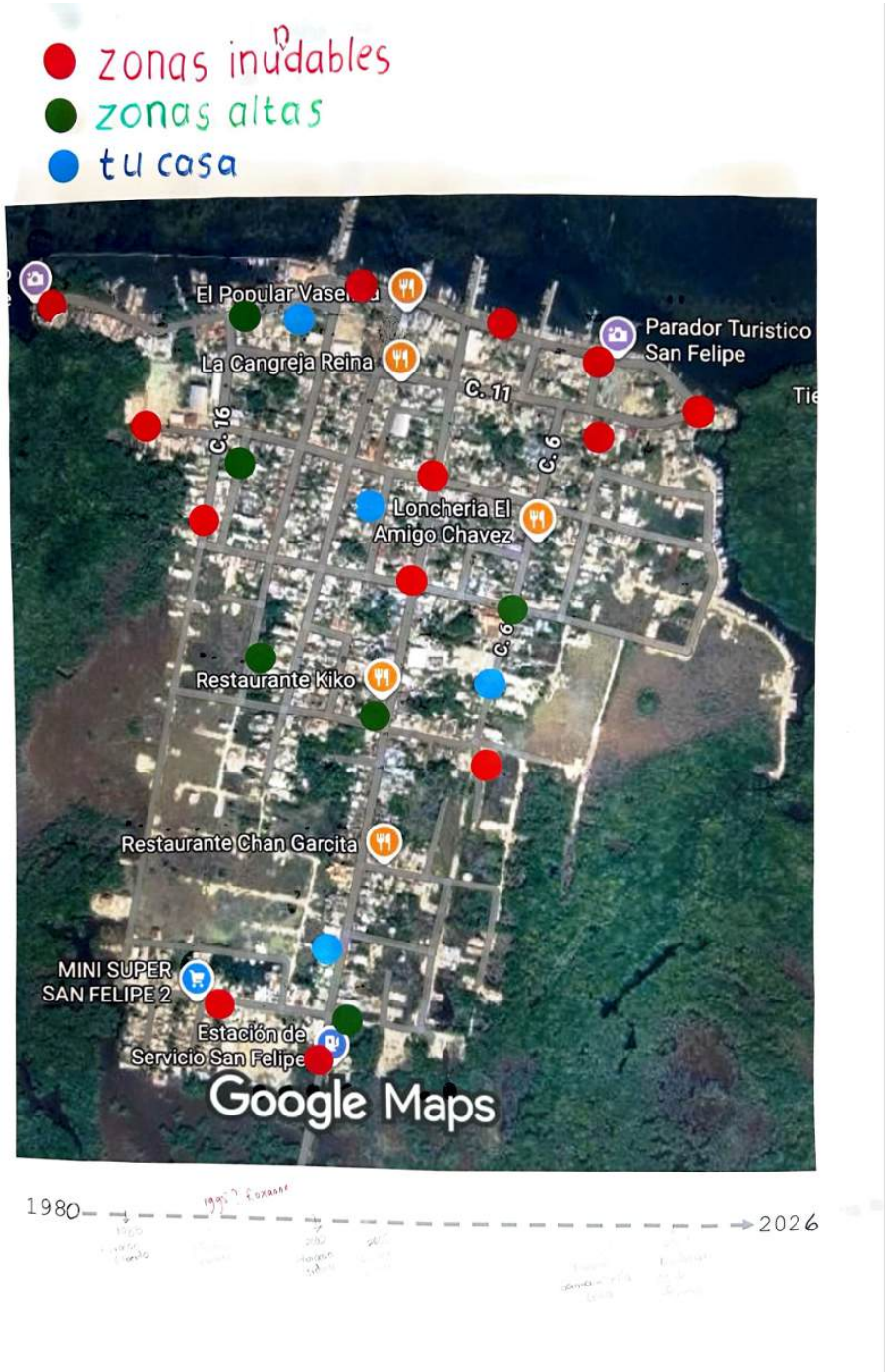


Figure G.3: Interviewee group 3



Figure G.4: Interviewee group 4

Appendix H

Interviews San Felipe

H.1 Attendance list interviews

A list has been made for the people who attended the interview. This attendance list can be requested at LIPC-UNAM.

Name/Nombre	Age/Edad	Cell phone number/Número de teléfono	Occupation
[redacted]		[redacted]	[redacted]
[redacted]	[redacted]	[redacted]	[redacted]
[redacted]	[redacted]	[redacted]	[redacted]
[redacted]	[redacted]	[redacted]	[redacted]
[redacted]	[redacted]	[redacted]	[redacted]
[redacted]	[redacted]	[redacted]	[redacted]
[redacted]	[redacted]	[redacted]	[redacted]
[redacted]	[redacted]	[redacted]	[redacted]
[redacted]	[redacted]	[redacted]	[redacted]
[redacted]	[redacted]	[redacted]	[redacted]
[redacted]	[redacted]	[redacted]	[redacted]

Table H.1: Attendance List / Lista de Asistencia

H.2 Spanish transcription interview 1

Orange = not useful
Blue = Interviewees Jennifer, Nuria, Estrella and Luisa
Green = Alec Torres-Freyermuth

Alguien... algún motor, alguna cosa... O alguien que se haya inundado... Sí. Si quieres agarrar este de acá, está igual de fácil.

"Bueno, pues como discusión llegamos que, por ejemplo, la calle toda esta del malecón se inunda, sobre todo cuando hay creciente. Y la calle principal que es la calle 10 se inunda sobre todo cuando hay lluvias. Y todo alrededor, pues como estamos alrededor eh dentro de un manglar... y que hay calles nuevas, entonces estas... cuando hay creciente igual se sale el agua. Por toda la parte de alrededor del poblado."

"Perfecto."

"¿Todos esos eventos afectaron sus casas?"

"Sí. Bueno, estas sí están muy documentadas. De hecho yo tengo una foto de mi casa que quedó así... devastada, desbaratada. Ah sí? Ah, pues sí... ¿Y de qué evento sería del del del? Del... sí yo tenía días de nacida. Nacida el 6. Yo nacida el 6. Y te acuerdas muy bien... Sólo la foto, sí... Me dejaron en paz. Ah, desbarató la casa... todo. Okay."

"Okay. Entonces entonces destrucción sí. Y el y los niveles pues varía desde... hasta las rodillas hasta..."

"No, sí, sí. Allí sí elevó mucho el agua en Isidoro. En Isidoro, o sea literal casi en el techo tenía que colgar las hamacas porque sí subió demasiado el agua. Ellos no quisieron salir por tercos y... Se quedaron acá. Sí."

"Por ejemplo, pero en una creciente normal, ¿hasta en tu casa hasta como cuánto le calculas que crece? Cuando tienes inundación..."

"Pues poco. Pero es por creciente, ¿no? Sí."

"¿O por lluvia?"

"Pues sí se inunda la calle, pero solo que cruce un un coche se inunda en mi casa... te avienta el agua. ¿Y cuando hay creciente? Cuando hay creciente pues sí. Entra. Sí, literal se va del lado... ¿Pero te llega hasta las rodillas o hasta el tobillo? No, como por acá. ¿Como al tobillo? Como... 15 centímetros."

"¿Y tú vives... allá. Acá vives, ¿no? Sí. Yo... esa es la tuya... y yo vivo aquí. Sí, aquí... Yo aquí... Okay."

"Entonces sí... ¿Será que lo pongo aquí abajito? ¿O aquí?"

"No, yo creo, yo creo que está bien. La otra duda era... en en lo en lo que en estas que les han tocado vivir, que son las que digamos las frecuentes, ¿si sube el agua rápido o o o van viendo que va subiendo el agua poco a poco? O sea, no no es de un momento para otro la la..."

"Cuando va por el viento, cuando va por el viento que va... Sí. De hecho la única vez... es esta. La del 2024, allí sí constantemente... nunca había entrado a nuestra casa. Y sí, tardó un rato porque salíamos y veíamos que... está en la esquina. Y salíamos otra vez y ya estaba en la puerta. O sea, iba elevando, creciendo. ¿Tú por dónde vives? Yo vivo aquí en el sur... O sea que sería de las zonas más alejadas del... Y también venía del del mar, digamos del... Sí, ese sí estuvo... Es que está tipo creciente, sí... iba la... Sí, la gente andaba en chalanitas porque nunca había entrado tanto... sí... sí estuvo alto eso. Sí."

"O sea, de la historia reciente, digamos que esa del 2024, que es este...febrero, ¿verdad? El día del San... sí. Sí, de ese sí he visto videos en Facebook. Está bien. "Porque por lo general, si crece... pon tú, como empieza a salir como a las 8 o 7 de la noche, y a las 10 ya no hay nada... ya ya bajó. Ya bajó. "¿Y deja mucho... mucha basura la inundación, o no? ¿Muchos escombros? Cuando son así bajas, no."

"Pero por ejemplo el de Delta, sí. Eh... ese... este... ¿Sí sabes? Esta... Sí. ¿Pero no entró mucha mucha agua de la Ciénega en Delta? ¿No? ¿O fue también del mar?"

"Ah, es que es que Delta sí les pasó cerca a ustedes. Pero eso no fue por creciente, hubo lluvias. Mucha lluvia. Y fue cuando se rompieron las calles, ya no podíamos ni salir ni entrar. Estaba lleno de lagartos y por... Panabá. O sea... por acá no. Buenas noches, adelante. ¿Qué tal, buenas noches?"

"No sé si si quieren empezar como... Sí... allá si quieres. Si si quieren irse a tomar un cafecito o algo mientras... Ah, gracias... No... ya tiene que pasar por aquí otra vez, dile a este... ¿cómo se llama? No, estoy bien... Bernardo. ¡Ah, sí! ¡Ah, pues ya lo conoces! Oye, déjame ir por una gorra, voy a por una gorra y un y un buff."

H.3 English translation interview 1

Orange = not useful
Blue = Interviewees Jennifer, Nuria, Estrella and Luisa
Green = Alec Torres-Freyermuth

"Someone... some motor, some thing... Or someone who is flooded... Yes. If you want to grab this one, it's just as easy."

"Well, during the discussion we came to the conclusion that, for example, this entire street of the Malecon (boardwalk) floods, especially when there is a spring tide (surge). And the main street, which is Street 10, floods especially when it rains. And everything around it, since we are in a mangrove area... and there are new streets, so these... when there is a spring tide, the water flows out there too. Over the entire area around the town."

"Perfect."

"Did all these events affect their houses?"

"Yes. Well, these... these are well documented. In fact, I have a picture of my house that looked like this... devastated. Oh yeah? Ah, well... And from which event would that be? From the... from Hurricane Isidore. Ah! Isidore? Yes, I was ten days old She remembers it very well... Only the photo... They showed me... ah, they destroyed the house... everything. Okay."

"Okay. So destruction, yes. And the water levels... varied from... up to the knees to..."

"No, yes, yes. There Isidore raised the water level a lot. En Isidoro, We had to... literally, she almost had to hang the hammocks by the ceiling, because the water rose too high. They didn't want to go to shelters, they stayed here."

"For example, during a normal spring tide, up to where do you estimate the water rises at your house?"

"Well, a little. But it's because of the spring tide, right? Yes."

"And from rain?"

"Well yes, the street floods, but since I... crossed a car, it floods my house... it throws the water inside. And when there is a spring tide? When there is a spring tide, well... it comes inside... But does it reach your knees or your ankles? No, about here. To the ankles? About... 15 centimeters."

"And you live... there. You live here, right? Yes. I... that's yours... and I live here. Yes, here... I live here... Okay."

"So, I... Should I put it a bit lower? Or here?"

"No, I think it's fine. The other question was... during the... during the floods they have experienced, and those are the, let's say, most frequent ones, does the water rise quickly or... or do they see the water rise little by little? It's not from one moment to the next."

"When it's because of the wind... when it's wind that... Yes. Actually, the only time that... this one. The one from 2024, there it flowed constantly... it had never entered our house before. And yes, it took a while, because we went outside and saw that it... was at the corner. And we went outside again and it was already at the door. So it just kept rising. Where do you live? I live here in the south... Oh, that is in one of the areas furthest from the... Yes. And it also came from the sea, let's say... that is that is... it was that spring tide... yes. Like people were navigating the streets in small boats. Because never had that much water come in."

"So from recent history that is for example the one from 2024, from...February, right? The day of San Felipe yes. From that one... I saw videos on Facebook. Okay. Because generally, when there is a spring tide... suppose it starts to rise around 8 or 7 in the evening and by 10 o'clock there is nothing left... it's already dropping... it already drained... And does it leave a lot behind... a lot of garbage? A lot of debris? That kind of stuff? When it's a low spring tide, no."

"But for example the one from Delta, yes. Uh... this... did you know... This one... Yes. But not much water came from the Cienega [swamp area] into the town during Delta? ¿No? ¿O fue también del mar?"

"The thing is... Delta did pass by you. You know It cannot be compared, there was rain... a lot of rain. We couldn't get in or out. It was full of lizards, and because of... Panabá. Let's say... here is not... Good evening, come in! Hello, good evening."

"I don't know if you want to start if... Yes... there, if you want. If you want to grab some coffee or something in the meantime. Ah, thank you... No... it has to happen sometime, tell... what's his name... I'm doing well. Bernardo. Ah yes... ah, we already know him. Hey, let me get a cap and a... I'm going for a cap and a neck warmer."

H.4 Spanish transcription interview 2

Orange = not useful
Blue = Interviewee Farneli
Green = Alec Torres-Freyermuth

"Entonces, aquí la la idea es muy sencilla. Nada más... aquí en el mapa, con unas este estampas rojas. Si nos indica... cuáles son las zonas que siempre tienen problemas de de inundación, en general. Las más críticas digamos en rojo y y a lo mejor en amarillo las que es más por lluvia o más..."

"Y un poco también si nos platica de... a qué se debe principalmente, o sea, cuáles son los fenómenos que las causan y qué tan frecuente ocurren. ¿Por crecida de mar? ¿Por alta mar? Esta... esta zona... siempre está inundada. Sube el agua. Es una de las partes más bajas. Okay. Sí. Y la parte más alta... viene saliendo por aquí... A ver la parte, ponle a ver... es una dos tres, es esta. Esta es la... a ver la parte... Esta es la parte... esa es la parte que de último se inunda. Okay. Con la creciente más alta... Y otra parte crítica, que es la más crítica dentro de esa situación... es esta. Que nos tapa la salida. Claro."

"Estamos entre dos eh ríos... uno entra así y sale en la gasolinera. Y el otro sale aquí... ya aparece también ahí por la gasolinera. Esos ríos meten agua, sube, y cuando quieres salir... aquí todavía no hay agua y allí ya tiene 20 centímetros. Okay. Y es y esa sí es un es un problema serio porque en huracanes si te llegas a descuidar... Sí, te quedas, te quedas adentro. Te quedaste en el pueblo."

"¿Sí? Y ya y ya de lo demás, pues de aquí esta agua va corriendo hasta acá... la de aquí va saliendo hasta acá... y va llenando el centro hasta hasta llegar a estas. Okay.

"Y este... ¿en en hasta dónde le ha tocado que llegue el agua? Pues en el huracán Isidoro entraron casi dos metros y medio de agua. Dos metros y medio de agua en en Isidoro, hasta acá... más o menos. Sí. Una cosa impresionante... Y en una en una crecida... Normal, normalmente son 20 centímetros, 30 centímetros en las calles. Okay. Sí. Entonces ahorita que viene la temporada de nortes, es cuando más se ven esos fenómenos, porque al entrar el norte... pega el viento del noreste... y empieza a meter agua. Sí, como que ahí están desprotegidos, ¿no? Más desprotegidos. Sí. No, y es es el viento que mete agua. Sí, sube, va subiendo... Va subiendo y hasta que hasta que inunda la mayor parte del pueblo."

"Sí. Y y esa cosa, esto también es, son zonas... nomás que esta área, es esta de acá, pues esta sí quedó alta, toda esta carretera quedó alta. Sí, sí como que da la impresión de que va subiendo, va subiendo, ¿verdad? Sí. Hacia allá, sí."

"Y y lo que estaban intentando aquí era que esto sea lo alto... y esto lo bajo... para que todas las calles tengan eh drenaje... pluvial. Okay. Que mucha gente no lo entiende... Ya, ya. Nosotros como pobladores queremos un drenaje pluvial. Que el agua no se estanque, porque revienta las calles. Ya."

"Sí, o sea que que se inunde pero que baje rápido. Sí, sí, como así como entró... y con las lluvias lo mismo pasa, y una y una zona inundable... a ver, esta es... esta es la 10, ¿verdad? Es esta de aquí. Sí. Que toda esta con la lluvia... se estanca. Se estanca el agua... y este y es un problema porque la calle se destruye más rápido. Okay. Y en cuanto a daños en las en las casas... ¿son más de digamos de lo que hay adentro, o también llegan a dañar, digamos, la estructura y eso... No. La casa lo que le pasa es eso, se empiezan a a a comer por el salitre. La humedad al subir el agua aumenta... Y le y empieza a comer. ¿Qué es lo que

está intentando la gente? Poner mampostería o piedra hasta un metro, metro y medio... y arriba el block, para tratar de proteger. Sí, y las instalaciones también veo que las ponen arriba, todo, todo, todas... siempre pensando en poner agua arriba. Sí."

"Eh hay que tomar en cuenta que también el pueblo ha subido como unos 20, 30 centímetros cada año, que pasen calles, hacían calles nuevas... iba subiendo, iba creciendo. Lo fuimos viendo por las casas. Habían casas que eran enormemente altas, y ahorita ya prácticamente ya están al nivel. Sí. Sí."

"Eso es lo que ha pasado en en muchos de los años. Este... este es un río... que corre hasta aquí... y prácticamente conecta hasta acá. Y este es el otro río que corre hasta aquí y sale hasta acá."

"Estos ríos prácticamente son, hoy en día esto es un un refugio de lanchas. De un puerto de abrigo Un puerto de abrigo, lo lo tuvimos que habilitar porque ya no había... Anteriormente los vientos del norte pegaban así... Y los muelles te servían de protección... cambiabas tu lancha de aquí y la pasabas aquí... y pasabas el norte sin ningún problema. Hoy el día que el norte está pegando aquí... o sea, sienten que hay un cambio en la en la en la dirección del viento. Ya viró el viento. Y ya el muelle ya no te sirve. Okay. Porque las lanchas se estropean o se hunden de plano. Cuando el viento estaba aquí... no había ningún problema. Los muelles eran súper súper súper. Ahora ya no. Ahora ya no, ya con ese norte que pega aquí vulnera el área, mete marejada... y empieza a hundir las lanchas o las empieza a destruir entre ellas, aporrear, aporrear en la rampa."

"Sí, ese es un... Esa es una de las cuestiones. Nosotros lo que optamos es que estamos aquí, somos turisteros, metemos las lanchas, metemos aquí... Y ya no tienen ningún problema. Donde quiera soplar el norte, ya no nos hace nada. ¿Y y la profundidad ahí del canal, ese no se les azolva? 60, 40... Con eso, con eso pasamos... puede tener hasta 2 metros... Ah. Sube el agua y ya. Ahí ahí puedes entrar a a sola palanca o de plano ya con motor... llegas hasta la última punta, creo que es es aquí, y nosotros hasta acá llegamos. Ajá."

"Pues muchas gracias por la información. Muy útil. Este... ¿es posible que me dé su nombre, edad? Sí, sí. Eh... ¿Lo puede apuntar? ¿Puedes apuntar el nombre y la edad? Voy a ir por una por una por una gorra y algo... ¡Ah, Bernardo! Ah, sí... ah, pues ya lo conoces. Oye, déjame ir por una gorra, voy a ir por una gorra y un y un buff."

H.5 English translation interview 2

Orange = not useful
Blue = Interviewee Farneli
Green = Alec Torres-Freyermuth

"So, the idea here is very simple. Just... here on the map, with some... red stickers. If you can point out to us... which areas generally always have flooding problems, in general. The most critical ones, let's say, in red, and... and maybe in yellow the ones that are more due to rain or more..."

""And a bit if you could also tell us... what causes that, primarily, or what the phenomena are that cause them and how often they occur. From high spring tides? From high seas? This... this area... is always underwater. The water rises. It is one of the lowest parts. Okay. Yes. And the highest part... ends up around here... Let's see... part... that's the part.... es una dos tres, es esta. Esta es la... a ver la parte... Esta es la parte... esa es la parte que de último se inunda. Okay. Con la creciente más alta... Y otra parte crítica, que es la más crítica dentro de esa situación... es esta. Que nos tapa la salida. Okay."

"We are located between two... rivers... one comes in like this, and comes out at the gas station. And the other comes out here... it also appears there by the gas station. Those rivers bring water, it rises, and when we want to leave... there's no water here yet, but over there it's already 20 centimeters. Okay. And that is a... it's a serious problem. Because during hurricanes, if you're not careful... you stay in there. You stay behind in the town. Yes. And as for the rest, the water runs from here to here... the one from here comes out, runs up to here... and fills the center until it reaches this one. Okay."

"And this... how high was the water that you have experienced? Well, during hurricane Isidore... the water stood almost two and a half meters high. Two and a half meters of water during Isidore... up to here... yes. Something impressive... And during a... a...s torm Normally it is 20 centimeters, 30 centimeters on the street. Okay. So now that the north winds season is coming, that is when these phenomena occur most often.

Because when the north wind... hits the northeast wind... and then it starts pushing water in. Yes, as if they are unprotected there, no longer protected... Yes. No, and it's the wind that brings the water. It rises ... and rises until it ... floods most of the town. Yes. And these parts... those are also... this is just because this stayed high, the whole road stayed high. Yes... yes, it gives the impression that it rises... that it rises..."

And what they tried here was that this is the high part... and this is the low part... so that all streets... have drainage... river drainage. Okay. Which many people don't understand... Yes, yes. we as residents want river drainage. So that the water doesn't stay stagnant, because then the streets break open. Yes."

"Yes, that it floods but also drops quickly... The way it came in, so... and with rain the same thing happens. And a flood-prone area... let's see, this is... is this Street 10, right? It's this one here. Yes. That the entire street... with the rain... the water stays stagnant... And it's a problem, because the street breaks faster. kay. And in terms of damage to the... to the houses... is it more... is it more from what's inside, or does it also damage the structure, let's say, and that sort of thing... No. To the house it's more this... they get eaten away by saltpeter. The moisture when the water rises, that increases... And it starts eating it away. What people try to do is to put masonry or stone. Up to a meter or a meter and a half... and above that the blocks... to try and protect it. Yes, and the utilities, I also see that they put them above the... all of them... all of them... always thinking of putting something on top. Yes."

"It must also be taken into account that the town over the past... every year has risen about 20, 30 centimeters. New streets were built... they were raised, raised. We noticed that with the houses. There were houses that were enormously high, and now... they are practically at ground level. Yes. Yes."

"That is what happened in... in... many of the years. This... this is a river... that runs up to here... and practically connects up to here. And this is the other river that runs up to here, and comes up to here."

"These days, those rivers are basically... a shelter for boats. A harbor. It was a docking port. We had to make it suitable, because we couldn't get in anymore. Before... when the north winds... they hit like this. And the piers... served as protection. You swapped your boat from here and brought it over here... and you weren't bothered by the north wind. Now that the north winds have changed... now the north winds hit here. Oof... the direction of the wind has changed. And that pier... is useless now. Okay. Because the boats get smashed or sink. When the wind was here... there was no problem. The piers were super... super... So not anymore. Now it's the north wind hitting here. That makes the area vulnerable, brings spring tides with it... and starts sinking boats... smashing them against each other, crushing them in the... in the waves."

"Yes, this is a... This is one of the things we have chosen... we are here... we are focused on tourism... We bring the boats inside, put them here... and they have no problems. No matter where the north wind blows from, it doesn't affect us. And the depth there of the channel... doesn't it silt up? 60, 40... And that is, That is enough for us... it can even be two meters big... Ah. The water rises and yes... There you can go in with just a paddle... or if necessary with a motor... You get to the furthest tip, I think it's... this is here, and we get up to here.. Well."

"Thank you very much for the information. Very useful. This... May I know your name and age? Yes. Could you write that down... Could you write down your name and age? I'm just going to grab a cap... Bernardo. Ah yes! ...Ah, you know him already. Hey. Let me just grab a cap... I'm going for a cap and a neck warmer."

Appendix I

Reference system

I.1 Reference system LiDAR and GPS data

As described in Section 4.2, the LiDAR data covers the northern part of San Felipe. The LiDAR data covering the northern part of San Felipe is provided by LIPC-UNAM. The Southern part of San Felipe is not covered by available data. The GPS measurements cover the complete city of San Felipe, see Figure 4.2. The GPS measurements and the LiDAR elevation map can be combined to generate a complete elevation map of San Felipe. As described in paragraph 4.4.1 GPS measurements in San Felipe are taken by pole, car and foot. The GPS measurements by the GPS Rover (see Section F.2) are taken relative to an unknown reference system. The exact locations of the GPS Pole measurements are visualised in Figure I.1. The location of the GPS Pole measurements correspond with Figure I.6.

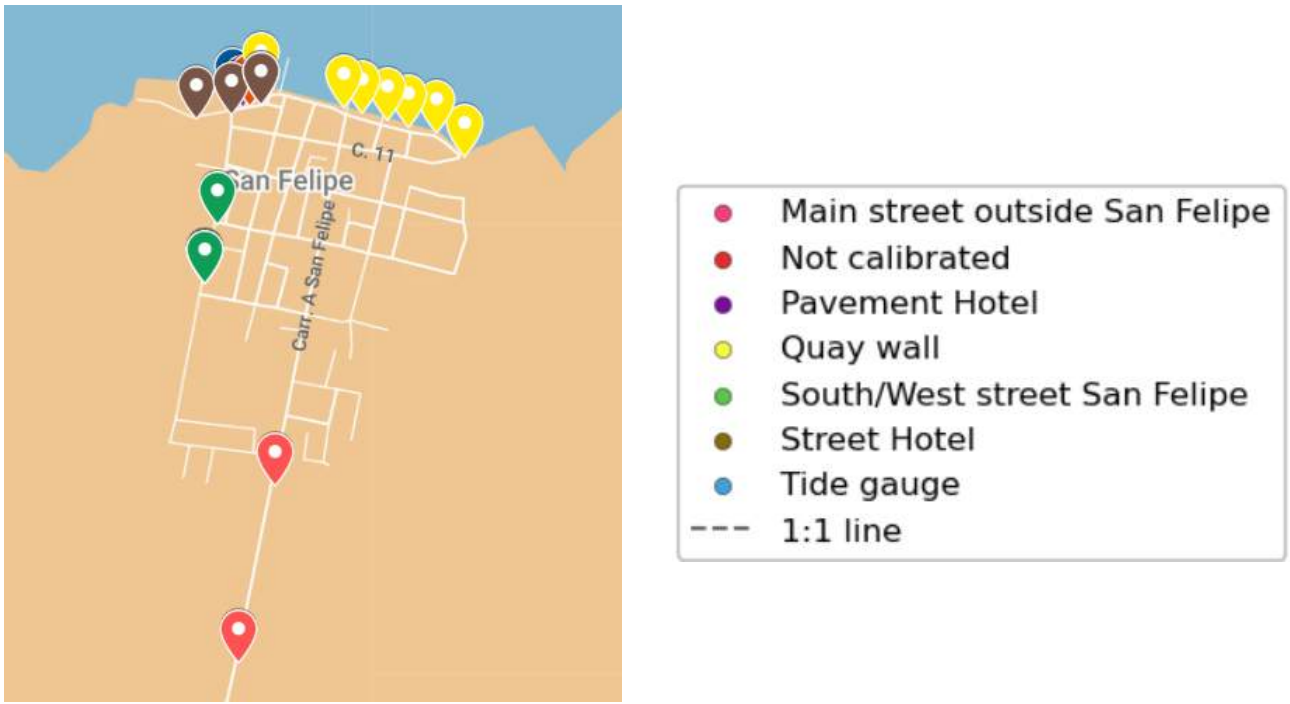


Figure I.1: GPS Pole Locations San Felipe with the corresponding location classification (Google, 2026b).

The LiDAR dataset has a different reference level. The LiDAR and GPS measurements in San Felipe need to be aligned into the same frame of reference, the unknown reference system of the GPS. The LiDAR data is compared with the GPS data in order to find a constant offset between the LiDAR and GPS data. The area used for this comparison is the northern part of the main road through San Felipe where the LiDAR data and GPS data overlap.

Figure I.2 shows the GPS Car and Pole measurements that overlap with the LiDAR data. The northern part of San Felipe is covered by GPS measurements and LiDAR elevation data, so this area is used for the comparison. The backpack GPS data is not taken into account in this comparison. During the measurements

the location of the backpack was not consistently on the same location (street, pavement etc.). The backpack GPS dataset is filtered and the transect of the backpack measured on the street is extracted. This part of the dataset is compared to the car GPS dataset and the difference between these datasets on the transect is used as the offset between the backpack measurements and the car measurements. As the car data and backpack data overlap in the area of the available LiDAR data, the car data is used for the comparison between GPS measurements and LiDAR data.

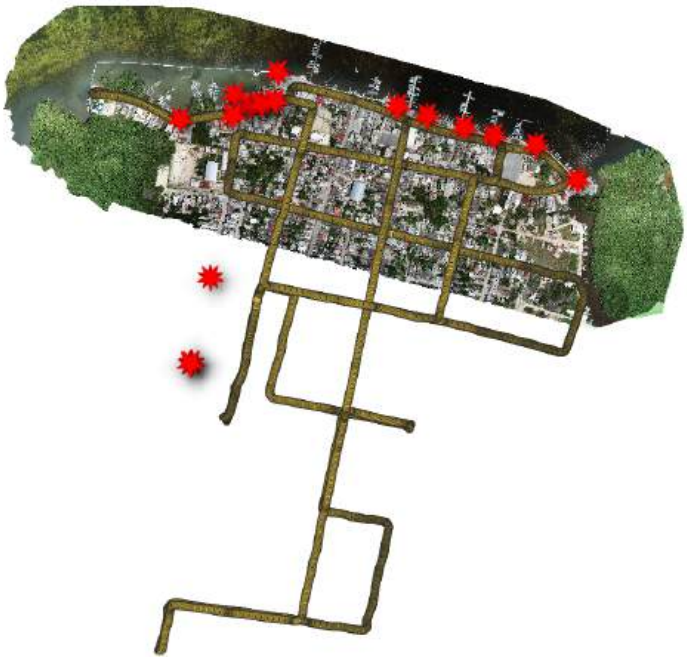


Figure I.2: Location LiDAR and GPS data. The red stars highlight the location of the GPS Pole measurements, the yellow dots the car and foot locations. The northern part of San Felipe is covered by both the GPS measurements and the LiDAR data.

The elevation of the LiDAR data at the locations of the GPS measurements are compared to the elevations measured by the GPS. Figure I.3 shows the difference in elevation for the GPS and LiDAR. On the y-axis the GPS measurements are plotted; on the x-axis the LiDAR sensor measurements. The dotted line (1:1 line) visualises where GPS measurements and LiDAR sensor show the same elevation. The data points are located above the 1:1 line, which means that the LiDAR sensor underestimates the elevation relative to the GPS measurements by the Rover.

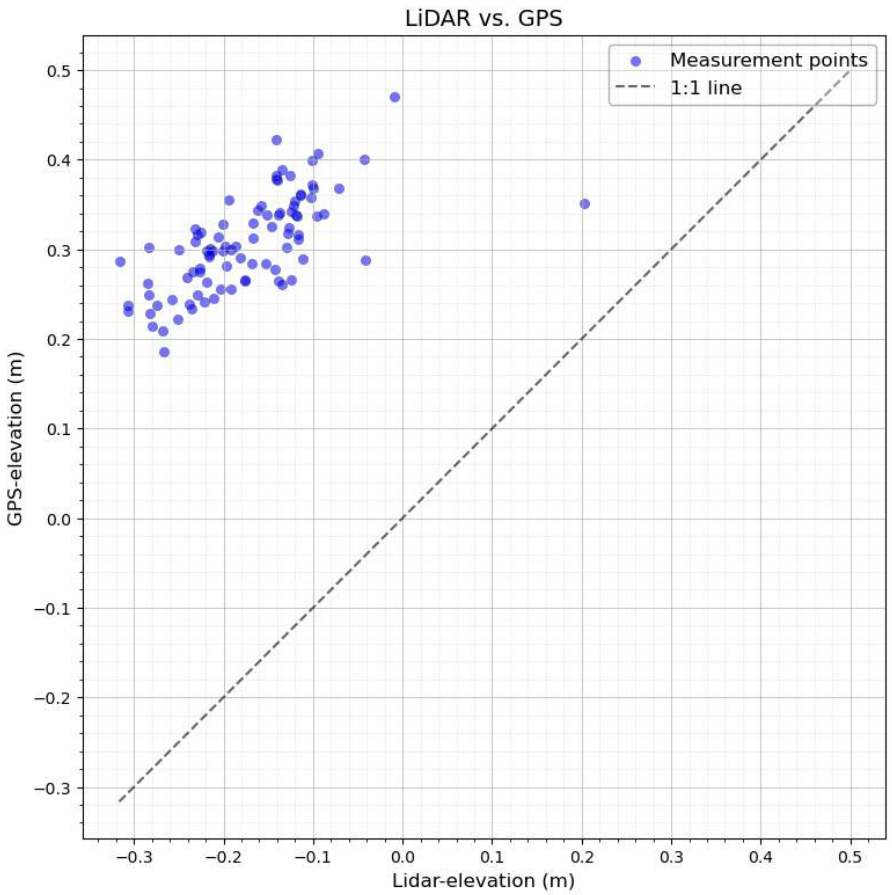


Figure I.3: Provided LiDAR data for north San Felipe compared with GPS car measurements. Overlapping points for the northern part of the main street are shown measured by the GPS and LiDAR. The GPS measurements show an absolute higher value than the LiDAR data.

I.2 Offset LiDAR and GPS

Both elevation measuring methods need to be aligned relative to the same frame of reference. As the LiDAR is relative to an unknown frame of reference, this results in a shift of the LiDAR data in the direction of the GPS data. After this shift both datasets can be used in the elevation model, as both are relative to the same reference system.

The systematic offset between the LiDAR data and GPS data is determined based on the median of the elevation differences for in total 91 points. This results in an offset of 0.48m. The uncertainty of these offsets are statistically calculated by a bootstrap (Henderson, 2005)(SciPy community, 2026).
By using the Bootstrap method, random samples are taken from all offsets between the GPS data and LiDAR data. This is used to analyse the distribution and accuracy of the offset. From the calculated differences (GPS and LiDAR) a total of 10,000 samples with replacement are generated. The bootstrap is used to simulate the experiment multiple times (UC Berkeley D-Lab, 2021). From each sample the median is calculated, as this is the middle value in the dataset, and thus takes outliers less into account (Höhle & Höhle, 2009). The standard error of the bootstrap is 7 mm.

To check the corrected LiDAR data (offset of 0.48m corrected), the root mean squared error is calculated to be 0.057m. This means that the corrected LiDAR datapoint differs 0.057m from the GPS datapoint. As can be seen in Figure I.4, the LiDAR data aligns with the GPS data, which means they are both relative to the same reference frame.

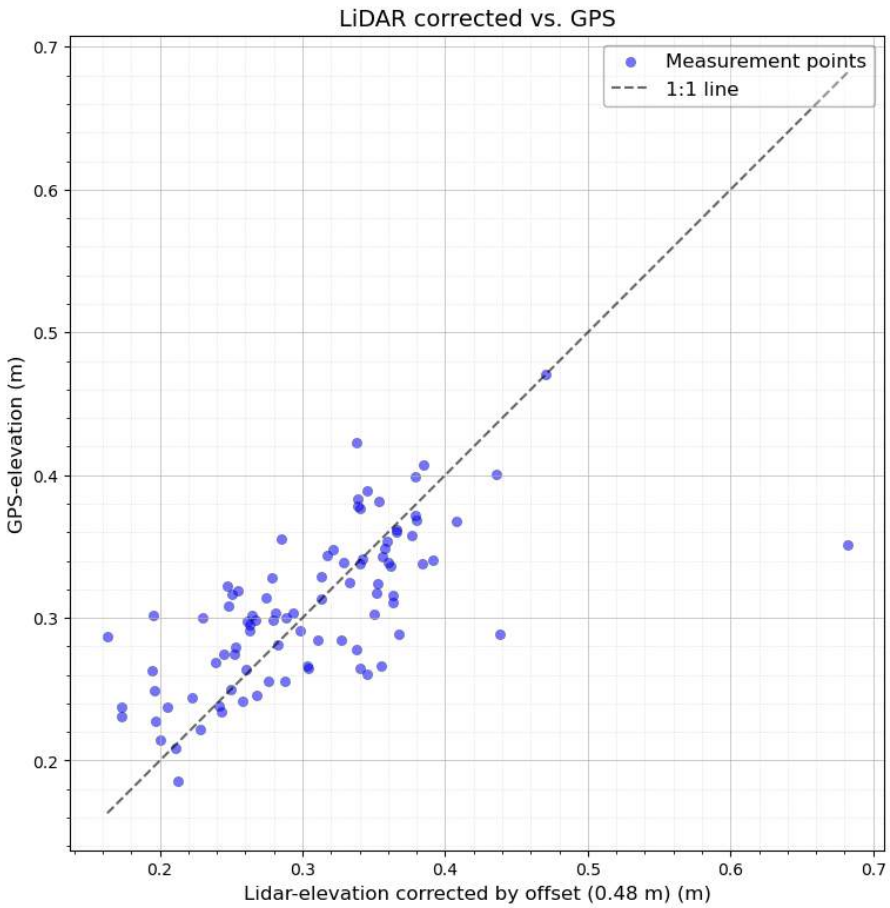


Figure I.4: Provided LiDAR data for north San Felipe compared with GPS car measurements including the calculated offset of 0.48 m. Overlapping points for the northern part of the main street are shown measured by the GPS and LiDAR.

I.3 Validation Offset GPS Pole

Alongside the car GPS data, the GPS Pole data can be used to validate the method used as explained in Section I.2. The pole measurements are taken at different location categories, such as the quay wall, street of the hotel etc. (see FigureI.1). The car GPS data takes the points on the main street (Carr. a San Felipe). To compare the GPS Pole measurements with the corrected LiDAR data, the points on the street of the Hotel San Felipe de Jesús can be used, as these pole measurements are taken on the street. Other pole measurement locations are not taken on the street, so the offset is not applicable to these points.

Figure I.6 shows how the GPS measurements points align with the LiDAR elevation after correction. Figure I.5 shows the points before correction. As can be seen in the Figures, the "Street Hotel" GPS measurement points align with the LiDAR elevation when adjusted with the offset of 0.48 m.

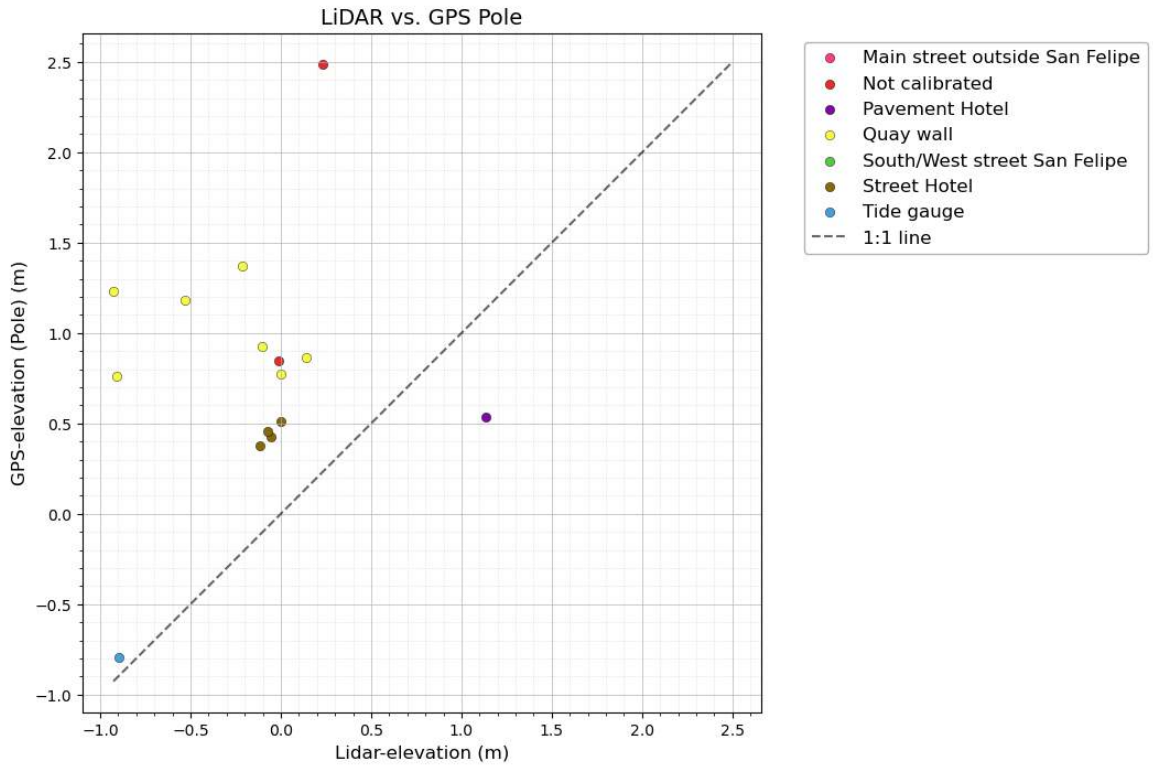


Figure I.5: Provided LiDAR data for north San Felipe (not corrected) compared with GPS Pole measurements. The y-axis shows the GPS measurements (m), the x-axis the Lidar elevation (m).

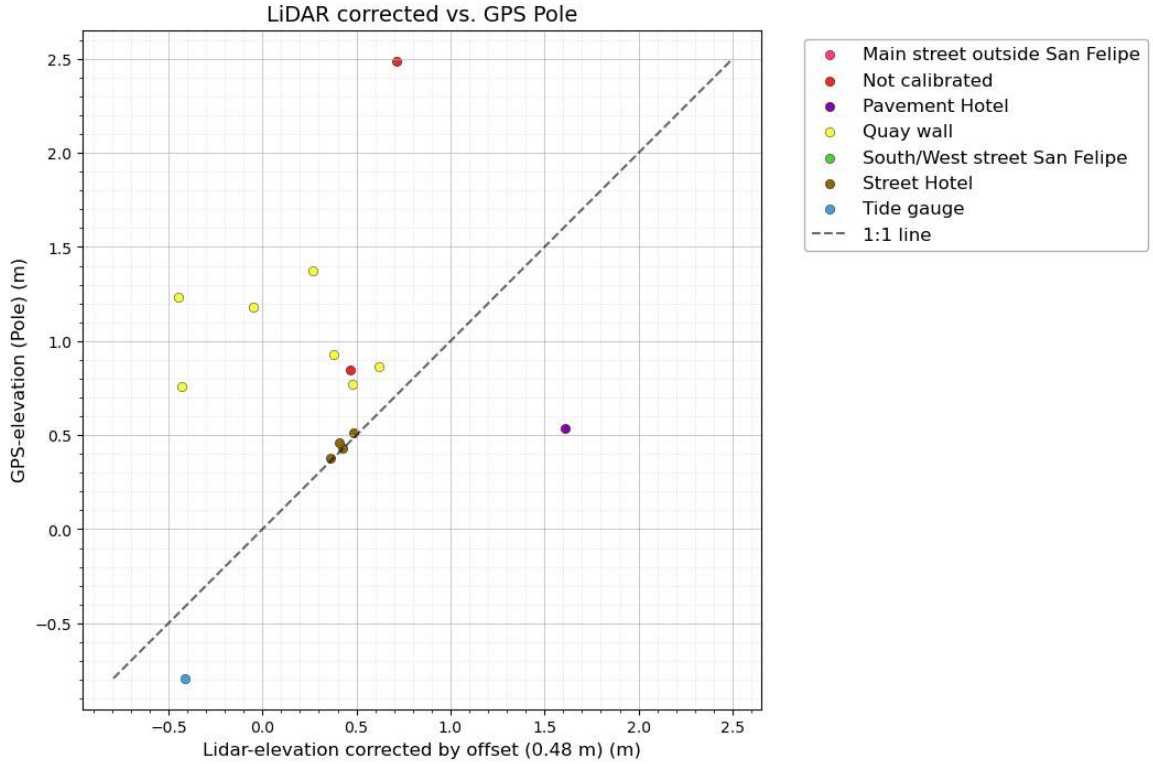


Figure I.6: Provided LiDAR data for north San Felipe corrected with the offset of 0.48 m compared with GPS Pole measurements. The y-axis shows the GPS measurements (m), the x-axis the Lidar elevation (m).

I.4 Interpolation San Felipe

The city of San Felipe is mapped by combining the available LiDAR data of the northern part of San Felipe with an interpolated map of the GPS car and backpack measurements. The southern part of San Felipe is mapped by IDW (Inverse Distance Weighted) interpolation. This interpolation method is based on the following principle: the relative distance of the unknown point to the known sample points is a measure to determine influence of the sample point to the unknown point (QGIS Project, 2025). The IDW interpolation method uses a p-value. The higher the p-value, the smaller the relative influence of GPS measurements points further away from the calculated point. Figure I.7 shows the interpolation that covers the whole area of San Felipe, interpolated with a p-value of 2.

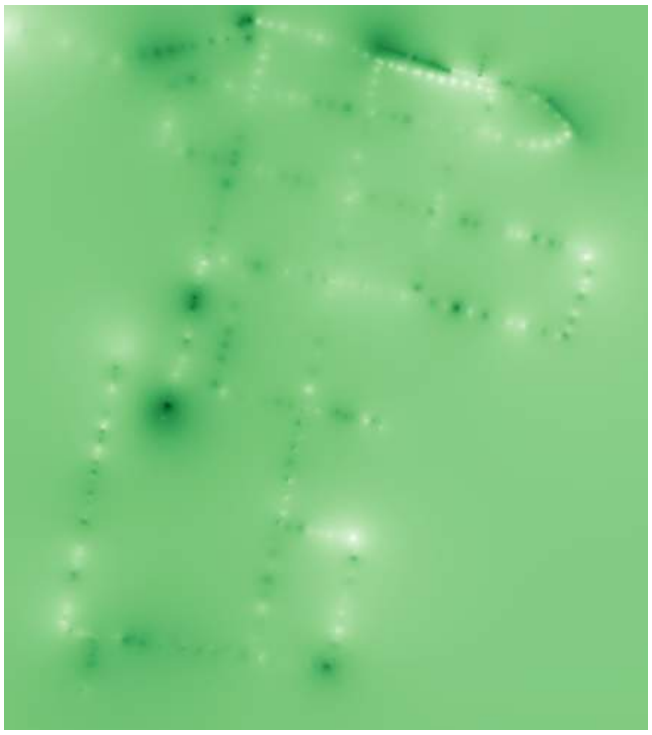


Figure I.7: Interpolated map of the elevation level based on Inverse Distance Weighted interpolation with a p-value of 2. The dark green areas represent the areas with the highest elevation, the white areas the lowest elevation.

I.5 Tidal gauge measurements

To establish a consistent vertical reference datum for the SFINCS and MODFLOW model, a temporary tide gauge was deployed in San Felipe during the fieldwork. The sensor recorded water distance data over a 5 hour period.

To determine the exact mounting height of the sensor (H_{sensor}) relative to the reference frame, a calibration was performed at the start of the monitoring period ($t = 0$). First, a GPS measurement was conducted to determine the absolute elevation of the bottom floor directly beneath the sensor. Simultaneously, a water depth measurement was taken using a physical staff to establish the exact water surface elevation at $t = 0$. By combining the initial sensor reading (the measured distance from the sensor to the water surface at $t = 0$) with the physical water surface height, the absolute elevation of the sensor was accurately established:

$$H_{\text{sensor}} = z_{\text{water_surface}}(t = 0) + \text{distance}_{\text{sensor}}(t = 0)$$

Following this, all subsequent raw sensor readings were converted to absolute water levels relative to the local GPS reference system by subtracting the measured distance from the fixed sensor height:

$$\text{Absolute Waterheight} = H_{\text{sensor}} - \text{distance}_{\text{sensor}}$$

Then the measurements are transformed to the same reference as the GPS measurements as can be seen in Figure I.8.

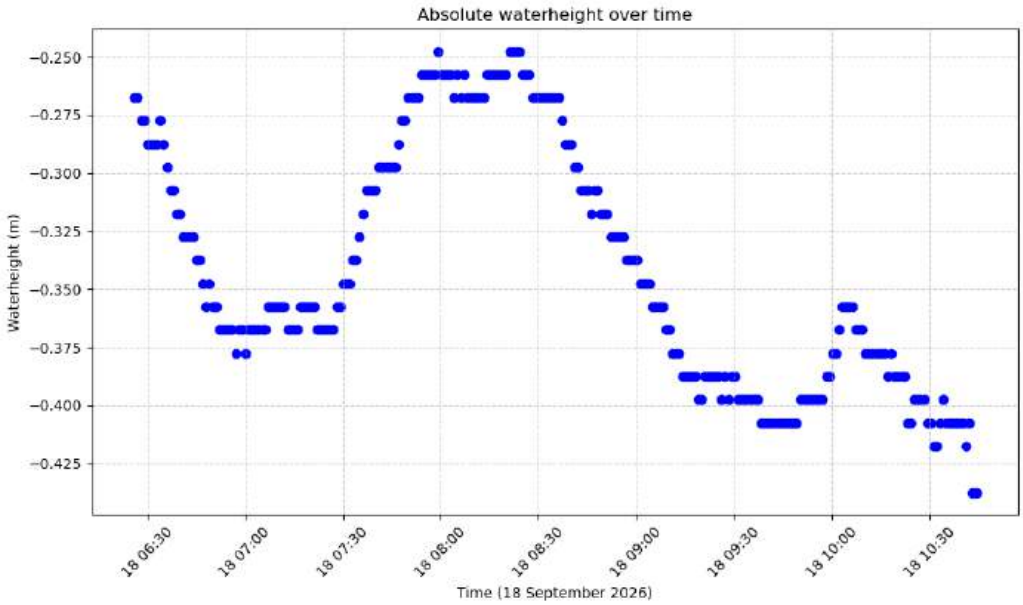


Figure I.8: Tide gauge measurements representing the absolute water height (m) over time. The total measurement period is 5 hours. The location of the measurements is 21°34'05.9"N 88°14'04.8"W.

I.6 GTSM Model comparison

The processed field measurements were compared against regional data. Water level time series were extracted from the Global Tide and Surge Model (GTSM, by Copernicus/ERA5 meteorological datasets) at the closest available station near San Felipe (Lat $21.5770°$, Lon $-88.3450°$).

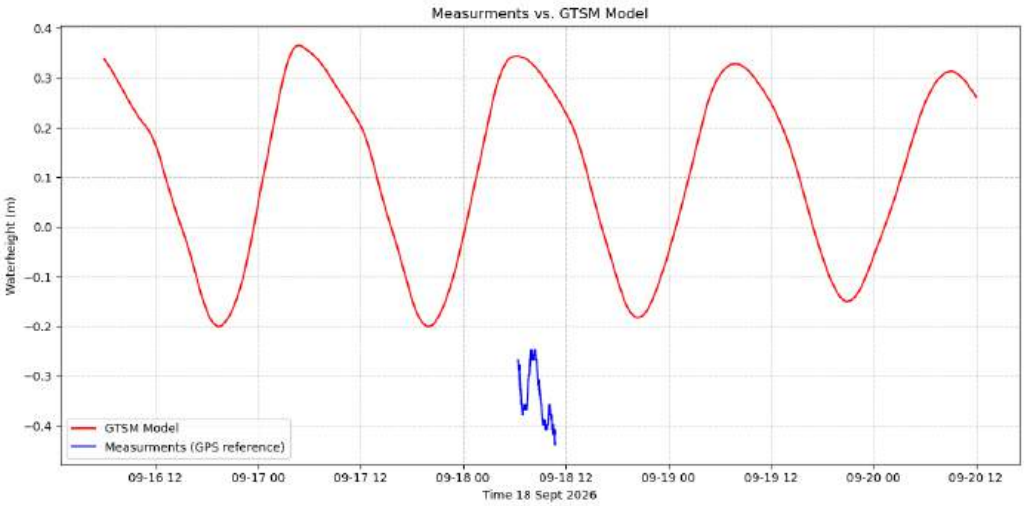


Figure I.9: Comparison between the GTSM model tide and field measurements (GPS reference) on September 18, 2026.

The model data was aligned with the field measurements. To determine the vertical offset between the GTSM model and the field observations, a RMSE-based optimisation (least-squares minimisation) was applied to find the optimal vertical offset. This resulted in a vertical offset of 0.656 m, which is subsequently used to correct the topographic (INEGI, 2026) and bathymetric (GEBCO Compilation Group, 2026) datasets. This adjustment ensures that the model elevations properly match the local GPS reference system.

I.7 Mangrove elevation correction

The downloaded topography from INEGI (INEGI, 2026) does not include the correct elevation of the mangrove areas on the barrier island and around San Felipe, since the top of the trees is measured. To correct the topography to the right bottom elevation of the mangrove, the elevation of the mangrove areas are altered using Esa Worldcover (Zanaga et al., 2022). These areas are assigned an elevation based on the measurements station data obtained from the "San Felipe Research Group". Based on measurement stations "SF-04" and "KBN-01", the average difference in mangrove elevation between the measurement stations and the downloaded topography is -2.2183m (offset correction included). The areas covered by mangroves are lowered by 2.2183m.

Appendix J

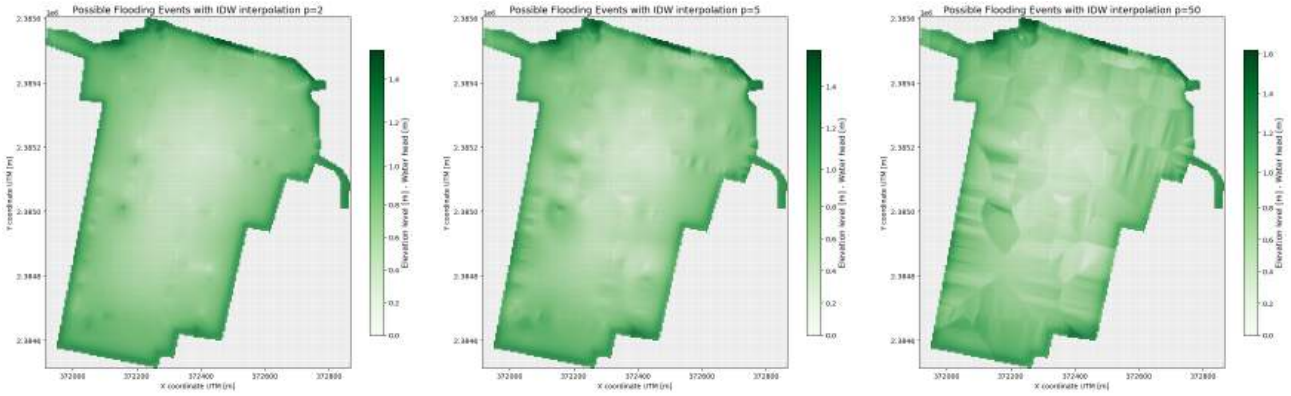
MODFLOW

J.1 Interpolated map

The GPS measurement points are used to make an interpolated map of San Felipe. As explained in Chapter I.4, an IDW interpolation is applied to the GPS points. The IDW interpolation method uses a p-value. The higher the p-value, the smaller the relative influence of GPS measurements points further away from the calculated point. To see the influence GPS points further away, the interpolation is performed with p is 2, 5 and 50.

Figure J.1 shows the difference in elevation level and water head in meter for the three different p-values. In Figure J.1a the interpolated surface is smooth as the relative weights of point further away from the calculated point are big compared to p=5 and p=50. The visualisation of p=50 (see figure J.1c) shows a more blocky surface as the relative weight of GPS points further away are relatively less important.

As the MODFLOW simulation gives the water head (m) for every location in San Felipe, it is best when the area between the GPS measurement points are calculated based on points further away to the calculated point. Therefore, a p-value of 2 is used for further simulation.



(a) Elevation level minus ground level for interpolation with p=2.

(b) Elevation level minus ground level for interpolation with p=5.

(c) Elevation level minus ground level for interpolation with p=50.

Figure J.1: Three plots for IDW interpolation method with p-values 2 (left), 5 (middle) and 50 (right). The values displayed in the plots are the difference between the elevation level and water head in m. Positive values mean that the elevation is higher than the water head at that location and thus no flooding.

J.2 Boundary and input data

The boundaries at the sea and mangrove are driven by the water levels at respective sides of the city. Figure J.2 shows the location where the water levels used at the boundary are measured. The precipitation data is measured at location 21°3000 N, 88°1500 W (retrieved from (Hersbach et al., 2023)).



Figure J.2: Location blue marker (21.577000 °N, -88.345000 °W) is used for the boundary condition at the sea. Location red marker (Lat 21.606000 °N, Lon -88.110000 °W) is used for the boundary condition around the town of San Felipe (Google, 2026a) The water level at sea is directly implemented at the sea boundary; the water level at the mangrove of San Felipe is shifted to the southern boundary as explained in Chapter 5.2.2.

As seen in Figure J.2, the mangrove water levels are retrieved from a point further away from San Felipe (red marker in Figure J.2). These waterlevels are used at the GHB boundary. The hydraulic head gradient between the varying water level and the boundary of San Felipe is multiplied by the conductance at the boundary. The conductance at the boundary is calculated based on the hydraulic conductivity, the depth of the aquifer and the distance from San Felipe to the external varying water levels in the mangrove. Figure J.3 shows the calculation parameters relative to the boundary of the model.

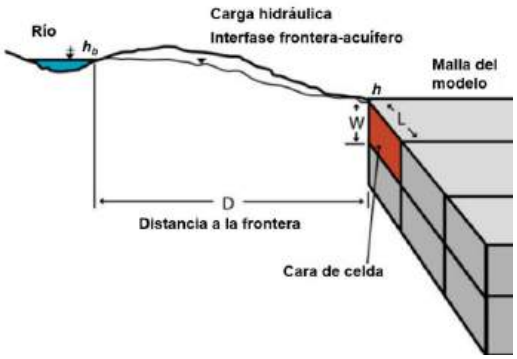


Figure J.3: Calculation of conductance for the general head boundary (Medina Rosado, 2024)

Equation J.1 shows the conductance calculation based on the parameters explained in Figure J.3.

$$C = \frac{k \cdot W \cdot L}{D} \tag{J.1}$$

where:

C = Conductance of the boundary cells $[m^2/d]$

k = Hydraulic conductivity $[m/d]$

W = Depth of aquifer $[m]$

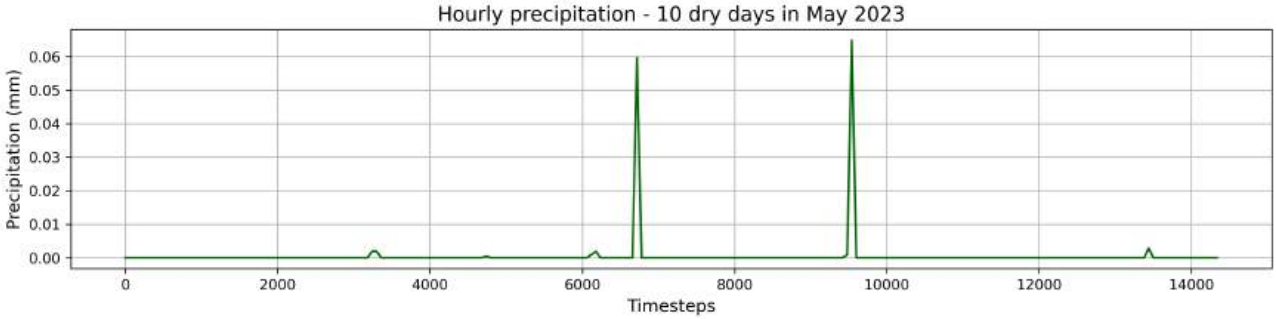
L = Cell size $[m]$

D = Distance from varying water level to boundary $[m]$

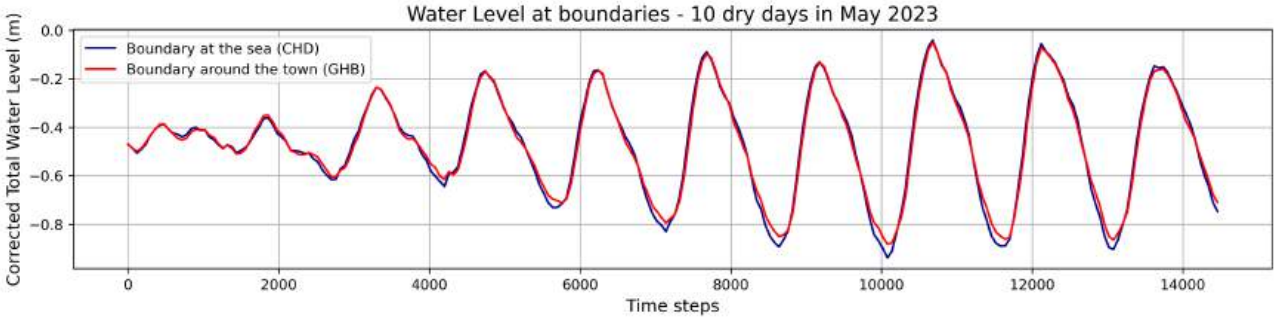
The aquifer depth is 6 m, with a cell size of 5 m and a distance to the mangrove water level point (red marker) of 1000 m. Strictly speaking, the actual distance is significantly greater, as the varying head data is derived from the mangrove area near Ría Lagartos. However, it is assumed that this water level variance is approximately equivalent in the mangroves surrounding San Felipe.

J.3 10 dry and wet days input and output MODFLOW

The period in May (01-05-2023 to 10-05-2023) is used as the dry period in the model. Figure J.4a visualises the rainfall in mm/h for each times step used in the model. The location of the precipitation data used is 21°3000 N, 88°1500 W (Hersbach et al., 2023). Figure J.4b shows the water levels at the sea boundary (CHD) and the mangrove boundary (GHB) of the model. The precipitation and water levels are the input for the dry simulation in MODFLOW. Figure J.5b shows the water levels for November. Based on both the dry and wet days it can be concluded that the water levels rise more rapidly in case of extreme precipitation.

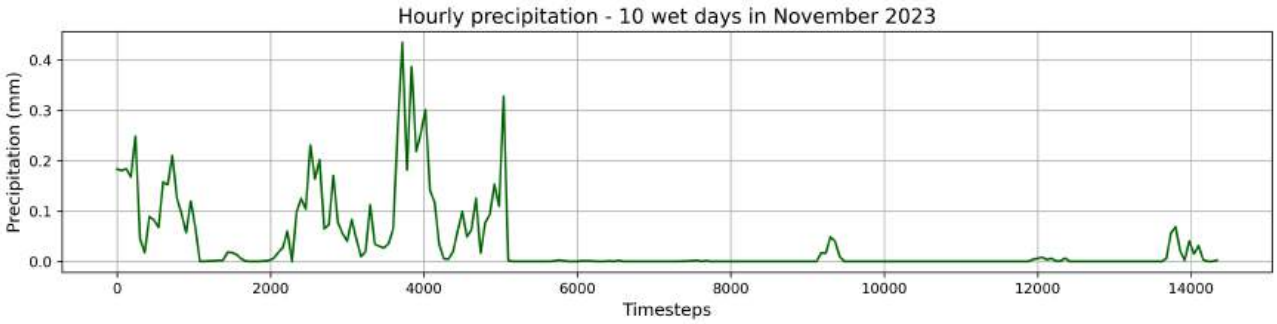


(a) Hourly precipitation data May 2023 at location 21°3000 N, 88°1500 W. Time step 0 corresponds to 01-05-2023 and 14000 to 10-05-2023. (Hersbach et al., 2023)

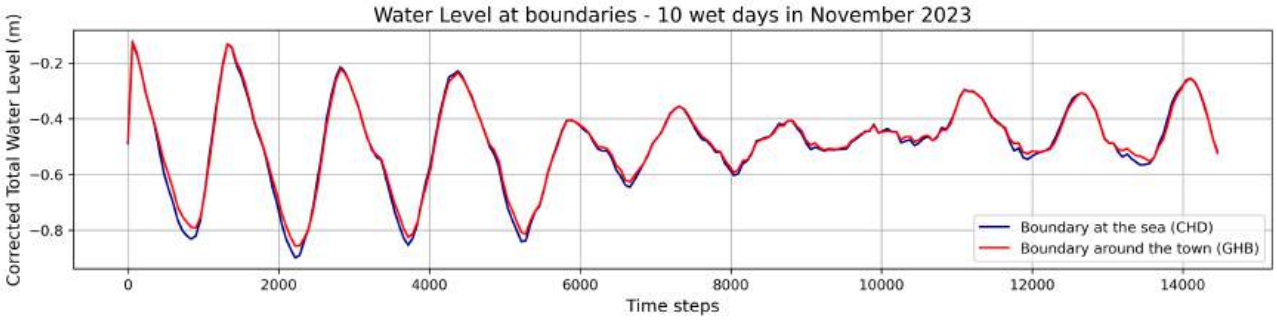


(b) The red line corresponds to the water levels at the mangrove boundary (GHB). The blue line corresponds to the boundary at sea (CHD). Time step 0 corresponds to 01-05-2023 and 14000 to 10-05-2023. (Copernicus Climate Change Service, 2022)

Figure J.4: Input data for precipitation and water levels at the boundaries May 2023 (10 dry days).



(a) Hourly precipitation data November 2023 at location 21°3000 N, 88°1500 W. Time step 0 corresponds to 01-05-2023 and 14000 to 10-05-2023 (Hersbach et al., 2023).



(b) The red line corresponds to the water levels at the mangrove boundary (GHB). The blue line corresponds to the boundary at sea (CHD). Time step 0 corresponds to 01-11-2023 and 14000 to 10-11-2023. (Copernicus Climate Change Service, 2022)

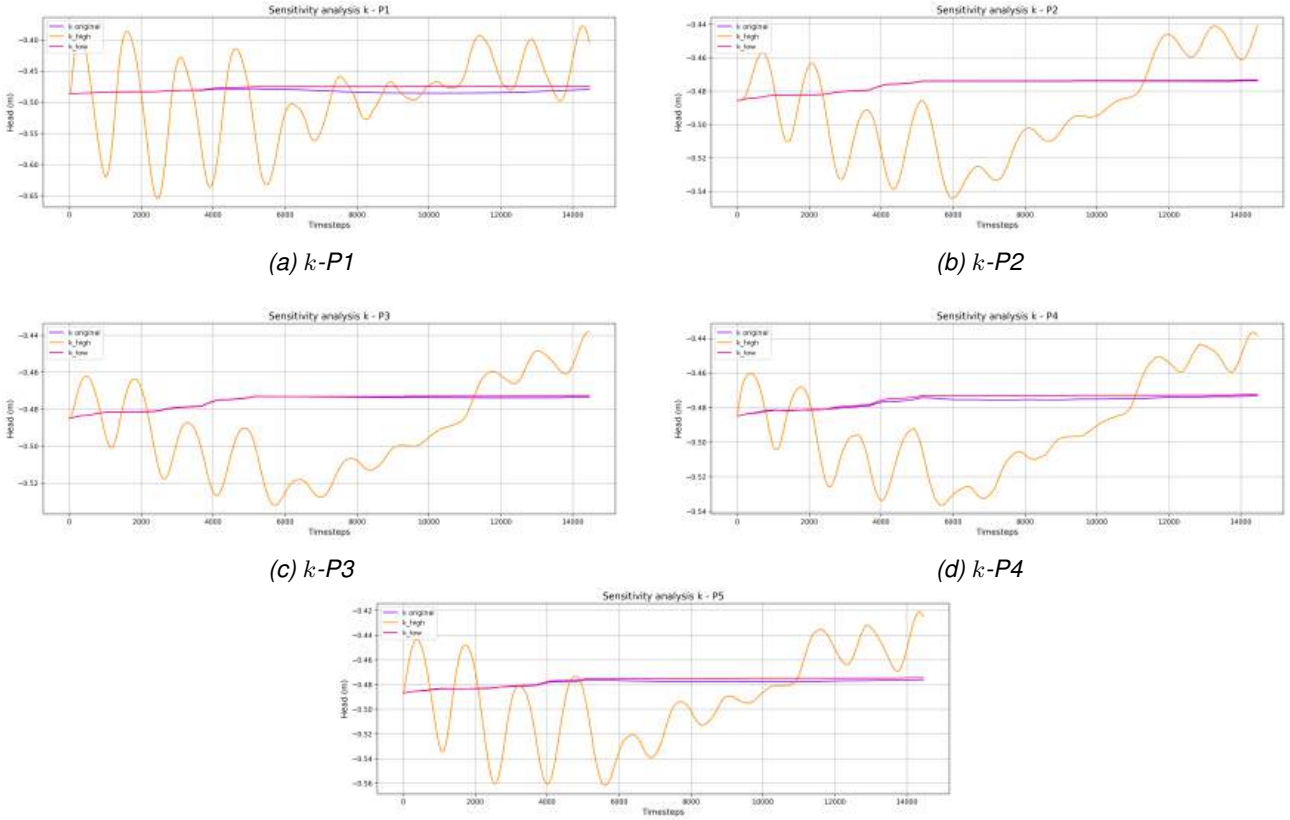
Figure J.5: Input data for precipitation and water levels at the boundaries November 2023 (10 wet days).

J.4 Sensitivity Analysis

The model parameters used in the MODFLOW model are evaluated based on their influence on the head elevation level outcome over time. The simulated time period is 01-11-2023 to 10-11-2023. The paragraphs below show the effect of an upper and lower bound of the following parameters: hydraulic conductivity, recharge coefficient, specific yield, offset of the water levels at the boundaries and the steady state start values for the CHD and GHB boundaries. Figures J.6, J.7, J.8, J.9 and J.10 show on the y-axis the head level in meters, on the x-axis the time steps of the simulation for the period of 10 wet days (01-11-2023 to 10-11-2023).

Hydraulic conductivity, k

Figure J.6 shows for each observation point (P1-P5) the effect of an upper and lower bound of the hydraulic conductivity (k).



(a) k-P1 *(b) k-P2*

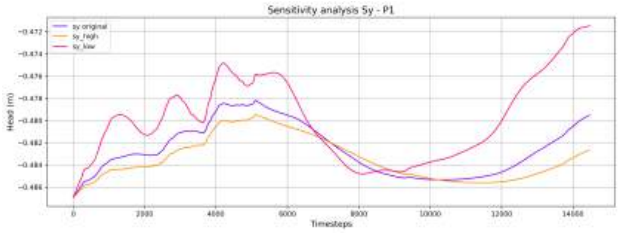
(c) k-P3 *(d) k-P4*

(e) k-P5

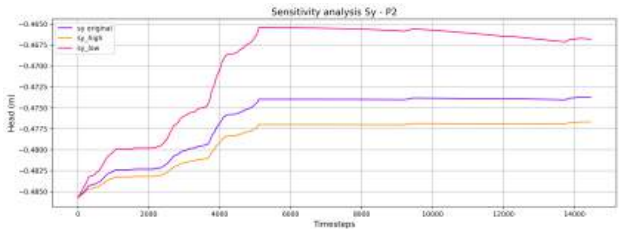
Figure J.6: Hydraulic conductivity (k) sensitivity analysis for 10 wet days in November (01-11-2023 to 10-11-2023). The hydraulic conductivity values range between 9×10^{-7} (low hydraulic conductivity, pink line) and 3×10^{-2} (high hydraulic conductivity, orange line). The 'baseline' is set to 5.54×10^{-4} (original hydraulic conductivity, purple line).

Specific yield, S_y

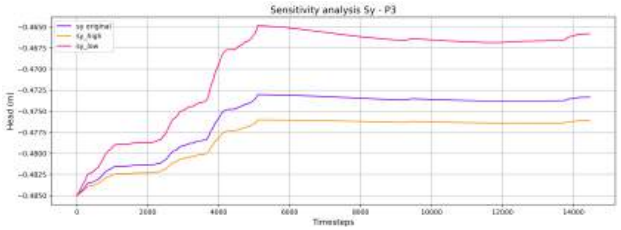
Figure J.7 shows for each observation point (P1-P5) the effect of an upper and lower bound of the specific yield (S_y).



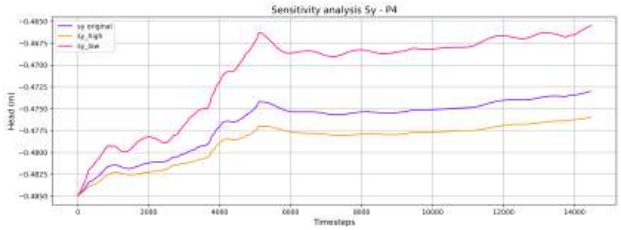
(a) S_y-P1



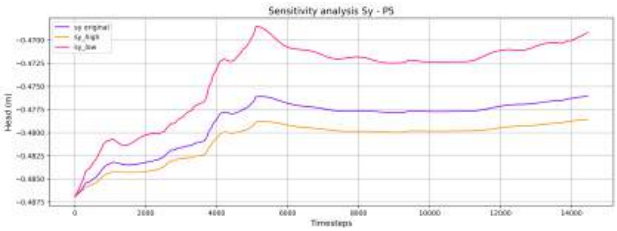
(b) S_y-P2



(c) S_y-P3



(d) S_y-P4

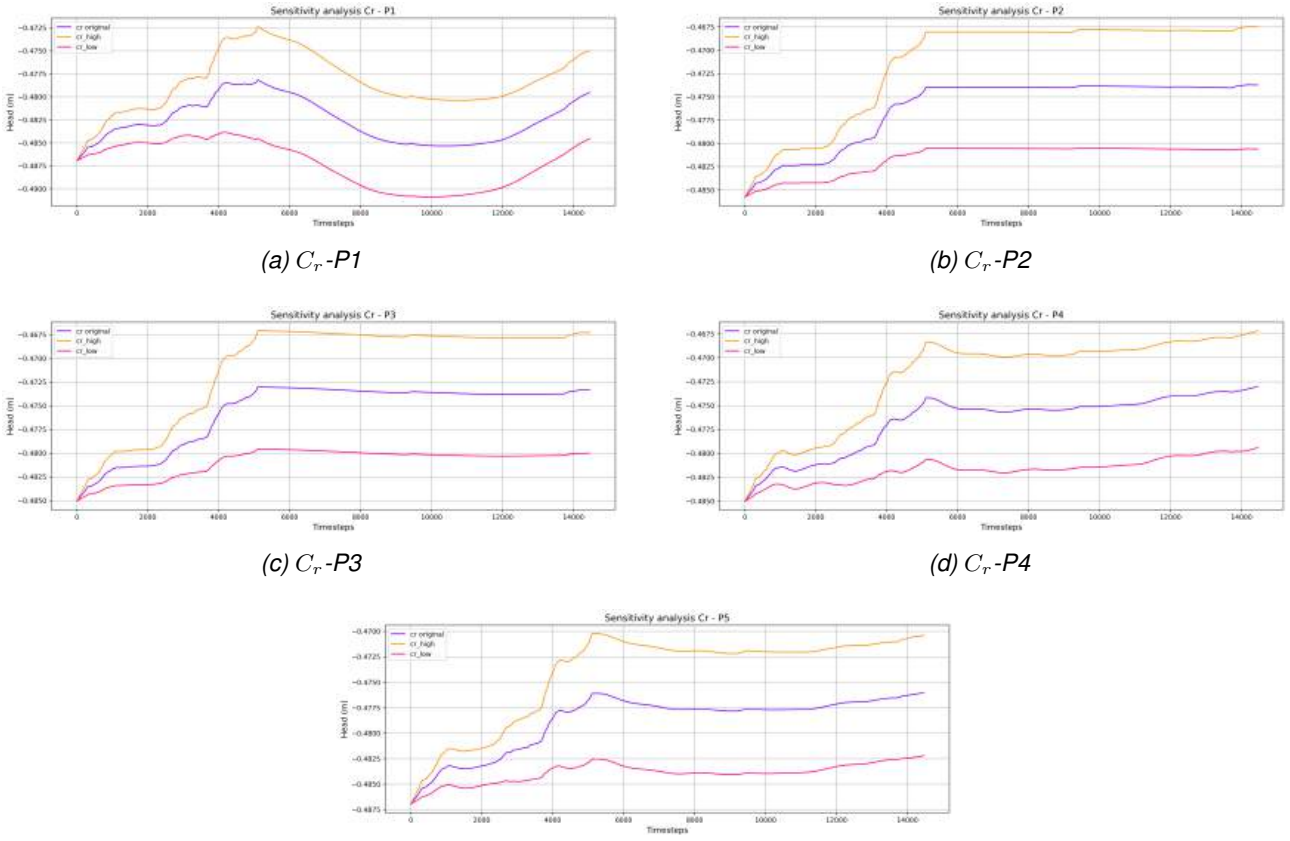


(e) S_y-P5

Figure J.7: Specific yield (S_y) sensitivity analysis for 10 wet days in November (01-11-2023 to 10-11-2023). The specific yield values range between 15% (low specific yield, pink line) and 35% (high specific yield, orange line). The 'baseline' is set to 26% (original specific yield, purple line).

Recharge coefficient, C_r

Figure J.8 shows for each observation point (P1-P5) the effect of an upper and lower bound of the hydraulic conductivity (C_r).



(a) C_r*-P1*

(b) C_r*-P2*

(c) C_r*-P3*

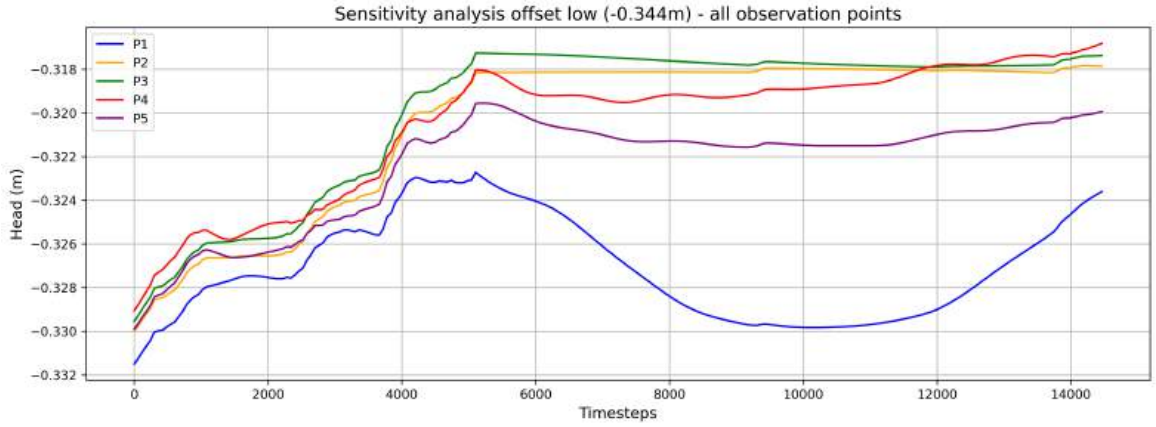
(d) C_r*-P4*

(e) C_r*-P5*

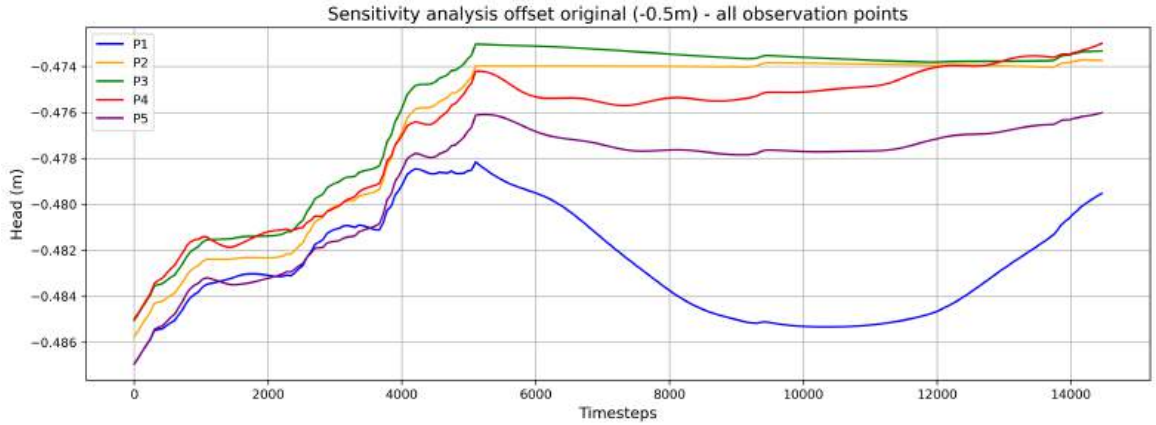
Figure J.8: Recharge coefficient (C_r) sensitivity analysis for 10 wet days in November (01-11-2023 to 10-11-2023). The recharge coefficient values range between 18% (low recharge coefficient, pink line) and 60% (high recharge coefficient, orange line). The 'baseline' is set to 40% (original recharge coefficient, purple line).

Offset

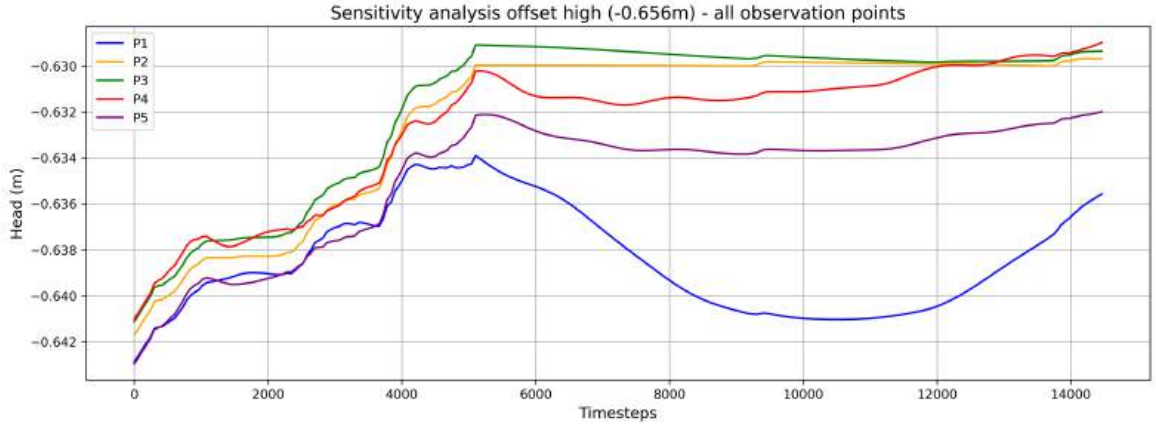
Figure J.9 shows for each observation point (P1-P5) the effect of an upper and lower bound of the offset.



(a) Low offset of the water levels $-0.344\ (m)$ for the CHD and GHB boundary.



(b) Original offset of the water levels $-0.5\ (m)$ for the CHD and GHB boundary.

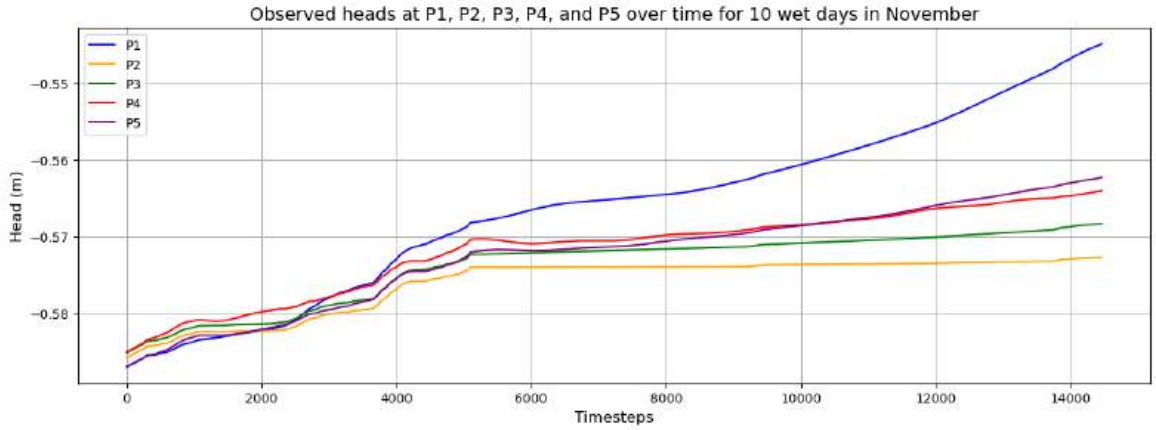


(c) High offset of the water levels $-0.656\ (m)$ for the CHD and GHB boundary.

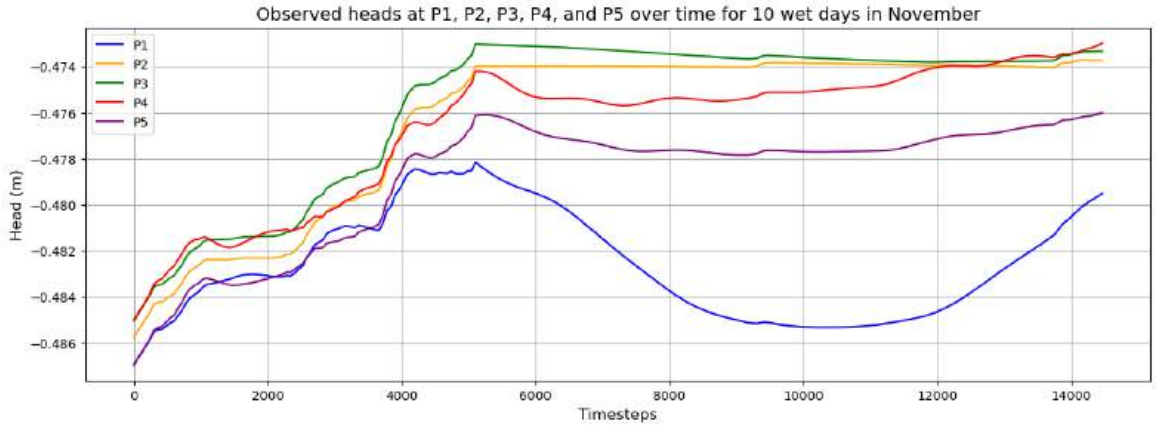
Figure J.9: Offset of the water levels sensitivity analysis for 10 wet days in November (01-11-2023 to 10-11-2023). The offset values range between $-0.344m$ (low offset) and $-0.656m$ (high offset). The 'baseline' is set to $-0.5m$ (original offset).

Steady state

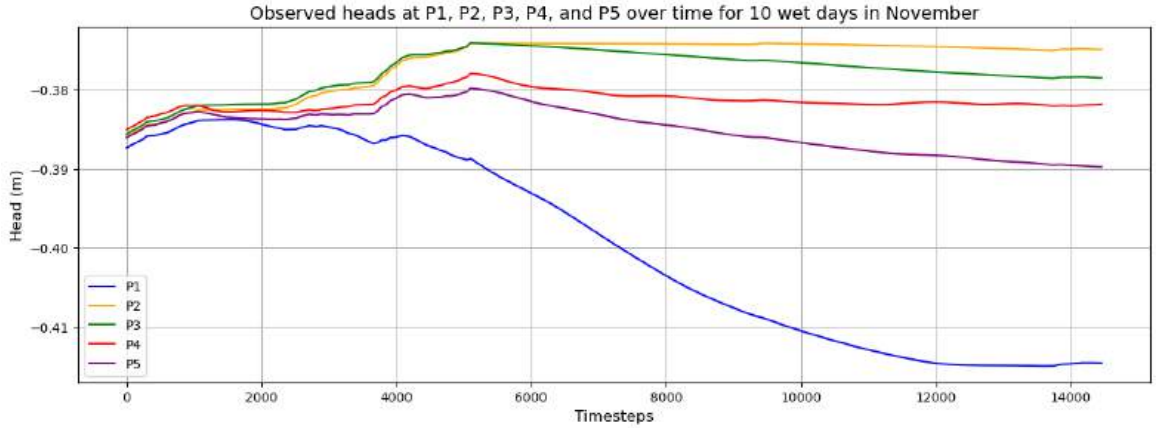
Figure J.10 shows for each observation point (P1-P5) the effect of an upper and lower bound of the steady state value.



(a) Low steady state with starting value $-0.588m$ for the CHD boundary and $-0.583m$ for the GHB boundary.



(b) Original steady state with starting value $-0.488m$ for the CHD boundary and $-0.483m$ for the GHB boundary.



(c) High steady state with starting value $-0.388m$ for the CHD boundary and $-0.383m$ for the GHB boundary.

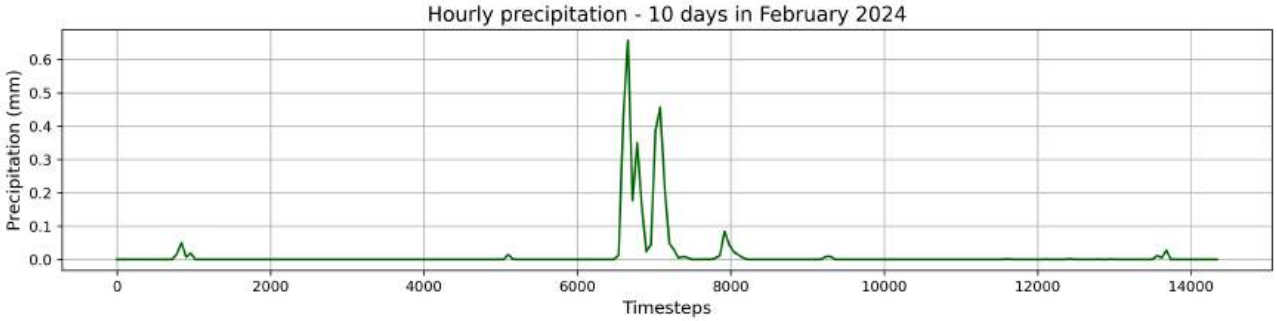
Figure J.10: Steady state sensitivity analysis for P1(blue), P2(orange), P3(green), P4(red) and P5(purple). The steady state time step is run with different values for the CHD and GHB boundary. The effect of the steady state is expressed in head level over time.

J.5 February 2024 storm

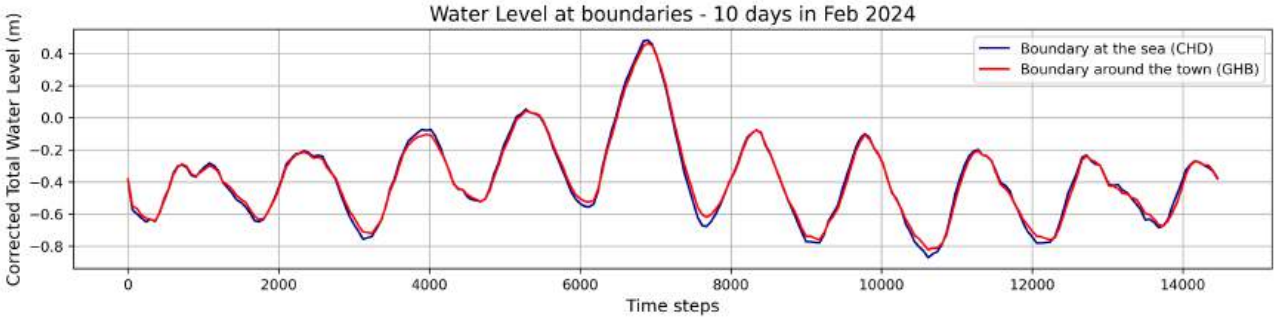
San Felipe experienced a flood on the 5th of February. To simulate the flooding in San Felipe, two time periods are selected and the head levels over time are analysed. The first is a simulation of the first ten days of February 2024, the second of the first twenty days of February.

J.5.1 February 2024 10 days

A simulation is done for 01-02-2024 to 10-02-2024. The input data for precipitation and the GHB and CHD boundary are shown in Figures J.11a and J.11b.



(a) Hourly precipitation data February 2024 at location 21°3000 N, 88°1500 W. Time step 0 corresponds to 01-02-2024 and 14000 to 10-02-2024(Hersbach et al., 2023).



(b) The red line corresponds to the water levels at the mangrove boundary (GHB). The blue line corresponds to the boundary at sea (CHD). Time step 0 corresponds to 01-02-2024 and 14000 to 10-02-2024. (Copernicus Climate Change Service, 2022)

Figure J.11: Input data for precipitation and water levels at the boundaries February 2024 (10 dry days during storm).

Based on the precipitation and water level forcing at the boundary, the evolution of hydraulic head over time can be modelled in San Felipe. Figure J.12 shows the change of head level over time (10 days) for each observation point (P1 to P5). The head elevation over time follows approximately the same pattern at location P2, P3, P4 and P5. However, observation point P1 shows a different behaviour. Until time step 6900 the head level at P1 is lower than the head levels at the other observation points. After time step 6900 the head level increases significantly and afterwards decreases towards the head levels of the other observation points. This different behaviour is forced by the water levels at the CHD boundary close to observation location P1.
Figure J.13 shows the groundwater head at 05-02-2024. It shows that for an entire lower domain, the heads are almost the same. This results that the overflow map is highly dependent on the elevation map.

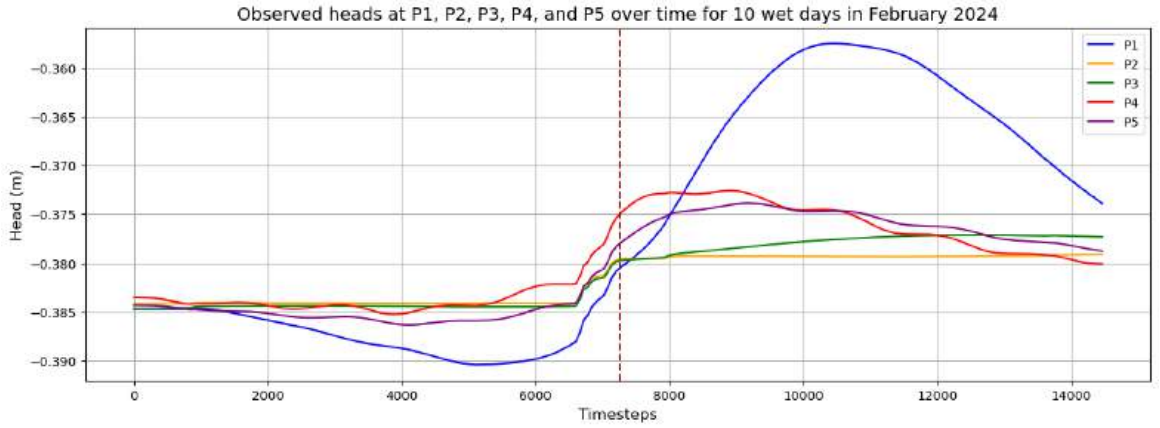


Figure J.12: Head level (m) over time at observation points (P1-P5). The time period is from 01-02-2020 to 10-02-2020.The vertical dashed line gives the time step of the flood during the 5th of February.

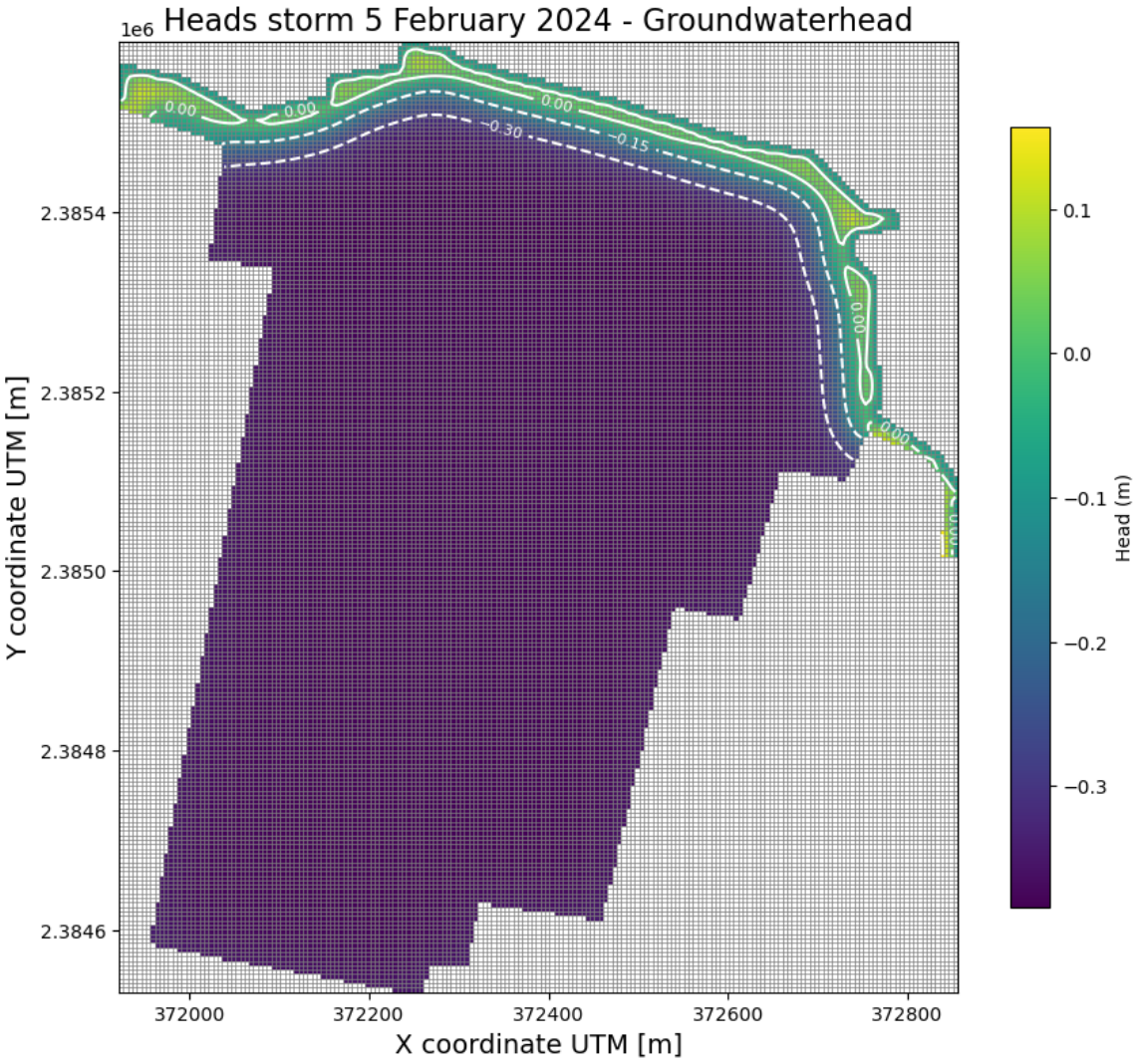
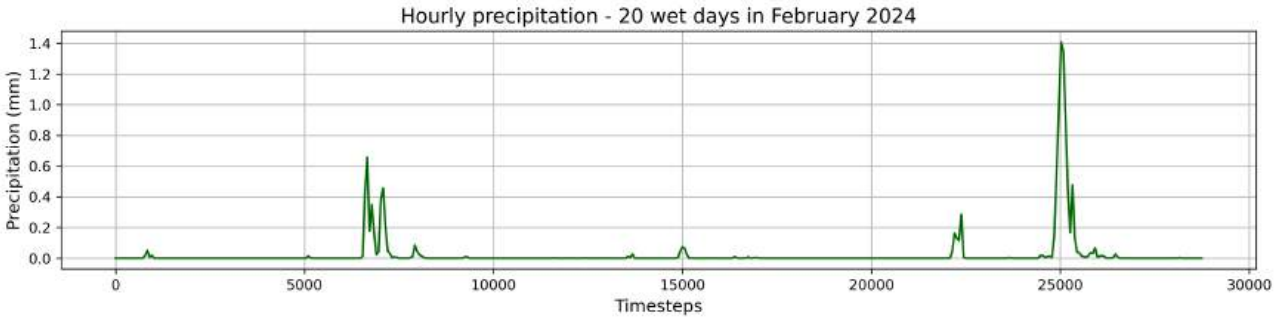


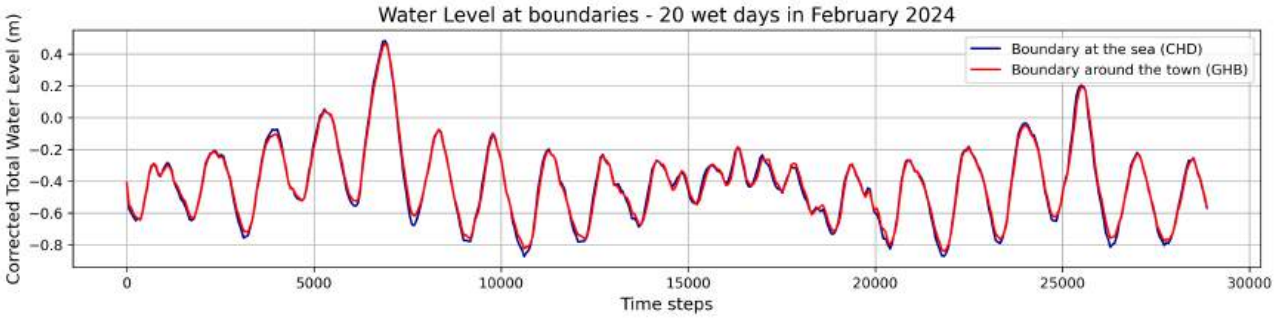
Figure J.13: Head levels (m) at 05 February 2024 for entire active domain

J.5.2 February 2024 20 days

A simulation is done for 01-02-2024 to 20-02-2024. The input data for precipitation and the GHB and CHD boundary are shown in Figures J.14a and J.14b.



(a) Hourly precipitation data February 2024 at location 21°3000 N, 88°1500 W. Time step 0 corresponds to 01-02-2024 and 28800 to 20-02-2024(Hersbach et al., 2023).



(b) The red line corresponds to the water levels at the mangrove boundary (GHB). The blue line corresponds to the boundary at sea (CHD). Time step 0 corresponds to 01-02-2024 and 28800 to 20-02-2024. (Copernicus Climate Change Service, 2022)

Figure J.14: Input data for precipitation and water levels at the boundaries February 2024 (20 dry days during storm). The time period is from 01-02-2024 to 20-02-2024.

Based on the precipitation and water level forcing at the boundary, the evolution of hydraulic head over time can be modelled in San Felipe. Figure J.15 shows the change of head level over time (20 days) for each observation point (P1 to P5). Agian, the head elevation over time follows approximately the same pattern at location P2, P3, P4 and P5. As observed in Figure J.12, the head level over time at location P1 differs from the other observation location.

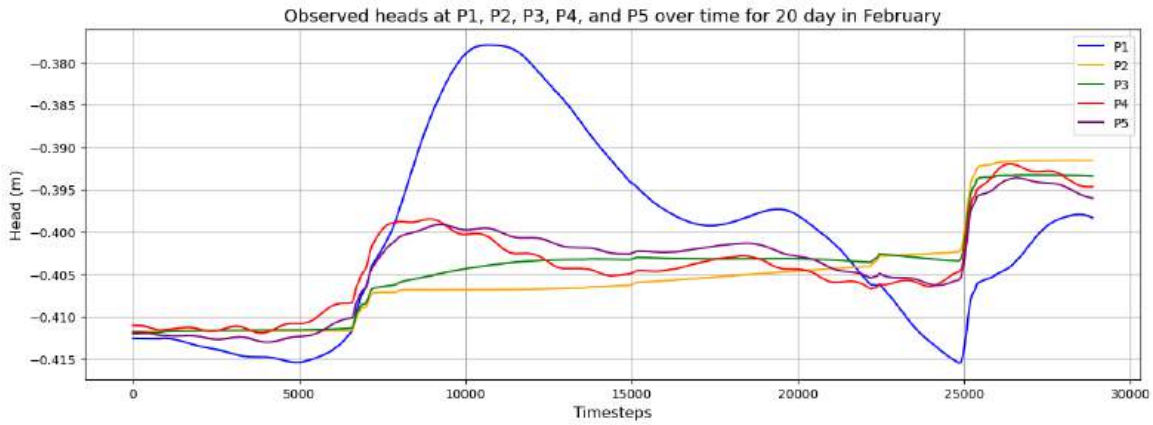


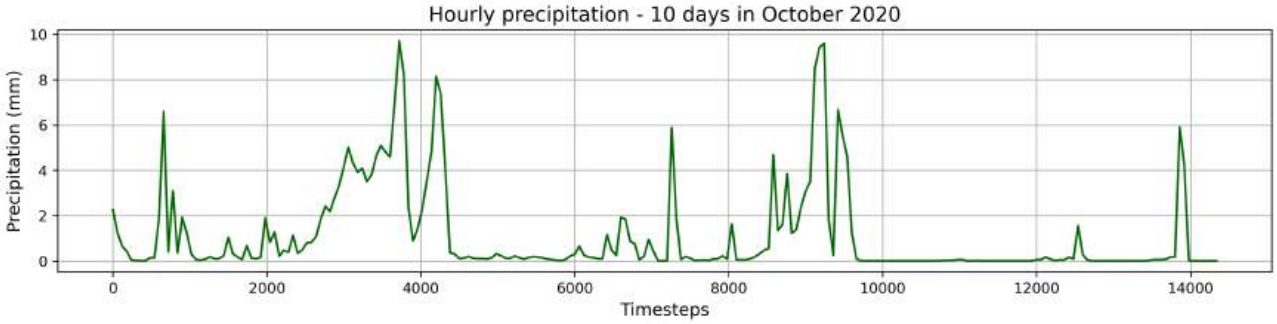
Figure J.15: Head level (m) over time at observation points (P1-P5). The time period is from 01-10-2020 to 20-10-2020.

J.6 October 2020 storm

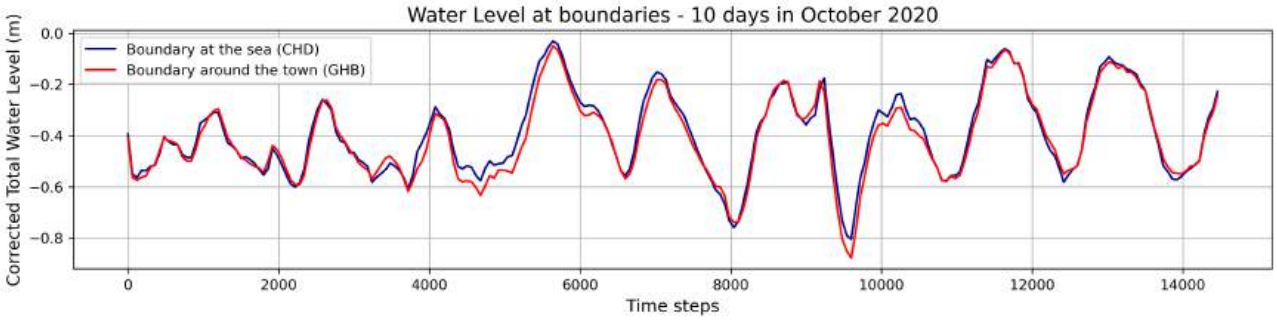
During the storms Gamma and Delta excessive precipitation values are measured in San Felipe. The groundwater model is run two time periods covering these heavy rainfall periods. The first is a simulation of the first ten days of October 2020, the second of the first twenty days of October.

J.6.1 October 2020 storm 10 days

The simulation is done for the time period 01-10-2020 to 10-10-2020. The input data for precipitation and GHB and CHD boundary are shown in Figures J.16a and J.16b. The precipitation data shows several moments in time with heavy rainfall.



(a) Hourly precipitation data October 2020 at location 21°3000 N, 88°1500 W. Time step 0 corresponds to 01-10-2020 and 14000 to 10-10-2020(Hersbach et al., 2023).



(b) The red line corresponds to the water levels at the mangrove boundary (GHB). The blue line corresponds to the boundary at sea (CHD). Time step 0 corresponds to 01-10-2020 and 14000 to 10-10-2020. (Copernicus Climate Change Service, 2022)

Figure J.16: Input data for precipitation and water levels at the boundaries October 2020 (10 days during hurricane Gamma and Delta).

Based on the precipitation and water level forcing at the boundary, the evolution of hydraulic head over time can be modelled in San Felipe. Figure J.17 shows the change of head level over time (10 days) for each observation point (P1 to P5). The head elevation over time follows approximately the same pattern at location P2, P3, P4 and P5. Observation point P1 shows a slight lower head elevation over time than the other observation point.

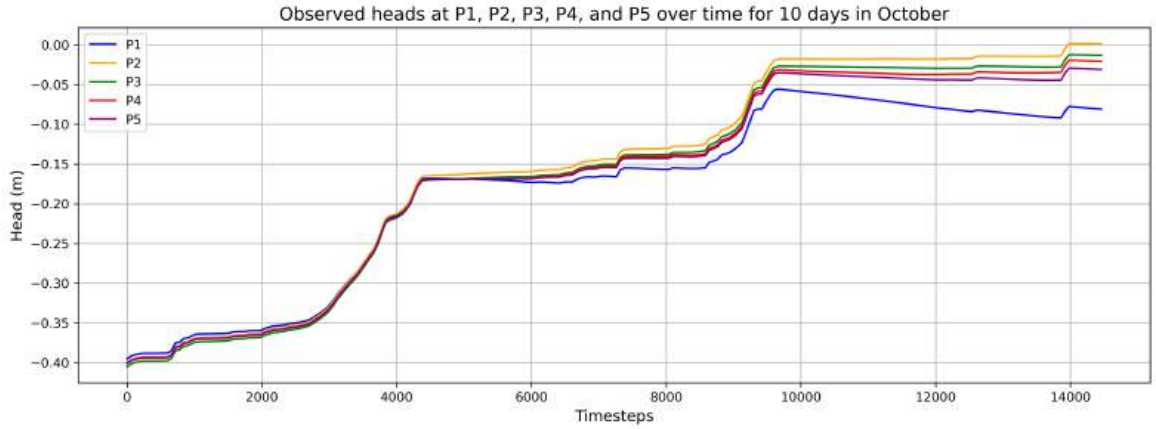


Figure J.17: Head level (m) over time at observation points (P1-P5). The time period is from 01-10-2020 to 10-10-2020 (10 days).

The head level over time at all observation points is given in Figure J.18. After 10 days, the highest head levels are reached at the observation points. As described in Section 5.2.5, a flood will occur in case the head level is higher than the elevation at that location. Figure J.18 shows the difference in elevation level and water head at all location within the domain of San Felipe. The green locations shows the areas that are safe for flooding, the red locations the areas more prone to flooding. After the first 10 days in October a flood occurs at approximately location [372400, 2384800] (red dot in Figure J.18).

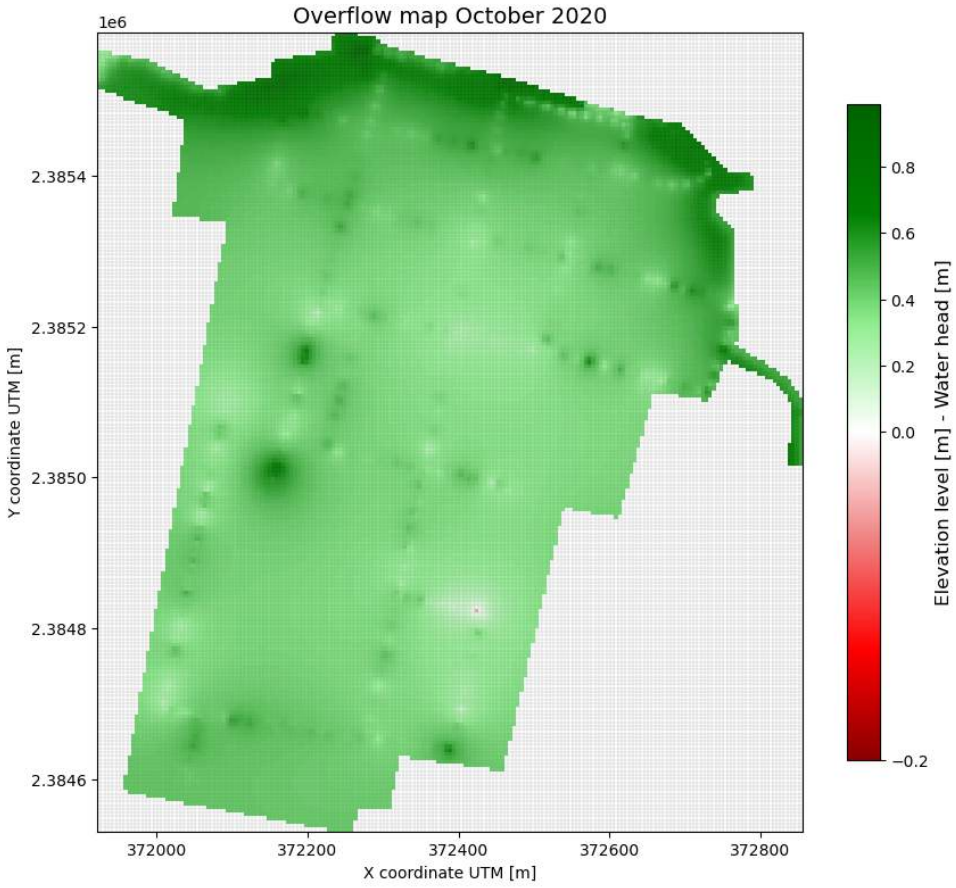
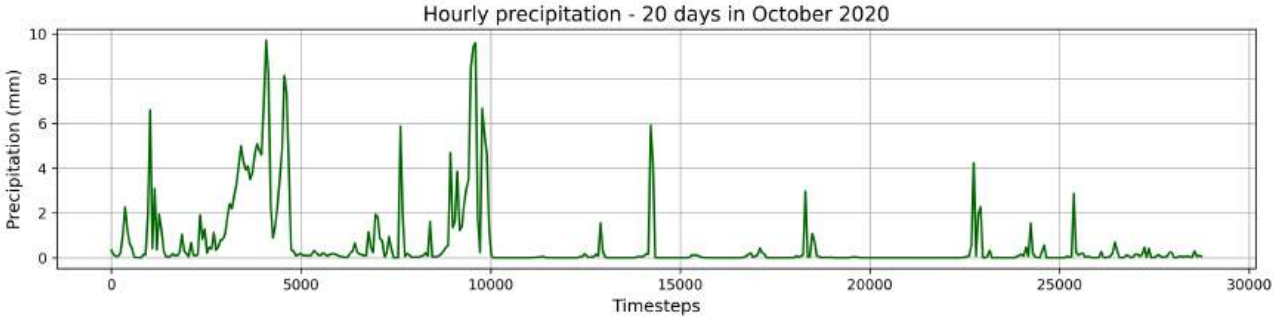


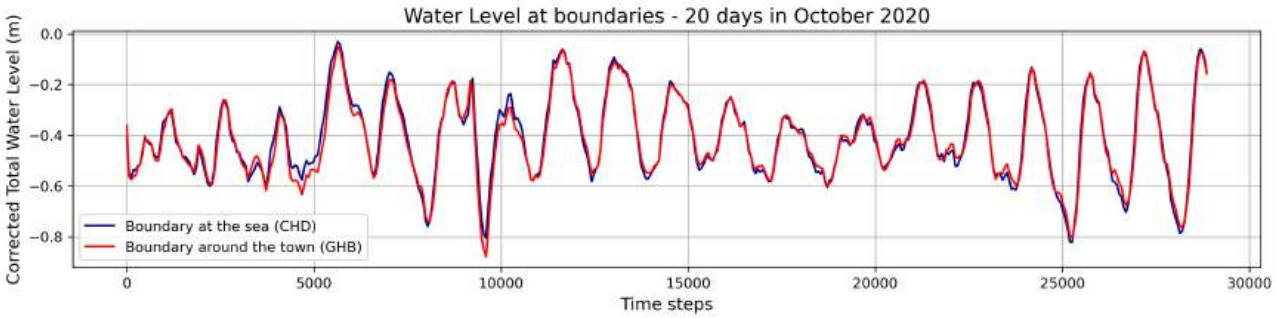
Figure J.18: Overflow map at 10-10-2020. Red shows the flooded areas modelled. Green shows the safe areas (no flooding). The critical areas are displayed in white, as these are the location that are close head levels where flooding occurs.

J.6.2 October 2020 storm 20 days

The simulation is done for the time period 01-10-2020 to 20-10-2020. The input data for precipitation and GHB and CHD boundary are shown in Figures J.19a and J.19. The first 14400 time steps have the same input data as the simulation for 10 days in October.



(a) Hourly precipitation data October 2020 at location 21°3000 N, 88°1500 W. Time step 0 corresponds to 01-10-2020 and 28800 to 20-10-2020 (Hersbach et al., 2023).



(b) The red line corresponds to the water levels at the mangrove boundary (GHB). The blue line corresponds to the boundary at sea (CHD). Time step 0 corresponds to 01-10-2020 and 28800 to 20-10-2020. (Copernicus Climate Change Service, 2022)

Figure J.19: Input data for precipitation and water levels at the boundaries October 2020 (20 days during hurricane Gamma and Delta). The time period is from 01-10-2020 to 20-10-2020

Based on the precipitation and water level forcing at the boundary, the evolution of hydraulic head over time can be modelled in San Felipe. Figure J.17 shows the change of head level over time (20 days) for each observation point (P1 to P5). The head elevation over time follows approximately the same pattern at location P2, P3, P4 and P5. Observation point P1 shows a slight lower head elevation over time than the other observation point.

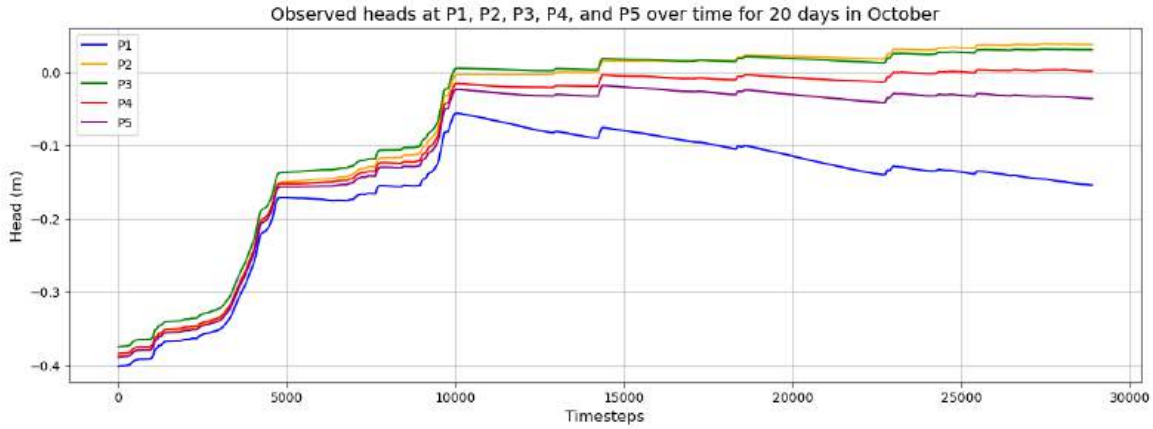


Figure J.20: Head level (m) over time at observation points (P1-P5). The time period is from 01-10-2020 to 20-10-2020.

J.7 Simulation time MODFLOW

The storm in February and the excessive precipitation rainfall in October are both modelled for a time period of 10 and 20 days. Figures J.11 and J.14 show that the first 10 days are covered by the same input data (precipitation and water levels at the boundaries). The same can be seen in Figure J.16 and J.19. The differences in head level over time for a time period of 10 and 20 days are described for February and October.

February
All observation locations show the same evolution of head level over time for the first 10 days for both simulation periods. When looking at the first 14400 time steps, the head level magnitude is slightly higher for the simulation of 10 days than the simulation of 20 days. The simulation of 20 days covers a larger time period. The second part of the simulation of 20 days shows approximately the same head level for observation location P2, P3, P4 and P5. The precipitation that occurs at time step 25000 is clearly visible. The simulation of 20 days shows a more stable response of head level in time than the simulation of 10 days, as the differences of head level over time are varying relatively less across the observation locations.

October
All observation locations show the same evolution of head level over time for the first 10 days for both simulation periods (10 and 20 days). The simulation covering a time period of 10 days shows the same patterns across P1, P2, P3, P4 and P5. The simulation of 20 days shows a larger time period. The second part of the simulated 20 days shows the same pattern as observed in the simulation of 10 days.

Based on the similarities observed in the simulations of 10 days and 20 days, it can be concluded that the running time is important. The simulation that covers 20 days, shows a more stable solution than the simulation of 10 days. From the simulations of February and October it can also be concluded that the overall response of the head over time is comparable for both time periods.

Appendix K

Building typologies



21.5642; -88.2336

Typology CL



21.5673; -88.2348

Typology CM



21.5646; -88.2337

Typology CH



21.5649; -88.2338

Typology ML



21.5667; -88.2346

Typology MM



21.5682; -88.2369

Typology MH



21.5664; -88.2322

Typology TC



21.5679; -88.2351

Typology TM



21.5639; -88.2336

Typology MT

Figure K.1: Representative buildings and their assigned typologies.

Appendix L

Structural Impact

L.1 Extracting flood hazard from SFINCS

A set of markers was selected using Google Earth which were used to store intermediate results in SFINCS output files for a specific set of numerical cells. The intermediate results are shown every 10 minutes of the simulation. Markers were placed on the streets of San Felipe at each cross-section and approximately every 50 m in between. The results, the maximum inundation level and the total inundation time, at these marker points are shown in Figure L.1 and Figure L.2.

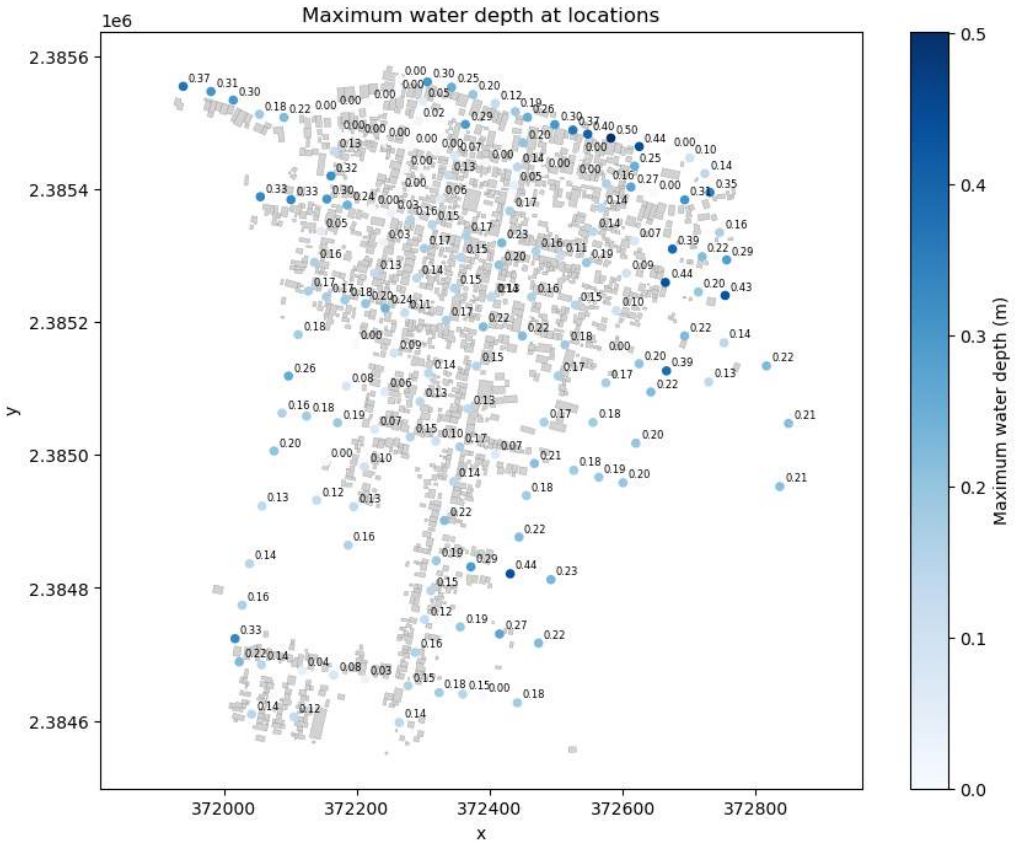


Figure L.1: Maximum inundation level for the set of markers in San Felipe according to the SFINCS simulation for the February 2024 flooding

L.2 K-Means Clustering

Initial attempts focused on defining spatial flood zones with uniform flood characteristics. However, analysis of the SFINCS results shows too much local variability in inundation depth and inundation duration. Neighbouring

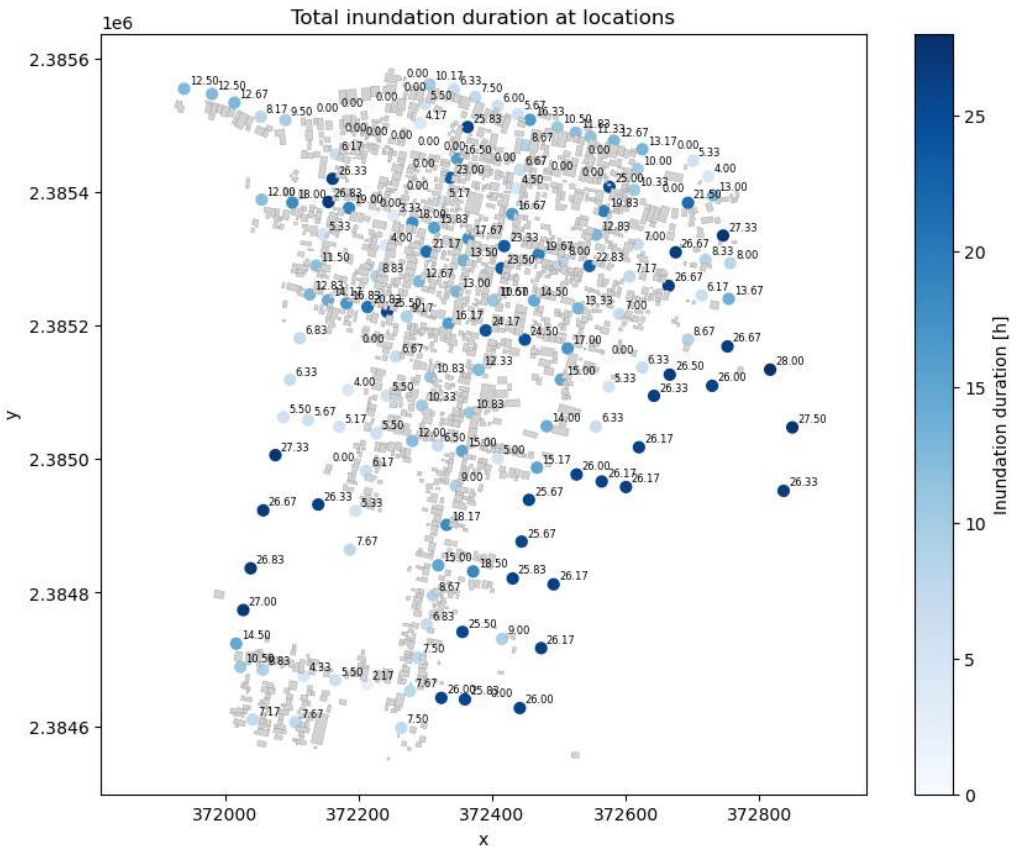


Figure L.2: Total inundation time for the set of markers in San Felipe according to the SFINCS simulation for the February 2024 flooding

marker points frequently shows substantially different flood characteristics. As a result, geographically defined hazard zones are considered unsuitable.

Instead, a K-Means clustering approach is applied to group model output points based on similarity in maximum inundation depth and inundation duration. The resulting clusters represent distinct flood regimes and are used as the basis for the damage assessment.

Clustering is performed on building-level flood parameters rather than observation points. Each building was assigned the flood conditions of its nearest observation point. This ensured that the clustering procedure reflected the actual distribution of the building stock within the study area instead of the spatial distribution of observation points.Buildings more than 50 m from the nearest observation point were excluded from the analysis because the representativeness of the assigned hydraulic conditions could no longer be guaranteed. In the further clustering process, observation points that are not closest to at minimum one of the buildings in San Felipe are also neglected. Both adjustments ensure a more accurate clustering that can be used to compare flood damage across buildings in San Felipe.

Although cluster validation metrics such as the silhouette score are evaluated, the clustering is not primarily intended to identify natural groupings within the data. Instead, clustering is used as a practical tool to partition buildings into groups with similar inundation characteristics. Therefore, the selected number of clusters is based on achieving sufficient homogeneity in inundation depth and duration within each cluster while maintaining a manageable number of representative building assessments.

Ten clusters were selected as a balance between the elbow method, silhouette score and practical applicability. Also, the mean and worst standard deviations decreased to acceptable values with ten clusters. Increasing the number of clusters beyond ten resulted in only marginal improvements in clustering performance, see Figure L.3, Figure L.4 and Figure L.5.

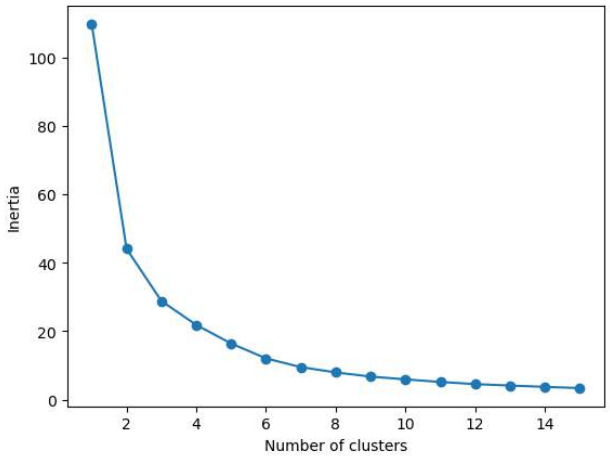


Figure L.3: Elbow method score for varying k from 2 to 15

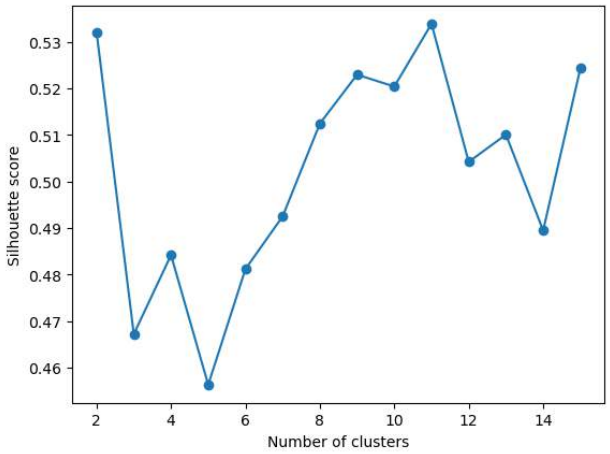


Figure L.4: Silhouette score for varying k from 2 to 15

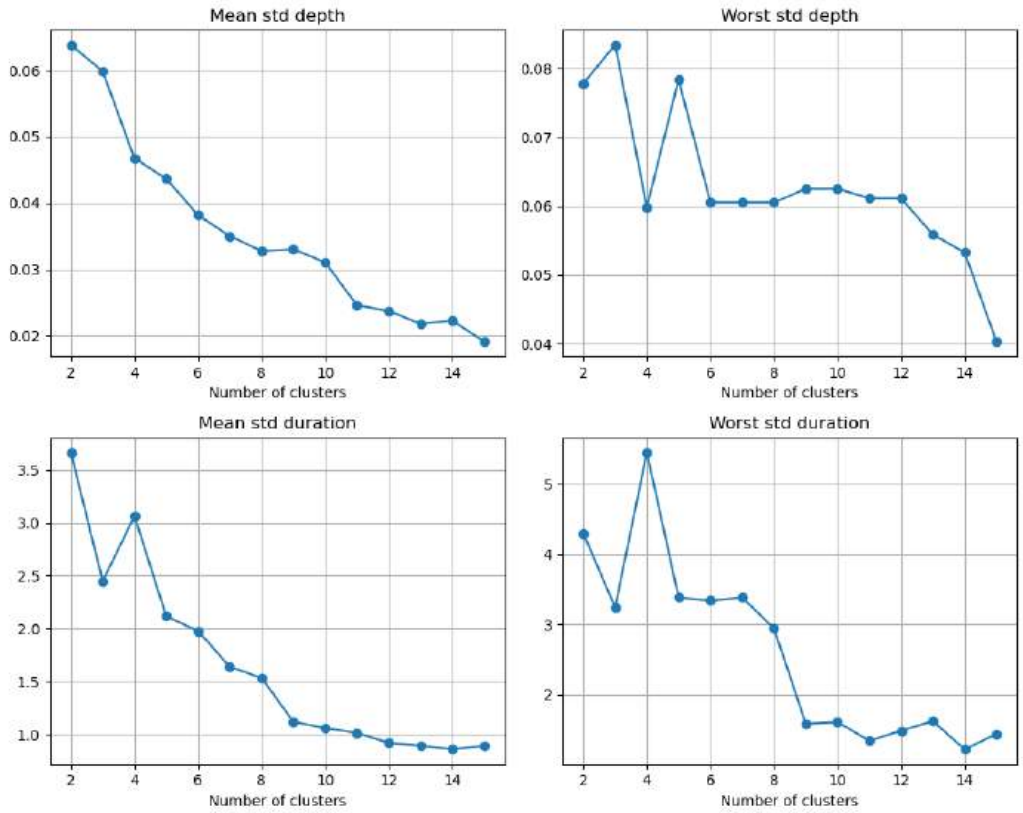


Figure L.5: Mean and worst standard deviations for varying k from 2 to 15

Appendix M

50-Year Return Period Calculation

M.1 Precipitation

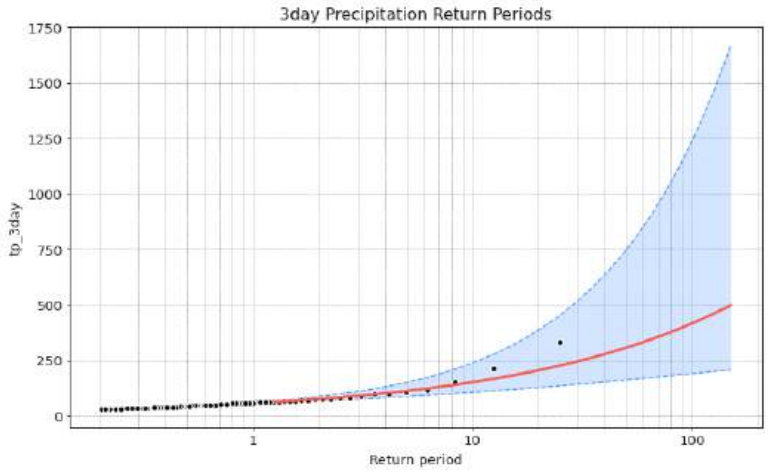


Figure M.1: 50-Year Return Period Calculation Wind

M.2 Storm Surge

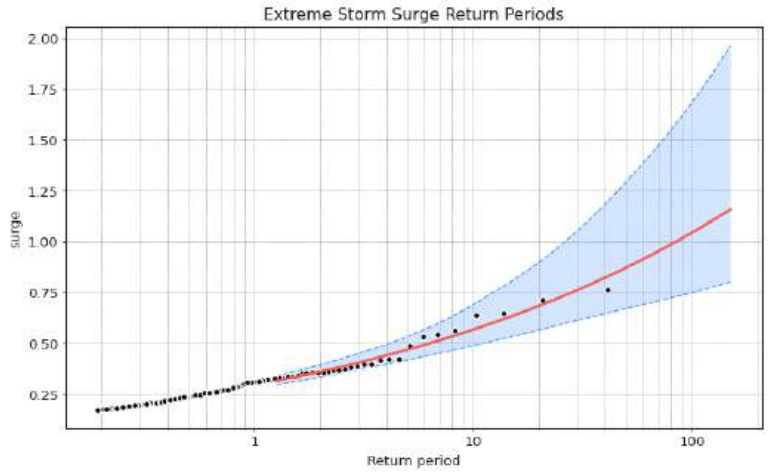
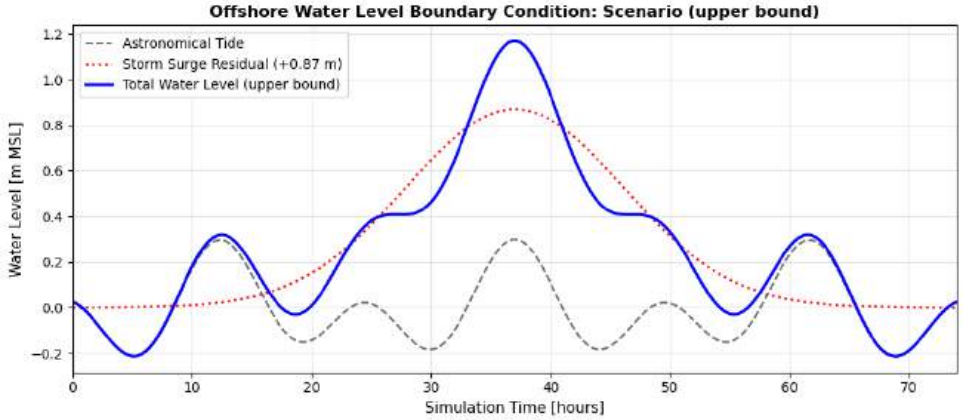


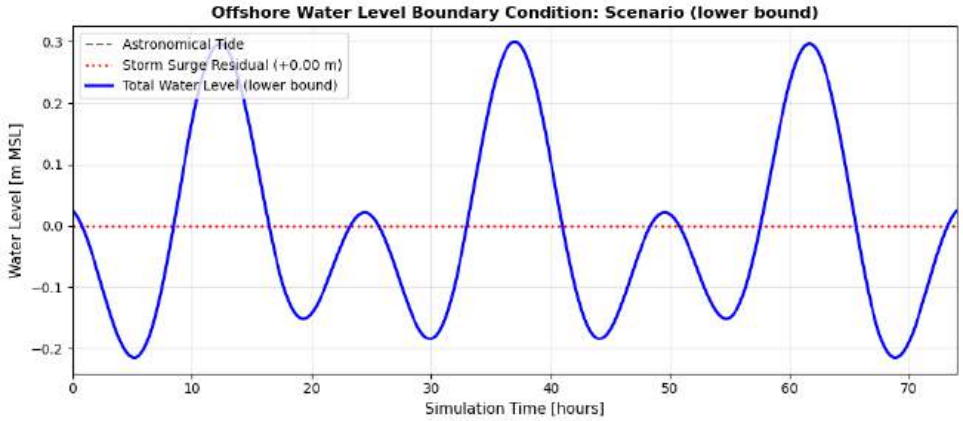
Figure M.2: 50-Year Return Period Calculation Storm Surge

Appendix N

Synthetic forcings

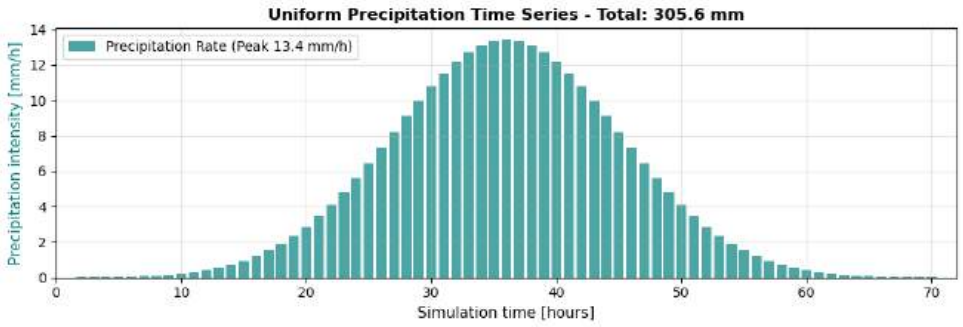


(a) Upper bound scenario (storm surge residual +0.87 m).

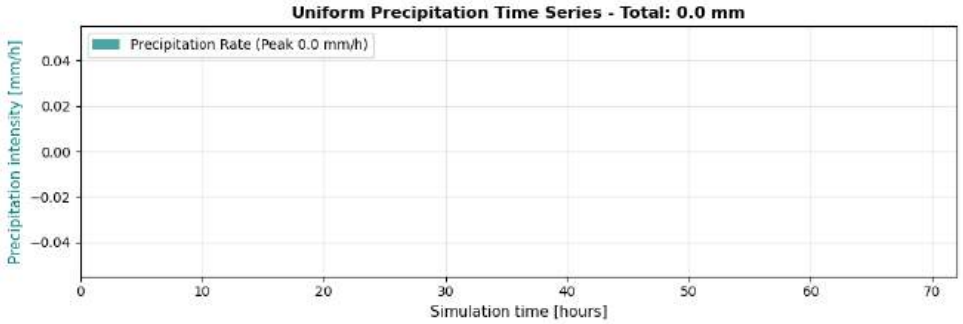


(b) Lower bound scenario (astronomical tide only).

Figure N.1: Offshore water level boundary conditions for the surge scenarios.



(a) Upper bound scenario (total 305.6 mm).



(b) Lower bound scenario (total 0.0 mm).

Figure N.2: Uniform precipitation time series for the precipitation scenarios.

Appendix O

Soil AI box with soil samples San Felipe

Soil samples are retrieved in San Felipe by staff of UNAM. The locations where soil samples are retrieved are shown in Figure O.1 and O.2.



Figure O.1: First location where soil sample 1 is retrieved



Figure O.2: Second location where soil sample 2 is retrieved

The samples were equally distributed in a soil AI box (set-up of box can be found in Figure O.3) and pictures are made of the two different soil samples, see Figures O.4 and O.5.



Figure O.3: Soil AI box



(a) First picture of Sample 1 in soil AI box- San Felipe

(b) Second picture of Sample 1 in soil AI box - San Felipe

Figure O.4: Pictures of soil sample 1 in soil AI box



(a) First picture of Sample 2 in soil AI box- San Felipe



(b) Second picture of Sample 2 in soil AI box - San Felipe

Figure O.5: Pictures of soil sample 2 in soil AI box

A pixel density of 11.22 px/mm is used, assuming that all soil is at the bottom of the box. The AI tool for soils from (deepsoil, 2026) processes Figures O.4 and O.5. This results in the grain-size distributions of Figures O.6 and O.7.



(a) First outcome of soil sample 1 after soil AI processing



(b) Second outcome of soil sample 1 after soil AI processing

Figure O.6: Pictures of outcomes after processing soil sample 1 in soil AI box



(a) First outcome of soil sample 2 after soil AI processing



(b) Second outcome of soil sample 2 after soil AI processing

Figure O.7: Pictures of outcomes after processing soil sample 2 in soil AI box